STRUCTURE-COMPOSITION-ACTIVITY RELATIONSHIPS

IN TRANSITION-METAL OXIDE AND OXYHYDROXIDE

OXYGEN-EVOLUTION ELECTROCATALYSTS

by

LENA TROTOCHAUD

A DISSERTATION

Presented to the Department of Chemistry and Biochemistry
and the Graduate School of the University of Oregon
in partial fulfillment of the requirements
for the degree of
Doctor of Philosophy

June 2014

DISSERTATION APPROVAL PAGE

Student: Lena Trotochaud

Title: Structure-Composition-Activity Relationships in Transition-Metal Oxide and Oxyhydroxide Oxygen-Evolution Electrocatalysts

This dissertation has been accepted and approved in partial fulfillment of the requirements for the Doctor of Philosophy degree in the Department of Chemistry and Biochemistry by:

Dr. Darren W. Johnson   Chairperson
Dr. Shannon W. Boettcher   Advisor
Dr. Mark C. Lonergan   Core Member
Dr. Richard P. Taylor   Institutional Representative

and

Kimberly Andrews Espy   Vice President for Research and Innovation;
                            Dean of the Graduate School

Original approval signatures are on file with the University of Oregon Graduate School.

Degree awarded June 2014

DISSERTATION ABSTRACT

Lena Trotochaud

Doctor of Philosophy

Department of Chemistry and Biochemistry

June 2014

Title: Structure-Composition-Activity Relationships in Transition-Metal Oxide and Oxyhydroxide Oxygen-Evolution Electrocatalysts

Solar water-splitting is a potentially transformative renewable energy technology. Slow kinetics of the oxygen evolution reaction (OER) limit the efficiency of solar-water-splitting devices, thus constituting a hurdle to widespread implementation of this technology. Catalysts must be stable under highly oxidizing conditions in aqueous electrolyte and minimally absorb light. A grand goal of OER catalysis research is the design of new materials with higher efficiencies enabled by comprehensive understanding of the fundamental chemistry behind catalyst activity. However, little progress has been made towards this goal to date.

This dissertation details work addressing major challenges in the field of OER catalysis. Chapter I introduces the current state-of-the-art and challenges in the field. Chapter II highlights work using ultra-thin films as a platform for fundamental study and comparison of catalyst activity. Key results of this work are (1) the identification of a $Ni_{0.9}Fe_{0.1}OOH$ catalyst displaying the highest OER activity in base to date and (2) that in base, many transition-metal oxides transform to layered oxyhydroxide materials which are the active catalysts. The latter result is critical in the context of understanding structure-activity relationships in OER catalysts. Chapter III explores the optical

properties of these catalysts, using *in situ* spectroelectrochemistry to quantify their optical absorption. A new figure-of-merit for catalyst performance is developed which considers both optical and kinetic losses due to the catalyst and describes how these factors together affect the efficiency of composite semiconductor/catalyst photoanodes. In Chapter IV, the fundamental structure-composition-activity relationships in $Ni_{1-x}Fe_xOOH$ catalysts are systematically investigated. This work shows that nearly all previous studies of Ni-based catalysts were likely affected by the presence of Fe impurities, a realization which holds significant weight for future study of Ni-based catalyst materials. Chapter V discusses the synthesis of tin-titanium oxide nanoparticles with tunable lattice constants. These materials could be used to make high-surface-area supports for thin layers of OER catalysts, which is important for maximizing catalyst surface area, minimizing the use of precious-metal catalysts, and optimizing 3D structure for enhanced mass/bubble transport. Finally, Chapter VI summarizes this work and outlines directions for future research.

This work contains previously published and unpublished co-authored material.

CURRICULUM VITAE

NAME OF AUTHOR: Lena Trotochaud

GRADUATE AND UNDERGRADUATE SCHOOLS ATTENDED:

> University of Oregon, Eugene
> University of Georgia, Athens

DEGREES AWARDED:

> Doctor of Philosophy, Chemistry, 2014, University of Oregon
> Master of Science, Chemistry, 2011, University of Oregon
> Bachelor of Science, Chemistry – ACS Certified, 2009, University of Georgia

AREAS OF SPECIAL INTEREST:

> Electrochemistry
> > Heterogeneous Catalysis
> Materials Science
> > Thin Films
> > Nanomaterials

PROFESSIONAL EXPERIENCE:

> Outreach Fellow, Center for Sustainable Materials Chemistry, 2012-2013
> > Completed curricula for 7 advanced chemistry labs and 4 lab-related demonstrations during 6-week internship at a rural Oregon high school, immediately benefiting ~30 students; emphasis on development of labs that generate zero hazardous waste and are economically sustainable for rural school districts

> Graduate Research Assistant, University of Oregon, 2010-2014
> > Inorganic materials research for solar energy conversion and storage; emphasis in electrochemistry and characterization of catalyst thin films and nanomaterials; mentor to graduate (4), undergraduate (6), and high school (2) student researchers

> Graduate Teaching Fellow, University of Oregon, 2009-2010
> > Taught three-term sequence of organic chemistry laboratory courses

GRANTS, AWARDS, AND HONORS:

Travel Award, University of Oregon Women in Graduate Sciences, June 2013

Outreach Fellowship, Center for Sustainable Materials Chemistry, 2012-2013

Best Poster, "Solution-Cast Metal Oxide Thin Film Electrocatalysts for Oxygen Evolution", UO Materials Science Institute / IGERT Conference, Sept. 2012

Cum Laude, Bachelor of Science, Chemistry – ACS Certified, University of Georgia, May 2009

HOPE Scholarship, University of Georgia, 2005-2009

Harris Scholarship, University of Georgia, 2005-2009

PUBLICATIONS:

Trotochaud, L; Young, S.L.; Ranney, J.K.; Boettcher, S.W. "Nickel-Iron Oxyhydroxide Oxygen-Evolution Electrocatalysts: The Role of Intentional and Incidental Fe Incorporation" Submitted for publication on March 8, 2014 to *Journal of the American Chemical Society*.

Trotochaud, L; Boettcher, S.W. "Precise Oxygen Evolution Catalysts: Status and Opportunities" *Scripta Materialia*, **2014**, *74*, 25-32.

Trotochaud, L; Mills, T.J.; Boettcher, S.W. "An Optocatalytic Model for Semiconductor–Catalyst Water-Splitting Photoelectrodes based on *In Situ* Optical Measurements on Operational Catalysts" *Journal of Physical Chemistry Letters*, **2013**, *4*, 931-935.

Trotochaud, L; Ranney, J.K.; Williams, K.N.; Boettcher, S.W. "Solution-Cast Metal Oxide Thin Film Electrocatalysts for Oxygen Evolution" *Journal of the American Chemical Society*, **2012**, *134*, 17253-17261.

Trotochaud, L.; Boettcher, S.W. "Synthesis of Rutile Phase $Sn_xTi_{1-x}O_2$ and $(SnO_2)_x/(TiO_2)_{1-x}$ Core/Shell Nanoparticles with Tunable Lattice Constants and Controlled Morphologies" *Chemistry of Materials*, **2011**, *22*, 4920-4930.

ACKNOWLEDGMENTS

This work is dedicated to those who inspired me and all who knew them,
but who left this world too early to see the full extent of their influence.

Amanda Dabney Holmes   1979-1997
Edward "Ted" Hafer   1965-2007
Eve Marie Carson   1985-2008
Nichole Mikko-Causby 1986-2013

TABLE OF CONTENTS

LIST OF FIGURES

Figure   Page

LIST OF TABLES

CHAPTER I

PRECISE OXYGEN EVOLUTION CATALYSTS: STATUS AND OPPORTUNITIES

Portions of this chapter were previously published as Trotochaud, L; Boettcher, S.W. "Precise Oxygen Evolution Catalysts: Status and Opportunities" *Scripta Materialia*, **2014**, *74*, 25-32. L.T. wrote the paper, performed the experimental work, and made the figures. S.W.B. was the principal investigator and provided editorial assistance.

Introduction

Splitting water to generate hydrogen fuel and oxygen gas ($2H_2O \rightarrow 2H_2 + O_2$) could provide for clean, scalable, global energy storage.[1,2] The water splitting reaction is composed of two half reactions, the hydrogen evolution and oxygen evolution reactions (HER and OER, respectively).

$$
\begin{array}{llll}
\text{HER} & 2H^+ + 2e^- \rightarrow H_2 & \text{(acid)} & (1.1) \\
& 2H_2O + 2e^- \rightarrow H_2 + 2OH^- & \text{(base)} & (1.2) \\
\\
\text{OER} & 2H_2O \rightarrow 4H^+ + O_2 + 4e^- & \text{(acid)} & (1.3) \\
& 4OH^- \rightarrow 2H_2O + O_2 + 4e^- & \text{(base)} & (1.4)
\end{array}
$$
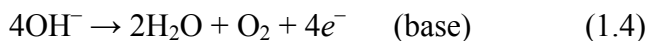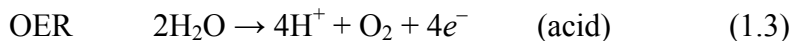
The slow kinetics of the OER limit the efficiency of both photon-driven and electricity-driven water splitting.[2,3] Generally accepted mechanisms for water oxidation include four sequential electron transfer steps. Each electron transfer is typically coupled with a proton transfer. The OER intermediates are stabilized by the catalyst, for example, as surface bound peroxo- or oxo- species. The relative stabilities of these intermediates and the activation barriers between them dictate which step is rate-determining and thus the overall water oxidation rate.[4] The identity of the surface intermediates depends on the reaction conditions (e.g. pH) and likely the catalyst material. Work to identify precise mechanistic pathways has been attempted[5] but conclusive evidence identifying intermediates is limited.[6] A mechanistic understanding of the rate-determining steps would provide insight into how structure and composition can be tuned to modify the energetics of the reaction intermediates and thus increase reaction rates.

One longstanding challenge in OER catalysis is that typically studied catalysts are poorly defined, which makes relating structural, compositional, and electronic features to the observed activity trends difficult. Well-defined catalysts allow for accurate assessment of the intrinsic activity and are needed for improving mechanistic understanding. Single crystals, precise nanoparticles, homogeneous molecular clusters, and ultra-thin films are reasonable model systems for studying catalytic processes and mechanisms, but significant challenges remain in precisely tuning composition and structure, unambiguously identifying the active sites, understanding changes to the structure *in situ*, and maintaining long-term stability for applications.

This chapter will examine recent advances in oxygen evolution reaction (OER) catalysis using well-defined/characterized systems and propose paths for improvement. First, a brief review is presented on our research on ultra-thin film catalysts (to be discussed in detail in Chapters II – IV), and compare those results to other well-defined systems. The thin film geometry is advantageous for study of heterogeneous catalysts because the deposited catalyst films are essentially "all surface". Through these experiments we have demonstrated that $Ni_{0.9}Fe_{0.1}OOH$ has the highest OER activity measured to date in basic media. Second, we discuss several recent reports that many OER electrocatalysts undergo structural and chemical changes during the OER in basic solution. We describe the implications of these findings on how OER catalysts are studied and, ultimately, designed.

The Need for Well-Defined OER Catalysts and Standardized Measurements

Increasing the surface area of heterogeneous OER catalysts usually decreases the overpotential for a given current density by introducing more active sites per unit geometric area. The resulting materials are often poorly defined structurally and their microscopic surface area, number of active sites, active-site distribution, compositional homogeneity, and electron and mass (e.g. bubble) transport properties are challenging to measure (and correct for). High-surface-area heterogeneous catalysts, while potentially of technological relevance, limit the ability to correlate experimental results with theoretical calculations.[4] For example, Trasatti[7] identifies RuO_2 and IrO_2 as the most active catalysts in both acid and base. This conclusion is not consistent with our work on well-defined

thin films of the same materials,[8] nor with other recent thin-film measurements on less well-defined but similar systems[9,10], which show a range of first row transition-metal oxides/hydroxides/oxyhydroxides to have higher activity than IrO_2 in basic solution. Recently published work by Bajdich et al., however, correlates well with experimental results on well-defined catalyst systems (including our ultra-thin films[8]), showing an enhancement in OER activity for doped $Ni_{0.25}Co_{0.75}OOH$ in comparison to a pure β-CoOOH surface.[11]

To quantitatively compare the activity of catalysts and uncover true structure/composition/activity relationships, a common performance metric is required. We find that the best metric is the turn-over frequency (TOF) at steady state (i.e. after stabilization of the potential in response to an applied current). The TOF is defined as the number of times per second a single active site (which we assume to be a single metal cation) evolves an O_2 molecule (by accepting four electrons from solution). Because TOFs are typically potential dependent (based on Butler-Volmer or Tafel kinetics),[12] the overpotential at which the TOF is measured must be reported. TOFs are often not reported due to difficulties in determining the amount of active catalyst in porous electrodes. Sometimes the surface area is estimated based on the capacitance of the electrode, however this is often inaccurate because the capacitance per unit real surface area can vary widely depending on surface chemistry and porosity.[13] Surface areas based on imaging the particle size distribution directly with an electron microscope, or obtained via gas-adsorption are more accurate,[14] as long as the catalyst is crystalline and the surface does not change under OER conditions. Such conditions, however, often do not hold (see discussion below).

Precise measurements of OER TOFs also require correct referencing to the thermodynamic potential of the oxygen couple in the electrolyte, as well as precise measurement of, and correction for, uncompensated solution resistance R_u. Errors in applied potential of as little as 20-30 mV can lead to order-of-magnitude errors in the reported TOF, due to the exponential dependence of TOF on driving force. We find that the simplest method for determining the thermodynamic OER potential is to measure the reversible hydrogen potential (RHE) by cycling freshly cleaned Pt in a H_2 sparged electrolyte solution. The point of zero current is 0 V vs. RHE, and the OER potential is

1.23 V positive of RHE. R_u can be minimized through use of a Luggin capillary and high concentrations of supporting electrolyte. Minimization of R_u is important to reduce errors associated with correction for R_u. We find that the best estimates of the R_u are obtained from high-frequency (~10–50 kHz) impedance measurements.[8] Under these conditions the impedance is purely resistive (phase angle near zero) and can be associated solely with the uncompensated series resistance.

For molecular catalysts, the relevant driving force for the oxidation reaction (i.e. the equivalent of the overpotential) is often not reported because chemical oxidants are used to drive the reaction instead of an electrode. However, the solution potential of oxidant couples (e.g. $Ce^{3+/4+}$ or $Ru(bpy)_3^{2+/3+}$) can be measured directly versus a reference electrode to estimate the driving force of the chemical oxidant. The lack of driving force data can lead to confusion over relative activity of molecular catalysts versus heterogeneous ones. Relatively large (~500 mV) driving forces are typically applied to molecular catalysts, as highly oxidizing reagents are used.

Single-Crystal Electrodes

For heterogeneous catalysts, single crystals provide a useful platform for the study of catalysis on precise surfaces. The difficulty in synthesizing high quality, sufficiently conductive single crystals of the desired oxides prohibits their routine use. Single-crystal OER results are limited.[15-17] In the absence of single crystals, study of catalytic activity on specific crystal faces is enabled by epitaxial growth on appropriate lattice-matched substrates.[18,19] Epitaxial growth of oxides, however, is also difficult.

Homogeneous Molecular Catalysts

Soluble homogeneous catalysts composed of molecularly defined complexes/clusters are useful model systems because the OER mechanism and possible intermediates are amenable to identification using powerful molecular analysis techniques (e.g. IR, NMR, etc.). Molecular Mn_3CaO_4 and Co_4O_4 cubanes have been targeted for their structural similarity to the Mn_4CaO_5 oxygen evolving complex (OEC) in photosystem II,[20-22] although no truly functional molecular OEC mimics have been reported to date. Ru complexes have received significant attention,[23] but the stability of

4

these complexes has been questioned.[24] Organic ligands are thermodynamically unstable under OER conditions, and it is unclear that conditions can be found to kinetically stabilize them. The intrinsic instability of the complexes makes it not always clear whether or not reported catalysis data originates from the molecule or the decomposition products.[25]

Because of the possibility for enhanced stability, all-inorganic clusters are promising models for the OER active sites. TOFs of 1.2 per Co have been reported for polyoxometalates tested by Hill and coworkers using a $[Ru(bpy)_3]^{3+}$ oxidant with an effective overpotential of ~480 mV.[26,27] Although some controversy exists about the pH range over which the catalyst is stable,[28] it appears to be a stable molecular catalyst between pH 6 and 8.[29,30] Recently published work by Vickers et al. confirms the stability of the polyoxometalate and its identity as the catalytically active species under the conditions originally described by Yin et al.[31] Based on their findings, the authors strongly caution against activity comparisons for molecular species studied under different experimental conditions. Recent unpublished data presented by Hill, suggests that substitution of the P with V in the polyoxometalate increases the activity by several orders of magnitude.[32] If correct, this would be the first demonstration that molecular modification of the single site catalysts leads to the ability to dramatically tune activity. To date, the activities of the most active homogeneous catalysts still lag behind those of heterogeneous ones.

Nanoparticles and Crystalline Powders

Advances in the synthesis of well-defined nanoparticles[33] as well as the routine availability of high-resolution TEM imaging and chemical composition mapping are allowing nanoparticle catalysts to serve as model systems that also can be utilized in applications. Suntivich et al. developed a useful rotating-disk electrode method for characterizing activities of nanoparticle OER catalysts. The nanoparticles are supported in a conducting carbon/Nafion composite film.[14] The carbon ensures that the nanoparticles are electrically wired to the substrate via low-resistance carbon percolation pathways. The Nafion binds the solid components together and also provides a degree of hydroxide ion conductivity. The surface areas of the catalyst powders are estimated from

SEM measurements and BET so that the specific surface-area activities can be compared. For stable particles of known crystal structure, accurate accounting of the number of surface atoms is possible, therefore enabling calculation of the TOF. The disadvantages of this technique are the potential for the background oxidation of the conductive C at high current densities. Benchmark activities for IrO_2 and RuO_2 nanoparticles were determined by Lee et al. using this method.[34] Tilley and coworkers studied well-defined supported Co_3O_4 nanoparticles of different sizes.[35] By independently measuring the surface area of the particles they concluded that there is no size dependence to the catalysis rate and that the activity increases simply as a function of increased surface area.

Nanoparticle perovskite oxides are interesting OER catalysts because the cations on both the A and B sites can be tuned within a common cubic ABO_3 crystal structure.[36] Shao-Horn and coworkers proposed a correlation between the OER activity and the occupancy of the e_g orbital of surface perovskite B-site metal cations.[37] The e_g orbital occupancy is related to the strength of the M-O bond, which has been implicated in the kinetics of the rate-determining reaction step.[38] Using this concept they identified the $Ba_{0.5}Sr_{0.5}Co_{0.8}Fe_{0.2}O_{3-\delta}$ (BSCF) as an active catalyst,[37] which appears to exhibit a per-metal site OER activity similar to $Ni_{0.9}Fe_{0.1}OOH$. As discussed below BSCF, however, is unstable under OER conditions, losing Ba and Sr to the solution, and appearing to yield a porous Co-Fe oxide or oxyhydroxide.[39,40] This instability leads to some uncertainty about the e_g occupancy of the surface Co or Fe atoms. It is unclear whether or not the e_g optimization principle is relevant specifically to BSCF or whether the correlation with the other perovskites is incidental.

Thin Films

Thin film electrocatalysts are useful for studies of structure/composition/activity relationships for a number of reasons,[8] including: (1) Electrons must only move through the thickness of the thin film to reach the underlying electrode (as opposed to μm to mm through a pellet, crystal or thick layer), and hence the electrocatalyst conductivity does not significantly influence the measured overpotential. (2) Many of the oxide materials commonly studied as electrocatalysts are semiconductors. Schottky barriers at the catalyst|solution and catalyst|metal-electrode interfaces could affect electron transport,

resulting in an additional overpotential that is dependent on the carrier concentration and crystalline quality of the semiconductor.[41] Films only a few nm thick are not thick enough to support a significant depletion region, and thus catalysis of different thin-film materials can be compared independent of carrier concentration and interfacial contact properties. (3) Catalyst compositions that are not accessible via electrodeposition or traditional high-temperature routes (e.g. due to phase separation) can be made because the film composition can be tuned by controlling the ratios of different metal ions added to the precursor solution. (4) It is difficult to accurately correct for variations in real versus geometric surface area (i.e. roughness factors) of high-surface area electrodes.[42] Ultra-thin films prepared from solution should have similar roughness factors that are at most a few times larger than unity. (5) Extensive porous structuring is limited by the ultra-thin film thickness, making the mass transport of evolving gases facile.

We developed a simple platform for deposition of ultra-thin films of metal oxide catalysts with arbitrary composition.[8] Solution casting of 2–3 nm thick films onto gold quartz-crystal-microbalance electrodes enabled quantitative comparison of the OER activity of many catalysts under essentially identical conditions. Steady-state electrokinetic (Tafel) data and TOFs for these thin films are shown in Figure 1.1. We demonstrated that $Ni_{0.9}Fe_{0.1}O_x$, with a Tafel slope of 30 mV dec^{-1} and a lower-limit TOF of 0.2 at 0.3 V overpotential, is one of the fastest OER catalysts in basic media. We also observed the *in situ* transformation of nanocrystalline Ni-containing films to redox active Ni hydroxide/oxyhydroxide phases (which are the active catalysts) as well as the inadvertent incorporation of Fe impurities from the electrolyte into the thin films (see more on both below). The composition, structure, and properties of the films can be measured using surface-analytical techniques in the absence of bulk contributions. These thin films can also be deposited on transparent substrates, enabling *in situ* optical characterization of working catalysts.[43] The disadvantage of this method is that the films are likely inhomogeneous on a molecular/nanoscopic scale, which prevents precise identification of active sites.

Thin films of cobalt phosphate (P_i)[44] and borate (B_i)[45] catalysts developed by Nocera and coworkers have been studied extensively over the past few years. The stability of these catalysts in near-neutral pH has enabled mechanistic studies under those

conditions. Surendranath et al. determined that the rate-limiting step in OER for CoP_i is preceded by a $1\ e^- + 1\ H^+$ proton-coupled electron transfer (PCET) step with phosphate in the buffered electrolyte acting as a proton acceptor.[44] Recent work by Farrow et al. compares the structure of the CoP_i and CoB_i using x-ray pair distribution function analysis.[46] They conclude that the higher activity with increased loading of the CoB_i catalyst is due to formation of microscopic domains of multilayer stacks (up to 3 layered sheets, with coherent domains ~3–4 nm in size), whereas the CoP_i material consists of smaller, single-layer domains. However the catalysts also operate under different pH conditions (pH 7 for CoP_i vs. pH 9.2 for CoB_i), which can also affect activity. The layered structure of this catalyst is similar to those of hydroxide/oxyhydroxide phases. Thin film NiB_i catalysts[47] with higher activities than the CoP_i or CoB_i catalysts have also been studied.[48] The dynamic properties and activity of the NiB_i catalyst will be discussed in more detail below.
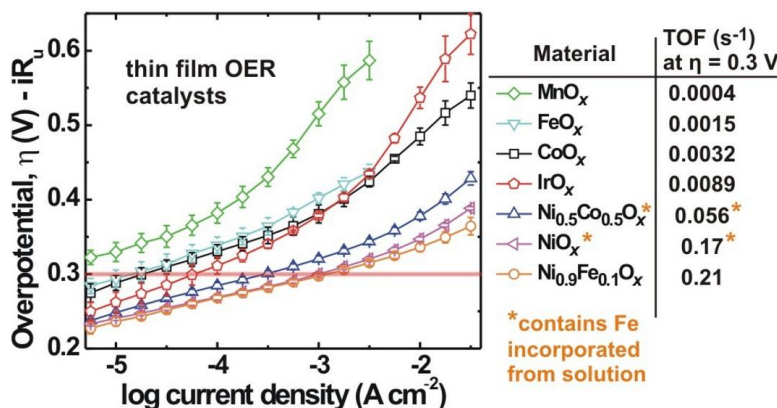
Figure 1.1. Comparison of steady-state Tafel measurements for ~2-3 nm thick films collected in 1 M KOH. The table shows the per-metal-atom TOFs calculated from the measured film mass and current at an overpotential η of 0.3 V. The film mass is precisely measured using a quartz crystal microbalance.

Subbaraman et al. studied electrodeposited metal hydroxide monolayer catalysts on Pt single crystals. They found that the "oxophilicity" of the metal cation (i.e. the M–OH bond strength) correlated with activity yielding an activity trend for hydroxides where Ni > Co > Fe > Mn,[49] similar to the trend we observe in our thin-film studies.[8] They use scanning tunneling microscopy to image the surface before and after electrochemical testing. They also observe that the deposited films are dynamic, changing

under OER conditions. This approach is powerful as it combines the ability to obtain near-atomic level resolution images of catalyst surfaces/particles and correlate those with measured activity, but without the growth of single crystals.

Smith et al. also recently reported a photochemical route to mixed-metal oxide films using organometallic precursors.[9] Various a-$Fe_{100-y-z}Co_yNi_zO_x$ compositions had high reported activities similar to the $Ni_{1-y}Fe_yOOH$ catalysts measured by us and others. But these films were relatively thick (~100–200 nm) with unknown porosity, number of active sites, and electrical properties, making direct activity comparisons impossible. Activities of selected well-defined OER catalysts are summarized in Table 1.1 and compared to the numbers obtained for the relevant thin film catalysts as described above.

Table 1.1. TOF Activities of Well-Defined OER Electrocatalysts

sample	ref.	electrolyte	η (mV)	TOF (s^{-1})	thin film sample^a	η (mV)	TOF (s^{-1})
IrO_2 NPs	34	0.1 M KOH	300	0.02	IrO_x	300	0.009
CoP_i	44	pH 7	300	0.00004	CoO_x	300	0.003
electrodep. CoO_x	50	0.1 M KOH	350	0.06	CoO_x	350	0.05
$[Co_4(H_2O)_2(PW_9O_{34})_2]^{10-}$	26	pH 8	480	1.3	CoO_x	480	1.5
electrodep. $Ni(OH)_2$	51	1 M KOH	420	0.04	$Ni(OH)_2{}^b$	420	0.23
electrodep. $Ni_{0.86}Fe_{0.14}(OH)_2$	51	1 M KOH	287	0.05	$Ni_{0.9}Fe_{0.1}O_x$	287	0.06
$Ba_{0.5}Sr_{0.5}Co_{0.8}Fe_{0.2}O_{3-\delta}$ NPs	37	0.1 M KOH	300	0.6^c	$Ni_{0.9}Fe_{0.1}O_x$	300	0.21
NiB_i	48	pH 13.85	325	1.7^d	$Ni_{0.9}Fe_{0.1}O_x$	325	0.82^d

^{a} Unless otherwise indicated, all thin film sample values are from ref. [8] and were collected in 1 M KOH. TOFs are lower limits assuming all metals in film are active.
^{b} Sample electrodeposited onto QCM in our lab from 0.1 M $Ni(NO_3)_2$ under Fe-impurity-free conditions.
^{c} Upper limit on TOF assuming only surface Co/Fe atoms are active.
^{d} NiB_i TOF calculation is based on integration of the cathodic wave in the cyclic voltammogram (CV), assuming 1.6 electrons passed per Ni center. Using the same method, we calculate a nearly identical TOF for the thin film sample of $(0.82 \times 1.6) = 1.3$.

Stability, Impurities, and Catalyst Transformation during the OER

Using traditional high-temperature synthesis methods, as-made OER catalysts are typically oxides such as NiO or Co_3O_4. However, most oxides are not thermodynamically stable under OER conditions. This fact can be seen by inspection of the potential-pH predominance-area (Pourbaix) diagrams.[52,53] In basic conditions at OER potentials, the predominant thermodynamically predicted phases of Ni and Co are NiOOH and CoOOH. We have observed, for example, that thin NiO films completely convert to NiOOH under

9

prolonged OER conditions at pH 14.[8] Evidence of the transformation can be seen in cyclic voltammetry (CV) experiments (Figure 1.2A).
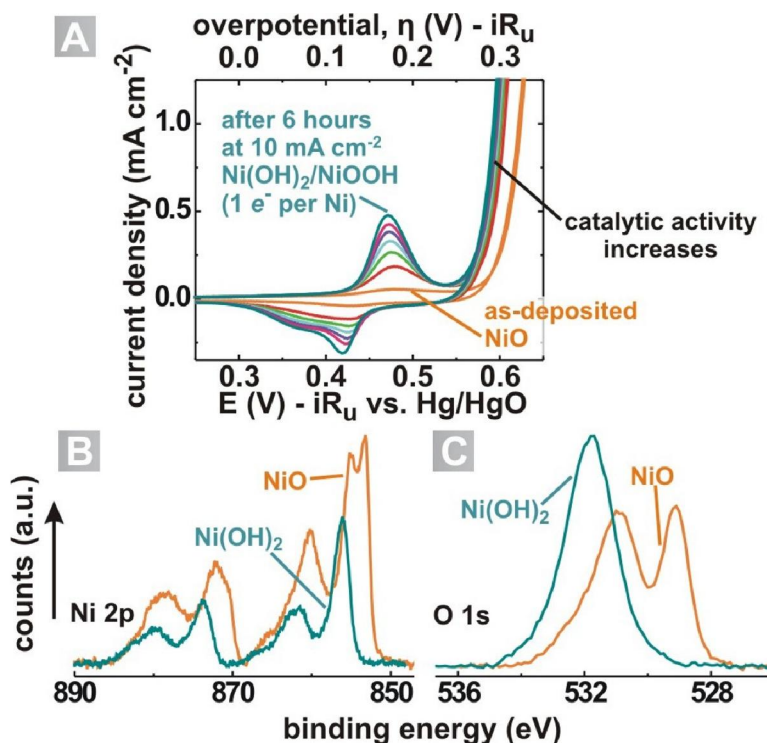
Figure 1.2. Electrochemical and spectroscopic evidence of *in situ* transformation of Ni-based oxides. (A) Periodic cyclic voltammograms track the transformation from the as-deposited crystalline NiO to the hydrous $Ni(OH)_2$/NiOOH, as evidenced by the increase in current passed during oxidation/reduction of the film. (B) Ni 2p and (C) O 1s X-ray photoelectron (XPS) spectra taken of an untreated film (orange) and after electrochemical treatment (teal) show changes characteristic for conversion from NiO to $Ni(OH)_2$.

CV scans collected for NiO films during 6 hr of electrochemical conditioning at 10 mA cm^{-2} (anodic) in 1 M KOH show an increase in the current associated with Ni redox prior to the OER current onset (Figure 1.2A). During OER, progressively more Ni atoms become accessible to the electrolyte, which is consistent with a structural transformation from a dense NiO to electrolyte porous NiOOH. Evidence for this transformation is also apparent by comparing the Ni 2p and O 1s X-ray photoelectron (XPS) spectra collected before and after electrochemical conditioning. Unlike the Ni-containing thin films, we found that Co_3O_4 was kinetically stable and did not convert to CoOOH. The surface atoms are still expected to have a chemical structure similar to CoOOH in 1 M base during the OER. Related behavior is likely for all transition metals

used for OER catalysis. These instabilities make the prediction and rationalization of OER activity based on solid-state oxide structures challenging, because the hydrated oxyhydroxide surface species that form are very different from the solid-state oxide structures (Figure 1.3).
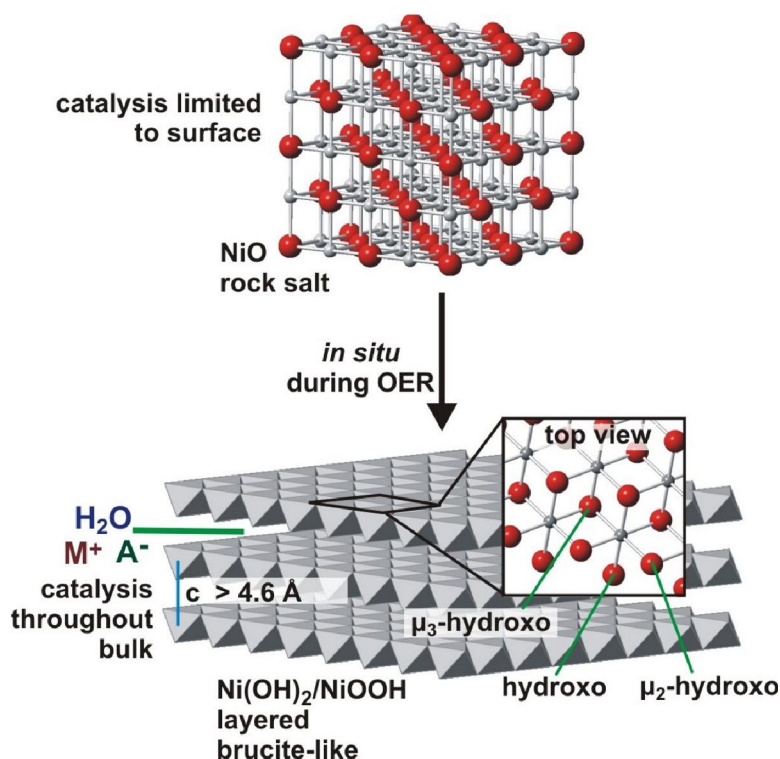
Figure 1.3. *In situ* transformation of as-synthesized NiO to layered NiOOH active catalyst. Thermally prepared thin films adopt the rock salt crystal structure. Electrochemical conditioning at OER potentials results in the formation of the highly active, layered, (Fe)NiOOH. The layered structure shown above is the more ordered β/β Ni(OH)$_2$/NiOOH. Structures with larger sheet spacing and turbostratic disorder are known as the α/γ Ni(OH)$_2$/NiOOH. The edges of the sheets are likely terminated with hydroxo and μ_2-hydroxo groups that are under-coordinated relative to the "bulk" μ_3-hydroxo bridges. Ions and solvent can move in-between the sheets, presumably making the "bulk" of the structure available for catalysis.

Lyons and coworkers have extensively studied the evolution of the surface electrochemistry of metal and metal oxide electrodes in the context of the OER.[54] They find that the surfaces are covered with layers of loosely octahedrally coordinated metal complexes that can be oxidized/reduced, which they call "surfaquo" groups. The surfaquo cations are likely the OER active sites and the concentration and electrical connectivity of these groups depend on the preparation method and history of the

electrode. The determination of the exact composition and structure of these surface sites/phases requires further investigation using *in situ* spectroscopic techniques,[54] although, as described above, the local coordination is likely similar to that of the thermodynamically favored oxyhydroxide phases.

The perovskite catalysts studied by Shao-Horn and co-workers[37] have varied kinetic stability in aqueous media. May et al. found that the surface of BSCF perovskite electrocatalysts quickly convert from the as-synthesized crystalline form to an amorphous layer during the OER.[39] The formation of this layer correlates with the loss of Ba and Sr, leaving behind a Co-Fe oxide or oxyhydroxide. The activity of the catalysts correlates with the thickness of the Co-Fe-O layer suggesting that it is the active catalyst. It also appears to be porous and is likely hydrated. The instability of BSCF might be expected, given that both Sr and Ba oxides are relatively soluble in base.[52,53] The formation of an amorphous surface layer was not observed for the less-active perovskites, such as $LaCoO_3$ and $LaMnO_3$.[52] This is consistent with the much lower solubility of La in basic solution.[52,53] The formation of hydrous amorphous phases might be a common attribute of highly active catalysts.

Despite the fact that they are typically the thermodynamically stable phases of metals under alkaline aqueous conditions, there has been limited direct work on the electrocatalytic properties of metal hydroxides/oxyhydroxides[49,51,55,56]. Lu and Srinivasan proposed that under OER conditions the surface of Ni anodes form an active NiOOH layer.[57] Hall studied $Ni(OH)_2$/NiOOH electrodeposited into porous Ni foam electrodes and found a 50-60 mV lowering of the OER overpotential compared to the bare Ni electrode.[58] Recently, Louie and Bell performed an extensive electrochemical and *in situ* Raman study on mixed $Ni_{1-y}Fe_y(OH)_2$ films.[59] They found that films with ~40% Fe show the lowest OER overpotential at 10 mA cm^{-2}, and they attribute changes in electrochemical behavior and activity of the films as the Fe content is increased with an increase in disorder of the crystal structure and a decrease in the average oxidation state of the Ni atoms.

Corrigan completed the most extensive work on $Ni(OH)_2$/NiOOH OER electrocatalysis in the late 1980s.[56,60] In his efforts to suppress the OER activity (which is a parasitic loss in batteries), he studied the role of iron[56] and other[51] metal impurities on

Ni(OH)$_2$ electrochemistry and OER activity. He found that Fe and Ce impurities improved the OER activity (overpotentials η reduced by >100 mV), while impurities including Cd, Zn and Pb decreased activity (η increased by ~20 mV).[51] Corrigan proposed that the synergistic effects of Ni and Fe on OER could be related either to changes in the conductivity of the catalyst film due to Fe-doping (in accord with previous claims that under anodic bias the formation of Ni^{4+} increases the resistance[57]) or by providing more favorable sites for OER intermediates,[56] but concluded that it is "unclear how the co-precipitated metal ions exert their influence on the OER".[51] To date, no significant progress has been reported on this important question.

The possibility that the incorporation of impurities from the electrolyte into the active catalysts dramatically affects activity complicates interpretation of experimental data. Markovic and coworkers discuss the effects of alkaline electrolyte impurities on the oxygen reduction and CO oxidation processes on Pt(111).[61] They report that anomalous electrochemical behavior results from the formation of 3-d transition metal (Co, Ni, Fe, Cr) hydroxides/oxyhydroxides after cycling in the alkaline electrolyte, which can catalyze or inhibit redox processes at the electrode surface. Similar to the findings of Corrigan,[56] we observe the incorporation of Fe impurities from the reagent-grade KOH electrolyte into Ni-based catalyst thin films.[8] Etching of glass electrochemical cells and sample substrates by basic electrolyte is also a concern, as additional impurities in borosilicate glass are introduced into the solution. Recent unpublished work in our group has shown that rigorous exclusion of borosilicate glass from the electrochemical cell and the use of ultra-high purity reagents can bring the level of incorporated Fe impurities below levels detectable by XPS.

Fe impurities may also be affecting the performance of NiB$_i$ films. For example, NiB$_i$ (in contrast to CoP$_i$ and CoB$_i$) requires several hours of anodization (depending of the concentration of the KB$_i$ electrolyte and the applied current density) to convert the catalyst to its most active state.[48,62] EXAFS and XANES show that the anodized catalyst is structurally analogous to NiOOH. Bediako et al. conclude that the disordered γ-NiOOH formed by anodization is more active for OER than the more-ordered β-NiOOH, which is in contrast with earlier results.[57,63] However, because reagent grade salts and electrolytes were used for the synthesis, NiB$_i$ likely also contains Fe absorbed from the solution, and

the active species could be a disordered $Ni_{1-y}Fe_yOOH$ / borate composite. This is consistent with the measurement of similar TOFs for the $Ni_{0.9}Fe_{0.1}OOH$ thin film electrodes in 1 M KOH[8] and the NiB_i electrodes in 1 M KOH / 1 M KNO$_3$ (pH 13.85) (Table 1.1).[48] We find that NiOOH kept Fe-free has a ~100-fold lower TOF of 0.01 at 325 mV overpotential.

Summary and Bridge

Well-defined nanoparticle and thin film electrocatalyst materials are expanding the approach to the design of OER catalysts. The use of thin film catalysts has led to the direct quantification of a range of intrinsic catalyst activities and the confirmation of $Ni_{1-y}Fe_yOOH$ as one of the best catalysts in basic solution. The dynamic nature of OER oxide/hydroxide/oxyhydroxide electrocatalysts, however, makes them challenging to study. Our view is that, typically, as-synthesized anhydrous oxides are not the active catalyst material. Efforts to design high-activity OER catalysts should account for the dynamic structures of these catalysts and the nearly unavoidable inclusion of Fe or other trace-metal impurities under practical operating conditions. Sophisticated techniques for the *in situ* characterization of catalyst surfaces are essential for understanding how the OER rates and mechanisms are affected by changes in structure and composition. In the context of the highly active $Ni_{0.9}Fe_{0.1}OOH$, key questions remain as to where the Fe is incorporated in the hydrous, layered structure and how it affects the OER mechanism.

The work in this dissertation addresses key knowledge gaps in field of OER electrocatalysis. Specifically, this research addresses four fundamental topics concerning catalyst properties and design that are essential for integration of these catalyst materials into functional water-splitting prototype devices: (1) the precise measurement and comparison of oxide/oxyhydroxide transition-metal OER electrocatalyst materials in basic media, (2) quantification of the optical and kinetic losses associated with these catalysts and how these factors affect the performance of a composite catalyst/semiconductor photoanode, (3) composition/structure/activity relationships in the highly-active $Ni_{1-x}Fe_xOOH$ catalyst system, including the effects of Fe impurities, and (4) the synthesis of nanoparticles with tunable lattice parameters that can be used as scaffolds for 3-dimensional structuring of highly active catalyst materials. The latter of these

14

(discussed in Chapter V) is relevant for efforts towards hierarchical structuring of OER catalysts to maximize loading and improve bubble and mass transport while minimizing optical losses. Such hierarchical structuring of highly-active, but optically absorbing catalysts, is an important direction for future work on optimization of composite photoanodes for use in water-splitting devices.

Chapter II details work on the solution synthesis, structural/compositional characterization, and OER electrocatalytic properties of ~2–3 nm-thick films of NiO_x, CoO_x, $Ni_yCo_{1-y}O_x$, $Ni_{0.9}Fe_{0.1}O_x$, IrO_x, MnO_x, and FeO_x. The thin-film geometry enables the use of quartz-crystal microgravimetry, voltammetry, and steady-state Tafel measurements to study the electrocatalytic activity and electrochemical properties of the oxides. This work directly addresses key knowledge gaps in the literature regarding intrinsic catalytic activity and stability of these materials, which arise due to the previous lack of a rigorous method for meaningful comparison of different catalysts.

This and all subsequent chapters of this dissertation contain previously published and/or unpublished co-authored material. Details regarding the contributions of each author and the bibliographic citation information for these publications can be found at the beginning of each chapter, directly after the chapter title.

CHAPTER II

SOLUTION-CAST METAL OXIDE THIN FILM ELECTROCATALYSTS FOR

OXYGEN EVOLUTION IN BASIC MEDIA

Portions of this chapter were previously published as Trotochaud, L; Ranney, J.K.; Williams, K.N.; Boettcher, S.W. "Solution-Cast Metal Oxide Thin Film Electrocatalysts for Oxygen Evolution" *Journal of the American Chemical Society*, **2012**, *134*, 17253-17261. L.T. wrote the paper, performed the experimental work, and made the figures. J.K.R. and K.N.W. were undergraduate students who, under the direction of L.T., performed preliminary work on the project to optimize the solution deposition methods for making the thin films. S.W.B. was the principal investigator and provided editorial assistance.

Introduction

The electrolysis of water to form hydrogen and oxygen gas (i.e. water splitting, $H_2O \rightarrow H_2 + \frac{1}{2}O_2$) provides a possible pathway for the large-scale storage of intermittent energy from the sun, wind, or other renewable sources.[1,2] The oxygen evolution reaction (OER) $2H_2O \rightarrow 4H^+ + O_2 + 4e^-$ (in acidic media) or $4OH^- \rightarrow 2H_2O + O_2 + 4e^-$ (in basic media) is kinetically slow and hence represents a significant efficiency loss in both electricity-driven and photo-driven water splitting.[2,3] Understanding the relationships between catalyst architecture, composition, and activity are critical for the development of catalysts with higher activities.

The early work on OER electrocatalysis has been reviewed by Trasatti[4] and Matsumoto[5]. The majority of this work was performed on thick electrodes fashioned by the hot-pressing of bulk powders or on electrodeposited films many microns thick. Such poorly-defined porous architectures make comparisons of different materials difficult as the measured catalytic response is influenced by the active surface area and the electron/mass transport properties in a manner that is difficult to correct for.[6] It has been noted that this is a key limitation in comparing experimental data with theoretical predictions.[7] Limited work has been performed on single crystals,[8,9] yet even when single crystals are available differences in electronic properties can prevent identification of the

16

basic relationships between structure, composition, and electrocatalytic activity. Despite these limitations, Trasatti formed a useful volcano relation by correlating the activities of the catalysts with the enthalpy of a lower to higher oxide transition and concluded that IrO_2 and RuO_2 are the most active OER electrocatalysts.[10] Recent density functional theory calculations by Rossmeisl et al. have attributed the high activity of these precious metal catalysts to the near thermochemical equivalence of each elementary step in the oxidation reaction.[11,12] First-row transition metal oxides containing Ni, Co, and Mn are typically considered to be of lower activity because the M-O bond strength is either too strong or too weak, thereby slowing the rate-limiting step.[7] Recently Subbaraman et al. studied electrodeposited metal hydroxide catalysts on Pt single crystals and also found that the oxophilicity of the metal cation (i.e. the M-OH bond strength) correlates with activity.[13] Nocera and co-workers have found evidence for the formation of such metal hydroxides in electrodeposited Ni-borate catalyst films.[14] Other reports indicate that mixed oxides, for instance $LaNiO_3$ and $NiCo_2O_4$, have higher activities than single-component oxides of the same elements.[15,16] Suntivich et al. reported the activities of a variety of perovskite electrocatalyst powders and found that the surface cation e_g orbital occupation correlated with the observed OER activity.[3] They used this descriptor to identify a perovskite catalyst, $Ba_{0.5}Sr_{0.5}Co_{0.8}Fe_{0.2}O_{3-\delta}$, with higher specific surface-area activity than IrO_2. The measurements were made using a rotating-disk electrode with well-defined oxygen transport[17] with the perovskite powders supported in a conducting carbon/Nafion composite film on the electrode surface. The surface areas of the catalyst powders were estimated from SEM measurements so that the specific surface-area activities could be compared. The disadvantages of this technique are the potential for the background oxidation of the conductive C at high current densities and the difficulty in processing powder-based catalysts into high-surface-area electrode architectures or combining them with semiconductors for light-driven water splitting.

Herein we report the solution-synthesis of ultra-thin-film metal oxide electrocatalysts onto quartz-crystal microbalance electrodes where the mass is measured and monitored *in situ*. The films are spun-cast from alcohol solutions of metal salts mixed with surfactant to reduce surface tension and promote film formation. Quick (~2 min), low-temperature (~300 °C) annealing decomposes the nitrate anions and surfactant

leaving a ~2–3 nm thick layer of the desired oxide on the conductive electrode surface. The films are useful for fundamental study for the following reasons: (1) The electrocatalyst conductivity does not significantly influence the measured overpotential because electrons must move only the thin-film thickness to reach the support electrode as opposed to μm to mm through a pellet, crystal or thick layer. (2) Many of the oxide electrocatalysts are semiconductors, and Schottky barriers at the catalyst|solution and catalyst|metal-electrode interfaces can impede electron transport and result in an additional overpotential that is dependent on the carrier concentration (i.e. doping) in the semiconductor.[5] Films < 5 nm thick are not sufficiently thick to support a large depletion region and therefore catalysis should be comparable independent from carrier concentration and interfacial contact properties. (3) The film composition can be exactly controlled by the metal ions added to the precursor solution. Compositions that are not accessible via traditional high-temperature routes (e.g. due to phase separation) or via electrodeposition can be made. (4) Variations in real versus geometric surface area (i.e. roughness factors) of high-surface-area electrodes are difficult to accurately correct for.[18] Ultra-thin films prepared from solution should have similar roughness factors that are at most a few times larger than unity. (5) The mass transport of evolving gases is facile due to lack of extensive porous structure.

We use the thin-film synthesis techniques developed here to quantitatively compare the OER activity of NiO_x, CoO_x, $Ni_yCo_{1-y}O_x$, $Ni_{0.9}Fe_{0.1}O_x$, IrO_x, MnO_x, and FeO_x catalysts, to study the films' electrochemical behavior, and to follow changes in the active catalyst structure during the OER. We show that $Ni_{0.9}Fe_{0.1}O_x$ is one of the best catalysts in basic media with OER catalytic activity more than 10-fold higher than IrO_x depending on the applied potential. We characterize the *in situ* transformation of the deposited Ni-containing films to redox-active Ni hydroxide/oxyhydroxide phases which are identified as the active catalyst. These thin-film OER catalysts are practically useful because the solution-deposition techniques can be used to couple them with semiconductor photoelectrodes for sunlight-driven water splitting, as well as to incorporate them into optimized high-surface-area electrodes for traditional water electrolysis applications.

18

Experimental Details

Preparation of Thin Film Precursor Solutions

Precursor solutions were prepared by dissolving metal nitrates [$Ni(NO_3)_2 \cdot 6H_2O$, 98% Alfa-Aesar; $Co(NO_3)_2 \cdot 6H_2O$, 98+% Sigma-Aldrich; $Fe(NO_3)_3 \cdot 9H_2O$, Mallinckrodt analytical grade; $Mn(NO_3)_2 \cdot 4H_2O$, 97+% Sigma-Aldrich] in ethanol at a concentration of 0.05 M. Triton X-100 (J.T. Baker) was added to give 0.15 g Triton per mmol of metal ions. For mixed-metal films, the salts were combined in the desired molar ratio to a total-metal-ion concentration of 0.05 M. Iridium chloride ($IrCl_3 \cdot xH_2O$, 99.9% Strem Chemicals) was used to make the IrO_x precursor solution. The $IrCl_3$ solutions were prepared at 0.025 M to ensure complete dissolution (with 0.15 g Triton/mmol Ir). The colored precursor solutions containing Ir, Co, Ni, and Co/Ni mixtures were stable indefinitely. The clear Mn precursor solution was stable for 2 - 3 weeks if not exposed to direct sunlight. A brown precipitate, presumably MnOOH,[19] was observed after prolonged time and/or sunlight exposure. The yellow-orange iron(III) nitrate solutions began to form an orange-brown precipitate after ~4 h due to formation of FeOOH.[19] Precursor solutions containing Fe were thus freshly prepared before each film deposition.

Thin Film Deposition and Annealing

Metal-oxide and mixed-metal-oxide thin films were deposited from precursor solutions by spin coating. Substrates, including Au/Ti QCM crystals (Stanford Research Systems), Si, indium-doped tin-oxide-coated glass (ITO, Delta Technologies), and Au/Ti-coated glass slides, were cleaned prior to deposition by ultrasonication for 30 min in a 6.25% (v/v) solution of Contrad-70 detergent (Decon Labs) in 18.2 MΩ cm ultrapure water at 45 °C, rinsed with ultrapure water, and dried by spinning at 5000 rpm for 90 s. Approximately 0.25 mL of precursor solution was cast onto a substrate which was then spun at 5000 rpm for 90 s. The films were annealed in air on a hot plate at 300 °C for 2 min for the thin QCM and Si substrates or 5 min for the thicker substrates.

Characterization

Microgravimetry measurements were made using a 5 MHz quartz crystal microbalance (Stanford Research Systems QCM200). The film mass was calculated from changes in resonance frequency using the Sauerbrey equation[20] $\Delta f = -C_f \times \Delta m$, where Δf is the observed frequency change (Hz), C_f is the sensitivity factor of the 5 MHz AT-cut

19

quartz crystal, and Δm is the change in mass per unit area (μg cm^{-2}). The crystal sensitivity factor C_f was determined by cathodic galvanostatic electrodeposition of Ag from a 50 mM solution of aq. $AgNO_3$ in 0.5 M HNO_3. A clean, bare QCM crystal was used as the working electrode and a coil of acid-cleaned Ag wire was used as the counter/reference electrode. Ag was electrodeposited at a current of -0.2 mA for 100 s. The change in resonance frequency was linear with total integrated charge associated with Ag deposition. For dry measurements, the QCM electrode was removed from solution after Ag deposition, rinsed gently with 18.2 MΩ cm H_2O, and dried with a N_2 stream. Resonance frequency shifts of ~ 1500 Hz were measured relative to the initial dry resonance frequency. The measurement was repeated 5 times. The dry sensitivity factor C_f determined was 58.3 ± 3.7 Hz μg^{-1} cm^2 where the error is $\pm 1\sigma$. This compares well with the expected value of 56.6 Hz μg^{-1} cm^2 for the 5 MHz AT-cut quartz crystal. To confirm that the solution-deposited thin films meet the rigid, uniform, thin-film requirement implicit in the use of the Sauerbrey equation,[21] the QCM resonance near 5 MHz was measured using AC impedance analysis. The fwhm of the resonance ($\sim$80 Hz) and thus quality factor was unchanged by deposition of the 2-3 nm film, while the resonance frequency shifted ~ 100 Hz. These measurements therefore indicate that visco-elastic losses associated with the thin films are not present and that changes in resonance frequency can be directly related to changes in film mass.[21] The total metal ion content of the thin films was determined from microbalance measurements of the dry films assuming full oxygen stoichiometry of the thermodynamically stable oxides, e.g. NiO, Co_3O_4, MnO_2, IrO_2, Fe_3O_4.

Grazing incidence X-ray diffraction (GIXRD) patterns were recorded on a Phillips X'Pert Panalytical diffractometer operating at 40 mA and 45 kV using monochromated Cu Kα_1 radiation (incident angle = 0.5°, λ = 1.541 Å, step size = 0.5°, integration time 20 s/step). Scanning electron microscopy (SEM) images were collected on a Zeiss Ultra 55 SEM at 5 kV. Samples for SEM imaging were deposited on Si wafers (the roughness of evaporated Au or ITO substrates made imaging the thin films difficult; see supporting information for images).

X-ray photoelectron spectroscopy (XPS) studies were carried out on an ESCALAB 250 (ThermoScientific) using an Al Kα monochromated (150 W, 20 eV pass

energy, 500 μm spot size) or a Mg Kα non-monochromated flood (400 W, 75 eV pass energy) source. The samples were charge-neutralized using an in-lens electron source combined with a low-energy Ar$^+$ flood source. Spectra were analyzed using ThermoScientific Avantage 4.75 software. The Au 4f$_{7/2}$ signal at 84.0 eV was used to calibrate the binding energy scale.

Electron probe microanalysis (EPMA) was performed using a Cameca SX-100 equipped with five tunable wavelength dispersive spectrometers. Operating conditions were 40° takeoff angle, beam current 20 nA and 50 μm spot size, with data collected at three different accelerating voltages (10, 15, and 20 keV). Experimental intensities were determined from the average of eight proximate positions on each sample. The exponential or polynomial background fit was utilized.[22] Quantitative elemental analysis was determined by comparing experimental *k*-ratios to simulated values using Stratagem thin film composition analysis software.[23]

Cross-sectional TEM samples were prepared by a focused ion beam (FIB) process with an FEI Helios DB-FIB, operated at 30 kV during ion milling and 5 kV for electron beam imaging. The sample was lifted out and transferred to the TEM grid *in situ* using an Omniprobe 200 micromanipulator and a Pt gas injection system (to add a protective Pt coating to the sample surface and for sample attachment to the probe and grid). The TEM lamella was thinned using a 30 kV, 93 pA beam (until the sample reached 500 nm thick), then polished to ~100 nm thickness using 5 kV, 16 pA. A final cleaning of the sample was performed at 2 kV, 10 pA.

Electrochemical Measurements

Electrochemical measurements were made in a cylindrical glass cell (see Figure 2.1) containing ~150 mL of 1 M KOH electrolyte solution (Fluka Analytical TraceSelect, ≥ 30%, diluted with 18.2 MΩ cm water) using a PARSTAT 2273 potentiostat operating in standard three-electrode mode. A Pt mesh separated by a 2-cm-diameter medium-porosity glass frit was used as a counter electrode. All potentials were measured versus a 1 M KOH Hg/HgO reference electrode (CH Instruments) housed in a custom glass Luggin capillary. The tip of the Luggin capillary was positioned ~1 - 2 mm from the surface of the working electrode to minimize uncompensated solution resistance, R_u. Samples deposited on QCM electrodes were connected to the working electrode lead of

the potentiostat through the crystal face bias connector of the QCM200. Working electrodes for samples deposited on Au/Ti or ITO coated glass were fabricated by contacting a wire to the sample surface using Ag paint. Ag paint was also applied around the edges of the ITO to minimize series resistance. The Ag paint was then sealed in inert epoxy (Loctite Hysol 1C) along with the contacting wire that was fed through a glass tube. Control experiments showed no background current from the epoxy. No significant differences in electrochemical response were observed for samples deposited on QCM, Au/Ti coated glass, or ITO coated glass electrodes. Data presented in the text represent measurements made on QCM electrodes unless otherwise indicated.
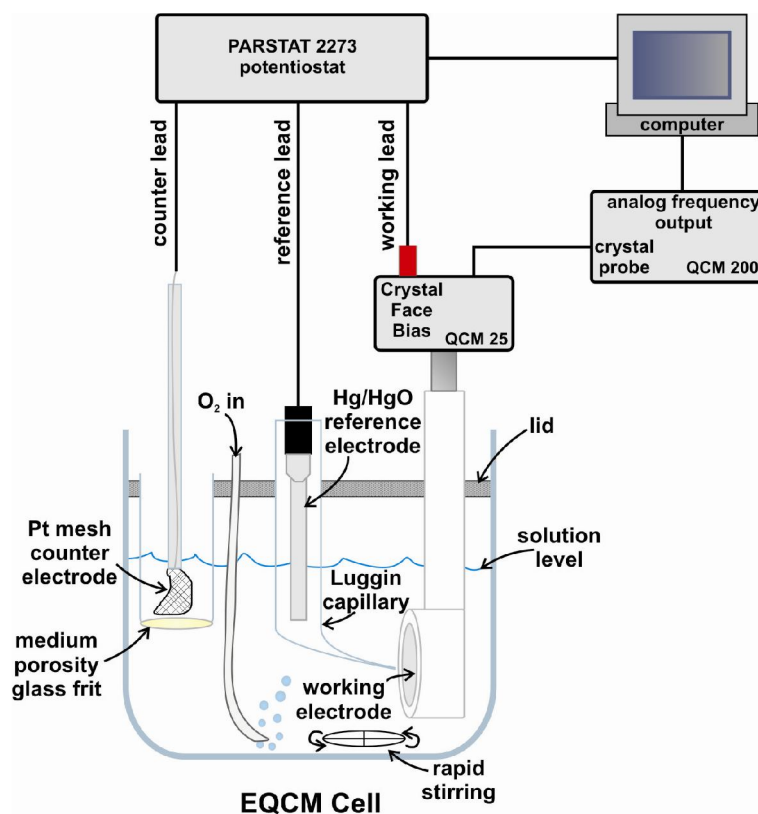
Figure 2.1. Schematic of electrochemical cell used to test electrocatalyst films. In some cases, Au/Ti or ITO coated glass electrodes were used as catalyst supports instead of the mounted QCM crystal.

The potential of the 1 M KOH Hg/HgO reference electrode was measured to be 0.929 V vs. the reversible hydrogen electrode (RHE) at pH 14 (i.e. 0.112 V vs. NHE). The RHE was fabricated by bubbling high-purity hydrogen over a freshly cleaned Pt

mesh in 1 M KOH. Ultra-high-purity O_2 gas was bubbled through the solution for at least 20 minutes prior to and throughout electrochemical measurements. Magnetic stirring was used to dislodge O_2 bubbles formed on the electrode surface. All electrochemical data was corrected for R_u, which was determined by equating R_u to the minimum total impedance in the frequency regime between 10 to 50 kHz where the capacitive and inductive impedances are negligible and the phase angle was near zero. R_u was 0.2 - 2 Ω for gold-coated substrates and ~1 - 5 Ω for ITO substrates. R_u was also determined by the current-interrupt method, but that was found to overestimate R_u leading to non-physical Tafel plots. The overpotential η was calculated using the equation $\eta = E_{measured} - E_{rev} - iR_u$ where $E_{measured}$ is the potential recorded vs. Hg/HgO, E_{rev} is the reversible potential of the OER vs. Hg/HgO (0.30 V at pH 14), and i is the current. Current densities are calculated using geometric surface areas.

Sources of Error and Error Propagation

Values reported for overpotential, current density, and Tafel slope are the average of three independent measurements on three different thin-film samples. The reported error is the standard deviation (σ) of the three measurements. The errors reported for the film loading values arise from small changes in the QCM resonance frequency due to inconsistencies when remounting the quartz crystal into the holder. To minimize this error the screw-on cap of the crystal holder was tightened the same amount for each measurement, and care was taken to orient the crystal in the holder in the same position for each measurement. To determine the error due to crystal mounting ($\sigma_{mounting}$), the oscillation frequency was measured 10 times for each sample by repeatedly removing and remounting the crystal in the holder. Furthermore, the film loading is also affected by the calibrated value of the sensitivity factor C_f, which was found to be 58.3 $\pm$ 3.7 Hz μg^{-1} cm^2 where the error is $\pm$ $1\sigma_{sensitivity}$ as determined from four independent measurements. The total error in the film loading is therefore found using:

$$\sigma_{\ell} = \sqrt{\left(\sigma_{mounting}\right)^2 + \left(\sigma_{sensitivity}\right)^2} \qquad (2.1)$$

The values of mass activity (A g^{-1}) are calculating from the film loading ℓ in g cm^{-2} and the measured current density J in A cm^{-2} at 0.3 V overpotential:

$$\text{mass activity} = \frac{J}{\ell} \qquad (2.2)$$

23

The values of turn-over frequency (TOF) are calculated from:

$$\text{TOF} = \frac{J \cdot A}{4 \cdot F \cdot m} \qquad (2.3)$$

where A is the surface area of the QCM electrode, F is Faraday's constant, and m is the number of moles of metal deposited in the film calculated from ℓ and the molecular weight of the metal oxide composing the film.

Since J and ℓ have independent uncorrelated sources of error, the propagation of uncertainty to the values of TOF and specific activity can be determined using:

$$\sigma_f = f\sqrt{\left(\frac{\sigma_J}{J}\right)^2 + \left(\frac{\sigma_\ell}{\ell}\right)^2} \qquad (2.4)$$

where σ_f is the propagated error, f is the calculated value of specific activity or TOF as determined using equation 2.2 or 2.3, respectively, and σ_J and σ_ℓ are the errors associated with J and ℓ, respectively.

$Ni_yCo_{1-y}O_x$ Mixed Oxides: A Case Study in Ultra-Thin Film Catalysis

$Ni_yCo_{1-y}O_x$ has been reported to be one of the most active non-precious metal catalysts for the OER with optimized materials exhibiting Tafel slopes between 40 and 60 mV dec^{-1}.[24-29] However, the catalytic activity of these materials appears highly dependent on a number of experimental factors, including the synthetic method and product morphology,[26-31] ageing and cycling of the electrode,[30,31] and type of electrode substrate.[28] The mechanism for the reported performance enhancement for the mixed oxide relative to NiO_x or CoO_x is unclear. We have therefore studied $Ni_yCo_{1-y}O_x$ OER catalysts in the thin-film geometry to provide new insight into the activity trends in the absence of confounding effects associated with high-surface area or thick-film architectures.

Characterization of As-Deposited Films

Following spin-casting of the metal oxide precursor solution, microbalance measurements showed that > 85% of the original film mass was lost during the first minute of heating at 300 °C due to the removal of nitrate, ethanol, and surfactant (Figure 2.2). Between 2 - 6 minutes at 300 °C, no further mass loss was measured. XPS analysis

showed no N in the annealed films, confirming the complete combustion of the nitrate salts. XPS data for the annealed IrO_x film shows a low-intensity feature at ~199 eV corresponding to the Cl 2p binding energy indicating that a trace amount of Cl (Cl : Ir < 0.02) remains in the sample. This feature disappears after electrochemical experiments performed in 1 M KOH, indicating that Cl is not present during catalysis measurements. No spectral features associated with K were observed in any of the XPS spectra, indicating that K does not incorporate from the KOH electrolyte.
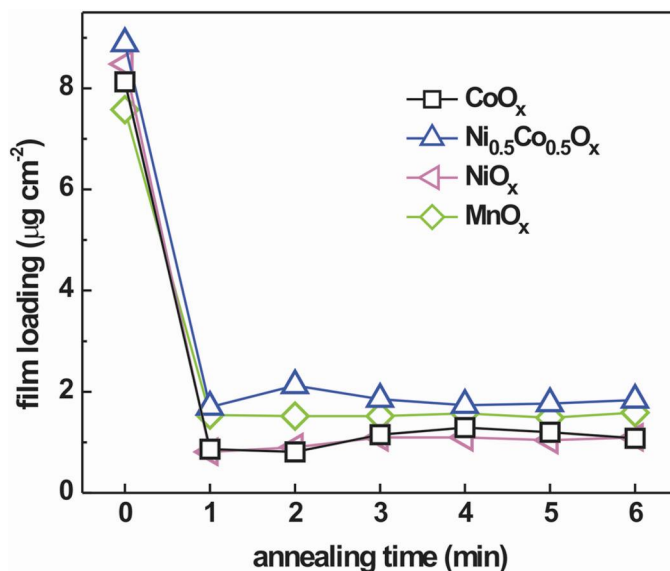
Figure 2.2. Changes in film mass as a function of annealing time. Samples were deposited onto 5 MHz AT-cut QCM crystals and heated on a hot plate at 300 °C for 1 min intervals. Mass losses due to annealing are complete after the first minute of heating. Small fluctuations in film loading with longer annealing times are within the error of the measurement, which arises from the removal and remounting of the quartz crystal into the holder between heating steps (see discussion of error below).

Average film thicknesses, determined from the film mass and density of the known oxide phases, ranged from 1.6 - 2.5 nm. Cross-sectional TEM analysis of the NiO_x films deposited on the Au/Ti electrodes confirmed an average thickness of ~2 nm. (Figure 2.3). Figure 2.4 shows representative SEM images taken of thin films deposited on Si substrates to facilitate SEM imaging. Except for MnO_x (to be discussed further below), all films show uniform coverage across the sample surface. At high magnification, nanoscale texturing of the $Ni_yCo_{1-y}O_x$ films can be seen to decrease as the

Ni content increases. Unlike the other oxides, the MnO_x precursor solution deposited on Si yielded a film of nanoparticles each ~15 - 20 nm across. The particles spontaneously form during the quick annealing process. However, these particles are not observed for MnO_x films deposited on Au/Ti coated substrates, as shown in Figure 2.5. Images of samples on Au/Ti coated surfaces are dominated by the underlying morphology of the Au, and the MnO_x films on Au/Ti appear similar to the other metal-oxide films. Differences in morphology between samples before (Figure 2.5) and after (Figure 2.6) electrochemical experiments are minimal for all films. Since the samples on Si were used only for film imaging and not in any electrochemical measurements, the observation of these MnO_x particles does not influence the interpretation of electrochemical data. Additional work would be required to understand the MnO_x particle growth process on Si, but it is likely related to the different substrate surface energies in the two cases.
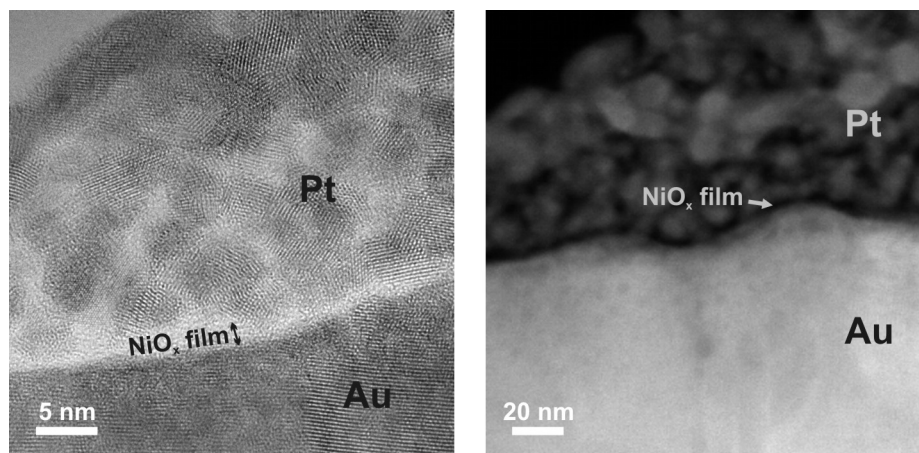
Figure 2.3. Cross-sectional transmission electron microscopy image of a NiO_x film deposited on Au/Ti coated glass showing uniform ~ 2 nm coverage across the polycrystalline Au surface. Imaging was performed on a FEI 80-300 keV aberration-corrected Titan S-Twin microscope operating at 300 keV, equipped with a standard field emission gun (S-FEG).

Grazing incidence XRD shows reflections corresponding to spinel Co_3O_4 and rock salt NiO for the CoO_x and NiO_x films, respectively (Figure 2.7). Patterns have been referenced to the sharp peak at 52° 2θ, which is an artifact of the single crystalline (100) Si substrate wafers. The broad feature centered at 55° 2θ is also an artifact of the (100) Si substrate. The sloping background due to the grazing incidence geometry has been
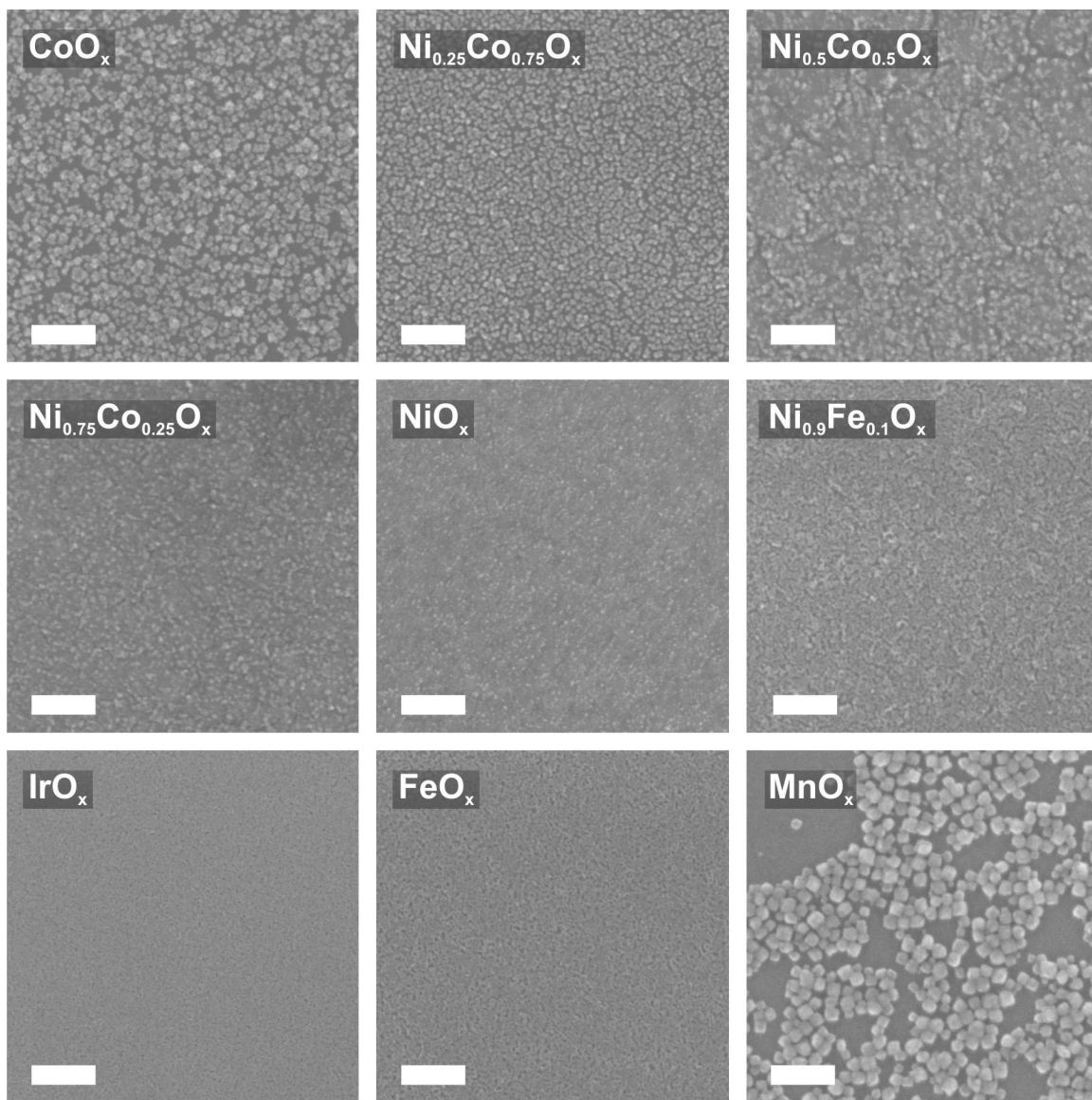
Figure 2.4. SEM images of the metal oxide films on Si directly following annealing. Scale bars are 100 nm. The nano-particulate morphology observed for the MnO_x film on Si is not observed for samples prepared on the Au/Ti electrodes used for electrochemical measurements, but is included here for completeness.

subtracted for clarity (see Figure 2.8). For $Ni_yCo_{1-y}O_x$ films, only one set of reflections is observed in each sample. For $y = 0.25$, reflections consistent with the spinel structure are observed. For $y = 0.5$ and 0.75, reflections for the rock salt structure are observed. For the $y = 0.5$ sample, the reflection centered at 63.7° 2θ lies between that of NiO (220) and Co_3O_4 (440) (at 62.9° 2θ and 65.2° 2θ, respectively). The lack of clear NiO (220) and Co_3O_4 (440) reflections suggests a single mixed $Ni_yCo_{1-y}O_x$ phase is present, as opposed
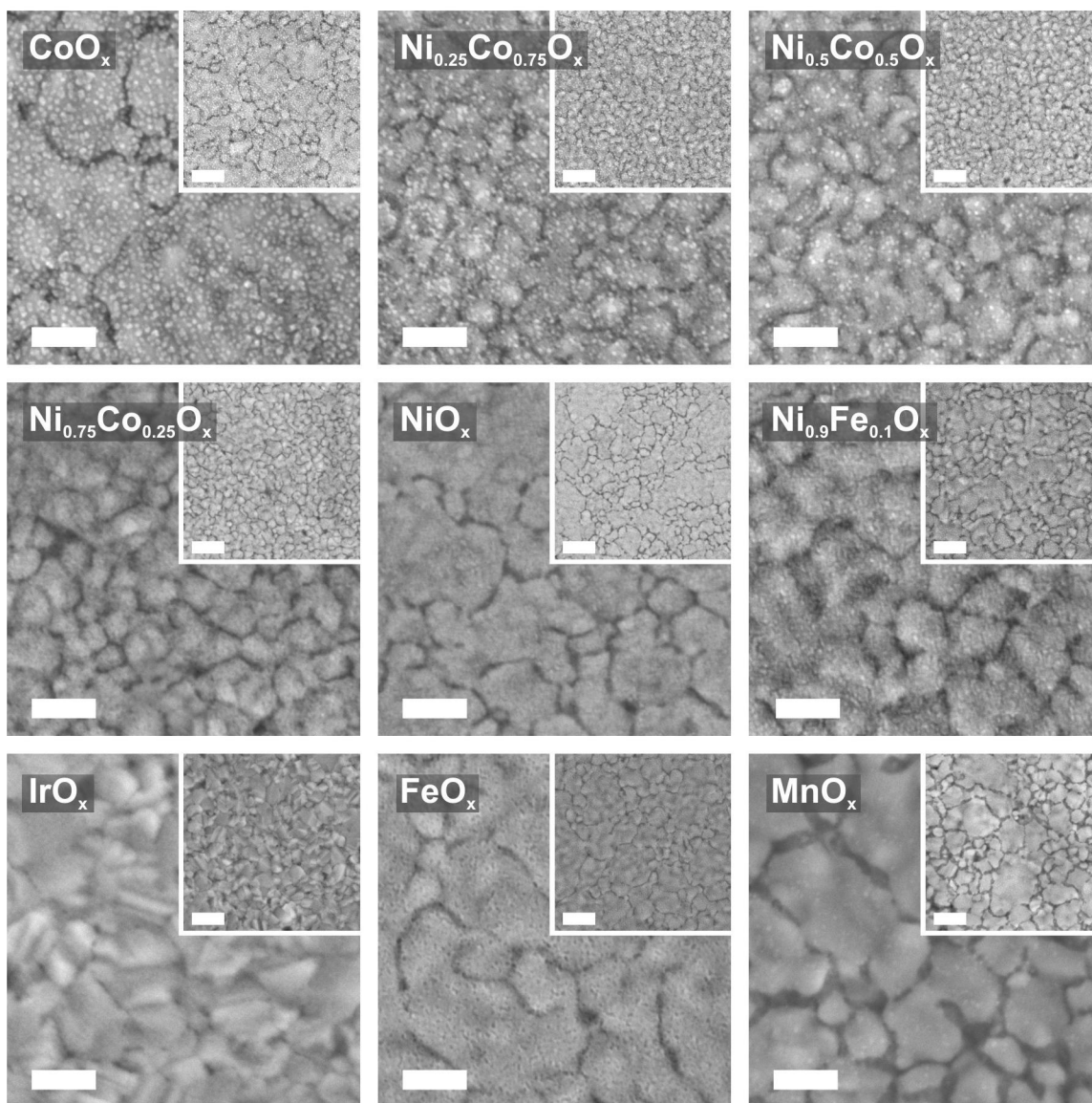
Figure 2.5. SEM images of the metal oxide films on Au/Ti coated glass directly following annealing. Scale bars are 100 nm; inset scale bars are 200 nm.

to a phase-separated mixture of the Ni and Co oxides, although a conclusive analysis is limited by the low intensity of the peaks for these ultra-thin-film samples.

Cyclic Voltammetry and the Effects of Electrochemical Conditioning

Figure 2.9 shows a series of cyclic voltammograms collected for a NiO_x film during several hours of galvanostatic conditioning at an anodic current density of 10 mA cm^{-2}. The as-deposited film shows a small reversible wave due to Ni redox processes, and OER current reaches 1 mA cm^{-2} at $\eta = 324$ mV. After one hour at 10 mA cm^{-2}, a wave
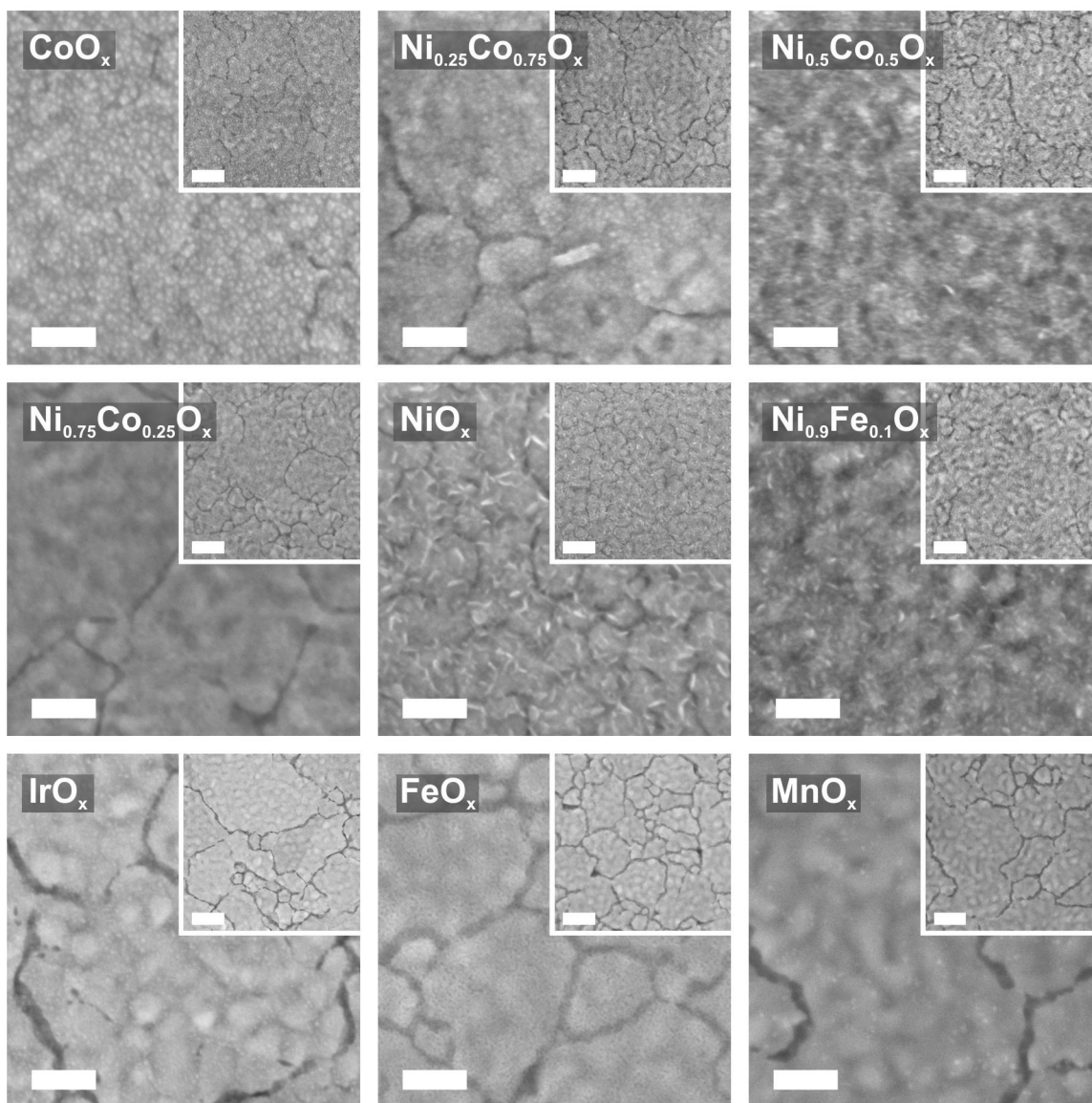
Figure 2.6. SEM images of the metal oxide films on Au/Ti coated quartz crystals after electrochemical experiments. Scale bars are 100 nm; inset scale bars are 200 nm.

corresponding to Ni^{2+} oxidation centered at 472 mV vs. Hg/HgO is observed. A corresponding broad reduction wave near 420 mV vs. Hg/HgO is also present, and the overpotential required for 1 mA cm^{-2} OER current has decreased to $\eta = 302$ mV (as discussed below, η is remarkably small given the minimal catalyst loading). As electrochemical conditioning continues, CV scans collected every hour show that the Ni^{2+} oxidation wave increases in area and the OER activity increases. Typically, after six hours of conditioning, no large changes were observed in subsequent CV scans with
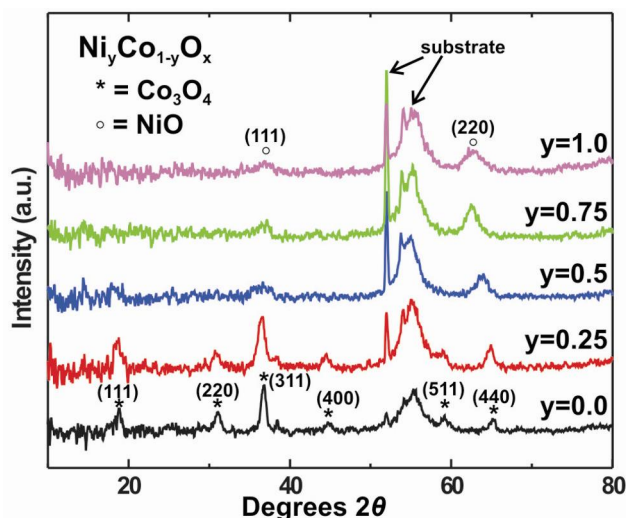
Figure 2.7. Grazing incidence XRD patterns of CoO_x, $Ni_yCo_{1-y}O_x$, and NiO_x films. Films were prepared by five consecutive depositions onto Si substrates.
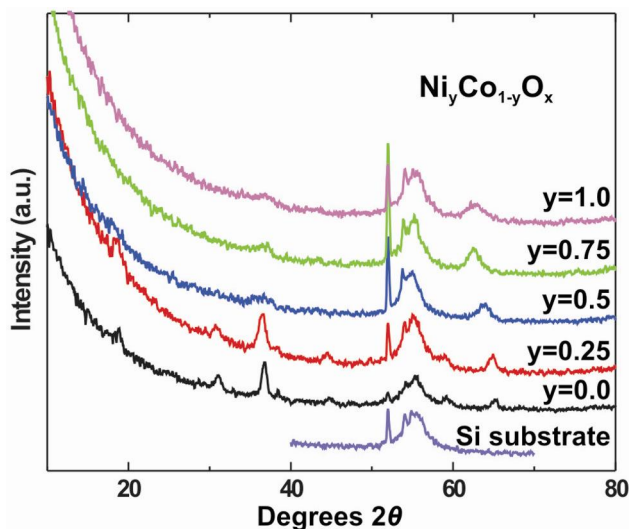
Figure 2.8. Raw XRD data showing the sloping background due to the grazing incidence geometry. The lower pattern is of the single crystalline Si substrate showing the prominent peaks near 52° and 55° 2θ. The intensity of the Si peaks, especially the sharp peak near 52° 2θ, is a function of substrate orientation which was not controlled.

additional conditioning. Integration of the total charge under the Ni^{2+} oxidation wave after 6 h of conditioning (1.5 mC cm^{-2}) in combination with QCM mass measurements (9.4×10^{15} Ni cm^{-2}) indicates that nearly all of the Ni centers in the film are electrochemically active (~1 electron per Ni). We note that some studies have assigned this wave to a $Ni^{2+}/Ni^{+3.67}$ redox process implying an ultimate limit of 1.67 e$^-$ per Ni as opposed to the simple 1 e$^-$ Ni^{2+}/Ni^{3+} process.[32]
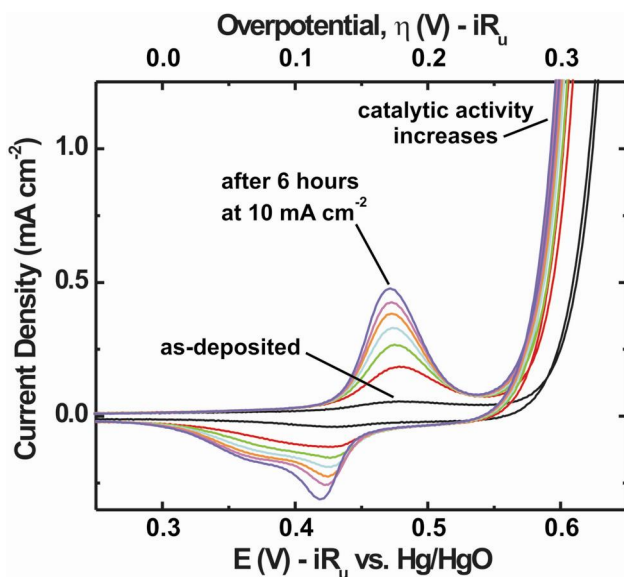
Figure 2.9. Cyclic voltammograms of a NiO$_x$ film during electrochemical conditioning collected at a scan rate of 20 mV s^{-1} in 1 M KOH. After collection of the initial (as-deposited) scan, subsequent scans were collected at 1 h intervals during anodic galvanostatic conditioning at 10 mA cm^{-2}.

The changes in the NiO$_x$ film voltammetry are attributed to the *in situ* formation of Ni(OH)$_2$/NiOOH hydroxide/oxyhydroxide species during the electrochemical conditioning process, which is depicted in Figure 2.10. The observed Ni^{2+} oxidation wave at 472 mV vs. Hg/HgO is assigned to the reversible Ni(OH)$_2$/NiOOH redox reaction.[33-35] Unlike the redox activity of the as-deposited NiO films which is limited to the surface Ni atoms, the layered Ni(OH)$_2$/NiOOH structure is composed of weakly interacting hydroxide layers that allow the intercalation of water and anions and therefore bulk redox activity (enabling also use in rechargeable battery electrodes).[35] The decrease in OER overpotential with increasing conversion of NiO to NiOOH indicates that the NiOOH is the active catalyst for OER. The Ni^{2+} oxidation wave for conditioned NiO$_x$ films shifted to higher potentials after soaking in KOH solutions for several hours (Figure 2.11). This observation is consistent with the conversion of the disordered α-Ni(OH)$_2$ formed after electrochemical conditioning (i.e. in the resting state of the catalyst) to the ordered β-Ni(OH)$_2$ polymorph upon aging in base, as has been observed previously.[35] (The aging of Ni(OH)$_2$ films will be discussed at length in Chapter IV).

31
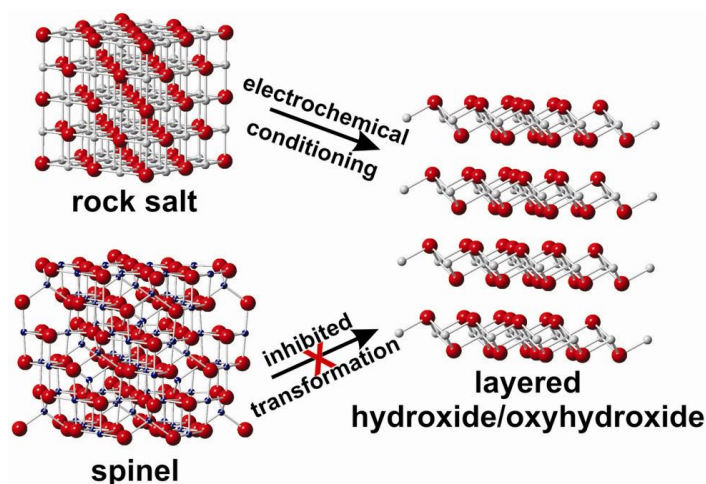
Figure 2.10. Proposed *in situ* transformation from the thermally prepared oxides to the layered hydroxide/oxyhydroxide structure as discussed in the text.
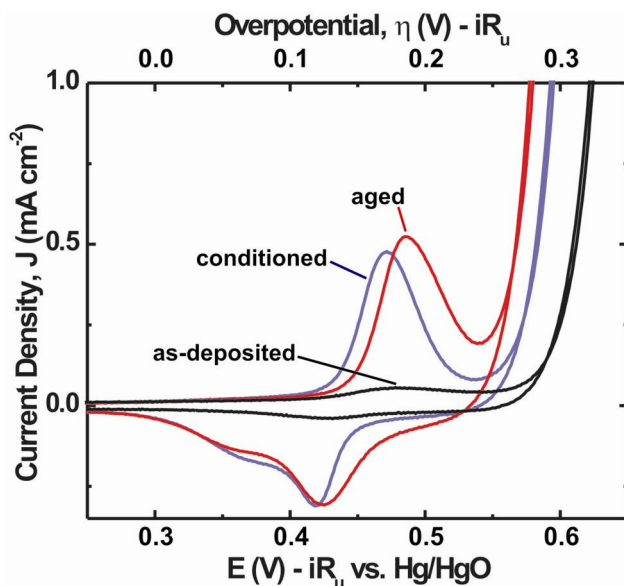
Figure 2.11. Voltammetry of a conditioned NiO_x film showing the effects of aging of the sample in 1 M KOH. The aged sample shows a shift in the positions of the redox wave to higher potentials and a decrease in potential for the onset of OER current. These observations are consistent with the conversion of the film from α-$Ni(OH)_2$ to the β-$Ni(OH)_2$ polymorph with aging in basic electrolyte solutions.[35] In this study, the change is reversible, such that after extended anodic polarization the voltammetry and catalytic activity returns to the initial values assigned to the α-$Ni(OH)_2$. Ageing of $Ni(OH)_2$ films will be discussed in more detail in Chapter IV.

Similar changes in voltammetry with conditioning were observed for all samples containing Ni (Figure 2.12). Figure 2.13 compares cyclic voltammograms for $Ni_yCo_{1-y}O_x$

32

films each conditioned for 6 h at 10 mA cm^{-2}. The potential experienced by the Ni-containing films during conditioning was initially near η = 0.6 - 0.7 V and gradually decreased to η = 0.3 - 0.4 V after 6 h. The voltammetry of the CoO$_x$ thin film did not change with conditioning. With increasing values of y, the conditioned Ni$_y$Co$_{1-y}$O$_x$ films showed increased Ni(OH)$_2$/NiOOH redox activity as well as decreases in overpotential required for oxygen evolution. Integrated charge for the oxidation and reduction waves (Q$_{ox}$ and Q$_{red}$) are plotted vs. Ni content in the inset of Figure 2.13. A linear background was subtracted for peak integration to correct for background capacitance and OER onset current (see Figure 2.14). Table 2.1 compares the integrated charge for each film (the average of Q$_{ox}$ and Q$_{red}$), normalized by the total metal ion content as well as Ni content in each film determined from microbalance measurements of the dry films. With increasing Co the fraction of electrochemically active Ni decreases. As all of the Ni centers would be electrochemically accessible upon the full conversion to the layered hydroxide phases, these results indicate that the addition of Co suppresses the *in situ* transformation from oxide to layered hydroxide phase.

Evidence for the proposed *in situ* transformation is found by comparing XPS spectra of the NiO$_x$ film before and after electrochemical conditioning. In the Ni 2p region (Figure 2.15a), the as-deposited NiO$_x$ film shows three main peaks for Ni 2p$_{3/2}$ at binding energies of 853.2, 855.1, and 860.2 eV. After electrochemical conditioning, peaks at 856.1 and ~862 eV are observed. These spectral differences indicate a transformation from NiO to Ni(OH)$_2$ that is consistent with the known Ni 2p$_{3/2}$ XPS spectra of NiO and Ni(OH)$_2$.[36-38] A change in binding environments can also be seen in the O 1s XPS region (Figure 2.15b). The as-deposited NiO$_x$ film shows two predominant peaks at 529.1 and 530.9 eV, while the conditioned film shows one peak at 531.7 eV. This is consistent with previous studies that compare the O 1s XPS spectra of NiO and Ni(OH)$_2$ samples.[35,37] The lower energy peak in the NiO spectrum is attributed to O-vacancy lattice defects.[36,38] The absence of these two peaks at lower binding energy in the conditioned sample indicates conversion to Ni(OH)$_2$. XPS analysis also shows the presence of Fe in the conditioned films, which originates from electrolyte impurities and could play an important role in the catalysis. We discuss the presence and influence of Fe below.
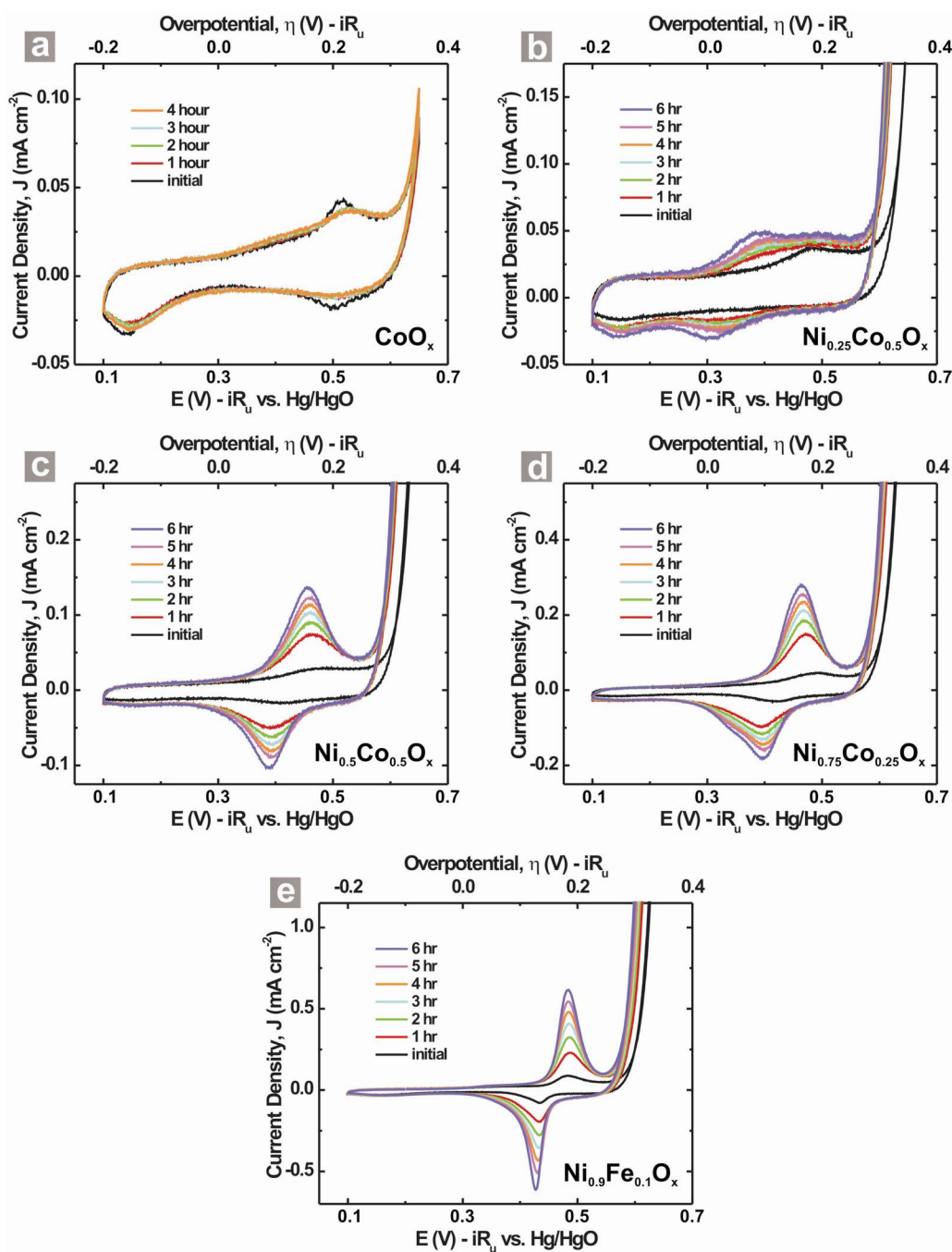
Figure 2.12. Changes in voltammetry behavior due to electrochemical anodic galvanostatic conditioning at 10 mA cm^{-2} for (a) CoO$_x$, (b) Ni$_{0.25}$Co$_{0.75}$O$_x$, (c) Ni$_{0.5}$Co$_{0.5}$O$_x$, (d) Ni$_{0.75}$Co$_{0.25}$O$_x$, and (e) Ni$_{0.9}$Fe$_{0.1}$O$_x$.
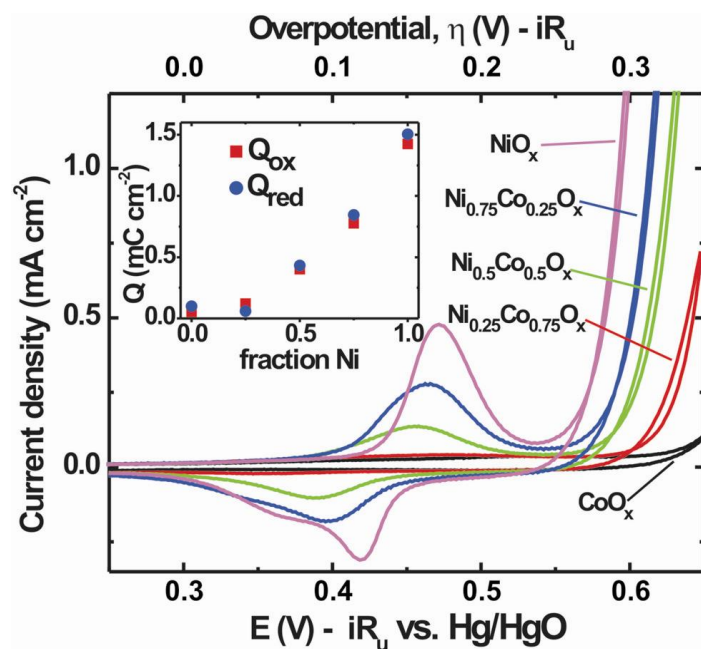
Figure 2.13. Voltammetry of the conditioned NiO_x, $Ni_yCo_{1-y}O_x$, and CoO_x films collected in 1 M KOH at a scan rate of 20 mV s^{-1}. All films containing Ni show an increase of the Ni^{2+} oxidation wave after electrochemical conditioning compared to the as-deposited films. Inset: the integrated charge Q for the redox processes as a function of Ni content.
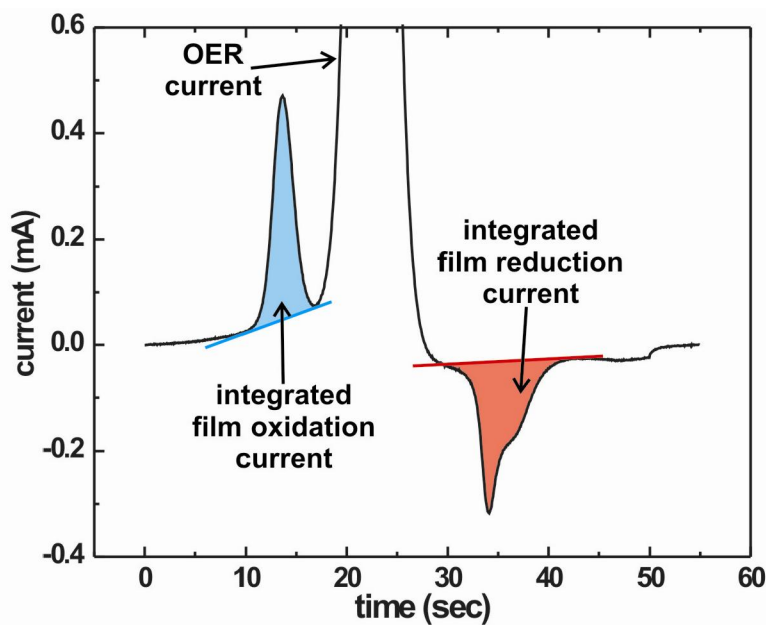
Figure 2.14. Example of linear background correction for determination of integrated charge associated with Ni redox chemistry. The red and blue lines represent the linear backgrounds and the shaded regions show the integrated areas for the film oxidation and reduction peaks.

35

Table 2.1. Integrated Charge for $Ni_yCo_{1-y}O_x$ Films[a]

sample	dry mass (µg)	e⁻ per metal	e⁻ per Ni
CoO_x	1.82	0.04	n/a
$Ni_{0.25}Co_{0.75}O_x$	1.54	0.07	0.27
$Ni_{0.5}Co_{0.5}O_x$	1.46	0.31	0.63
$Ni_{0.75}Co_{0.25}O_x$	1.44	0.61	0.82
NiO_x	1.56	1.00	1.00

[a]All values are ± ~10% due to uncertainties in mass measurements (as discussed previously)
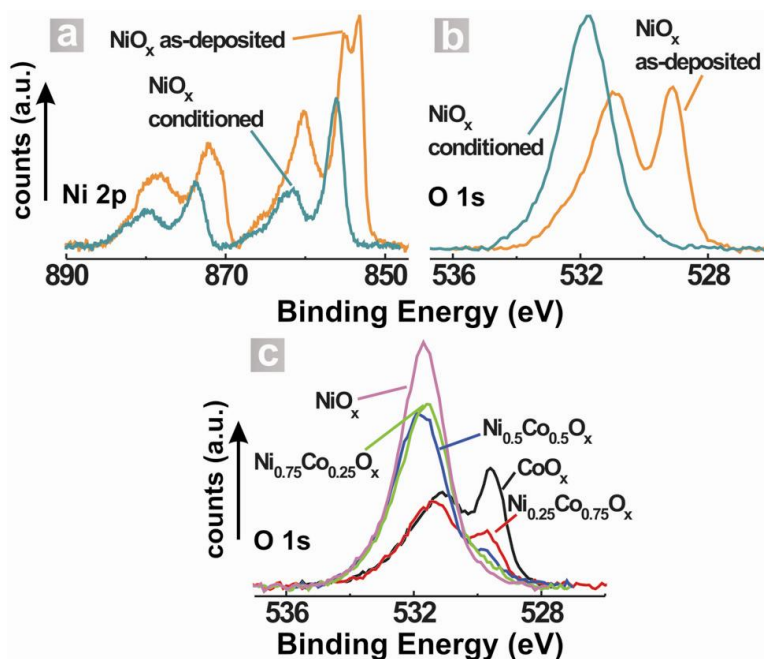
Figure 2.15. Comparison of the Ni 2p (a) and O 1s (b) XPS spectra of a NiO_x thin film before and after electrochemical conditioning. Electrochemically conditioned samples were driven to 0.2 V vs. Hg/HgO prior to XPS analysis. The evolution of the O 1s peak for the conditioned $Ni_yCo_{1-y}O_x$ samples is shown in panel c. The background signal has been subtracted from all spectra.

Figure 2.15c compares the O 1s peak for the $Ni_yCo_{1-y}O_x$ samples after conditioning at 10 mA cm^{-2} for 6 h. After accounting for adventitious oxygen-carbon species (see Figure 2.16 and discussion below), the spectra are fit well by one or two peaks attributed to metal-oxygen species. These peaks, centered near 529.6 eV and 531.7 eV, are assigned to metal-oxide (spinel) and metal-hydroxide (brucite) species, respectively, based on previous studies of Co and Ni oxides and hydroxides.[36-40] The

spectrum of the CoO$_x$ sample contains the spinel peak and an additional peak at 531.1 eV, which is attributed to surface O defects in the Co$_3$O$_4$ spinel.[39,40] As the Ni content of the films is increased, the spinel peak diminishes and the brucite peak increases in intensity. Even for samples with 75% Ni, a small shoulder near 529.6 eV shows that the complete transformation to the layered hydroxide structure is prevented.

The O 1s spectra for the Ni$_y$Co$_{1-y}$O$_x$ films were fit to multiple peaks in order to study the effect of film composition on the *in situ* transformation from oxide to hydroxide/oxyhydroxide during catalysis. Fits for O 1s XPS spectra for the Ni$_y$Co$_{1-y}$O$_x$ samples can be seen in Figure 2.16a-e. Analysis of the C 1s spectra (Figure 21.6f) shows that there are several carbon-oxygen species in the sample, likely due to the presence of adsorbed adventitious carbon compounds. Several steps were taken during fitting of the O 1s spectra to remove the contributions from these adventitious species. The C 1s spectra was first fit to four peaks centered near 289.0 (peak **A**), 287.8 (peak **B**), 286.6 (peak **C**), and 285.0 eV, which correspond to species O=C–O, O=C, C–O, and C–H, respectively. The approximate positions of the corresponding O 1s ester, ether, and ketone peaks were obtained from López et al.[41] (at 533.7, 532.8, and 532.2 eV, respectively). The position of the ester (O=C–**O,** peak **a**) oxygen is set at 533.7 ± 0.2. The positions of the ether (C–O, peak **b**) and ketone (**O**=C–O and O=C, peak **c**) oxygens are constrained to -0.9 ± 0.2 and -1.5 ± 0.2 relative to the position of the ester peak. During fitting iterations, the full-width at half maximum (fwhm) of the component O 1s peaks were set to 1.6 eV (a reasonable value based on the fwhm of the C-H C 1s peak), except when fitting the spinel oxide peak near 529.6 eV as this peak has been reported to be somewhat narrower than other oxide and hydroxide species.[39,42] Additional peaks (1 or 2) were then added to account for the metal oxide and hydroxide species in the films. As mentioned previously, the positions of these remaining peaks are consistent with previously reported XPS analyses of cobalt and nickel oxide and hydroxide.[36-40] Finally, the total integrated intensities of the ester, ether, and ketone peaks were constrained to be consistent with the atomic percents of the species as indicated by the C 1s fit (i.e. **a** = **A**; **b** = **C**; **c** = **A** + **B**).

The Co 2p$_{3/2}$ XPS spectra also show evidence for changes from an oxide to hydroxide-like environment. Co 2p$_{3/2}$ XPS spectra show characteristic "shake-up"

satellite peaks due to the Co^{2+} d^5 high-spin electron configuration.[36,40,43] These peaks are expected to grow after conversion from spinel Co_3O_4 (predominantly Co^{3+}) to $Co(OH)_2$ (Co^{2+}). Shake-up satellites are only observed (see Figure 2.16g) in the samples with higher Ni concentrations such as $Ni_{0.5}Co_{0.5}O_x$ and $Ni_{0.75}Co_{0.25}O_x$. This suggests that the CoO_x and $Ni_{0.25}Co_{0.75}O_x$ samples show limited incorporation of Co into the hydroxide structure as Co^{2+}, which is consistent with the hypothesis that Co inhibits the *in situ* transformation to the layered double hydroxide structure.

Quartz Crystal Microgravimetry

During electrochemical measurements, films deposited on quartz crystals were monitored for mass changes. No mass loss was observed, indicating that the films did not dissolve or degrade in solution. For example, the QCM resonance frequency for as-deposited CoO_x and the electrochemically conditioned CoO_x was constant to within a few Hz (i.e. ± 0.05 μg cm^{-2}). For films containing Ni, the film mass increased significantly (1.3 - 1.9 μg cm^{-2}) during electrochemical conditioning, such that the final mass was around twice that of the initial as-deposited film. The increase in mass after electrochemical cycling for NiO_x and $Ni_yCo_{1-y}O_x$ films is consistent with several processes,[35] including conversion from the as-deposited oxide NiO (MW = 74.69 g mol^{-1}) to the hydroxide $Ni(OH)_2$ (MW = 92.72 g mol^{-1}), incorporation of iron impurities (see discussion below), and intercalation of water between the layered hydroxide sheets. The ability to both quantify the precise mass of the initial dry deposited films and confirm that the ultra-thin films are stable under operational conditions using electrochemical QCM measurements is important for comparing and understanding the observed OER activities.

Catalytic Activity of the $Ni_yCo_{1-y}O_x$ System and the Role of Fe Impurities

Steady-state Tafel measurements for the $Ni_yCo_{1-y}O_x$ films are presented in Figure 2.17. Tafel slopes were fit to the linear region of the data below 1 mA cm^{-2}. Consistent with the voltammetry measurements (Figure 2.13), the overpotential decreases as the Ni content of the film increases. CoO_x shows the highest overpotentials and Tafel slope (42 mV dec^{-1}), while NiO_x shows the lowest overpotentials and Tafel slope (29 mV dec^{-1}). No synergistic effect is apparent upon mixing of the two oxides, and the activity simply decreases as Co is added to NiO_x, in contrast with previous reports on electrodes with higher surface area.[24-28,44] The data are consistent with the hypothesis shown in Figure
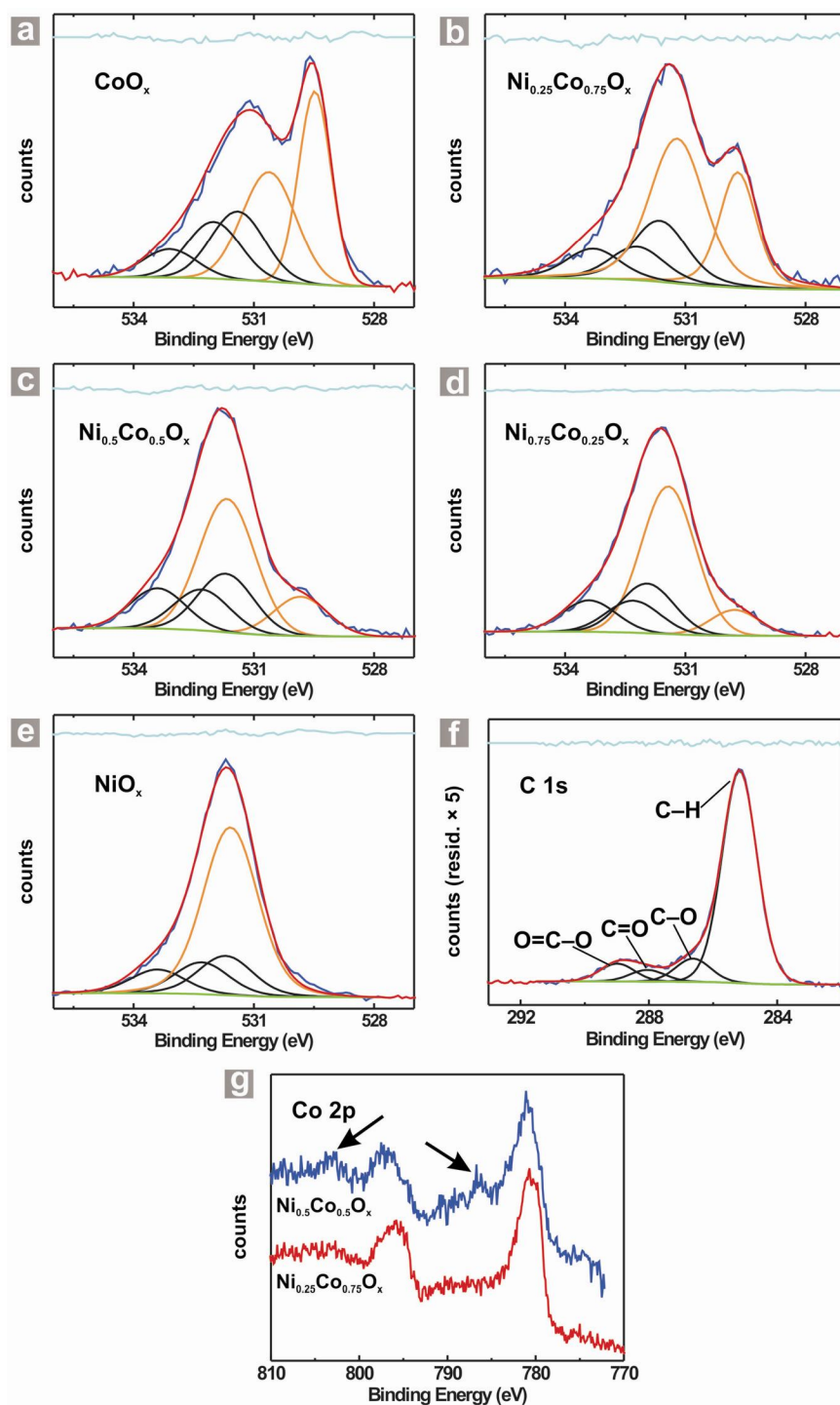
Figure 2.16. Fits of XPS O1s spectra for the (a) CoO_x, (b) $Ni_{0.25}Co_{0.75}O_x$, (c) $Ni_{0.5}Co_{0.5}O_x$, (d) $Ni_{0.75}Co_{0.25}O_x$, and (e) NiO_x conditioned thin films. Plotted in each are: the raw data (dark blue), fitted peaks for adventitious carbon species (black), metal oxide peaks (orange), the total fitted peak envelope (red), the background (green), and the fit residuals (light blue). An example fit of the C 1s spectra is shown in (f) for the NiO_x thin film. Co $2p_{3/2}$ spectra (g) only contain Co^{2+} shake-up satellite peaks (indicated by arrows) for samples with higher ($\geq$ 50%) Ni concentrations.

39

2.10, where the rock salt NiO undergoes an *in situ* transformation to the layered hydroxide/oxyhydroxide phase, while the initial presence of Co that favors the spinel-type oxide inhibits this transformation. Because the ultra-thin-film architectures studied here are essentially "all surface" the observed electrochemical response is particularly sensitive to these changes. These observations could also be important for understanding previously studied $Ni_yCo_{1-y}O_x$ systems,[23-27,40] where similar chemical changes are likely occurring at the outer surfaces of the particulate catalysts but perhaps masked by the various convoluting factors associated with catalysis measurements on porous electrodes mentioned earlier. After formation of the hydroxide/oxyhydroxide catalyst during conditioning, the NiO_x films are remarkably active, passing 20 mA cm^{-2} at an overpotential of 370 mV despite having an average thickness of only ~2 nm.

Previous work by Corrigan on electrochemical cycling of thicker (0.5 mg cm^{-2}) electrodeposited $Ni(OH)_2$ films has shown that iron impurities in KOH electrolyte solutions increase OER activity.[33] The catalytic activity of thinner films (50 µg cm^{-2}) was
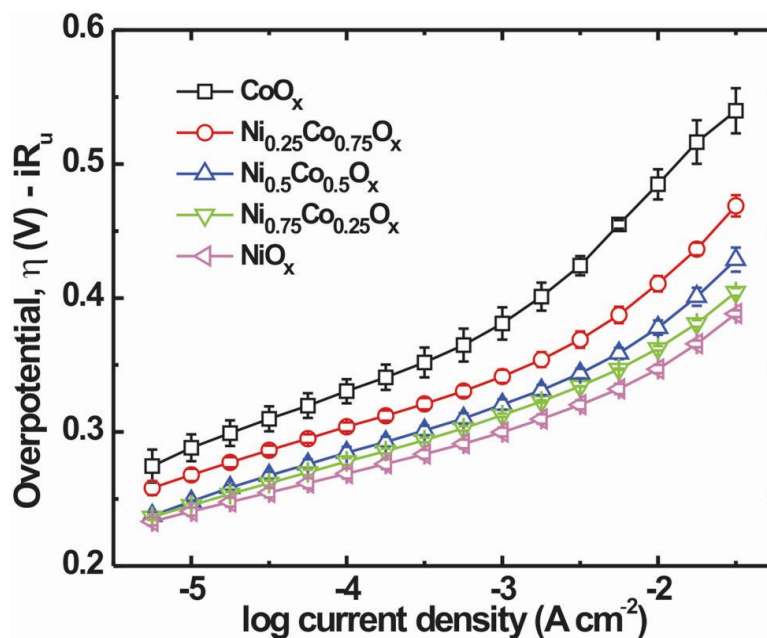
Figure 2.17. Steady-state Tafel measurements for conditioned NiO_x, $Ni_yCo_{1-y}O_x$, and CoO_x films collected in 1 M KOH. Each data point represents a galvanostatic measurement held for at least 15 minutes and is the average of three different electrode samples (1 QCM and 2 Au/Ti coated glass electrodes). Note that some error bars are smaller than the symbols.

shown to be affected more than thicker films, as the relative fraction of iron in the thinner film was greater. The effects were similar for films cycled in KOH solutions containing trace iron and for films where iron was co-precipitated with Ni during film deposition. With 10% co-precipitated iron, Corrigan measures a Tafel slope of 25 mV dec^{-1}, similar to what is measured here (the activity per Ni site is compared quantitatively below).

We used the highest-purity KOH available to prepare the 1 M KOH electrolyte which had < 40 ppb Fe based on the lot analysis provided by the supplier. Fe impurities may also enter the solution from the glass electrochemical cell during exposure to basic solution. To determine the extent of iron incorporation into the $Ni_yCo_{1-y}O_x$ films, the composition of the films before and after conditioning was analyzed by XPS and EPMA (Table 2.2). Both techniques indicate the presence of Fe in the conditioned NiO_x and $Ni_yCo_{1-y}O_x$ films, consistent with Corrigan's work.[33] The amount of Fe incorporated also depended on the Ni content in the film; the NiO_x films incorporated the most Fe, while Fe in the CoO_x films was below the detection limit. These results suggest that Ni-containing films scavenge Fe from the solution. (This is reminiscent of the high affinity of natural Fe(II)/Fe(III) hydroxides known as carbonated green rust for Ni^{2+} in iron-rich ocean waters,[45,46] which has been implicated in the oxygenation of ancient Earth's atmosphere.[46,47]) Pre-electrolysis of the KOH electrolyte solution (~10 cm^2 Ni mesh anode and cathode, 1 week at 3 V) to remove Fe and other impurities reduced the quantity of Fe incorporation by roughly a factor of two. A key result of these studies is therefore that the active catalyst material in the Ni-based films includes Fe (e.g. $Ni_yFe_{1-y}OOH$) and that the incorporation of Co limits its formation. As shown in Figure 8 and discussed below, direct synthesis of $Ni_{0.9}Fe_{0.1}O_x$ from the solution precursor increases slightly the activity of the catalyst film relative to the conditioned NiO_x films. Understanding the detailed role of Fe in the OER mechanism as well as the possible differences between Fe incorporated during film deposition or during electrochemical conditioning are important directions for future studies, and will be discussed in Chapter IV.

Table 2.2. Fe Content of Thin Films

Conditioned Sample	Fe/(Ni+Co)	
	EPMA	XPS
CoO_x	0	0
$Ni_{0.5}Co_{0.5}O_x$	0.034	0.11
NiO_x	0.18	0.14
NiO_x, electrolyzed KOH	0.035	0.079

Samples containing Ni also show a Mg 1s peak centered at ~1304 eV in XPS spectra after electrochemical treatment. The amount of Mg incorporated into the samples during electrochemical cycling is ~ 3 atomic % in NiO_x films and less in films with lower Ni concentrations. The Mg 1s peak is not observed in the XPS spectra measured on any of the samples before electrochemical treatment, nor in the conditioned CoO_x sample. The incorporation of Mg into these samples is presumably from Mg impurities in the electrolyte solution, as is the case with Fe impurities. Interestingly, trace Mg and Fe electrolyte impurities incorporate readily into NiO_x films, but are not found in the other metal oxide films studied. While the effect of Fe impurities on catalysis has been previously investigated,[33] understanding the effect of Mg impurities on NiO_x OER catalytic activity will require additional study.

Thin Films as a System for Comparing Catalytic Activity of Metal Oxides

The simplicity of the ultra-thin film solution deposition coupled with the precise QCM film mass measurements enables direct comparison of different materials. Figure 2.18 shows Tafel measurements for several known OER catalysts prepared as films by solution deposition. Relevant values of catalytic activity derived from these Tafel measurements, including Tafel slope and the turn-over frequency (TOF, defined as mol O_2 per mol metal per second), can be found in Table 2.3. Remarkably, the activity measured for the best catalyst studied here, $Ni_{0.9}Fe_{0.1}O_x$ is roughly 10-fold higher than that of IrO_x, which is traditionally considered to be one of the most active OER catalysts.[10] We note that the reported TOFs are lower limits because all of the deposited metal cations may, in some cases, not be in direct contact with the electrolyte. However, given that the films are on average only roughly 10 monolayers thick, and that they also likely contain sub-nm porosity resulting from the combusted organic surfactant used in

42

the precursor solution, the reported TOFs are certainly less than a factor of ten different from the true intrinsic values.

It is useful to compare the data measured in the thin-film electrode format with other measurements of catalyst activities. The active $Ni_yFe_{1-y}O_x$ samples derived from electrochemical conditioning of the thin film oxides are similar to the cathodically electrodeposited $Ni(OH)_2$ studied by Corrigan in the late 1980's.[32-34] Corrigan compared OER activities for $Ni(OH)_2$ with a variety of transition metal ion additives in 1 M KOH and found that the addition of ~10% Fe yielded the best performance.[33,34] At an overpotential of 287 mV, Corrigan measured a current of 0.1 A for 5.7 µmol of catalyst, equivalent to a TOF of 0.05 s^{-1}. At the same conditions we measured a similar TOF of 0.06 ± 0.01 s^{-1} for the conditioned $Ni_yFe_{1-y}O_x$ thin film catalysts, supporting the hypothesis that the NiO catalysts studied here form Fe-containing hydroxide phases under OER conditions. More recently Merrill and Dougherty[48] and Li et al.[49] have also measured OER activity of electrodeposited $Ni_yFe_{1-y}(OH)_2$ similar to that reported by
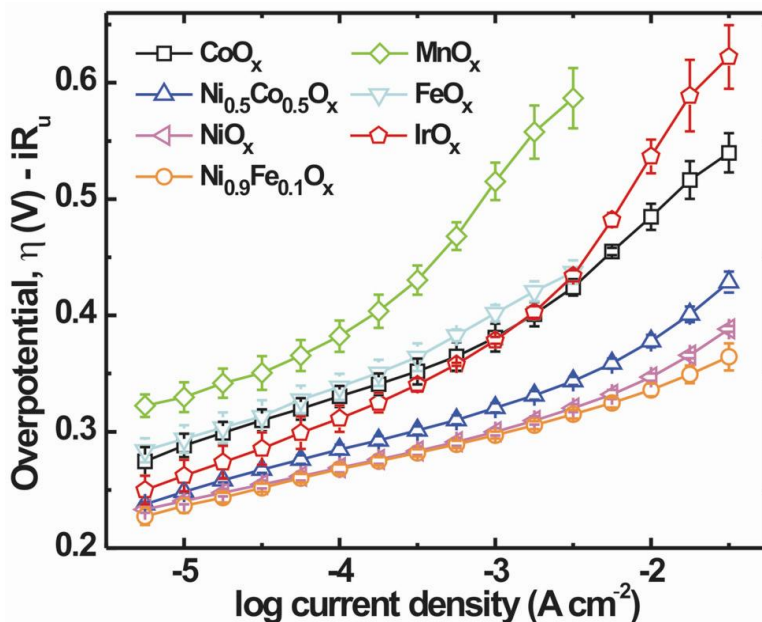
Figure 2.18. Comparison of steady-state Tafel measurements for ultra-thin films synthesized in this study collected in 1 M KOH. Each data point represents a galvanostatic measurement held for at least 15 minutes and is the average of three different electrode samples (1 QCM and 2 Au/Ti coated glass electrodes). Note that some error bars are smaller than the symbols.

Corrigan. Direct comparison to that data, however, is not possible because the quantity of catalyst measured was not reported.

Recently there has been significant work on CoO_x-based catalysts for water oxidation in neutral to basic aqueous media. Surendranath et al. studied the water oxidation mechanism for CoO_x/phosphate (Co-Pi)[50] thin films with known Co content in near-neutral pH.[51] Based on that data, we calculate a TOF of 4×10^{-5} s^{-1} at $\eta = 300$ mV. This is ~80-fold slower than we find for CoO_x and ~5000-fold slower than the $Ni_{0.9}Fe_{0.1}O_x$. A key difference between these measurements is the electrolyte pH. Co-Pi operates at near neutral pH's, which is advantageous for coupling to semiconductor absorbers that are unstable in basic or acidic media. Measurements made here were performed in 1 M KOH. Further studies are needed to quantify and understand the operation and stability of $Ni_{0.9}Fe_{0.1}O_x$ as a function of pH.

Yeo and Bell investigated CoO_x and $Ni(OH)_2$ films electrodeposited onto roughened metal electrodes and reported that high-work-function metals such as Au enhanced the CoO_x[52] and $Ni(OH)_2$[53] OER activity in 0.1 M KOH for the first few monolayers of deposited oxide. At $\eta = 350$ mV they found a TOF for 0.4 monolayers of CoO_x on Au of 1.7 s^{-1}, much higher than the TOF measured for a thicker film (~87 monolayers) of 0.06 s^{-1}. At $\eta = 350$ mV we found a lower limit TOF for the CoO_x film (~17 monolayer-equivalents calculated as in ref 48) of 0.050 ± 0.023 s^{-1} assuming every Co was active, consistent with the findings of little support-induced activity enhancement beyond the first few CoO_x monolayers observed by Yeo and Bell. For $Ni_{0.9}Fe_{0.1}O_x$ we found a TOF at $\eta = 350$ mV of 2.8 s^{-1} on the Au/Ti QCM crystals. Similar TOFs were measured for $Ni_{0.9}Fe_{0.1}O_x$ samples on ITO electrodes (Figure 2.19), demonstrating negligible enhancement from the Au support for the $Ni_{0.9}Fe_{0.1}O_x$ films measured here.

The measured TOFs can also be compared to those obtained for all-inorganic molecular catalysts such as $[Co_4(H_2O)_2(PW_9O_{34})_2]^{10-}$ (Co$_4$POM), which appear to be the fastest known homogeneous water oxidation catalysts.[54] A TOF of 5 s^{-1} for the Co$_4$POM cluster (or ~1.3 s^{-1} per Co) was measured at pH 8 using Ru(bpy)$_3^{3+}$ (bpy = 2,2'-bipyridine) as a molecular oxidant (E° = 1.24 V vs. NHE, equivalent to $\eta = 480$ mV).[55] We measured a TOF for the CoO_x film at $\eta = 480$ mV of 1.5 ± 0.3 s^{-1}, similar to that of the molecular catalyst.

Table 2.3. Comparison of Metal Oxide Thin Film OER Activity[a]

	η @ 1 mA cm^{-2} (mV)	dry film loading (μg cm^{-2})	J @ η = 0.3 V (mA cm^{-2})	mass activity @ η = 0.3 V (A g^{-1})	TOF (s^{-1}) @ η = 0.3 V	Tafel slope (mV dec^{-1})
MnO$_x$	514 ± 22	1.13 ± 0.08	0.002 ± 0.0009	1.8 ± 0.8	0.0004 ± 0.0002	49 ± 3
FeO$_x$	405 ± 4	1.63 ± 0.08	0.012 ± 0.007	7.6 ± 4.5	0.0015 ± 0.0009	51 ± 3
IrO$_x$	378 ± 4	4.12 ± 0.14	0.063 ± 0.036	15 ± 8.7	0.0089 ± 0.0050	49 ± 1
CoO$_x$	381 ± 12	1.32 ± 0.14	0.020 ± 0.009	15 ± 6.8	0.0032 ± 0.0014	42 ± 1
Ni$_{0.25}$Co$_{0.75}$O$_x$	341 ± 5	1.62 ± 0.09	0.079 ± 0.018	49 ± 11	0.0099 ± 0.0023	36 ± 1
Ni$_{0.5}$Co$_{0.5}$O$_x$	320 ± 4	1.06 ± 0.08	0.30 ± 0.07	280 ± 70	0.056 ± 0.014	35 ± 2
Ni$_{0.75}$Co$_{0.25}$O$_x$	312 ± 1	1.04 ± 0.09	0.47 ± 0.05	452 ± 64	0.089 ± 0.013	33 ± 1
NiO$_x$	300 ± 3	1.13 ± 0.10	1.01 ± 0.22	896 ± 206	0.17 ± 0.04	29 ± 0.4
Ni$_{0.9}$Fe$_{0.1}$O$_x$	297 ± 0.3	1.17 ± 0.14	1.24 ± 0.04	1065 ± 129	0.21 ± 0.03	30 ± 1

[a] See previous discussion of the origin and propagation of uncertainties.
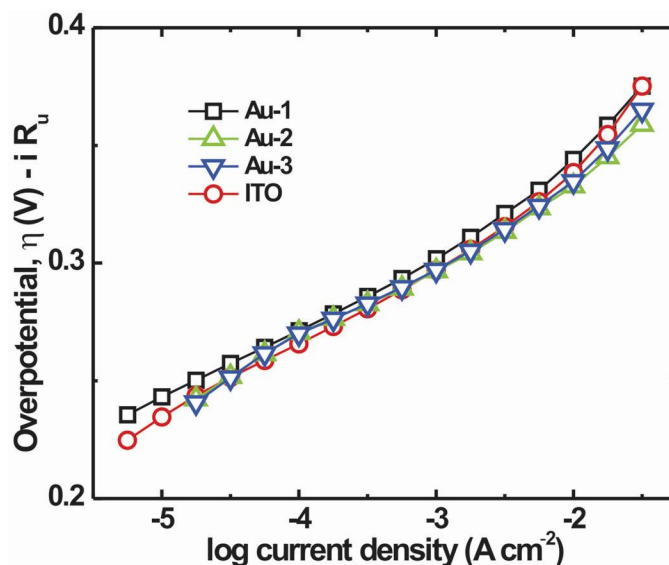
Figure 2.19. Tafel plot showing four different $Ni_{0.9}Fe_{0.1}O_x$ thin films samples. Three of the samples were deposited on Au/Ti coated substrates and one (shown as red circles) was deposited on ITO-coated glass. The Au electrode surface does not impart any significant enhancement to the catalysis for these materials.

$Ni_{0.9}Fe_{0.1}O_x$ studied here appears to be one of the most active OER catalysts in basic media known. The $Ni_{0.9}Fe_{0.1}O_x$ is superior to the IrO_x control catalyst films synthesized in our lab with TOFs up to 2 orders of magnitude higher than IrO_x depending on η (Table 2.3 and Figure 2.18). These IrO_x control films have a comparable activity to IrO_2 nanoparticles recently measured in 0.1 M KOH by Lee et al. using a controlled rotating disk technique.[56] Lee et al. found that at $\eta = 300$ mV ~5-nm-diameter IrO_2 particles had a mass activity of 11 A g^{-1} and a specific surface-area activity of 1.5×10^{-5} A cm^{-2}. Assuming a surface Ir density of $\sim 1 \times 10^{15}$ cm^{-2} (corresponding to the stable (110) surface) this yields a TOF at $\eta = 300$ mV of 0.02 s^{-1}. We measured a similar mass activity of 15 A g^{-1} and a lower-limit TOF (based on total Ir) of 0.009 s^{-1} for the IrO_x thin films. The agreement between these different measurements confirms the suitability of the IrO_x films as controls for comparison to other catalysts. Hydrous IrO_x nanoparticles have also been studied which appear to show higher OER activity.[14,57] From Tafel data reported for hydrous $IrO_x \cdot nH_2O$ nanoparticle films by Bediako et al., we calculate a TOF at $\eta = 300$ mV of ~0.4 s^{-1} at pH 12.5.[14] In that case, the electrochemically active sites are determined from the integrated charge of voltammetry sweeps. We found that these films

46

were not stable at pH 14 and therefore were unable make a direct comparison of the TOF to the films studied here.

We can compare $Ni_{0.9}Fe_{0.1}O_x$ to the BSCF material reported recently by Suntivich et al., which was reported as one of the fastest known OER catalysts in basic media with specific surface-area activity 10-fold higher than IrO_2. The mass activity of the $Ni_{0.9}Fe_{0.1}O_x$ catalyst ($\sim 10^3$ A g^{-1} at $\eta = 300$ mV) is 100 times higher than that of the ball-milled BSCF nanoparticle material measured in 0.1 M KOH at $\eta = 300$ mV.[3] However, the BSCF nanoparticle size was large (~ 230 nm), with the interior of the particles inactive. It is more useful, therefore, to compare intrinsic activities such as the TOF. At low overpotentials of ~ 300 mV the BSCF has a TOF of ~ 0.6 s^{-1}, calculated based on the measured surface-area and known crystal structure of the BSCF sample,[58] and assuming only the Co/Fe cations are active (and the Sr/Ba inactive). This is similar to the lower-limit $Ni_{0.9}Fe_{0.1}O_x$ TOF of 0.21 s^{-1}, which was calculated based on the total Ni and Fe content of the film. At higher η the $Ni_{0.9}Fe_{0.1}O_x$ catalyst appears superior due to the lower Tafel slope of ~ 30 mV dec^{-1} compared to the BSCF Tafel slope of ~ 50 mV dec^{-1}.

The $Ni_{0.9}Fe_{0.1}O_x$ therefore has similar activity to the best-reported previous catalysts (BSCF) and roughly an order of magnitude higher activity than precious-metal IrO_2 catalysts in basic media. It contains only inexpensive earth-abundant elements, and can be easily deposited on arbitrary substrates by the solution method described here. One possible reason for the high activity of the NiOOH-based catalysts is that the catalytic activity occurs within the three-dimensional layered hydroxide/oxyhydroxide structure, which is different than typical solid materials where catalysis occurs only at surface sites. The role of three-dimensional structure on the electrocatalytic properties is intriguing and a focus of our current studies in this area and will be discussed in Chapter V.

Conclusions and Bridge

We developed a simple synthesis route to deposit OER catalysts of arbitrary composition as films only a few nm thick. The films were deposited on quartz crystal microbalance electrodes where the mass was measured and monitored *in situ* and the chemical/structural features of the films could be probed *ex situ* using surface analytical

techniques. This provided a method to study the activity and electrochemical properties of heterogeneous electrocatalysts independent of other confounding factors associated with thick porous films. The method can be easily extended to other important heterogeneous electrocatalyst systems (for example, CO_2 reduction[59,60]). By examining a series of metal oxide thin films, we found that $Ni_{0.9}Fe_{0.1}O_x$ is a more active OER catalyst than IrO_2 in basic media with similar activity to optimized BSCF perovskite catalysts[3] - the current state-of-the-art. We also found no evidence for a synergistic effect between Co and Ni oxides in the mixed oxide catalyst films, which is different from previous findings.[24-28,44] For all films containing Ni, we observed an *in situ* structural transformation from oxides to layered hydroxides/oxyhydroxides that correlates directly with increased catalytic activity, indicating that the layered hydroxide/oxyhydroxide catalysts are the active catalysts. The simple synthesis methods used here allow for the straight-forward incorporation of the electrocatalysts with semiconductor photoelectrodes for sunlight-driven water splitting, as well as for use in designer three-dimensional high-surface-area electrodes for optimized alkaline water electrolysis.

This chapter detailed work investigating the catalytic activity of several transition-metal oxide catalyst materials for the oxygen evolution reaction. The optical properties of electrocatalysts are also important for photoelectrochemical water splitting because colored catalysts on the surface of semiconductor photoelectrodes parasitically absorb photons and lower the system efficiency. In Chapter III, we present a model that describes the coupling of colored OER electrocatalyst thin films with semiconductor photoelectrodes. We use this model to define an "opto-catalytic" efficiency (Φ_{o-c}) based on experimental optical and electrokinetic data collected in basic solution. Because transition metal oxides, hydroxides, and oxyhydroxides often exhibit electrochromism, *in situ* spectroelectrochemistry is used to quantify the optical absorption of active NiO_x, CoO_x, $NiCoO_x$, $Ni_{0.9}Fe_{0.1}O_x$, and IrO_x catalyst films at OER potentials. This work quantitatively shows that ultra-thin catalyst films are appropriate to optimize the performance of water-splitting photoelectrodes and thus assists in the design and study of efficient photoelectrochemical water-splitting devices.

CHAPTER III

AN OPTO-CATALYTIC MODEL FOR SEMICONDUCTOR-CATALYST

WATER-SPLITTING PHOTOELECTRODES

Portions of this chapter were previously published as Trotochaud, L; Mills, T.J.; Boettcher, S.W. "An Optocatalytic Model for Semiconductor–Catalyst Water-Splitting Photoelectrodes based on *In Situ* Optical Measurements on Operational Catalysts" *Journal of Physical Chemistry Letters*, **2013**, *4*, 931-935. L.T. wrote the paper, performed the experimental work, and made the figures. T.J.M., a graduate student, assisted with refining the composite semiconductor-catalyst model and calculations. S.W.B. was the principal investigator and provided editorial assistance.

Introduction

Photochemical water electrolysis to form hydrogen and oxygen gas (i.e. solar water splitting, $H_2O \rightarrow H_2 + \frac{1}{2}O_2$) provides a pathway for the large-scale conversion and storage of solar energy.[1,2] Water-splitting photoelectrochemical (PEC) cells typically consist of at least two classes of materials: (1) inorganic semiconductors or molecular chromophores that absorb sunlight to generate excited electron-hole pairs, and (2) electrocatalysts that facilitate the fuel-forming hydrogen and oxygen evolution reactions (HER and OER, respectively).[1] In particular, the OER (e.g. $4OH^- \rightarrow 2H_2O + O_2 + 4e^-$ in basic media) is kinetically slow and a significant source of efficiency loss in both electrically driven and photodriven water electrolysis.[2,3]

The separate optimization and development of materials for either semiconductor photoelectrodes or electrocatalysts has been studied for several decades.[1,4,5] Recently, significant effort has been extended to incorporate OER catalysts with semiconductor photoanodes and understand the response of the composite systems.[5-22] The optical properties of the catalyst layer affect the light absorption of the underlying semiconductor substrate, but have not been quantitatively addressed. Furthermore, the transition-metal oxide, hydroxide, and oxyhydroxides used as OER electrocatalysts often exhibit electrochromism (and thus have applications also in "smart" windows[23,24]). The optical properties of these catalysts measured in the resting state are therefore expected to differ

from those measured at operational potentials. Because of the tradeoff between increased parasitic optical absorption and decreased overpotential as film thickness is increased,[21] quantitative evaluation of the underlying optical, catalytic, and semiconductor device processes is important for uncovering the design principles governing the performance of composite photoelectrode systems.[25]

Here, we present a model for composite PEC current-potential response that includes both catalytic and optical measurements made *in situ* during oxygen evolution for a range of electrocatalyst materials. Recently, we reported the solution synthesis and catalytic activities of several OER electrocatalyst thin-film materials, including NiO_x, $NiCoO_x$, CoO_x, IrO_x, and $Ni_{0.9}Fe_{0.1}O_x$ which we found had the highest activity of any OER electrocatalyst in basic media.[26] Here, we report the quantitative analysis of the optical properties of these thin films under OER conditions using *in situ* spectroelectrochemistry. The combined electrokinetic and *in situ* optical absorption data are used to define an "opto-catalytic" efficiency (Φ_{o-c}). Φ_{o-c} is a function of catalyst loading. At optimal catalyst loading, Φ_{o-c} is a quantitative measure of the utility of a particular electrocatalyst for composite semiconductor-catalyst PEC water splitting systems.

Experimental Details

Sample Preparation

Thin films were solution-cast from ethanolic solutions of metal nitrate salts as reported previously. A full characterization of the physical and electrochemical properties of the thin film electrocatalysts can be found in our previous work.[26] Tin-doped indium oxide (ITO) coated glass substrates (Delta Technologies) were used for spectroelectrochemical experiments. Before optical measurements, films containing Ni were galvanostatically conditioned for 6 hr at 10 mA cm^{-2} (anodic) in ultrapure 1 M KOH (Fluka Analytical TraceSelect, $\geq$ 30%, diluted with 18.2 MΩ cm water) to convert from the oxides to the active oxyhydroxides.[26] Ultrahigh-purity O_2 gas was bubbled through the solution for at least 20 min prior to and throughout electrochemical conditioning.

For samples containing Ni, thin strips (< 1 mm wide) of Au/Ti were evaporated onto the ITO substrates prior to sample deposition to reduce series resistance and yield more uniform potential distribution across the ITO during the anodic conditioning. The substrates were masked so that samples could be positioned in the cell without the Au strips in the light path. Electrodes were fashioned by attaching tinned-Cu wire to the conductive ITO surface using Ag paint (Ted Pella). Ag paint was applied along the top edge of the ITO to contact both of the Au strips. The painted area was then sealed in inert epoxy (Loctite Hysol 9460) along with the contacting wire that was fed through a glass tube. Control experiments showed no background current from the epoxy.

Electrochemical Measurements

All electrochemical data were corrected for uncompensated series resistance R_u, which was determined by equating R_u to the minimum total impedance in the frequency regime between 10–50 kHz where the capacitive and inductive impedances are negligible and the phase angle was near zero. R_u was typically ~2–6 Ω for electrodes made using ITO. The overpotential η was calculated using the equation $\eta = E_{measured} - E_{rev} - iR_u$ where $E_{measured}$ is the potential recorded vs. Hg/HgO, E_{rev} is the OER reversible potential vs. Hg/HgO (0.30 V at pH 14), and i is the current. Current densities are calculated using geometric electrode surface areas. The steady-state electrokinetic data were collected galvanostatically as reported previously.[26]

The spectroelectrochemical cell for transmission measurements consisted of a 1 cm polished glass cuvette containing ultrapure 1 M KOH, a Hg/HgO reference electrode (CH Instruments) filled with 1 M KOH, and a Ni mesh counter electrode (Figure 3.1). The potential of the 1 M KOH Hg/HgO electrode was measured to be 0.929 V vs. the reversible hydrogen electrode (RHE) at pH 14 (i.e. 0.112 V vs. NHE). The RHE was fabricated by bubbling high-purity hydrogen over a freshly cleaned Pt mesh in 1 M KOH. The cuvette was placed in a sample holder (Avantes CUV-ALL-UV/VIS) connected via fiber optic cables to a tungsten halogen light source and an OceanOptics USB2000 spectrometer. The counter and reference electrodes were carefully positioned in the spectroelectrochemical cell so as not to encounter the path of the light source. The cuvette containing only electrolyte was used as a blank for the *in situ* measurements. Samples were positioned with the back side of the substrate facing the light source.
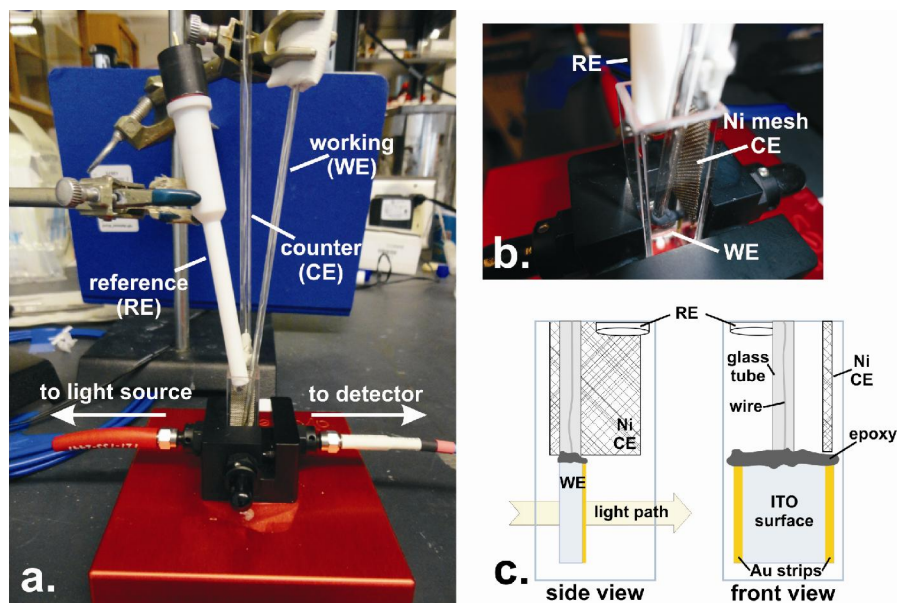
Figure 3.1. (a.) Spectroelectrochemical cell for *in situ* optical measurements (side view). (b.) Close-up of electrodes in glass cuvette cell (angled front view). (c.) Schematics of the cell. The Hg/HgO RE is positioned at the very top of the cell, just below the electrolyte surface. The Ni mesh CE is positioned above the WE sample and out of the light path. Inert epoxy covers the surface of the ITO-coated substrate where the electrode wire and silver paint make contact to the ITO and the Au strips, sealing the wire inside of the glass tubing. Electrode components above the electrolyte fill level have been excluded for clarity.

In Situ Reflection Sample Holder Fabrication

Reflection spectra were collected for each film using a PerkinElmer Lambda 1050 UV/VIS/NIR spectrometer with an integrating sphere attachment. A Spectralon (Labsphere) target was used as a 100% reflectance standard. The samples were positioned at the back of the sphere in a custom liquid cell (see Figure 3.2). The individual pieces of the cell are designed specifically to mimic the interfaces of the *in situ* spectroelectrochemical cell shown in Figure 3.1. The 1" hole cut into the center of two Al plates that make up the cell holder is the same size as the hole at the back of the integrating sphere where light hits the sample. The liquid cell is constructed for each sample by first placing the front Al plate (i.e. the one that will be closest to the light source) on a flat surface. A glass microscope slide (which mimics the glass wall of the cuvette) is inserted into the 1 mm deep trough cut into the Al plate. Next, a 1" o-ring is positioned to act as a spacer between the glass slide and the sample. The sample is

52

positioned next with the ITO-coated sample side facing up (away from the light source). A second o-ring is positioned on the sample-side of the ITO aligned with the light-path hole. A glass slide with evaporated Pt on Ti is inserted into the 1 mm trough in the second aluminum piece such that only about 2 mm of the evaporated Pt is contacting the solution (i.e. the Pt is not intersecting the light path). The second Al piece is then tightened down with thumbscrews onto the stack so that the o-rings act as liquid-tight seals. The void space in the center of the o-rings is then filled with electrolyte using a 27-gauge hypodermic needle penetrating the o-ring. A second hypodermic needle penetrates the o-ring to act as an air vent during electrolyte filling. This venting needle is left in the o-ring during electrochemical measurements to enable escape of any evolved O_2 or H_2 gases.
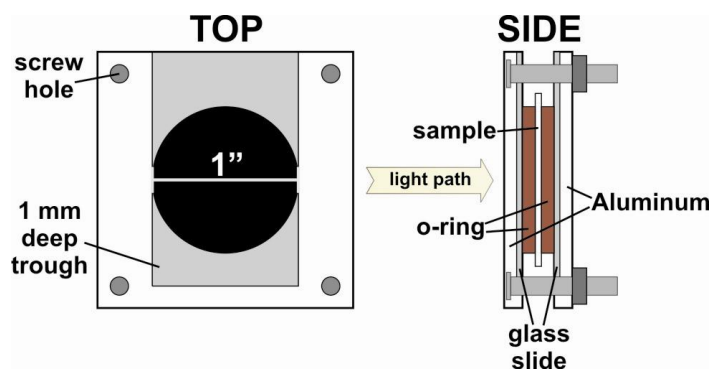
Figure 3.2. Schematic of the custom liquid cell holder used for reflection measurements.

Electrical contacts are made to the ITO surface and the Pt using tinned-Cu wire and silver paint applied around the outer edge of the o-ring. The Pt-coated glass slide was used as the reference/counter electrode using the potentiostat in 2-electrode mode. A constant anodic current density of 0.1 mA cm^{-2} was applied to the sample working electrode, which was sufficient to oxidize the catalyst films without generating visible oxygen bubbles at the electrode surface. Reflection spectra collected at higher current densities (0.5 and 1.0 mA cm^{-2}) where some small bubbles started to form did not show significant differences from those taken at 0.1 mA cm^{-2}.

In situ Measurement of Catalyst Transmission

For optical measurements, catalysts were deposited onto ITO-coated glass substrates from ethanolic solutions of metal salts containing surfactant to decrease

surface tension and promote even film coverage.[26] Annealing at 300° C for 5 min resulted in ~2 nm films with uniform coverage across the surface of the substrates. All films containing Ni were electrochemically conditioned in 1 M KOH by applying 10 mA cm^{-2} (anodic) for 6 h prior to optical measurements. This conditioning process converts the Ni-containing oxides to oxyhydroxides that are the active catalyst materials.[26] *In situ* optical experiments were performed in a spectroelectrochemical cell (Figure 3.1). The optical transmission spectra of the conditioned films were measured at constant applied potentials after waiting 30 s to reach steady state. Figure 3.3A shows a cyclic voltammogram (CV) along with the potentials used for the steady-state measurements. Figure 1B shows each transmission spectrum collected from 0.0–0.60 V vs. Hg/HgO in 0.05 V increments. The transmission remains constant until ~0.5 V vs. Hg/HgO, which is near the peak of the Ni^{2+}/Ni^{3+} oxidation wave. This behavior is consistent with previous studies of electrochromism in NiO$_x$ and Ni(OH)$_2$.[27-29]
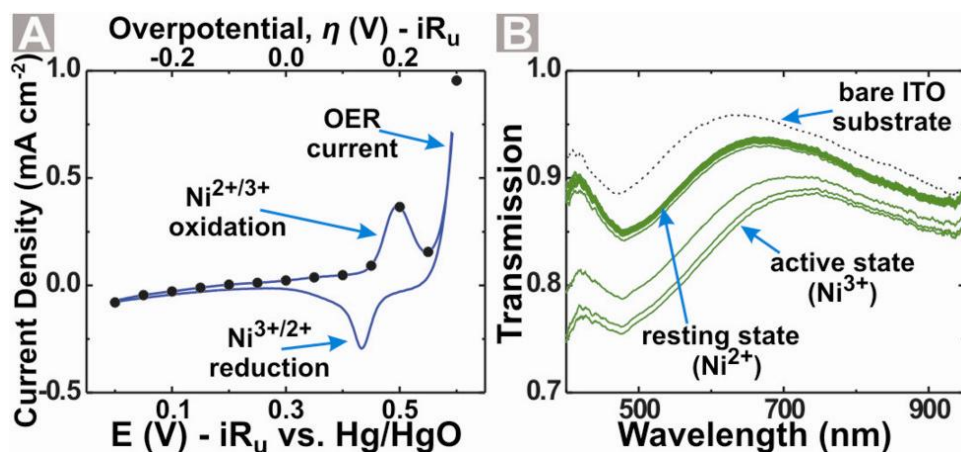
Figure 3.3. (A) Cyclic voltammogram (CV) of a NiO$_x$ film on ITO collected in the spectroelectrochemical cell. Points overlayed on the CV indicate the potentials where steady-state optical measurements were made. The CV was collected in 1 M KOH at 20 mV s^{-1}. (B) UV-Vis transmission spectra of a conditioned NiO$_x$ film held at constant potentials. 13 spectra are shown for the NiO$_x$ film, each taken at 0.05 V intervals starting at 0 V and increasing to 0.6 V vs. Hg/HgO.

Figure 3.4 shows the transmission spectra for NiO$_x$, NiCoO$_x$, CoO$_x$, Ni$_{0.9}$Fe$_{0.1}$O$_x$, and IrO$_x$ thin films in the resting (reduced) and catalytically active (oxidized) states. Spectra for the resting film states were collected at 0 V applied vs. Hg/HgO. Spectra for the active states were collected at 1 mA cm^{-2} applied anodic current. This current density

54

was sufficient to oxidize the films to their active state without generating visible bubbles at the electrode surface. At higher currents where small bubbles were visible the transmission spectra did not significantly change. Only samples containing Ni displayed a significant difference in optical transmission between the resting and active catalyst. For all the Ni-containing films, optical switching between the active and resting states correlated with the positions of the Ni^{2+}/Ni^{3+} oxidation and reduction waves, respectively, in the voltammetry. The electrochromic response is completely reversible upon cycling, which is not always observed in thicker films.[29]
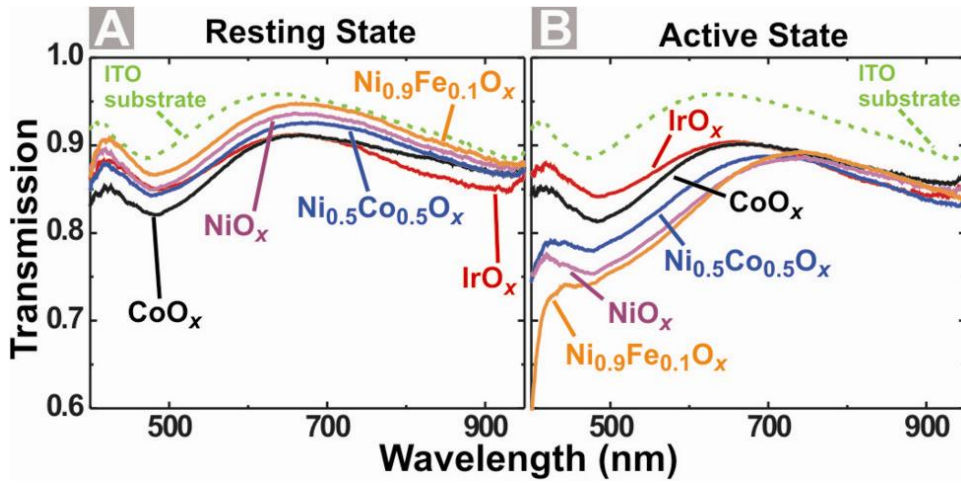
Figure 3.4. *In situ* spectroelectrochemical measurements of resting (A) and active (B) catalyst films. The dashed line shows the transmission spectrum of the ITO substrate. The catalyst spectra shown are not corrected for reflection or absorption of the ITO substrate. The cuvette filled with electrolyte was used as a blank for the measurement.

Modeling the Efficiency of a Composite Semiconductor-Catalyst Photoanode

The measured optical and electrokinetic data were used to predict how changing the thickness of the catalyst films would affect the photocurrent and photovoltage at maximum power for a composite photoelectrode. Figure 3.5 shows a schematic of the composite photoelectrode considered. The relevant input parameters depend on the material properties. For example, if the catalyst is on n-Fe_2O_3 with a band gap $E_g = 2.2$ eV, only photons with $\lambda \leq 560$ nm are absorbed in the semiconductor. As an example, we analyze an n-type photoanode with $E_g = 1.8$ eV ($\lambda \leq 690$ nm). Under 1 sun illumination and in the absence of catalyst optical absorption, we choose an initial short-circuit photocurrent $J_{ph,i} = 10$ mA cm^{-2} and a dark saturation current $J_o = 6.8 \times 10^{-23}$ A cm^{-2} such

that the photoelectrode outputs an open circuit voltage V_{oc} = 1.2 V based on the ideal diode equation (see below). These parameters represent those suitable for an efficient photoanode component of a tandem PEC water splitting device.[1] The photovoltage output is referenced to the reversible potential for the water oxidation reaction $E(O_2/OH^-)$, meaning that the photocurrent onset potential would be at +0.03 V vs. the reversible hydrogen electrode (RHE). For simplicity, we assume that J_o of the bare photoanode is not modified by the addition of a catalyst layer. This implies that the semiconductor and catalysis processes occur in series and that the semiconductor Fermi level is pinned at the surface (for instance by the catalyst or via buried semiconductor junction). This model therefore does not include changes to interface band-bending or surface recombination rates with the addition of the catalyst, which appear to be important for some materials systems such as Fe_2O_3/Co-Pi.[6]
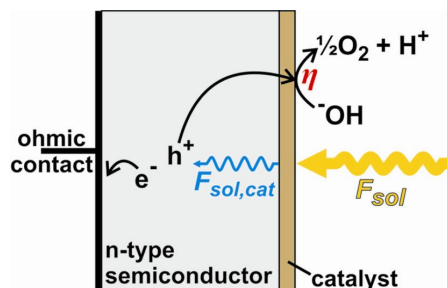
Figure 3.5. A composite PEC photoanode where the catalyst thin film attenuates the solar flux that reaches the semiconductor photoelectrode.

Optical Modeling and Measurements to Extract Catalyst Absorption a_c

  Transmission and reflection experiments were used to determine the absorption probability of a photon that encounters that catalyst layer. To do this, we consider the optical events that occur in the liquid cell for each measurement. Figure 3.6 gives cross-sectional view of the liquid cell for the three different measurements that were made for each set of experiments. For all measurements, the incident beam intensity I_o is shown entering from the left side of the cross-section. For the transmission experiments, the detector is on the right side of each cross-section, while in the reflection experiments, the detector is on the left side of each cross-section.
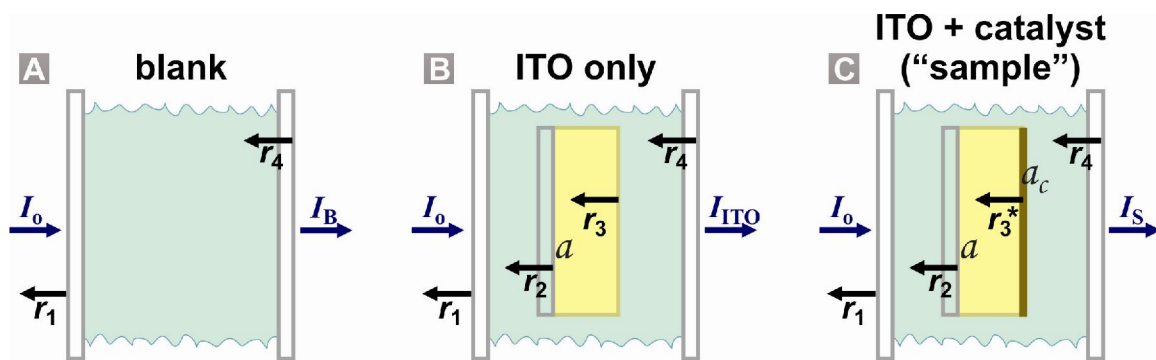
Figure 3.6. Cross-sectional view showing the light path through the *in situ* liquid cell. The symbols *a* and *r* signify absorption and reflection probabilities, respectively, with the subscripts indicating the location of the optical event as described below. The spatial location of the arrows and symbols along the vertical scale of the diagrams is not significant.

Note that in all cases, $r_1 = r_4 = r$, as these interfaces are both glass-air. We assume that reflection at the substrate glass-water interface (the ITO is coated onto Corning 1737F optical glass) and at the two water-glass interfaces at the walls of the liquid cell are negligible due to the similar refractive indices (optical glass $n \approx 1.5$; water $n \approx 1.3$) and that there is no absorption in the glass over the relevant range (400–690 nm). To simplify the analysis we ignore second-order and higher reflections, because the contribution to the overall reflection is small.

Figure 3.6A depicts the blank measurement. At each glass (shown as grey lines) to air (surrounding white space) interface the reflection probability is $r_1 = r_4 = r$.

Figure 3.6B depicts a measurement of the bare ITO substrate (shown as a yellow box). In addition to r_1 and r_4, there are two additional first-order reflection events at the front and back surfaces of the ITO layer, with probabilities r_2 and r_3, respectively. Additionally, the probability that a photon that is not reflected at the first ITO surface will be absorbed in the ITO layer is a.

Figure 3.6C depicts a measurement of the electrocatalyst films that includes the ITO and the catalyst layers. The ultra-thin and porous nature of the films makes it inappropriate to consider them as optical layers with well-defined front and back reflection probabilities. Since the film thicknesses are deeply sub-wavelength ($\sim\lambda/100$), we assume that the entire film experiences the full intensity of the light reaching the ITO/catalyst interface. We therefore treat the ultra-thin catalyst by allowing for a

modification to the reflectivity of the ITO-water interface (i.e. r_3 changes to r_3^*) while also including the probability a_c of absorbing a photon in the catalyst for any photons that reach the interface.

We then solve the resulting system of equations that describe the transmission and reflection of the blank (A), substrate (B), and sample (C) spectra for a_c as a function of wavelength. The transmission data collected for measurement (A) T_B are given by

$$T_B = \frac{I_B}{I_o} = (1-r)^2 \tag{3.1}$$

as there are no absorption events and the transmission probability at each glass-air interface is $(1-r)$. Measurement (A) was experimentally used as a blank to normalize substrate (B) and sample (C) measurements. The experimental transmission data collected for the ITO substrate (B) T_{ITO} are given by

$$T_{ITO} = \frac{I_{ITO}}{I_B} = (1-r_2)(1-a)(1-r_3) \tag{3.2}$$

The experimental transmission data for the samples (C) T_S are given by

$$T_S = \frac{I_S}{I_B} = (1-r_2)(1-a)(1-r_3^*)(1-a_c) \tag{3.3}$$

The experimental reflection data for the blank (A) R_B are given by

$$R_B = r + (1-r)r \tag{3.4}$$

The experimental reflection data collected for the substrate (B) R_{ITO} are given by

$$R_{ITO} = r + (1-r)r_2 + (1-r)(1-r_2)(1-a)^2 r_3 + (1-r)(1-r_2)(1-a)^2(1-r_3)r \tag{3.5}$$

Again, we only account for first-order reflections, but do account for the absorption probability of the reflected photons (e.g. that a photon reflected at r_4 could be reabsorbed in the ITO layer on its way to the detector). The experimental reflection data collected for measurement (C) R_S are given by

$$R_S = r + (1-r)r_2 + (1-r)(1-r_2)(1-a)^2 r_3^* + (1-r)(1-r_2)(1-a)^2(1-r_3^*)(1-a_c)^2 r \tag{3.6}$$

Equations 3.2–3.6 describe the five types of optical measurements using the six variables r, r_2, a, r_3, r_3^*, and a_c. r_2, the wavelength-dependent reflection probability at the Corning 1737F glass-ITO interface (Figure 3.6 B and C), is calculated from tabulated data[30,31] for the two materials using the Fresnel equation:

58

$$r_2(\lambda) = \frac{(n_{ITO} - n_g)^2 + k_{ITO}^2}{(n_{ITO} + n_g)^2 + k_{ITO}^2} \qquad (3.7)$$

where n_{ITO} and n_g are the real parts of the refractive indices of ITO and 1737F glass, respectively, and k_{ITO} is the complex part of the refractive index of ITO.

Reflection spectra were collected independently using an integrating sphere. Figure 3.7 shows reflection measurements for R_B, R_{ITO}, and R_s as described above. Spectra for catalysts in their active state are shown as solid lines, while spectra for the resting Ni-containing catalysts are shown as dashed lines. In order to measure the reflection of the samples in their active (oxidized) state, a custom liquid cell holder was used, which is depicted in Figure 3.2. Only samples containing Ni displayed a significant difference in reflection between the resting and active catalyst. The reflection probability r can be determined from the measurement of R_B (see eq. 3.4). This leaves the four equations 3.2, 3.3, 3.5, and 3.6 and four unknowns a, r_3, r_3^*, and a_c. This system of equations was solved for a_c for each catalyst type using Wolfram Mathematica 8.0.4, giving four solutions, only one of which gave physical values for a_c (i.e. values of $0 \leq a_c \leq 1$). (See Appendix A for solution for a_c calculated using Mathematica.)
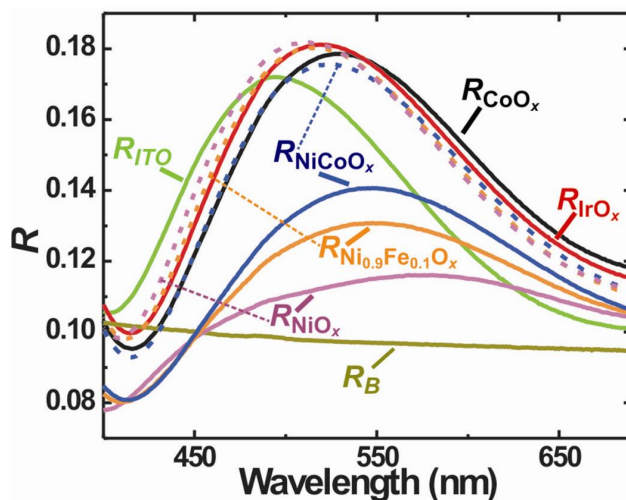
Figure 3.7. Data collected for reflection measurements in equation 3.4–3.6. R_S for the different catalysts are differentiated by using the sample name as the subscript for R. For the Ni-containing catalysts, reflection spectra for the resting catalysts are shown as dashed lines.

Defining and Determining the Opto-Catalytic Efficiency

In a composite PEC as shown in Figure 3.5, the catalyst determines the magnitude of both the photocurrent loss due to parasitic optical absorption and the photovoltage loss due to the kinetic overpotential. To model the parasitic optical absorption of the catalyst, the optical absorption of the catalyst layer, corrected for reflection and absorption by the ITO substrate, is needed. We extract the wavelength-dependent absorption probability of a photon that reaches the catalyst, a_c, by accounting for the absorption and reflection at each film and interface, respectively, in the experiment cell as described previously. The transmission probability for photons entering the catalyst layer is then $T_c(\lambda) = 1 - a_c(\lambda)$. The wavelength-dependent *effective* absorption coefficient $\alpha(\lambda)$ of the catalyst is given by

$$\alpha(\lambda) = \frac{-\ln(T_c(\lambda))}{t_o} \tag{3.8}$$

where $\alpha(\lambda)$ has units of cm^{-1} and t_o is the effective film thickness obtained for each film using quartz crystal microgravimetry and the catalyst density.[26] The calculated values of $\alpha(\lambda)$ for the different catalyst thin films are shown in Figure 3.8A.
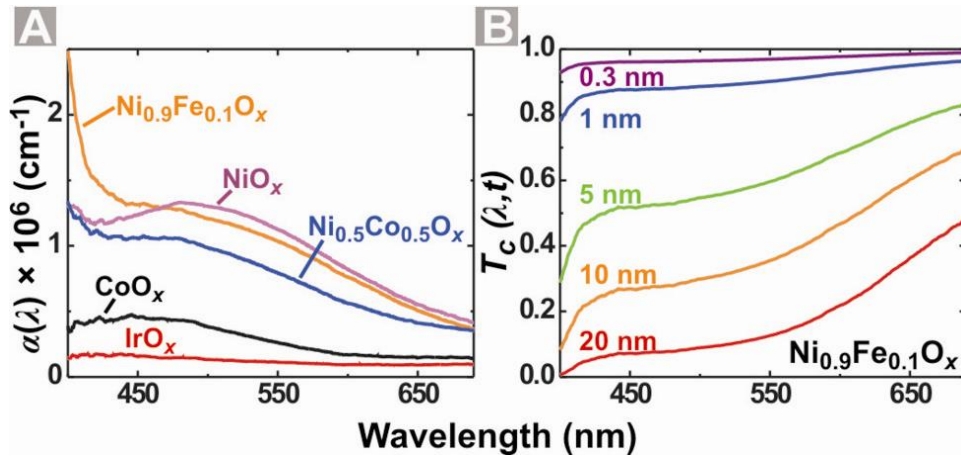
Figure 3.8. (A) Effective absorption coefficient $\alpha(\lambda)$ calculated for the active catalyst films. (B) Predicted transmission probabilities $T_c(\lambda)$ for Ni$_{0.9}$Fe$_{0.1}$O$_x$ films of varying thickness t.

The predicted optical transmission T_c through the catalyst is then a function of the film thickness t as shown in Figure 3.8B for the Ni$_{0.9}$Fe$_{0.1}$O$_x$ film. The solar flux incident

on the semiconductor surface that is transmitted through the catalyst thin film $F_{sol,cat}(\lambda,t)$ is given by

$$F_{sol,cat}(\lambda,t) = F_{sol}(\lambda)T_c(\lambda,t) \qquad (3.9)$$

Where $F_{sol}(\lambda)$ is the solar flux defined by the ASTM AM 1.5 standard. We define the catalyst optical efficiency $\varphi_{opt}(t)$ as

$$\varphi_{opt}(t) = \frac{\int_{\lambda_1}^{\lambda_2} F_{sol,cat}(\lambda,t)d\lambda}{\int_{\lambda_1}^{\lambda_2} F_{sol}(\lambda)d\lambda} \qquad (3.10)$$

where $F_{sol}(\lambda)$ and $F_{sol,cat}(\lambda,t)$ are integrated over the wavelength range relevant for the underlying semiconductor for a catalyst film of thickness t. Here λ_1 is 400 nm and is determined by the spectrometer range, and λ_2 is 690 nm, the threshold for absorption in the 1.8 eV bandgap photoanode under consideration.

Figure 3.9A shows $\varphi_{opt}(t)$ for varying film thicknesses. Relevant photocurrent losses occur even for films thinner than 10 nm. $\varphi_{opt}(t)$ is incorporated into the ideal photodiode equation to account for the catalyst optical properties in the composite photoelectrode current-voltage (J-V) response

$$J = \varphi_{opt}(t)J_{ph,i} - J_o\left(\exp\left(-\frac{qV_{diode}}{nkT}\right) - 1\right) \qquad (3.11)$$

where J is the total current, J_o is the dark saturation current, V_{diode} is the voltage dropped across the photodiode (i.e. the difference in the quasi-Fermi level in the semiconductor bulk and the catalyst layer), q is the elementary charge, n is the diode ideality factor (assumed $n = 1$), k is Boltzmann's constant, and T is temperature (300 K). For $Ni_{0.9}Fe_{0.1}O_x$, the J-V responses for different catalyst thicknesses ($t = 0.3$–20 nm) are shown in Figure 3.9B.

There will also be a voltage drop due to the catalytic overpotential η for driving oxygen evolution. We define η as a function of film thickness t assuming that the number of active sites increases linearly with film loading, leading to a linear increase in current with film mass at a given η. This is appropriate for porous or ion-permeable films,[26] e.g. $NiOOH$ or $CoOOH$, where such activity scaling has been observed.[32,33] Because the
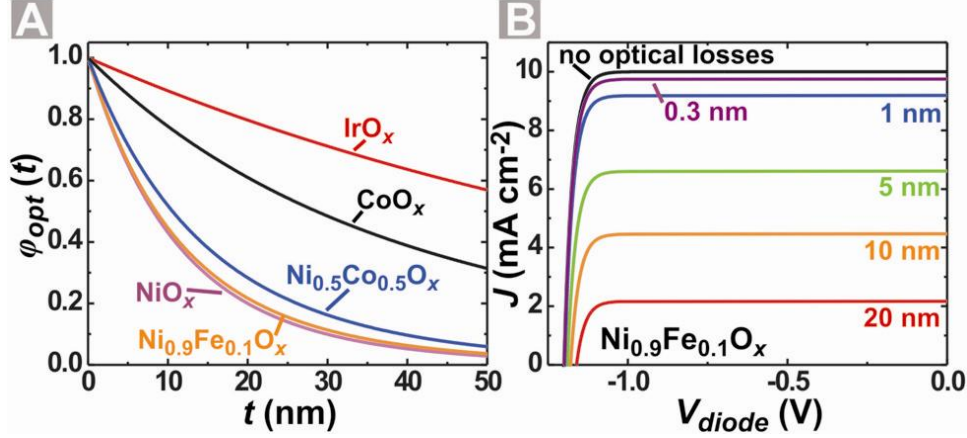
Figure 3.9. (A) Optical efficiency $\varphi_{opt}(t)$ calculated from eq 3.10 for the catalysts as a function of film thickness t. (B) Calculated photoelectrode J-V curves using eq 3.11 for the $Ni_{0.9}Fe_{0.1}O_x$ catalyst in the absence of kinetic overpotentials. The photovoltage is negative for an n-type photoanode relative to the reference potential, $E(O_2/OH^-)$, based on the electrochemical convention.

steady-state electrokinetic data[26] are not completely linear on a semi-log "Tafel" plot, they were fit to third-order polynomial functions

$$\eta(t,J) = A\log\left(\frac{J}{t}\right)^3 + B\log\left(\frac{J}{t}\right)^2 + C\log\left(\frac{J}{t}\right) + D \tag{3.12}$$

where J is the current density the catalyst is required to pass and A, B, C, and D are constants determined by the polynomial fit.

The total voltage across the photoelectrode accounting for η is $V_{total} = V_{diode} + \eta$. Rearranging eq 4 to incorporate η yields

$$V_{total} = -\frac{nkT}{q}\ln\left(\frac{\varphi_{opt}(t)J_{ph,i} - J}{J_o} + 1\right) + \eta(t,J) \tag{3.13}$$

The steady-state electrokinetic data and polynomial fits are shown in Figure 3.10A. Current-voltage curves for the $Ni_{0.9}Fe_{0.1}O_x$ catalyst of varying thickness ($t = 0.3$–20 nm) calculated using eq 3.13 are shown in Figure 3.10B.

Figure 3.10B shows that each catalyst thickness has different maximum power output P_{max}. The maximum power output of the photoelectrode in the absence of optical and kinetic losses (i.e. no catalyst) $P_{o,max}$ is 10.8 mW cm^{-2} ($V = -1.10$ V; $J = 9.77$ mA cm^{-2}). The "opto-catalytic" efficiency, Φ_{o-c} is

$$\Phi_{o-c} = \frac{P_{max}}{P_{o,max}} \tag{3.14}$$
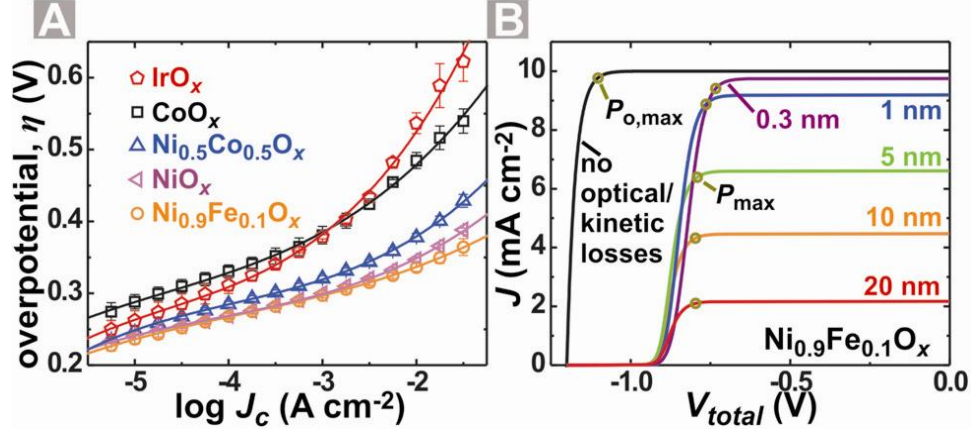
Figure 3.10. (A) Steady-state electrokinetic data (points) and corresponding polynomial fits (lines) for the catalyst thin films (data from ref. 26) (B) Photoelectrode current-voltage curves calculated using eq 3.13 for the $Ni_{0.9}Fe_{0.1}O_x$ catalyst as an example. The potential is referenced to the thermodynamic OER potential set at 0 V on this scale. The n-type photoanode produces a photovoltage that yields photocurrent due to water oxidation at potentials negative (cathodic) of the OER reference, thus converting solar energy to stored chemical energy. The maximum power point is calculated relative to the thermodynamic OER potential. For a complete discussion of these definitions, see ref. 1.

where P_{max} is the maximum power of the composite photoelectrode. Φ_{o-c} is the relevant figure-of-merit for catalyst performance.[*] The maximum values of Φ_{o-c} as a function of thickness are labeled in Figure 3.11. For the most active Ni-based catalysts, Φ_{o-c} peaks for sub-nm catalyst loading – i.e. only about 2 monolayers.

This result can be explained as follows. The kinetic loss η decreases roughly as the log of the film thickness. For example, with a Tafel slope of 30 mV dec^{-1}, a ten-fold increase in catalyst thickness reduces the voltage loss by 30 mV. However, in the thin limit (where the total optical absorption by the catalyst is small) a ten-fold increase in film thickness will lead to roughly a ten-fold increase in optical loss. Furthermore, the decreased J_{ph} associated with increased catalyst loading decreases the photovoltage output of the semiconductor based on eq 3.11. These factors combine to drive the optimal

---

[*] Maximizing Φ_{o-c} for the photoanode catalyst does not necessarily result in a higher water-splitting efficiency in a tandem photoanode/photocathode configuration. The overall water-splitting efficiency also depends on the characteristics of the photocathode component of the device. However, in an optimized tandem device, absorber bandgaps will be minimized to maximize the absorbed sunlight and hence photocurrent, which will constrain the total photovoltage available for driving water splitting. Thus, classes of catalysts with high Φ_{o-c}, and therefore low parasitic optical absorption and low overpotentials, are expected to be optimal for those situations as well.
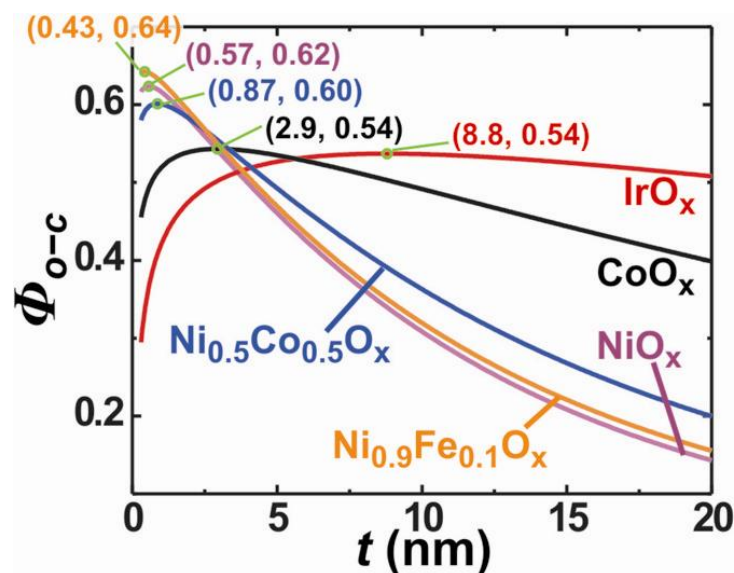
Figure 3.11. Opto-catalytic efficiency Φ_{o-c} plots for the catalysts as a function of film thickness, t.

catalyst loadings to ultra-thin films, where the optical losses are low (i.e. less than ~ 10%). The highly absorbing, but highly active, Ni-based catalysts show a precipitous drop in Φ_{o-c} after the optimal film thickness. For the less active, but more-transparent films such as IrO_x the peak in Φ_{o-c} is broad and lower than that of the $Ni_{0.9}Fe_{0.1}O_x$. This analysis therefore quantitatively shows that very low loadings of active catalysts, even when highly colored, yield the highest efficiency photoanodes.

Conclusions and Bridge

In conclusion, we have quantified the effects of parasitic catalyst optical absorption and overpotential losses on the efficiency and measurable photoresponse characteristics of composite semiconductor-catalyst systems. We defined a new efficiency figure-of-merit Φ_{o-c} that accounts for both optical and voltage efficiency terms, which are both important for applications in photoelectrochemical water splitting. Maximizing Φ_{o-c} led to an optimal film thickness that was sub-nm for the most active Ni-based catalysts. This simple model can be used to evaluate arbitrary catalyst-semiconductor combinations and determine the relative utility of catalysts with a range of optical properties and activities. The results reported here should therefore assist in the design and study of composite catalyst-semiconductor photoelectrodes.

64

In Chapters II and III, $Ni_{0.9}Fe_{0.1}OOH$ was identified as a highly active catalyst for the oxygen evolution reaction, and its optical properties were investigated and found to be compatible with incorporation into composite photoanodes for solar-water-splitting. However, little is known about how Fe enhances the activity of the Ni-based catalysts, and Chapter II in particular leaves many questions regarding the effects of Fe impurities in these materials. A fundamental understanding of composition/structure/activity relationships in highly active catalysts is critical for design of new materials. In Chapter IV, we report electrochemical, *in situ* electrical, photoelectron spectroscopy, and X-ray diffraction measurements of $Ni_{1-y}Fe_y(OH)_2/Ni_{1-y}Fe_yOOH$ thin films to investigate the changes in electronic properties, OER activity, and structure as a result of intentional and impurity-based Fe incorporation. We developed a simple method for purification of KOH electrolyte that uses precipitated bulk $Ni(OH)_2$ to absorb Fe impurities. Cyclic voltammetry on rigorously Fe-free $Ni(OH)_2/NiOOH$ reveals new Ni redox features and no significant OER current until >400 mV overpotential, different from previous reports which were likely affected by Fe impurities. Additionally, we show that previous reports of increased activity for β–NiOOH are due to incorporation of Fe-impurities during the crystallization process. Through-film *in situ* conductivity measurements show increases in film conductivity with Fe addition, but this change is not sufficient to explain the observed differences in activity. Measurements of activity as a function of film thickness are consistent with the hypothesis that Fe exerts a partial-charge-transfer activation effect on Ni, similar to that observed for noble-metal electrode surfaces. These results presented in Chapter IV have significant implications for the design and study of NiOOH-based OER electrocatalysts.

CHAPTER IV

NICKEL-IRON OXYHYDROXIDE OXYGEN-EVOLUTION

ELECTROCATALYSTS: THE ROLE OF INTENTIONAL AND

INCIDENTAL IRON INCORPORATION

Portions of this chapter were submitted for publication as Trotochaud, L; Young, S.L.; Ranney, J.K.; Boettcher, S.W. "Nickel-Iron Oxyhydroxide Oxygen-Evolution Electrocatalysts: The Role of Intentional and Incidental Fe Incorporation" to the *Journal of the American Chemical Society* on March 8, 2014. S.L.Y. was a graduate student who, under the direction of L.T., collected several of the data points in Figure 4.15. J.K.R. was an undergraduate student who, under the direction of L.T., performed preliminary work to optimize film deposition conditions. L.T. wrote the paper, performed the rest of the experimental work, and made the figures. S.W.B. was the principal investigator and provided editorial assistance.

Introduction

        The electrolysis of water to form H_2 and O_2 gas (i.e. water splitting, $H_2O \rightarrow H_2 + \frac{1}{2}O_2$) could enable the large-scale storage of intermittent energy from the sun, wind, or other renewable sources.[1,2] The kinetically slow oxygen evolution reaction (OER) $2H_2O \rightarrow 4H^+ + O_2 + 4e^-$ (in acid) or $4OH^- \rightarrow 2H_2O + O_2 + 4e^-$ (in base) represents a significant efficiency loss in water-splitting systems.[2,3] Identifying more-efficient, stable, earth-abundant catalysts for the OER is a significant challenge.

        $Ni_{1-x}Fe_xOOH$ oxyhydroxide electrocatalysts have been under intense study because they are the most active catalysts measured in basic media.[4-14] We previously compared thin films of OER catalysts deposited on quartz-crystal microbalance (QCM) electrodes and found that $Ni_{0.9}Fe_{0.1}OOH$ has an OER turn-over-frequency (TOF) >10-fold higher than IrO_x.[11] The high activity, along with the ability to deposit thin films with low optical absorption using solution-processing, makes $Ni_{1-x}Fe_xOOH$ catalysts appealing for use in solar water-splitting devices.[11,15] We note, however, that $Ni_{1-x}Fe_xOOH$ OER catalysts have been known for over 25 years[14,16,17] and the measured activities (per-Ni) appear to vary little despite differences in synthesis.[4,8,10,18,19] Large-

scale combinatorial screening has further shown that OER catalysts with both Ni and Fe have the highest activity.[18,20,21] The addition of other elements (e.g. Ce, Al, Co) may have additional effects, but does not appear to dramatically enhance the activity. Differences in intrinsic activity, however, are difficult to evaluate without a quantitative determination of a TOF.

Despite the large number of studies that indicate that both Ni and Fe are essential for high OER activity in base, little progress has been made on understanding the role of Fe in increasing the OER activity. Corrigan proposed several hypotheses, including that Fe enhances the electrical conductivity of NiOOH.[16] Electrochemical studies show an anodic shift of the Ni redox waves with increasing x in $Ni_{1-x}Fe_xOOH$,[8,9,16] indicating changes in the electronic structure. The details of theses changes and their precise effect on the catalysis mechanism remain unknown.

Incorporation of Fe also changes the physical structure of $Ni(OH)_2$/NiOOH, but clear structure/activity relationships in $Ni_{1-x}Fe_xOOH$ OER catalysts have not been established. $Ni(OH)_2$/NiOOH adopts a brucite (theophrasite) structure, with layers of metal-(oxy)hydroxide sheets separated by water and aqueous ions.[22,23] The redox-activity and porous, hydrated, ion-permeable nature of $Ni(OH)_2$/NiOOH indeed enables its use in commercial Ni-metal hydride rechargeable batteries.[24] The registry and spacing between the layers is affected by the synthetic conditions, aging in basic electrolyte, and by prolonged application of an oxidizing potential.[25-30] Earlier work using X-ray absorption[5,7,31] and Mössbauer[32-34] spectroscopies shows that Fe^{3+} substitutes for Ni^{2+} in α-$Ni(OH)_2$. Louie and Bell recently used *in situ* Raman spectroscopy to provide evidence that Fe in NiOOH modifies the Ni–O local environment, which correlates with increasing OER activity.[8]

One major challenge in understanding the fundamental role of Fe on NiOOH OER activity, electronic properties, and physical structure has been the difficulty in measuring rigorously Fe-free catalysts; sub-ppm levels of Fe in electrolyte readily incorporate in NiOOH.[11,16,35] Here we report a simple method using high-purity $Ni(OH)_2$ precipitate as an Fe-absorbent to remove trace Fe from KOH electrolyte. We then investigate the relationship between electrical conductivity, substrate type, and structural order on measured OER activities as a function of Fe content in $Ni_{1-x}Fe_xOOH$ films. Our

67

major findings are that: (1) Fe incorporation increases NiOOH conductivity >30-fold but that the increased conductivity is not sufficient to explain the increased activity in thin film samples; (2) contrary to previous findings in unpurified electrolytes (for example, see refs. 8,9,30,36-40), pure NiOOH is a poor catalyst for OER, independent of degree of order, and that prolonged anodic polarization and/or aging in KOH electrolyte does not increase pure NiOOH activity; and (3) Fe affects the NiOOH electronic structure by inducing partial-charge-transfer in a manner similar to high-work-function surfaces studied by Bell and co-workers.[37,41] These results are critical to further elucidate periodic trends of pure metal (oxy)hydroxide OER activities,[42] compare experimental results with theoretical predictions,[43-45] and ultimately design catalysts with higher activity.

Experimental Details

Characterization

Microgravimetry measurements were made using a 5 MHz quartz crystal microbalance (Stanford Research Systems QCM200). The film mass was calculated from changes in resonance frequency using the Sauerbrey equation[46] $\Delta f = -C_f \times \Delta m$, where Δf is the observed frequency change (Hz), C_f is the sensitivity factor of the 5 MHz AT-cut quartz crystal (58.3 ± 3.7 Hz μg^{-1} cm^2; see ref. 11 for description of C_f calibration), and Δm is the change in mass per unit area (μg cm^{-2}). Grazing incidence X-ray diffraction (GIXRD) patterns were recorded on a Philips X'Pert Panalytical diffractometer operating at 30 mA and 50 kV using monochromated Cu Kα_1 radiation (incident angle = 0.2°, λ = 1.541 Å, step size = 0.05°, integration time 25 s/step). Scanning electron microscopy (SEM) images were collected on a Zeiss Ultra 55 SEM at 5 kV. X-ray photoelectron spectroscopy (XPS) studies were carried out on an ESCALAB 250 (ThermoScientific) using a Mg Kα non-monochromated flood source (200 W, 75 eV pass energy). The use of a Mg source is critical for detecting low concentrations of Fe. Use of a typical Al source results in the overlapping of Ni LMM Auger features with the Fe 2p peaks, making detection of low Fe concentrations impossible. The samples were charge-neutralized using an in-lens electron source combined with a low-energy Ar$^+$ flood source. Spectra were analyzed, including satellite subtraction for the non-monochromated X-ray source,

using ThermoScientific Avantage 4.75 software. The C1s peak for adventitious hydrocarbons at 285.0 eV was used for binding energy calibration.

Electrochemical Measurements

All electrochemical measurements were made in PTFE or polypropylene beakers containing 1 M KOH electrolyte solution (Fluka Analytical TraceSelect, $\geq$ 30%, diluted with 18.2 MΩ·cm H_2O). Based on the lot analysis and assuming no Fe in the 18.2 MΩ·cm H_2O, we calculate <36 ppb Fe in the 1 M KOH solution. All electrochemical cell components were cleaned prior to experiments with 1 M H_2SO_4 and rinsed with copious quantities of 18.2 MΩ·cm H_2O. A BioLogic SP300 potentiostat was used operating in two-electrode mode for film deposition, three-electrode mode for cyclic voltammetry (CV) measurements, and four-electrode bipotentiostat mode (two synchronized working electrodes) for through-film conductivity measurements. A carbon cloth (Fuel Cell Earth, untreated) counter electrode was used for film deposition, while a Pt wire counter electrode housed in a custom polypropylene compartment separated by porous polypropylene was used for CV and conductivity measurements. Pt counter electrodes were cleaned periodically by dipping in aqua regia for ~20 s. A new piece of carbon cloth was used for each deposition solution. Potentials in 3- and 4-electrode modes were measured versus a 1 M KOH Hg/HgO reference electrode (CH Instruments). The potential of the 1 M KOH Hg/HgO reference was measured to be 0.928 V vs. the reversible hydrogen electrode (RHE) in 1 M KOH. The RHE was fabricated by bubbling high-purity hydrogen over a freshly cleaned Pt coil in 1 M KOH. Samples deposited on QCM electrodes were connected to the working electrode lead of the potentiostat through the crystal face bias connector of the QCM200. Through-film conductivity measurements were made on Au/Ti/quartz interdigitated array (IDA) electrodes (ALS Co.; 2 μm line width, 2 μm gap, 2 mm length, 65 pairs). The reference and counter electrode leads on the IDA electrodes were not used. The voltammetry data presented here were collected on QCM Au/Ti electrodes unless otherwise indicated. For certain measurements, a glassy carbon (GC) rotating disk electrode (RDE) (Pine Instruments) was used at 1500 rpm.

High-purity O_2 gas was bubbled through the KOH electrolyte for at least 20 min prior to electrochemical measurements. Magnetic stirring was used to dislodge O_2 bubbles formed on the QCM electrode surface. Electrochemical data were corrected for

69

uncompensated series resistance R_u, which was determined by equating R_u to the minimum total impedance in the frequency regime between 10 to 50 kHz where the capacitive and inductive impedances are negligible and the phase angle was near zero. R_u was ~1 - 3 Ω for QCM substrates and ~4 - 6 Ω for the GC-RDE substrate. The overpotential η was calculated using the equation $\eta = E_{measured} - E_{rev} - iR_u$ where $E_{measured}$ is the potential recorded vs. Hg/HgO, E_{rev} is the reversible potential of the OER vs. Hg/HgO (0.30 V in 1 M KOH calibrated as described above), and i is the current. Current densities are calculated using geometric surface areas.

Film Thickness and TOF Calculations

Effective film thicknesses were calculated by integrating the $Ni^{3+/2+}$ reduction wave, assuming 1 e⁻ per Ni atom and a (001)-oriented $Ni(OH)_2$ film (i.e. a sheet of $Ni(OH)_2$ lying flat on the substrate surface) with an average monolayer thickness of 8 Å for α-$Ni(OH)_2$.[47] We label this an "effective" film thickness because the $Ni(OH)_2$ sheets do not all lie flat on the substrate. For films on QCM substrates, the assumption of 1 e⁻ per Ni correlates well with the measured mass of deposited catalyst films, and is consistent with our previous work.[11] We note that others have calculated up to ~1.67 e⁻ per Ni,[29,30] meaning that the 1 e⁻ per Ni used here may underestimate the intrinsic catalyst TOF.[48,49] For thicker films deposited for conductivity measurements, thicknesses were measured using a stylus profilometer.

Turn-over-frequency (TOF) values reported here are defined as the moles of O_2 evolved per mole of Ni in the catalyst per second. The TOFs are calculated at specified series-resistance-corrected overpotentials by averaging the current of the forward and reverse CV sweeps (taken at a scan rate of 10 mV s⁻¹), subtracting the average current of the forward and reverse sweeps of the bare substrate at the same overpotential, and dividing by the moles of Ni determined as described above.

KOH Electrolyte Purification

For rigorously Fe-free measurements, the 1 M KOH electrolyte was purified as follows. In a H_2SO_4-cleaned 50 mL polypropylene centrifuge tube, ~2 g of 99.999% $Ni(NO_3)_2{\cdot}6H_2O$ were dissolved in ~4 mL of 18.2 M$\Omega{\cdot}$cm H_2O. 20 mL of 1 M KOH was added to precipitate high-purity $Ni(OH)_2$. The mixture was shaken, centrifuged, and the supernatant decanted. The $Ni(OH)_2$ then underwent three washing cycles by adding ~20

mL of 18.2 MΩ·cm water and ~2 mL of 1 M KOH to the tube, redispersing the solid, centrifuging, and decanting the supernatant. Finally, the tube was filled with 50 mL of 1 M KOH for purification. The solid was redispersed and mechanically agitated for at least 10 min, followed by at least 3 h of resting. The mixture was centrifuged, and the purified KOH supernatant was decanted into a H_2SO_4-cleaned polypropylene bottle for storage.

Film Deposition

Prior to film deposition, substrates were cycled three times in 1 M KOH from 0.0 – 0.8 V vs. Hg/HgO. Substrates were rinsed with 18.2 MΩ·cm H_2O before being transferred to the deposition solution. Films of $Ni(OH)_2$ were cathodically deposited from unstirred solutions of 0.1 M $Ni(NO_3)_2$·$6H_2O$ (Sigma-Aldrich, 99.999% trace metals basis) in 18.2 MΩ·cm H_2O. As-deposited $Ni(OH)_2$ films showed no XPS signal for Fe (see discussion below). For films containing co-deposited Fe, the total metal content in the deposition solution was held at 0.1 M, and $FeCl_2$·$4H_2O$ (Sigma Aldrich, >98%) was added. The solutions were purged with N_2 gas for at least 20 min before adding $FeCl_2$·$4H_2O$ to prevent precipitation of insoluble FeOOH. Typical depositions at -0.1 mA cm^{-2} for 120 s gave effective film thicknesses of ~40 nm (see Figure 4.1 for a typical deposition profile and QCM frequency measurement). After deposition, films were rinsed by dipping in H_2O before being transferred to the electrochemical cell. The Fe:Ni ratio in the films was higher than in the deposition solutions, however any given Fe content in solution consistently produced films with the same Fe content ($< \pm 4\%$) as determined by XPS. All film Fe contents reported here are those measured by XPS.

Results and Discussion

Iron Impurities and Their Removal

The ability to make rigorously Fe-free control measurements on $Ni(OH)_2$/NiOOH is critical for understanding the role of Fe. Previous work has shown that Fe impurities readily incorporate into $Ni(OH)_2$/NiOOH films during electrochemical experiments.[11,16] Corrigan showed that Fe-impurity levels as low as 1 ppm in KOH electrolyte significantly affect the activity of $Ni(OH)_2$, particularly for thinner films where the incorporated Fe makes up a larger percentage of the film.[16] To minimize the effects of Fe impurities, we eliminated all glass components from our electrochemical cell (which are

71
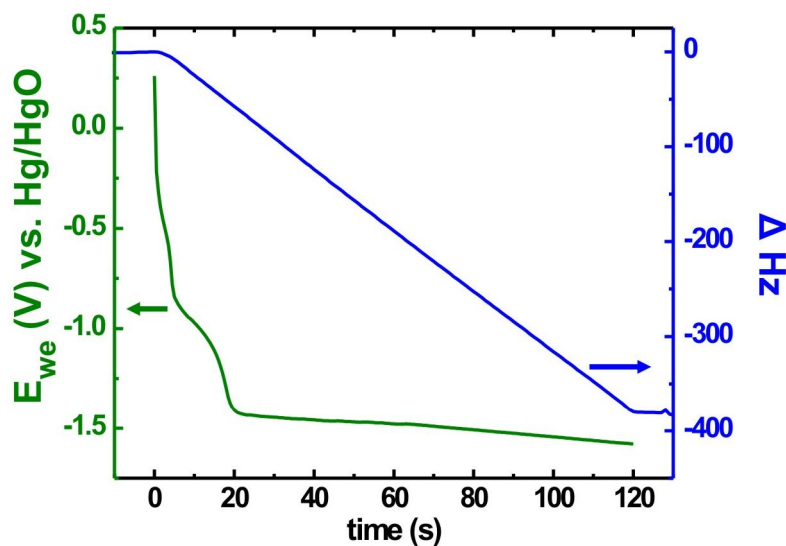
Figure 4.1. Potential vs. time deposition profile for a Ni(OH)$_2$ film deposited at 0.1 mA cm^{-2} for two minutes and the corresponding QCM frequency change profile.

etched by KOH), clean all cell components with H$_2$SO$_4$ before each experiment, use the highest purity KOH electrolyte available, and use high-purity Ni(NO$_3$)$_2$ (99.999%) for film deposition. As shown in Figure 4.2a, no Fe is detected by XPS in as-deposited Ni(OH)$_2$ films. Despite these precautions, we find significant Fe incorporation into Ni(OH)$_2$ after electrochemical experiments.

Figure 4.2b shows a series of CV cycles of a Ni(OH)$_2$ film deposited on a GC-RDE. At a rotation rate of 1500 rpm, OER activity increases with each CV cycle. The Fe 2p XPS signal (Figure 4.2a) is evident after 5 CV cycles, and the atomic ratio of Ni:Fe is quantified as 95:5. XPS depth profiling shows that after only 5 CV cycles, Fe is incorporated throughout the film and not just at the film surface (see Figure 4.3), consistent with the electrolyte-permeable structure and previous results from Auger electron spectroscopy depth profiling.[16] The film spent a total of ~12 min rotating in the electrochemical cell from beginning to end of this CV experiment. Figure 4.2a shows that a different Ni(OH)$_2$ film which was simply rotated in the KOH electrolyte for 12 min (i.e. with no applied potential) also has significant Fe incorporation (98:2 Ni:Fe). In fact, the presence of Fe impurities in the KOH electrolyte also increases the OER activity of the bare Au substrate (see Figure 4.4), although an extensive analysis of these changes was not completed.

72
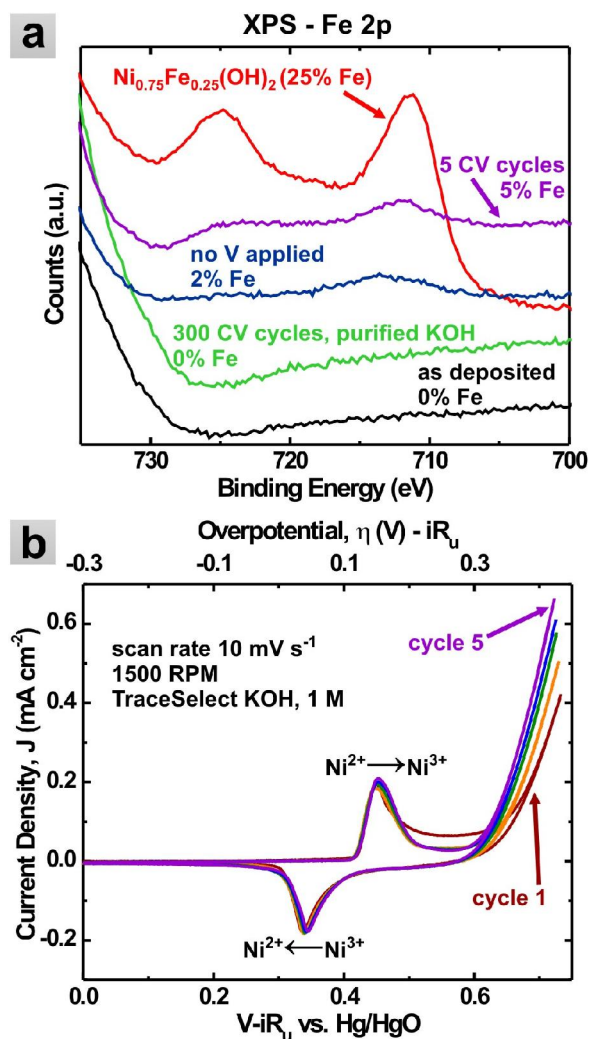
Figure 4.2. (a) XPS Fe 2p spectra for Ni(OH)$_2$/NiOOH thin films after 5 CV cycles in TraceSelect KOH (purple, Figure 4.2b), 12 minutes in TraceSelect KOH electrolyte with no applied potential (blue), and 300 CV cycles in purified KOH (green). Spectra for an as-deposited film containing no Fe (black) and a film with 25% co-deposited Fe (red) are shown for reference. The increase in intensity for binding energies above ~730 eV is due to the onset of an O KLL Auger peak. Spectra are offset on the y-axis for clarity. (b) Cyclic voltammogram of a Ni(OH)$_2$ film deposited on a GC-RDE. With each subsequent CV cycle, OER current increases due to Fe incorporation.

To measure the electrochemical behavior of Fe-free Ni(OH)$_2$, we developed a simple purification procedure. As described above, we found that Ni(OH)$_2$ readily absorbs Fe without an applied potential. We therefore suspended high-purity Ni(OH)$_2$ powder prepared by precipitation (i.e. of the same composition as the catalyst) in the electrolyte to adsorb all Fe impurities prior to electrochemical testing of Fe-free Ni(OH)$_2$

73

films. Figure 4.2a shows no detectable Fe 2p XPS signal in a $Ni(OH)_2$ film after 300 CV cycles in the purified electrolyte. All subsequent measurements were conducted in electrolyte purified by this method unless otherwise indicated.
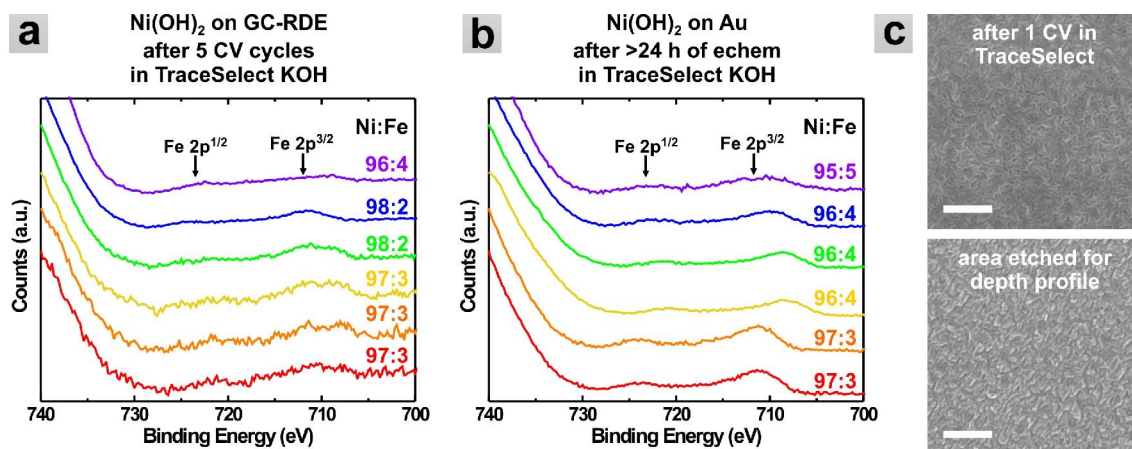
Figure 4.3. XPS depth profiles of $Ni(OH)_2$ films exposed to Fe impurities. (a) Film on GC-RDE substrate after 5 CV cycles in TraceSelect KOH. (b) Film after 1 day of electrochemical experiments in TraceSelect KOH. In each plot, the top-most spectrum is before starting the depth profile. Each subsequent spectrum is after 60 s of etching with an Ar^+ beam (3 kV, 2 µA) over a 4 mm × 4 mm area. (c) SEM images of a $Ni(OH)_2$ film cathodically deposited at -0.1 mA cm^{-2} for 2 min onto Au/Ti QCM substrate before (top) and after (bottom) etching for XPS depth profile. The underlying Au substrate is apparent after Ar^+ etching indicating a substantial fraction of the film was etched by the ion beam. Scale bars are 200 nm.

Effects of Fe on Electrochemical Redox Behavior and Crystal Structure

Prolonged cycling or aging (in the absence of an applied potential) of $Ni(OH)_2$ electrodes in basic electrolyte has been shown to convert the disordered, as-deposited α-$Ni(OH)_2$ to the more crystalline β-form.[29,37,47,50-53] Multiple studies have concluded that β-$Ni(OH)_2$ is significantly more active for OER than the α-$Ni(OH)_2$.[38,47,54] Such observations are important in the context of understanding the role of three-dimensional structure on the OER activity, as well as in providing insight to guide theory.[55] Given the extreme sensitivity of the OER activity on Fe impurities,[16] it is possible that previous studies of β-$Ni(OH)_2$ formed by aging/recrystallization are contaminated with Fe. Furthermore, the role of crystallinity in $Ni_{1-x}Fe_xOOH$ with intentional Fe addition has not been previously studied and could provide additional insight into the enhanced activity.
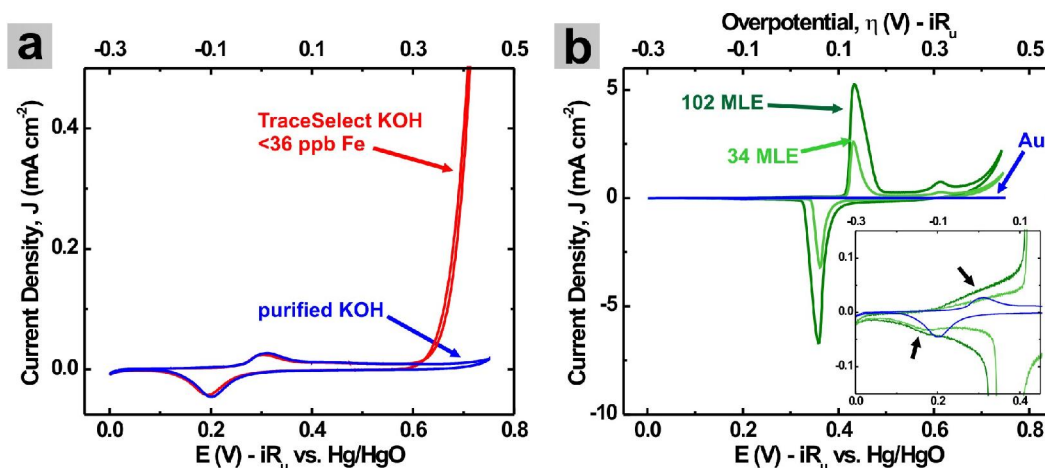
Figure 4.4. (a) Voltammograms collected using a bare Au/Ti QCM electrode (10 mV s^{-1}). The redox waves are due to oxidation and reduction of the Au surface. The presence of Fe in the TraceSelect KOH electrolyte apparently affects the OER activity of the bare Au substrate, as indicated by the changes in OER current magnitude and onset potential. (b) Voltammograms collected for Ni(OH)$_2$ films on Au/Ti QCM electrodes (10 mV s^{-1}). Magnification in inset shows that even for the thick films of Ni(OH)$_2$ deposited (here, 102 and 34 monolayer-equivalents, or ~82 and ~27 nm), the Au redox wave (indicated by arrows) is present just before the Ni oxidation and reduction waves. This is consistent with the electrolyte permeability of the (oxy)hydroxides.

The transition from as-deposited α-Ni(OH)$_2$ to β-Ni(OH)$_2$ can be observed by X-ray diffraction (see Figure 4.5 and also ref. 47). For GIXRD experiments, films ~150-200 nm thick were deposited (10 min, -0.1 mA cm^{-2} cathodic) on Au substrates. Figure 4.6a shows SEM images of these films before and after aging in purified 1 M KOH at 40 °C for ~24 h. Films electrodeposited on Au have a spongy platelet-like structure. After aging, the platelet size observed by SEM increases. In general, films containing Fe had a larger platelet size than those without Fe. Thinner films and films deposited on GC tended to be composed of smaller platelets (see Figures 4.7-4.10 for additional SEM images of samples discussed in this work).

Figure 4.6b shows GIXRD patterns for films before and after aging. All diffraction patterns show increased peak intensity after aging, indicating an increase in the film crystallinity. The patterns obtained after aging for the Fe-free Ni(OH)$_2$ film agree with the pattern for β-Ni(OH)$_2$ (Figure 4.5 and ref. 47). The peak near 19° 2θ corresponds to the (001) β-Ni(OH)$_2$ reflection whose intensity is related to the registry between the Ni(OH)$_2$ sheets along the c-axis (Figure 4.6c). The fact that the β-Ni(OH)$_2$ reflections
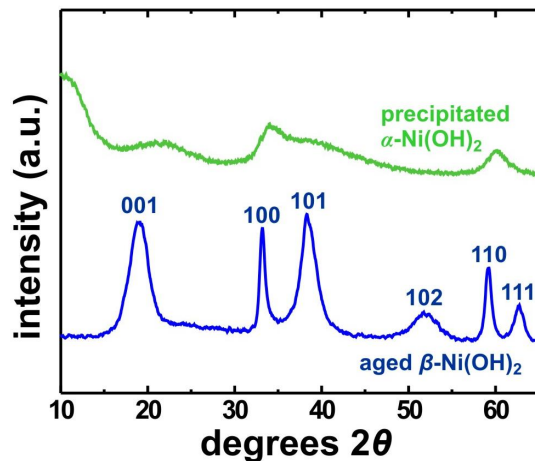
Figure 4.5. X-ray powder diffraction patterns for freshly precipitated α-Ni(OH)$_2$ and aged β-Ni(OH)$_2$. The powders were synthesized by precipitation of a solution of Ni(NO$_3$)$_2$ in 18.2 MΩ cm H$_2$O with 1 M TraceSelect KOH. The precipitates were washed 3× with water (with ~25 mL of ~0.1 M KOH added to keep the solids from dissolving) and dried in air. Dry powders were ground and mounted onto glass slides using silicone-based vacuum grease.

remain relatively low-intensity and broad could indicate the persistence of some disordered α-Ni(OH)$_2$, which is consistent with voltammetry results that show two main oxidation waves after aging (see below).

The pattern of the as-deposited Ni$_{0.75}$Fe$_{0.25}$(OH)$_2$ also shows weak reflections associated with β-Ni(OH)$_2$. After aging Ni$_{0.75}$Fe$_{0.25}$(OH)$_2$, sharp peaks at ~11° and 23.5° 2θ emerge and the (001) β-Ni(OH)$_2$ reflection is diminished. These new peaks match those of mixed Ni-Fe layered double hydroxides (NiFe-LDH; fougèrite/pyroaurite mineral structure) with 25-50% Fe synthesized by co-precipitation,[56] topochemical,[57] or mechanochemical[58] methods, with the peaks at ~11° 2θ and 23.5° 2θ corresponding to the (003) and (006) reflections, respectively. The NiFe-LDH unit cell increases along the c-axis (~2 nm, depending on the identity of the interlayer anions) compared to that for β-Ni(OH)$_2$ (0.46 nm) and comprises three sheets of metal cations (see Figure 4.6c). The NiFe-LDH structure has a significantly larger inter-sheet spacing compared to that of β-Ni(OH)$_2$ because the increased charge of Fe^{3+} relative to Ni^{2+} is compensated by the movement of additional anions (and associated water) into the spaces in-between the sheets.[32,33,59] (Note that the formal composition for these hydrated NiFe-LDH structures is [Ni$^{II}_{1-x}$Fe$^{III}_x$(OH)$_2$]$^{x+}$[x/nA^{n-}]$^{x-}$·zH$_2$O, where A = anions. We use the simpler

76
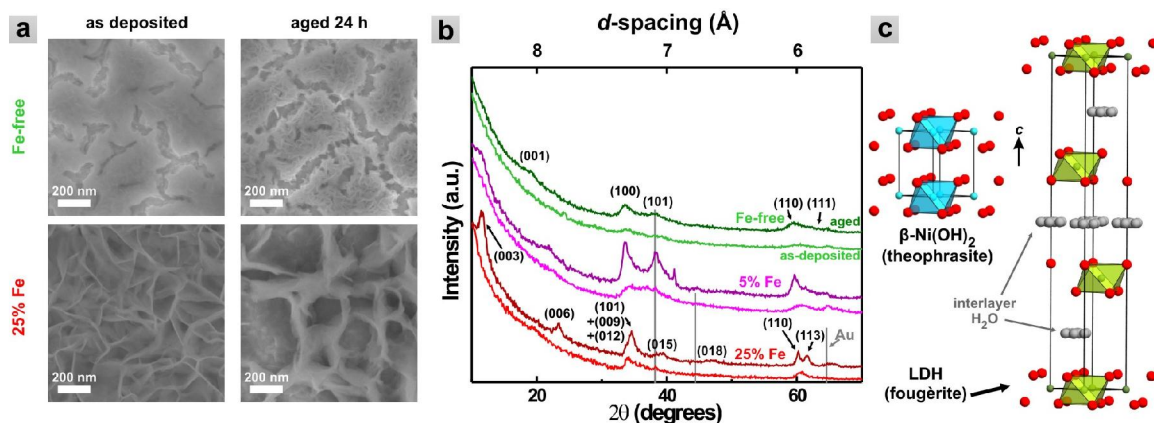
Figure 4.6. (a) SEM images of $Ni(OH)_2$ and $Ni_{0.75}Fe_{0.25}(OH)_2$ films as-deposited and after 24 h of aging in 40° C 1 M KOH. (b) Grazing-incidence GIXRD patterns of $Ni_{1-x}Fe_x(OH)_2$ films for $x = 0$, 0.05, and 0.25 as-deposited (lower, lighter color shades) and after aging (upper, darker color shades) in 40° C 1 M KOH for 24 h. The pattern for the Au substrate is shown (in grey) for reference, and Au may contribute slightly to the intensity of the peaks near 38° 2θ and the background near 44.4° and 64.6° 2θ. The sloping background is due to the grazing-incidence geometry and has not been subtracted to preserve the peaks near 11° 2θ. Indices with the green pattern (top) are for β-$Ni(OH)_2$ and those with the red pattern (bottom) are for the Ni-Fe layered double hydroxide (NiFe-LDH). (c) Crystal structures of β-$Ni(OH)_2$ (theophrasite; ICSD 28101) and NiFe-LDH (fougèrite; ICSD 159700 – note that this is the all-Fe analogue) viewed roughly along the [110] direction. The unit cell edges are indicated by dark lines. Red = OH; blue = Ni^{2+}; green = Ni^{2+}/Fe^{3+}; grey = water. H-atoms in both structures and interlayer anions in the LDH structure are omitted for clarity.

$Ni_{1-x}Fe_x(OH)_2$ formula and have excluded the interlayer anions from Figure 4.6c for

clarity.) The pattern for aged $Ni_{0.95}Fe_{0.05}(OH)_2$ shows both a peak at 11° 2θ, indicating a

NiFe-LDH phase, and a weak broad peak at ~22° 2θ that is not directly assignable to

either the NiFe-LDH or the pure β-$Ni(OH)_2$ phases. This peak at ~22° 2θ could be

assignable to α-$Ni(OH)_2$ (see Figure 4.5), which also has water and ions between the

metal-hydroxide sheets, although with a smaller inter-sheet spacing than the NiFe-LDH.

It is therefore possible that $Ni_{0.95}Fe_{0.05}(OH)_2$ contains a mixture of NiFe-LDH and α-

$Ni(OH)_2$ phases. All the diffraction data collected, however, are consistent with (1)

increased crystallinity and long range order perpendicular to the (00l) family of planes

with aging (i.e. increased registry between the sheets), and (2) increased spacing between

metal cation sheets in the catalyst films upon substitution of Fe^{3+} for Ni^{2+}. The increased

intersheet spacing would be expected to facilitate OH^-/O_2 transport through the film, but

would limit electronic interactions between active sites on adjacent layers along the c-axis.
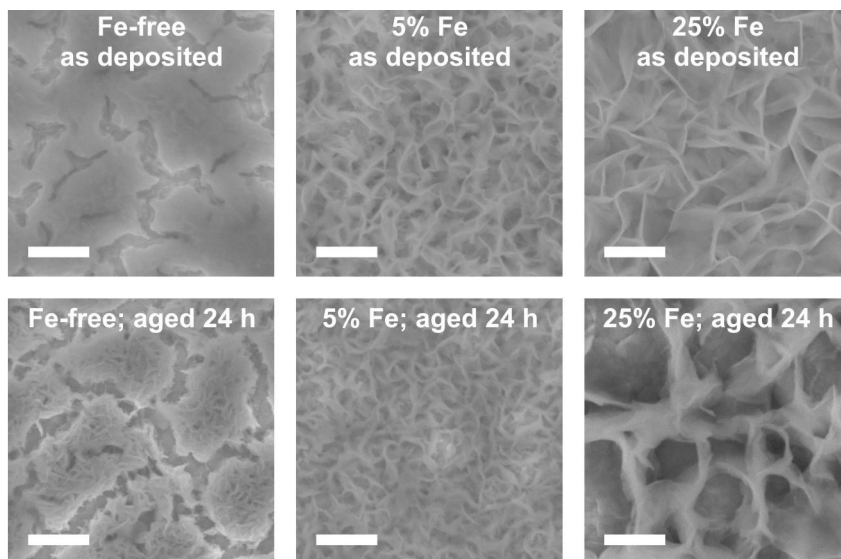
Figure 4.7. SEM images of films used for XRD experiments shown in Figure 4.6b. Films were cathodically deposited onto Au/Ti QCM substrates at -0.1 mA cm^{-2} for 10 min. Films were aged in 40° C purified 1 M KOH for 24 h. Scale bars are 200 nm. (Fe-free and 25% Fe images also shown in Figure 4.6a.)
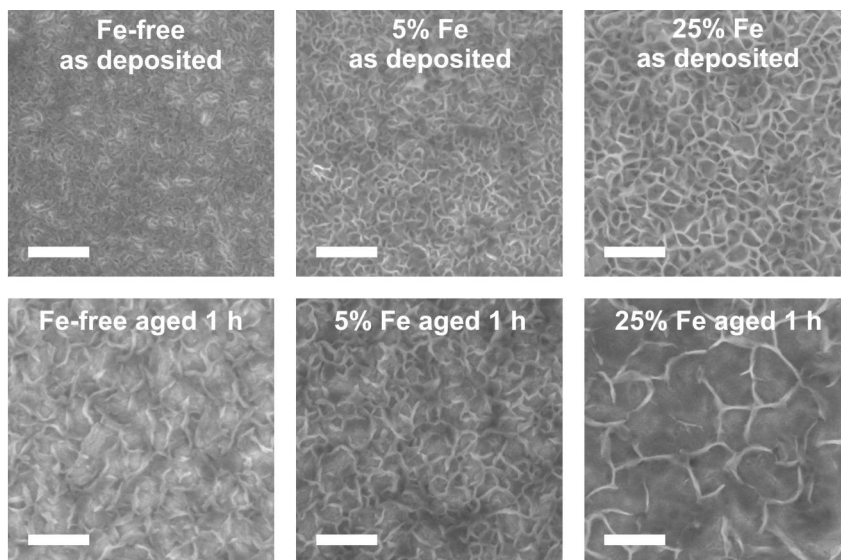
Figure 4.8. SEM images of films used for aging experiments shown in Figure 4.11. Films were cathodically deposited on Au/Ti QCM substrates at -0.1 mA cm^{-2} for 2 min. Samples were aged for 12 periods of 5 min (total aging time of 1 h) in 40° C purified 1 M KOH. Scale bars are 200 nm. (Fe-free images are also shown in Figure 4.10.)
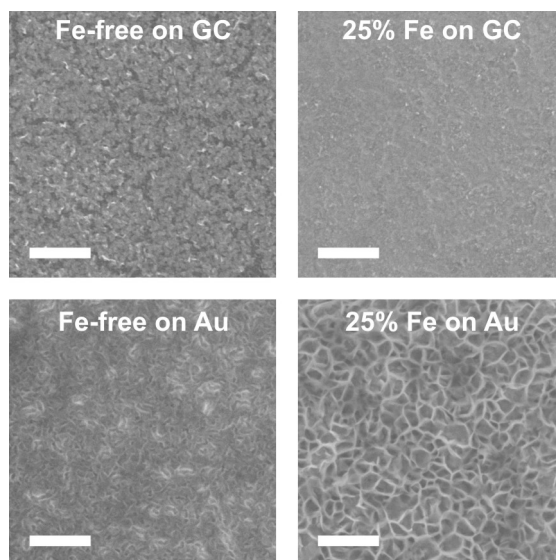
Figure 4.9. SEM images comparing film morphology on GC-RDE (top) and Au/Ti QCM (bottom) substrates. Films were cathodically deposited at -0.1 mA cm^{-2} for 2 min. Scale bars are 200 nm. (Fe-free on Au also shown in Figure 4.8.)
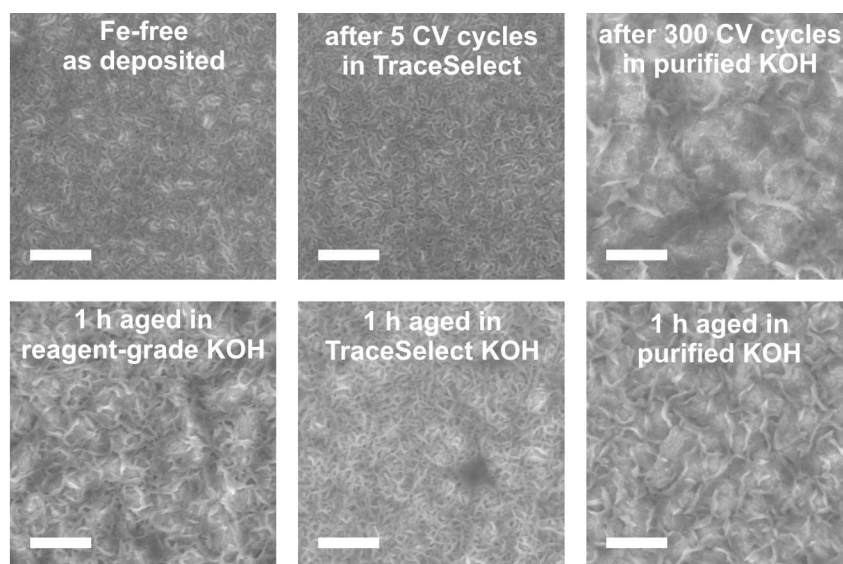
Figure 4.10. SEM images showing effects of aging and electrochemical cycling on Ni(OH)$_2$ film morphology. Films were deposited on Au/Ti QCM substrates at -0.1 mA cm^{-2} for 2 min. Images at top right and top left are from samples described in Figure 4.2a. Images on bottom from left to right are from samples whose electrochemical data are shown in Figures 4.11b, 4.11a, and 4.11d. Scale bars are 200 nm.

Previous studies of the α-Ni(OH)$_2$ to β-Ni(OH)$_2$ transformation with aging report a corresponding anodic shift in the β-Ni(OH)$_2$/β-NiOOH redox wave relative to that of the as-synthesized α-Ni(OH)$_2$/γ-NiOOH, as well as a lower onset potential for the OER on β-Ni(OH)$_2$ (e.g. see refs. 8,16,25,30,47,60). These observations have long been interpreted to indicate that β-Ni(OH)$_2$/β-NiOOH has an intrinsically higher OER activity than α-Ni(OH)$_2$/γ-NiOOH due to its structure.[38,47] For example, Louie and Bell age Ni(OH)$_2$ films in 10 M KOH and observe a 40 mV anodic shift of the redox peaks and a 20-fold increase in OER activity at $\eta = 0.3$ V.[8] They argue that the incorporation of Fe impurities should be negligible due to the absence of an applied potential during the aging process, but the possibility of Fe incorporation cannot be conclusively ruled out as the lower detection limit of Fe for elemental analysis was reported to be ~3%. The anodic shift of redox waves and increases in OER activity are also indicative of Fe incorporation.[16] Our results show that even in the absence of an applied potential (i.e. during aging in KOH electrolyte), Fe incorporation into Ni(OH)$_2$ does occur and significantly affects electrochemical behavior. The films investigated by Louie and Bell were approximately the same thickness (~70 nm) as those studied here (~40–60 nm), and thus we would expect the extent of Fe impurity incorporation to be similar (~2% total metals) or higher (due to the use of 10 M KOH aging solution).

To further study these effects we conducted systematic aging experiments for Ni(OH)$_2$, Ni$_{0.95}$Fe$_{0.05}$(OH)$_2$, and Ni$_{0.75}$Fe$_{0.25}$(OH)$_2$ films in different purity electrolytes. Films were subjected to 5 min periods of aging at 40° C in 1 M KOH. After each aging period, CV data were collected. This process was repeated to give a total of 13 CV data sets (including as-deposited) and a total aging time of 60 min for each sample.

Figure 4.11a and b show the changes in CV behavior of Ni(OH)$_2$ in the presence of Fe impurities. When aged in either the TraceSelect KOH (Figure 4.11a) or reagent-grade KOH (Figure 4.11b) that was not subsequently purified, the redox peaks shift to higher potentials and the OER activity increases. In both electrolytes, the redox peaks shift by similar amounts. XPS shows Ni:Fe ratios of 96:4 and 92:8 after 1 hr of aging in the TraceSelect-aged and reagent-grade-aged films, respectively. The OER activity increase is greater in the reagent-grade-aged films relative to those aged in the TraceSelect KOH, consistent with more Fe in reagent-grade KOH resulting in more Fe

incorporation into the film. Films with co-precipitated Fe show little change in electrochemical behavior with aging even in the purified electrolyte. Films with 5% (Figure 4.11c) or 25% (Figure 4.11e) co-precipitated Fe show no change in OER activity. Only the oxidation wave for the sample with 5% Fe shifts to higher potentials. The lack of significant changes to the OER activity for $Ni_{0.75}Fe_{0.25}(OH)_2$ films as a function of aging (and hence crystallization) suggests that the long-range order and inter-sheet registry is unimportant for the active site OER activity. It also suggests that the OER activity is not related to structural defects within $Ni_{0.75}Fe_{0.25}OOH$, but inherent to the mixed Ni-Fe oxyhydroxide sheet.

The electrochemical behavior of $Ni(OH)_2$ films aged in purified KOH electrolyte is different from that of previous reports[8-10,17,34,36-38,47,49,60-64] and different from what we
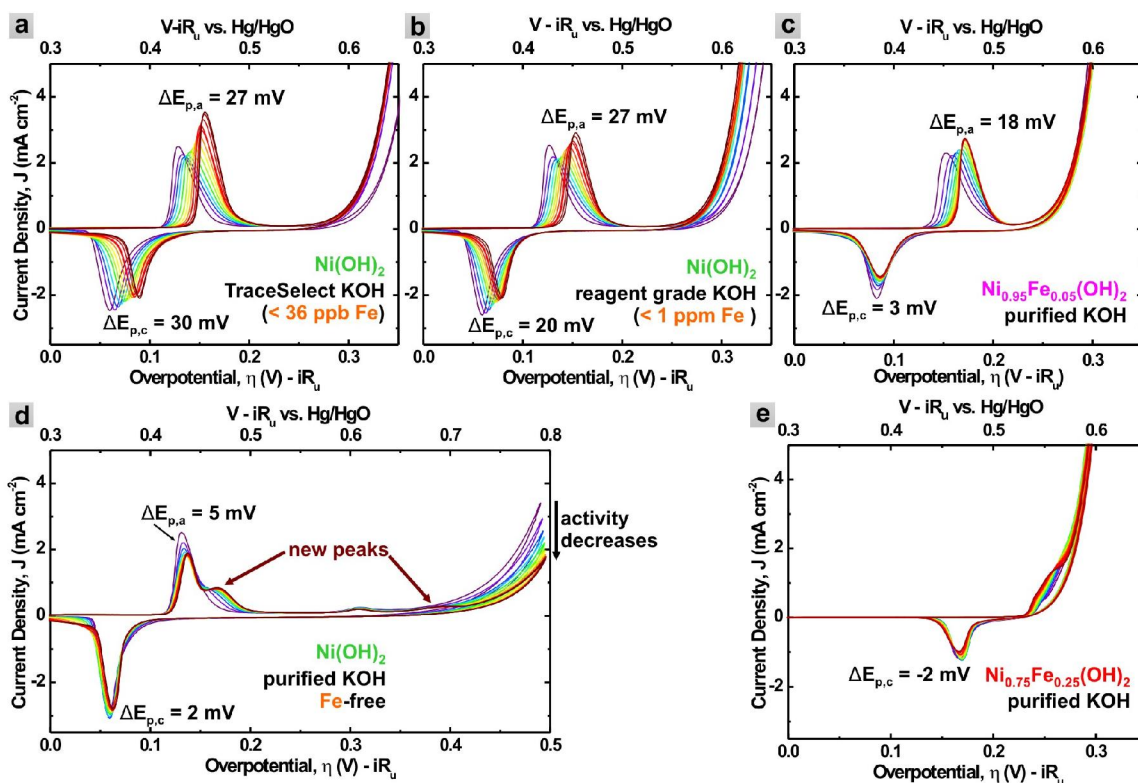
Figure 4.11. Cyclic voltammograms taken during aging of films in various purities of KOH. A total of 13 CV scans are shown for each sample; one for the initial as-deposited film (dark purple), and one additional scan after each 5 minute aging period up to a total of 1 h aging (dark red). The changes in the anodic and cathodic wave positions ($\Delta E_{p,a}$ and $\Delta E_{p,c}$) are labeled for each set of CVs. (No $\Delta E_{p,a}$ value is shown for the $Ni_{0.75}Fe_{0.25}(OH)_2$, as the oxidation wave is partially obscured by OER current.)

81

observe in the unpurified electrolyte. First, instead of a gradual anodic shift in the Ni(OH)$_2$ oxidation wave (as is observed in the unpurified KOH), a decrease in the original anodic peak intensity and emergence of a new oxidation wave at more anodic potentials (~0.47 V vs. Hg/HgO) is observed in the purified KOH (Figure 4.11d). No significant OER current is observed until >400 mV overpotential. Furthermore, Ni(OH)$_2$/NiOOH aged in the purified KOH shows a decrease in OER activity with increased aging time – opposite to what others have observed. The decrease in OER activity with aging may be due to a decrease in the number of active sites if they are associated with defects (e.g. stacking faults)[22,27,65,66] or edges[42,67] in the more-ordered β-Ni(OH)$_2$ films or due to reduced OH$^-$/O$_2$ transport rates within the interlayer volume. No Fe is observed in the XPS analysis of Ni(OH)$_2$ aged in the purified electrolyte. These data show that significant redox wave shifting and increases in OER activity only occur in the presence of Fe impurities and are not the result of formation of β-Ni(OH)$_2$. These results are important in the context of the theoretical effort that has been extended toward understanding the activity, electronic, and structural properties of Ni-based catalysts,[43,44,68-71] including experimental studies that have aimed to relate OER activity to fundamental properties such as the "oxophilicity" of the cation.[42]

The lack of OER activity until very positive potentials for the Fe-free NiOOH films reveals additional electrochemical features in the voltammetry. For the un-aged film, a small oxidation peak at ~0.6 V vs Hg/HgO is observed. Another small oxidation peak appears at ~0.7 V vs. Hg/HgO upon aging in concert with a larger peak at ~0.47 V vs. Hg/HgO. The wave at 0.6 V vs. Hg/HgO may be due to the formation of a small amount of Ni^{4+}, perhaps at the edges of the α-Ni(OH)$_2$/γ-NiOOH sheets (or other sites representing only a small fraction of the Ni atoms). Revised Pourbaix diagrams for Ni suggest the formation of NiO$_2$ at OER potentials ($\eta > $ ~0.22 V) at pH 14,[72] and other studies have indicated the presence of Ni^{4+} at elevated potentials.[31-33,38,48,49,73] The oxidation waves that grow in at 0.47 and 0.7 V vs. Hg/HgO are attributed to ordered β-NiOOH, as they arise in concert with the increased diffraction intensity due to β-Ni(OH)$_2$. The new oxidation waves were also observed in a film aged for 24 h (see Figure 4.12), which is the same film for which the GIXRD pattern is shown in Figure 4.6b. The small

82

peak at 0.7 V vs. Hg/HgO has not been reported previously, likely due to interference from the OER onset current when Fe impurities are present.
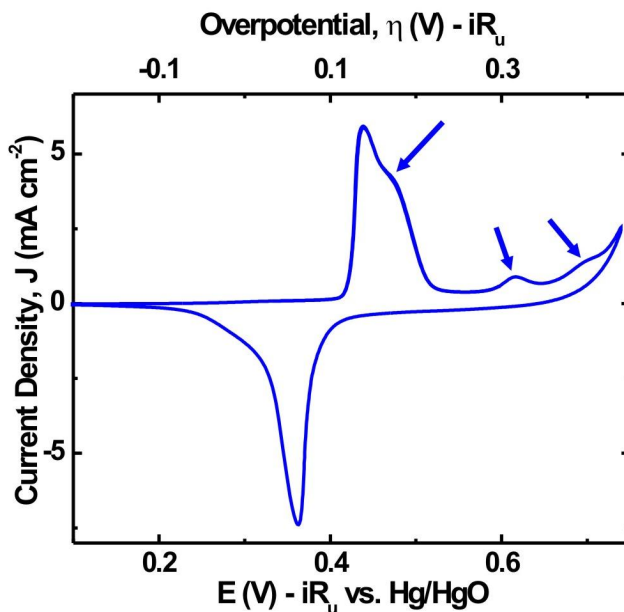
Figure 4.12. Voltammogram collected for an Fe-free $Ni(OH)_2$ film after aging in 1 M KOH at 40° C for 24 h, drying in air for and performing GIXRD and XPS analysis, and then re-immersion in 1 M KOH (10 mV s^{-1}). The waves discussed in the main text at 0.47, 0.6, and 0.7 V vs. Hg/HgO are clearly visible (indicated here by arrows).

Previously, Corrigan also removed most Fe impurities from the electrolyte by prolonged electrolysis (5 days in a polypropylene container using a 1 kg Hg cathode 50 cm^2 and a 3 cm^2 high purity Ni anode, <0.005% Fe w/w).[16] The CV behavior he reported for $Ni(OH)_2$/NiOOH films cycled in that purified electrolyte is similar to what we measure for films aged in our purified electrolyte, including the appearance of the peaks at 0.47 and 0.6 V vs. Hg/HgO after aging. The new peak observed here at 0.7 V vs. Hg/HgO appears to have been obscured by OER current in CVs collected by Corrigan, suggesting that the electrolyte purification used here is more-effective at removing Fe.

In light of these findings, it is likely that previous studies of highly-active $Ni(OH)_2$/NiOOH-based catalysts were affected by Fe impurities. For example, recent work has found that the Ni-borate (NiB$_i$) OER catalyst operating at pH 9.2 has short-range structure analogous to NiOOH.[40,49,74] NiB$_i$ requires prolonged anodization to reach its most active state. Using a combination of electrochemical and structural studies, it was argued that a significant population of Ni^{4+} is required for high OER activity, and that the

more-active anodized structure resembles that of γ-NiOOH rather than β-NiOOH.[49] These conclusions, like ours, are in conflict with the long-held view that β-NiOOH has a higher intrinsic OER activity. However, we conducted prolonged constant-current-density anodization of NiOOH in Fe-free KOH and found a decrease in activity over ~12 h at both 1 mA cm^{-2} and 10 mA cm^{-2} (Figure 4.13). It is possible that the anodization of NiB$_i$ films resulted in the incorporation of Fe from the electrolyte and that the increased activity of the anodized NiB$_i$ catalyst is due to the formation of a mixed Ni-Fe oxyhydroxide. Further experiments on NiB$_i$ under Fe-free conditions would be required to test this hypothesis.
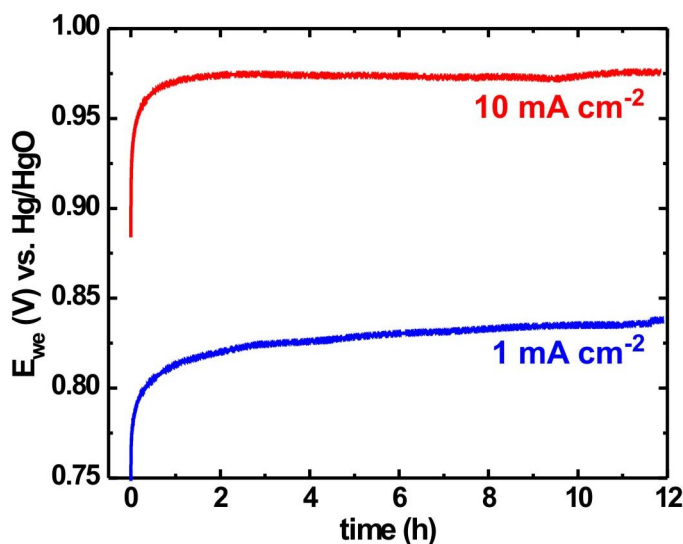
Figure 4.13. Chronopotentiometry results for an Fe-free NiOOH film held at constant current densities of 1 mA cm^{-2} (blue curve, lower) and 10 mA cm^{-2} (red curve, upper) for ~12 h. No increase in activity is observed after prolonged anodization in the purified Fe-free electrolyte.

Electronic Conductivity in Ni$_{1-x}$Fe$_x$OOH

Electrocatalysts must be sufficiently conductive to pass charge through the catalyst film with negligible potential drop. In cases where the catalyst is not sufficiently conductive, a portion of the applied potential will drop across the catalyst film to drive the current transport. This would lead to a lower apparent catalytic activity relative to a more-conductive film. It is known that NiOOH is conductive while Ni(OH)$_2$ is an insulator.[75] Corrigan hypothesized that Fe increases the conductivity of NiOOH, which

might explain the enhanced activity of $Ni_{1-x}Fe_xOOH$ relative to $NiOOH$.[16] However, the conductivity of $Ni_{1-x}Fe_xOOH$ as a function of potential and Fe content has not previously been measured.

To measure the through-film conductivity *in situ* under relevant conditions, the films were deposited onto IDA electrodes. The two IDA leads were shorted together and a total Au/Ti surface area of ~0.1 cm^2 was submerged in the deposition solution. Films were deposited at -0.1 mA cm^{-2} (cathodic) for 20 min. Deposition occurred on top of the IDA fingers and spanned the gap spaces (Figures 4.14a and 4.14b). After drying, cracking is observed due to contraction of the porous films. Dry films on the IDA electrodes were ~0.8–1.5 μm thick as determined by SEM and stylus profilometry. CVs were collected in a three-electrode configuration with the two IDA working electrodes shorted together (Figure 4.14c).

Steady-state *in situ* film conductivity measurements were performed by applying a constant potential offset between the two IDE working electrodes (WE1 and WE2) of 10 mV while WE1 was held constant relative to the reference electrode for 2-5 min until the measured current stabilized. During this dual-working-electrode conductivity experiment, the current measured at each working electrode can be described as the sum of faradaic and through-film-conduction components:

$$I_{WE1} = I_{OER1} + I_{cat1} + I_{cond} \tag{4.1}$$

$$I_{WE2} = I_{OER2} + I_{cat2} - I_{cond} \tag{4.2}$$

where I_{WE1} and I_{WE2} are the total currents measured at each working electrode, I_{OER} is the current from the OER, I_{cat} is the current from catalyst oxidation, and I_{cond} is the through-film conductivity current. Because the working electrodes are symmetric, $I_{OER1} \approx I_{OER2}$ and $I_{cat1} \approx I_{cat2}$. Thus $I_{WE1} - I_{WE2} \approx 2I_{cond}$. The effective catalyst film conductivities σ are estimated by:

$$\sigma = \frac{I_{cond} w}{Nld\Delta V} \tag{4.3}$$

where w is the IDA gap spacing, N is the number of electrodes (here $N = 130$), l is the length of each electrode, d is the film thickness, and ΔV is the voltage offset between WE1 and WE2 (here $\Delta V = 10$ mV).[76] We use the term effective conductivity to account for the fact that this calculation assumes a dense, uniform slab across the electrode array

with a thickness much less than the spacing between the IDA electrode fingers such that current flows essentially linearly across the finger gap. Because these conditions not rigorously met here, the values reported are taken as lower-bound estimates of the intrinsic conductivities.

The effective conductivities are shown in Figure 4.14d. All reduced films have low conductivities, independent of Fe concentration. A sharp increase in conductivity is
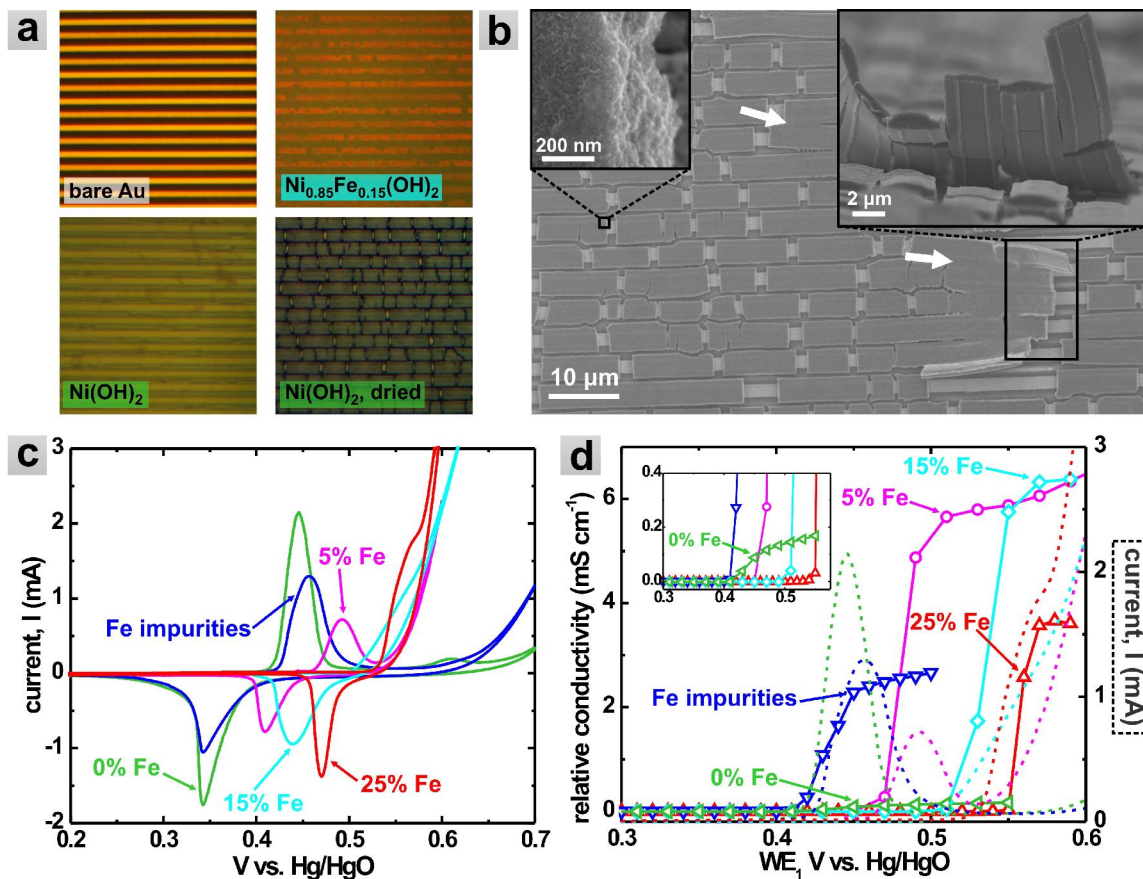
Figure 4.14. (a) Optical microscope images of IDA electrodes bare and with deposited films. Upon drying, cracking of the films is observed, but the films are crack free when kept wetted. (b) SEM images of $Ni(OH)_2$ film on an IDA electrode. Despite cracking, continuous regions of the film can be seen which span the gap spaces (indicated by white arrows). (c) CV scans of $Ni_{1-x}Fe_x(OH)_2/Ni_{1-x}Fe_xOOH$ films deposited on IDA electrodes. Currents are not normalized for differences in film thickness and potential values are not corrected for series resistance. (d) Conductivity data (points with solid connecting lines) for the same films. The potential onset of conductivity correlates with the position of the hydroxide/oxyhydroxide oxidation wave shown as dotted lines for each film. The inset shows an enlarged region to make the conductivity turn-on for the rigorously Fe-free film apparent.

observed upon Ni oxidation. The conductivity turn-on shifts to higher potentials with increasing Fe-content, and correlates with the position of the $Ni^{2+/3+}$ oxidation wave (dashed lines, Figure 4.14d). Oxidized NiOOH under Fe-free conditions has $\sigma \approx 0.1$ to 0.2 mS cm^{-1}. Samples with 5%–25% Fe have $\sigma \approx 3.5$ to 6.5 mS cm^{-1}, all more than an order of magnitude higher than the Fe-free films. NiOOH films without intentionally added Fe measured in the unpurified electrolyte have $\sigma \approx 2.5$ mS cm^{-1}, consistent with substantial Fe incorporation over the duration of the dual-electrode *in situ* conductivity experiment.

These experiments show that Fe increases the conductivity of NiOOH. β-NiOOH is an n-type semiconductor,[77] and doping with Fe could change the carrier concentration. The 30-60 fold increase in conductivity would be expected to have a dramatic effect on the performance of NiOOH catalysts under conditions where the potential drop needed to transport current across the film was a substantial fraction of the total applied overpotential, i.e. for sufficiently thick films. For a 100-nm thick Fe-free NiOOH film passing a current density of 10 mA cm^{-2}, less than 1 mV would drop due to resistive losses. For typical films ~40 nm thick on Au substrates, we measure a ~200 mV difference between the overpotential required to drive 10 mA cm^{-2} for NiOOH versus $Ni_{0.75}Fe_{0.25}OOH$. The conductivity difference between NiOOH and $Ni_{0.75}Fe_{0.25}OOH$ cannot account for the difference in apparent activity. The conductivity differences would, however, be important for device architectures where much thicker films (i.e. $\gg$ 1 μm) are needed, and these measurements provide guidance for the design of such architectures.

Activity Enhancement via Partial Charge Transfer between Ni and Fe

Yeo and Bell compared the OER activity of NiOOH films with varying thicknesses and showed that on noble metal substrates the OER TOF increases for films less than few monolayers in thickness.[41] The effect was most pronounced on Au and smaller on less-electronegative Pd substrates. The increase in activity is attributed to partial electron transfer from the NiOOH to the more-electronegative noble metal substrate, thus modifying the electronic properties of the Ni^{3+} centers. The effect is strongest for the first few monolayers because the cations are close to the substrate interface. Past a critical film thickness, the average Ni center was too far away from the

interface to feel the electron-withdrawing effect of the substrate, and the measured activity was that of bulk NiOOH.

Electrodeposited Ni-Fe mixed hydroxides contain Fe predominantly as Fe^{3+}.[31,34,78] Under OER conditions, E-pH (Pourbaix) diagrams predict both Fe^{3+} and Fe^{4+}.[79] In principle partial-charge transfer between Fe and $Ni^{3+/4+}$, as has been proposed by Corrigan et al.,[34] could enhance the activity via a similar mechanism as the Au support. In support of this hypothesis, the potential of the $Ni^{2+/3+}$ couple in $Ni_{1-x}Fe_xOOH$ depends on the Fe content (e.g. see Figure 4.14c and also ref. 8). Adding Fe makes it more difficult to oxidize Ni^{2+} leading to $Ni^{3+/4+}$ with more oxidizing power and thus possibly faster OER kinetics. If the Fe exerts a similar electron withdrawing effect on Ni as does the Au substrate, the thickness-dependence of the OER TOF for NiOOH on Au observed by Yeo and Bell would be diminished after Fe incorporation because the Fe would be distributed throughout the film (thus "activating" all Ni centers).

Figure 4.15 compares the TOF as a function of thickness for Fe-free NiOOH and $Ni_{0.75}Fe_{0.25}OOH$ on Au and GC. The number of active sites was assumed to be equal to the number of electrochemically active Ni sites obtained from integration of the $Ni^{2+/3+}$ wave. The slopes of the fit lines indicate the magnitude of the TOF thickness dependence. For both catalysts, the thickness dependence is greater on Au than on GC, consistent with the higher work function of Au compared to C (Au 5.1-5.5 eV; C 5.0 eV).[80] The difference in work function for the electrode surface in base under oxidizing conditions, however, is likely different from those of the pure elements measured in vacuum due to surface oxidation of the Au to form AuO_x (which is seen in CV scans, see Figure 4.4) and the possibility of oxidation of the C and contamination by adventitious adsorbed hydrocarbon species. Another explanation for the activity enhancement is the formation of a bimetallic Au-Ni oxide/hydroxide at the electrode surface, which Yeo and Bell consider based on *in situ* Raman measurements.[41] The lower activity on the GC substrates could be due to the inability of C and Ni to form such a bimetallic oxide under these conditions.

Figure 4.15 also shows that for both substrates the TOF thickness dependence is less for $Ni_{0.75}Fe_{0.25}OOH$ than for the NiOOH. On Au, the TOF increases by more than 2 orders of magnitude for NiOOH over the measured thickness range, while the TOF for

$Ni_{0.75}Fe_{0.25}OOH$ changes by less than an order of magnitude. On C, the NiOOH TOF increases by about an order of magnitude over the thickness range measured, while
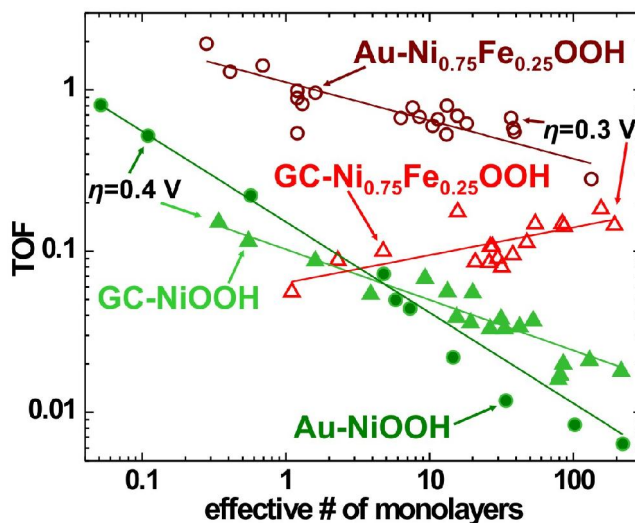
Figure 4.15. Turnover frequency (TOF) as a function of film thickness for Fe-free NiOOH (closed symbols) and $Ni_{0.75}Fe_{0.25}OOH$ (open symbols). Films on Au (circles) show a greater thickness dependence than films on GC (triangles) for both catalysts. Lines are fit to the data using a power function $y = ax^b$ (see Table 4.1 for fit values). TOF values were calculated at $\eta = 0.3$ V for $Ni_{0.75}Fe_{0.25}OOH$ and $\eta = 0.4$ V for NiOOH.

Table 4.1. Fitting Parameters for Data in Figure 4.15 [a]

sample	substrate	a	a error	b	b error	R^2
NiOOH	Au	0.152	0.005	-0.562	0.012	0.999
	GC-RDE	0.103	0.004	-0.313	0.018	0.941
$Ni_{0.75}Fe_{0.25}OOH$	Au	1.118	0.059	-0.237	0.034	0.710
	GC-RDE	0.064	0.013	0.172	0.053	0.411

[a] Data were fit using Origin 8.0 to power functions with the general equation $y = ax^b$. The value of b is an indication of the degree of TOF thickness-dependence (with larger magnitude of b indicating greater thickness dependence).

$Ni_{0.75}Fe_{0.25}OOH$ shows no significant change with film thickness. These results are consistent with the hypothesis that the Fe enhances the activity of NiOOH through a Ni–Fe partial-charge-transfer activation process occurring throughout the film similar to that which occurs for thin layers on Au.

Corrigan et al. found evidence from *in situ* Mössbauer spectroscopy of partial electron transfer away from Fe^{3+} accompanying the oxidation of Ni^{3+} to Ni^{4+}.[34] There is substantial evidence from X-ray absorption[31,49,73] and Mössbauer[32-34] experiments that Ni^{4+} and/or Fe^{4+} are present in $Ni_{1-x}Fe_xOOH$ at OER potentials. Axmann and Glemser studied $Ni_{1-x}Fe_xOOH$ using Mössbauer spectroscopy and found high-spin Fe^{4+} without observing quadrupole splitting, indicating a regular (i.e. no Jahn-Teller distortion) octahedral geometry around Fe.[32] The authors propose a model to explain their results whereby clusters of one regular $Fe^{IV}O_6$ octahedron surrounded by six regular $Ni^{IV}O_6$ octahedra create discreet M^{4+} domains within sheets that otherwise consist of M^{3+} ions. It may be that such M^{4+} domains within $Ni_{1-x}Fe_xOOH$ are the OER active sites. Further experimental and theoretical study to measure the electronic density-of-states, map the domain structure, and identify reaction intermediates with changes in Fe content are needed to better describe the electronic structure of $Ni_{1-x}Fe_xOOH$.

Conclusions and Bridge

We tested several mechanisms by which Fe has been predicted to increase the catalytic activity of $Ni(OH)_2/NiOOH$ for the OER. We showed that the conductivity of $Ni(OH)_2/NiOOH$ increases by >30-fold upon co-precipitation with Fe, but that these differences cannot explain the observed increase in activity. The effect of film thickness on TOF was investigated, and it was found that films with co-deposited Fe showed a lower thickness-dependence than Fe-free films. This is consistent with a Fe-induced partial-charge-transfer mechanism, which activates Ni centers throughout the catalyst film. We studied the structure and activity of $Ni_{1-x}Fe_x(OH)_2/Ni_{1-x}Fe_xOOH$ films as a function of aging. All films studied showed an increase in crystallinity with aging, while only those exposed to Fe impurities showed an increase in OER activity. This shows that the absorption of Fe impurities is responsible for the dramatic increase in activity of aged $Ni(OH)_2/NiOOH$ and disproves the long-held view that β-NiOOH is intrinsically more active for the OER than γ-NiOOH. The results also indicate that previous reports of highly-active $Ni(OH)_2$-based OER catalysts include Fe impurities. Long range order (or disorder), however, is apparently unimportant to the catalytic activity in the $Ni_{1-x}Fe_xOOH$ system. These results further underscore the importance of recognizing and accounting

for the effects of impurities on the performance of heterogeneous electrocatalysts. They are also important for comparison with theoretical predictions and ultimately a complete understanding of the origins of high activity in $Ni_{1-x}Fe_xOOH$-based OER electrocatalysts.

The work in this dissertation up to this point has involved the study of catalyst materials for the oxygen evolution reaction. In Chapter III, we explored some of the complexities involved in integrating a catalyst into a water-splitting photoanode, specifically the effects of parasitic optical absorption on photoanode performance. Our results showed that to maximize photoanode performance, very thin catalyst films are required. Additional challenges to consider when optimizing efficiency and practicality of the photoanode are mass (and electron) transport and catalyst loading. The removal/escape of bubbles from the catalyst surface is desirable to maintain access to catalytic sites. Ideally, one would want to have as many catalytic centers as possible in order to decrease OER overpotential. But the optical requirement of a thin film limits the amount of catalyst that can be used per unit surface area. One way to increase catalyst loading and facilitate mass transport would be by designing transparent, conductive high-surface-area hierarchical structures to use as catalyst supports. The 3-D structure of conductive catalyst supports could be designed across multiple length scales to facilitate escape of evolving O_2 while maximizing real surface area, and thus catalyst loading per unit volume.

Chapter V describes the synthesis of Sn-Ti mixed nanoparticles that could be used to make such catalyst supports. Specifically, the goal of this work was to find a support material that could accommodate thin epitaxial layers of the precious-metal rutile oxides IrO_2 and RuO_2 and mixed $Ir_{1-y}Ru_yO_x$, which are some of the only OER catalysts that are highly active and stable under acidic conditions. For these materials in particular, use of a thin film on a high-surface-area support has the added economical benefit of increasing the atom efficiency of the precious-metal by maximizing number of active sites per mass of metal. The work in Chapter V details the solvothermal synthesis of $Sn_xTi_{1-x}O_2$ solid-solution and $(SnO_2)_x/(TiO_2)_{1-x}$ core/shell nanoparticles with tunable lattice parameters and morphologies over the range of $0 \leq x \leq 1$. Rutile-phase particles with solid-solution or core/shell architectures are synthesized by combining titanium isopropoxide [Ti(O-*i*-

Pr)$_4$] with Sn-containing precursors (SnCl$_4$ or SnO$_2$ nanoparticles, respectively) to favor rutile crystal growth over the typically observed anatase-phase TiO$_2$. The transition from the anatase to the rutile TiO$_2$ phase is associated with increasing concentration of the Sn precursor. In the absence of Ti-precursor, SnO$_2$ nanowires with diameters < 5 nm are formed from SnCl$_4$ under the reaction conditions. This work represents initial steps towards the development of designer supports for specific OER catalysts.

CHAPTER V

SYNTHESIS OF RUTILE PHASE TIN/TITANIUM OXIDE SOLID-SOLUTION AND
TIN OXIDE/TITANIUM OXIDE CORE/SHELL NANOPARTICLES WITH
TUNABLE LATTICE CONSTANTS AND CONTROLLED MORPHOLOGIES

Portions of this chapter were previously published as Trotochaud, L.; Boettcher, S.W. "Synthesis of Rutile Phase $Sn_xTi_{1-x}O_2$ and $(SnO_2)_x/(TiO_2)_{1-x}$ Core/Shell Nanoparticles with Tunable Lattice Constants and Controlled Morphologies" *Chemistry of Materials*, **2011**, *22*, 4920-4930. L.T. wrote the paper, performed the experimental work, and made the figures. S.W.B. was the principal investigator and provided editorial assistance.

Introduction

Mixed-metal oxide nanomaterials are of interest for their applications as gas sensors,[1-4] heterogeneous catalysts and catalyst supports,[4-8] and electrode materials.[7,9-11] In particular, solid solutions of the tin and titanium dioxides, hereafter denoted as $Sn_xTi_{1-x}O_2$, have received attention for their photocatalytic activity for oxidation of organic molecules[12,13] and for their use in dimensionally stable anodes (DSA®).[14,15] Our interest in the $Sn_xTi_{1-x}O_2$ system concerns the latter application, with the eventual goal of designing oxide based electrocatalysts with precise nanostructures where rutile-phase transparent-oxide hosts are coupled with thin shells of highly-active, but precious, rutile-phase oxides such as RuO_2 and IrO_2. Precise control is needed in the design and fabrication of such materials if they are to be incorporated into high-performance electrodes.[14,16]

The tunability of nanoparticle (NP) materials involves control of shape, size, composition, and crystal structure. A variety of methods for synthesizing metal oxide and mixed-metal oxide NPs exist that provide varying levels of such control over the reaction products.[17-24] This study involves a fundamental investigation of nanoscale SnO_2–TiO_2 mixed oxides and aims to improve synthetic control over crystal structure and morphology by understanding and manipulating nucleation and growth processes.

TiO_2 is used for dye-sensitized solar cells, and extensive work has been done to investigate the properties of these materials.[25-31] Bulk TiO_2 crystallizes predominantly in

the anatase or rutile phases. Solution-based syntheses of TiO_2 NPs largely yield products with the anatase crystal structure.[32-37] In many cases organic capping ligands are effective in controlling the morphologies of anatase TiO_2 NPs by preferentially binding to certain crystal facets, thus inhibiting particle growth along these crystallographic directions.[17,32,36] Few studies, however, report the synthesis of phase-pure rutile TiO_2 NPs.[38-43] Those syntheses that do yield rutile TiO_2 are performed under highly acidic aqueous conditions, making the reactions incompatible with organic stabilizing ligands (which are soluble in organic solvents such as ethanol). Without surface stabilizing agents, these aqueous reactions yield products that are morphologically ill-defined aggregates of needle or rod-shaped particles.[44-47]

SnO$_2$ nanostructures have been synthesized by methods including high-temperature thermal oxidation,[48-50] hydrothermal,[51-54] nonaqueous solution,[55-57] and sol-gel[58,59] techniques. SnO_2 crystallizes only in the rutile structure (cassiterite). The majority of reports describing SnO_2 NPs describe morphologies including crystalline nanorods,[51,54,60] nanobelts,[49] and nanowires of various aspect ratios with lengths ranging from several[50,53] to hundreds[48,49] of microns, and diameters as small as 3.4 nm.[54] These have useful dimensions for gas-sensing applications.[51] Several solution-based methods produce uniform spherical particles less than 5 nm in diameter.[56-58]

Bulk systems of the mixed SnO_2–TiO_2 oxides have been explored previously. Studies on the thermal, electronic, and structural properties of bulk $Sn_xTi_{1-x}O_2$ solid solutions are reported for both theoretical[61-64] and experimental samples prepared by high-temperature solid-state reactions of mixtures of SnO_2 and TiO_2 powders.[65-68] The bulk products of these high-temperature SnO_2–TiO_2 reactions are morphologically ill-defined micropowders.

Reports of $Sn_xTi_{1-x}O_2$ nanoscale systems are few and are largely focused on application of the products to photocatalysis. These solution-based techniques, which include hydrothermal,[69,70] sol-gel,[71] and polyol-mediated[72] methods, provide limited synthetic control over $Sn_xTi_{1-x}O_2$ NP morphology and crystal structure. The transition from anatase to rutile with increased tin-doping has been noted, however the ratio of tin required to complete this transformation seems largely dependent on the particular synthetic method. For example, Zhao et al. recently reported a hydrothermal method in

which the pure rutile product was obtained for $Sn_{0.06}Ti_{0.94}O_2$,[69] while Asokan et al. synthesize $Sn_{0.5}Ti_{0.5}O_2$ wires that maintain the anatase crystal structure by an electrospinning method.[73] To the best of our knowledge, there have been no reports of non-aqueous growth of $Sn_xTi_{1-x}O_2$ NPs mediated by organic ligands.

Particle composition and morphology has also been controlled through the use of pre-formed NP seeds as nucleation sites. In aqueous solution, Li et al.[47] used pre-formed rutile TiO_2 NP seeds (average size = 6.9 nm) to induce the rutile structure in their pure TiO_2 products, although manipulation of reaction time and temperature generated anatase/rutile mixed products in some cases. Qi et al. reported the formation of rutile TiO_2 particles in aqueous solution by addition of $SnCl_2 \cdot 2H_2O$ to the $TiCl_4$ hydrolysis reaction mixture.[74] The authors propose that the SnO_2 nuclei formed during hydrolysis act as a heterogeneous nucleation template for rutile TiO_2 growth. However, the [Sn]/[Ti] molar ratio was varied only up to 0.1, and the particle morphology remains poorly-defined and polydisperse. Tao et al. report that nanocrystalline rutile TiO_2 shells form on the surface of wollastonite ($CaSiO_3$) particles in the presence of $SnCl_4$.[75] The anatase-to-rutile phase transition occurs with increasing $SnCl_4$ content and is observable by x-ray diffraction (XRD) analysis. The authors propose that the reactive $SnCl_4$ precursor quickly forms SnO_2, which then induces heterogeneous nucleation of rutile titania, but they did not address the local environment of the tin atoms in their final products. The SnO_2 NP seeding method has not previously been extended to create mixed-oxide $(SnO_2)_x/(TiO_2)_{1-x}$ core/shell NP structures, nor has the nucleation and growth of these hetero-epitaxial NP products been studied in any detail.

Here, we report a study of the solvothermal synthesis of phase-pure rutile nanoparticles containing mixtures of tin and titanium oxide. A key facet of the synthesis is that Sn-precursors are introduced into the reaction mixture either as pre-formed SnO_2 NPs or as a reactive molecular $SnCl_4$ precursor. In the SnO_2 NP seeded-growth method, we hypothesize that using a rutile seed as a template lowers the activation energy for TiO_2 rutile formation by eliminating the energy barrier to nucleation. For the *in situ* $SnCl_4$ nucleation method, we hypothesize that the presence of the reactive Sn-precursor in the initial solution and in the product affects the overall thermodynamics of the reaction, preferencing formation of a Sn/Ti solid-solution mixed rutile product relative to

the anatase phase. We show that introducing SnO_2 NP seeds yields product with characteristics consistent with the $(SnO_2)_x/(TiO_2)_{1-x}$ core/shell architecture, while using the molecular $SnCl_4$ precursor generates $Sn_xTi_{1-x}O_2$ solid-solution particles. The products are characterized to reveal insights into the nucleation and growth of these two different SnO_2–TiO_2 mixed-oxide NP architectures. Such understanding is key to the effective design of mixed-oxide nanoscale systems with complex and controlled structure.

Experimental Details

Chemicals and Materials

Titanium isopropoxide [Ti(O-*i*-Pr)$_4$]; 97%), oleylamine (OM; 70%, tech. grade), oleic acid (OA; 90%, tech. grade), and tin(IV) chloride ($SnCl_4$; 99%) were obtained from Sigma-Aldrich. Benzyl alcohol (min. 98%) was obtained from EMD. Absolute ethanol (CH_3OH; 200 proof), tetrahydrofuran (THF; ultra pure, BHT stabilized), and cyclohexane (99%) were obtained from Mallinckrodt. All chemicals were used without further purification. All water used in reactions was purified to 18.2 MΩ-cm with a Barnstead Nanopure Analytical ultrapure water system (model D11901). TEM grids (carbon type-B, 200 mesh, copper; ultrathin carbon film on holey carbon support film, 400 mesh, copper) were purchased from Ted Pella. Acid digestion vessels (Parr Instrument Company, vessel number 4744, 45 mL) with PTFE-liners were used for the solvothermal reactions.

Characterization

Powder x-ray diffraction (XRD) patterns were recorded on a Bruker D8 Discover diffractometer operating at 40 mA and 40 kV using monochromated Cu Kα$_1$ radiation (λ = 1.541 Å, step size = 0.2 or 0.5°, integration time 10 or 20 s/step). XRD samples were prepared by mounting washed, air-dried NP powders onto borosilicate glass microscope slides using silicone-based vacuum grease as the mounting agent. For XRD particle size analysis, a silicon powder standard was used to determine the instrumental line broadening (FWHM = 0.12° 2θ for the Si (111) reflection). Powder XRD patterns were fit using Fityk[76] software (version 0.9.3). All reflections in the full diffraction patterns were fit to Gaussian functions using the standard nonlinear least-squares Levenberg-Marquardt method. Fitting errors in peak positions were typically less than 0.05° 2θ, even

in the case of broad and/or overlapping peaks. Fitting errors for values of peak FWHM were typically less than 0.1° 2θ.

Transmission electron microscopy (TEM) analysis of NP morphology was performed on a FEI Technai G^2 Spirit microscope operating at 120 keV, equipped with an SIS Megaview III CCD camera. Most TEM samples were prepared by dropcasting 4 μL of soluble NP samples (see below) onto TEM grids using a micropipette. The grids were rinsed to remove excess organics by careful submersion in ethanol using self-closing tweezers. To minimize particle aggregation on the grids due to drying effects, some TEM samples were prepared using an aerosol method (see Supporting Information for aerosol apparatus setup). For TEM particle size data, particle moments (i.e. average diameters accounting for particle anisotropy) were measured manually using ImageJ software. Average sizes are reported $d_{avg,Sn\chi}$ or $d_{avg,sd\chi} = x \pm y$ nm, where x is the average measured particle moment and y is the unbiased standard deviation.

Single pulse (5 μs, 30° pulse; 6 s recycling delay) solid-state ^{119}Sn MAS NMR of selected samples was carried out on a Bruker Avance DSX300 MHz WB NMR spectrometer with ^{119}Sn operating at 111.9 MHz. A Bruker 4 mm double resonance MAS probe along with a 4 mm Zirconia rotor system were used at a spinning speed of 14 kHz. The ^{119}Sn chemical shift was referenced to SnO_2 at -604 ppm relative to the standard $(CH_3)_4Sn$. Solid-state MAS NMR spectra were fit to Gaussian/Lorentzian lineshapes using Dmfit (version 20071105b).[77]

Synthesis of SnO$_2$ NP Seeds

SnO$_2$ seed NPs were synthesized as reported previously by Ba et al.[56] Briefly, 1 mL (8.8 mmol) of $SnCl_4$ was added dropwise to 20 mL benzyl alcohol with vigorous stirring. The reaction mixture was then heated in a temperature-controlled oil bath at 100°C for 24 hrs. The temperature was then increased to 110°C, which was maintained for an additional 8 hrs. The resulting white precipitate was collected via centrifugation. A small amount of precipitate was dried in air on a borosilicate glass microscope slide for XRD analysis. The remaining precipitate was dispersed in 20 mL THF, giving a slightly yellow dispersion with a NP seed content of ~33 mg/mL (~0.22 M). This NP seed solution was subsequently used for the seeded growth method. The molarity of the seed

solution was confirmed by weighing the product following thermal combustion of organics at 700°C.

Synthesis of Core/Shell (SnO$_2$)$_x$/(TiO$_2$)$_{1-x}$ NPs via Seeded Growth

Vigorous stirring was maintained throughout the addition of all chemical reagents. For a typical synthesis, X mmol seeds were measured (based on the calculated molarity of the SnO$_2$ seed solution) into borosilicate glass test tubes. The THF was allowed to evaporate to near dryness in a fume hood under N$_2$ gas flow (the solids were left visibly moist to encourage resolubilization). Under vigorous stirring, 3 mmol OA (1.06 mL), 2 mmol OM (0.94 mL), and 10 mmol ethanol (0.58 mL) were added sequentially. Typically, the solution was visibly clear and colorless or very slightly yellow upon sufficient mixing of the reagents. Next, a stoichiometric amount of nanopure water (2 mmol, 36 µL) was added dropwise to the reaction mixture. Addition of water sometimes slightly clouded the solution temporarily. This is minimized by maintaining sufficient stirring during H$_2$O addition. Then Y mmol Ti(O-i-Pr)$_4$ was added dropwise, such that X + Y = 1 mmol. Addition of Ti(O-i-Pr)$_4$ caused the clear solution to turn a slight yellow color due to the formation of titanium oxocarboxyalkoxide complexes, which has been shown to decrease the hydrolytic susceptibility of the titanium precursor.[78,79] The test tubes were then sealed in Teflon-lined stainless steel autoclaves. The reactions were heated to 180°C in an electric oven and this temperature was maintained for 18 hours. After cooling to room temperature in air, the autoclaves were opened and ~2 mL of ethanol were added to precipitate the NPs from the supernatant. The samples were then homogenized with stirring, and a small amount (3 – 5 drops) of this unwashed reaction mixture was dissolved in 10 mL cyclohexane. These solutions were later used for TEM analysis. Samples were typically stable suspensions and somewhat optically scattering. Their dispersibility in organic solution is due to the presence of organic capping ligands at the surface. The stability of the particles in solution is dependent on the washing procedure of the as-prepared samples, with unwashed samples being the most dispersible and staying suspended for weeks, and samples washed with multiple portions of ethanol showing limited solubility and precipitating in as little as 2 – 3 hours.

The remaining reaction mixtures were then centrifuged, washed with ~5 mL ethanol, dispersed, and centrifuged again. The supernatant was then decanted. This

washing procedure was performed three consecutive times. The samples were then dried in air to give powders, which were homogenized for XRD analysis. Selected powder samples were used for solid-state NMR experiments without further treatment. The dried powders were slightly yellow for the pure TiO_2 samples, and sample colors became progressively darker with increasing tin concentration, approaching a brown color for the pure SnO_2 samples. A similar color transition was observed in the post-reaction supernatant solutions. Thermal combustion of these supernatant solutions at 700°C left little (< 1 mg) to no residue, implying that the color change is due to partially decomposed ligands and that all inorganic reagents added are incorporated into the NP powder products. The washed, dried powders also lost their color upon heating to 500°C in air (see Figure 5.1), suggesting that the color of the products is also due to the presence of partially decomposed ligand impurities.
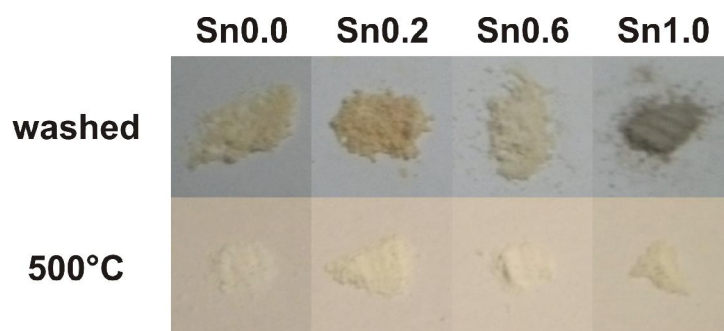
Figure 5.1. The top row shows four nanoparticle samples after the standard treatment used in this study (triple-washing with ethanol followed by air drying). To remove residual organics and organic capping ligands, the samples were heated in an electric furnace (ramp rate = 8°C/min) to 500°C and held for four hours. The bottom row shows the same powder samples after the heat treatment. The samples lose their color during the heating process, suggesting that the coloration is due to the presence of organic material.

$Sn_xTi_{1-x}O_2$ Solid-Solution NPs via In Situ Nucleation

The procedure for the *in situ* nucleation method is similar to that for the seeded-growth method. In place of the THF seed solution, a solution of 0.5 M $SnCl_4$ in ethanol prepared immediately prior to the reaction setup was used as the Sn-containing precursor. Addition of $SnCl_4$ to ethanol was performed in a fume hood, as the resulting reaction is exothermic and immediately releases HCl gas. All other experimental parameters and workup conditions were identical to those described above. Qualitative observations

regarding solubility and colors of the reaction products were similar to those for products made by the seeded-growth method.

Differential Scanning Calorimetry

The amorphous DSC control samples were prepared as follows. For amorphous TiO_2, 1 mmol $Ti(O-i-Pr)_4$ was added to 4 mL ethanol with stirring. 3 drops of nanopure water were added to immediately form a white precipitate. The precipitate was collected by centrifugation and dried in an electric oven at 100 °C for 30 min, giving a white powder. For amorphous SnO_2, 1.7 mmol $SnCl_4$ was added slowly to 4 mL ethanol with stirring. 0.5 mL nanopure water was added. The clear solution was then stirred on a hotplate at 90°C until dry, giving a white powder. For the amorphous 0.5 mix: 1.7 mmol $Ti(O-i-Pr)_4$ was added to 4 mL ethanol with stirring. 1.7 mmol $SnCl_4$ was added slowly with stirring. The clear solution was then stirred on a hotplate at 90°C until mostly dry, leaving a sticky residue. This residue was heated in an electric oven at 100°C for 1 hr to give a light pink powder. DSC experiments were performed on a TA Instruments DSC 2920. 5 mg of sample powder was loaded into standard aluminum DSC sample pans (Instrument Specialists Inc.) and crimp sealed. The heating rate was 20°C min^{-1} for all samples.

Aerosol TEM Grid Preparation Method

A can of pressurized air duster (generic, CFC-free) was securely mounted to a ring stand in a fume hood and equipped with a small plastic tube (included) to focus the air stream. 5 μL microcapillary tubes (Drummond Microcaps®) were immersed in the sample solutions and then mounted to the ring stand with a stainless-steel clip such that the end of the microcapillary tube was positioned approximately 2 mm from and directly in front of the tip of the air-stream focusing straw. An initial "target" sample was prepared using blue food dye as the sample and white paper at the back of the hood as the target. Quickly depressing and releasing the handle of the pressurized air can draws the solution out of the microcapillary tube, producing a circular spray pattern on the paper approximately 10 cm in diameter. Without moving the aerosol apparatus, the empty "target" tube is carefully removed and replaced with one containing the NP solution. A TEM grid is positioned between the target paper and the apparatus in the center of the target spray pattern and the compressed air handle is quickly depressed and released,

coating the TEM grid with the NP solution. The grid was not rinsed or treated otherwise following the aerosol application.

Sample Nomenclature

Sample names are differentiated for the two synthesis methods in the following way: χ, defined by χ = mmol Sn / (mmol Sn + mmol Ti), is a number between 0 and 1 indicating the mole fraction of tin-containing precursor in the reaction mixture. The samples are differentiated as Snχ for the *in situ* SnCl$_4$ nucleation method, and sdχ for the seeded growth method. For example, Sn0.5 corresponds to a sample prepared using the *in situ* nucleation method with 0.5 mol fraction of SnCl$_4$, and sd0.2 is a sample prepared using the seeded growth method with 0.2 mol fraction of SnO$_2$ NP seeds.

Results

Powder XRD

Wide-angle XRD patterns were collected to determine the crystal structures and lattice constants of the products and are shown in Figure 5.2. Data from the XRD analysis for selected diffraction reflections for all samples is summarized in Table 5.1. Values for *d*-spacings were calculated from the fitted peak positions and based on the Bragg condition for reflection ($d = \lambda/2 \sin \theta$). For samples containing both the anatase and rutile phases, the mass fraction of rutile is estimated from:

$$W_R = I_R / (0.886 I_A + I_R) \tag{5.1}$$

where W_R is the mass fraction of rutile, 0.886 is a unit-less correction factor to account for the differences in scattering intensities due to the different crystal structures, and I_A and I_R are the integrated intensities of the anatase (101) and the rutile (110) reflections, respectively.[80]

<u>*In Situ* SnCl$_4$ Nucleation Method</u>

The Sn precursor content was varied from 0-100 mol %, while the total inorganic precursor amount was held constant at 1 mmol. In the absence of Sn precursors, the TiO$_2$ NPs crystallized only in the anatase phase, as evidenced by the single peak near 25.3° 2θ corresponding to the (101) anatase reflection. The onset of a second set of XRD reflections is observed between 2-5 mol % SnCl$_4$ (Figure 5.2a). The peak at 27.3° 2θ corresponds to a rutile (110) reflection near that of pure TiO$_2$ (27.4° 2θ), and all other

101

reflections in this set can also be indexed to the rutile phase. The rutile reflections increase in intensity relative to anatase reflections with increasing $SnCl_4$ concentration. The positions of the rutile reflections undergo a shift to lower 2θ with increasing $SnCl_4$ concentration, approaching the expected values for pure SnO_2. Reflections indicating the presence of anatase in the products are absent for $SnCl_4$ concentrations exceeding 15%.

Seeded-Growth Method

The powder XRD patterns for SnO_2–TiO_2 mixed-oxide samples prepared by the seeded growth method are different from those of the *in situ* nucleation method (Figure 5.2b). When no SnO_2 seeds are present in the reaction mixture, only reflections corresponding to anatase TiO_2 are observed in the XRD pattern. A decrease in intensity of the anatase reflections is observed with increasing SnO_2 seed concentration. Rutile reflections are first observed for products synthesized with 3-5% seeds. Unlike the *in situ* nucleation method, the rutile (110) reflection appears at ~27° 2θ, which is intermediate to that of the pure TiO_2 (27.4° 2θ) and pure SnO_2 (26.6° 2θ) positions. The positions of the rutile reflections shift to lower 2θ with increasing seed concentration, and continue to approach the expected values for pure SnO_2. Reflections corresponding to the anatase phase are observed only for samples synthesized with SnO_2 seed concentrations less than 50%.

Particle Size Analysis from XRD

Particle size was estimated from the XRD patterns using the Scherrer equation:

$$D = \frac{K\lambda}{\beta \cos\theta} \qquad (5.2)$$

where D is the average particle diameter, K is the dimensionless particle shape factor, λ is the wavelength of the incident x-rays, β is the FWHM of the Bragg reflection in radians (corrected for instrumental broadening), and $\cos\theta$ is the position of the Bragg reflection in degrees θ ($2\theta/2$). The value of K depends on the morphologies of the particles measured; we use a K value of 0.9, which is the value typically used for spherical particles or as an estimation of K when the sample morphology is unknown or polymorphic. Particle sizes were calculated from all reflections between 20° – 60° 2θ. Figure 5.3 summarizes the particle sizes calculated for the anatase (101) and the rutile (110) and (101) reflections. The calculated particle sizes are also presented in Table 5.1.

102
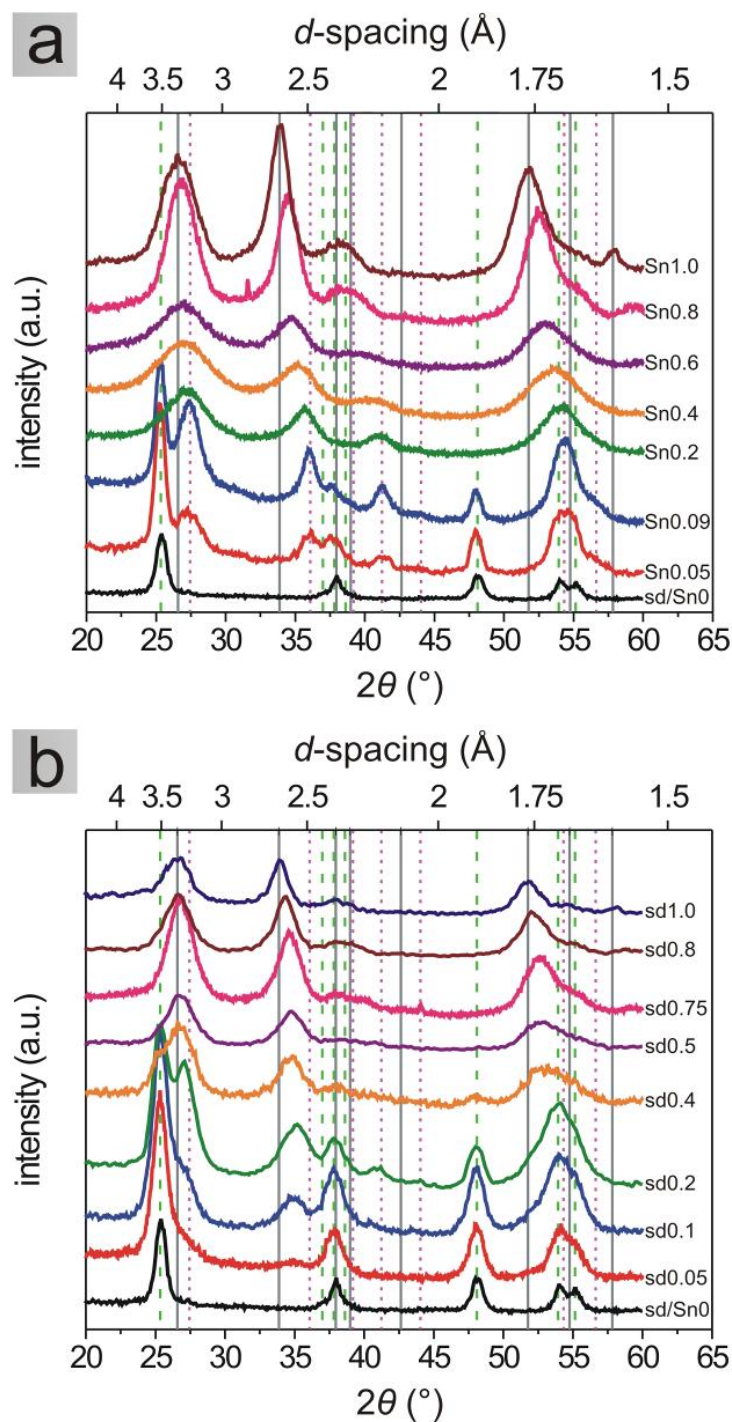
Figure 5.2. Powder XRD patterns for SnO_2–TiO_2 mixed-oxide samples obtained from the *in situ* nucleation method (a) and the seeded-growth method (b). Vertical reference lines for anatase TiO_2 (dash), rutile TiO_2 (dot), and rutile SnO_2 (solid) reflections are included as a guide for the eye. Intensity units are arbitrary and the data sets have been offset vertically to show the evolution of the powder patterns with increasing tin concentration. Patterns have been smoothed by 3-point adjacent-averaging but are not background corrected.

Table 5.1. XRD Analysis of Anatase (101) and Rutile (110) and (101) Reflections of SnO_2–TiO_2 Mixed Samples[a]

	peak position (2θ °)			d-spacing (Å)			Scherrer particle size (nm)			W_R[b] (%)
	A(101)	R(110)	R(101)	A(101)	R(110)	R(101)	A(101)	R(110)	R(101)	
sd/Sn0	25.29	--	--	3.52	--	--	7.5	--	--	0.00
Sn5	25.28	27.28	35.99	3.52	3.27	2.49	10.5	4.1	7.6	41.9
Sn9	25.30	27.35	36.01	3.52	3.26	2.49	10.7	4.8	7.7	60.9
Sn20	--	27.14	35.65	--	3.28	2.52	--	2.5	4.1	100
Sn40	--	27.05	35.15	--	3.29	2.55	--	2.1	2.9	100
Sn60	--	27.00	34.67	--	3.30	2.59	--	2.2	3.1	100
Sn80	--	26.83	34.48	--	3.32	2.60	--	3.6	4.7	100
Sn100	--	26.60	33.86	--	3.35	2.65	--	3.2	5.2	100
sd5	25.31	26.84[c]	35.10[c]	3.52	3.32	2.55	7.3	4.7	3.2	20.5
sd10	25.32	26.98[c]	34.89[c]	3.51	3.30	2.57	6.7	4.6	4.3	32.2
sd20	25.31	27.04	35.10	3.52	3.30	2.56	7.5	4.8	4.4	55.7
sd40	25.07	26.74	34.75	3.55	3.33	2.58	8.0	3.7	4.2	88.4
sd50	--	26.77	34.70	--	3.33	2.58	--	3.7	4.4	100
sd75	--	26.72	34.62	--	3.33	2.59	--	3.9	4.3	100
sd80	--	26.62	34.29	--	3.35	2.61	--	3.8	4.7	100
sd100	--	26.61	33.93	--	3.35	2.64	--	4.8	6.6	100

[a] A and R denote anatase and rutile, respectively.

[b] W_R is the weight-percent rutile, as defined in the text.

[c] Values for these peak positions are from fitting two peaks from a large peak with a small shoulder, as seen in Figure 5.2. This introduces a large level of uncertainty in these specific data points.

Differences in particle sizes extracted from different Bragg peaks are indicative of anisotropic particle shapes. This topic will be addressed further in the discussion section. Uncertainties in particle sizes from the Scherrer equation can arise from peak fitting (in the peak position and FWHM) and the chosen value of K. In our case, the latter of these is presumed to dominate, as uncertainties in β and θ from peak fitting are small (typically $\pm 0.1°$ 2θ and $\pm 0.05°$ 2θ, respectively). We also note that the Scherrer equation provides the mean size of crystalline domains in the sample along the particular crystallographic axis, which may be smaller than the particle size. In other words, the Scherrer equation gives a lower limit of particle size if the particles consist of multiple grains. Here, TEM imaging of the products formed from both $SnCl_4$ and SnO_2 NP precursors show lattice fringes that are continuous over entire particles (Figure 5.4, insets), indicating that the particles are single grain. In accord with this finding, the particle sizes determined via the Scherrer analysis of the powder XRD patterns agree with those determined by TEM analysis within the error estimates of each measurement (Figure 5.3).
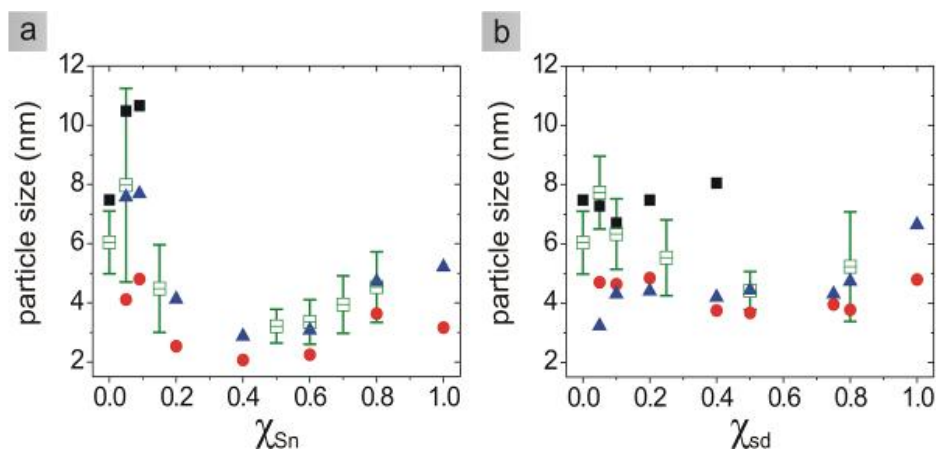
Figure 5.3. Particle sizes calculated from XRD reflections using the Scherrer equation and TEM images for the *in situ* nucleation method (a) and the seeded growth method (b). Open symbols with error bars represent data obtained from TEM analysis. Each set of solid symbols represents data obtained from a different XRD reflection as follows: squares = anatase (101); circles = rutile (110); triangles = rutile (101). The same XRD data is presented in numerical form in Table 5.1.

Non-uniform strain in the crystal lattice can also contribute to peak broadening. Williamson-Hall plots are typically used to deconvolute broadening due to particle strain from that due to size.[81] However, even for large values of strain, the magnitude of peak

broadening is less than that caused by small (< 10 nm) particle size.[82] For such small particles, size broadening dominates, especially since the lattice mismatch between the rutile TiO_2 and SnO_2 is relatively small. As expected, Williamson-Hall plots generated for select samples did not provide meaningful analyses, thus the particle sizes we obtain from XRD patterns were not corrected for non-uniform strain.

Transmission Electron Microscopy Analysis

As expected for high-temperature solvothermal reaction conditions,[32,78] TEM analysis shows that all products of both synthetic methods were crystalline with no evidence of amorphous material. The absence of amorphous material in the nanoparticle powder products was confirmed by differential scanning calorimetry experiments, where exothermic peaks associated with crystallization were not observed for the nanoparticle samples (Figure 5.4).
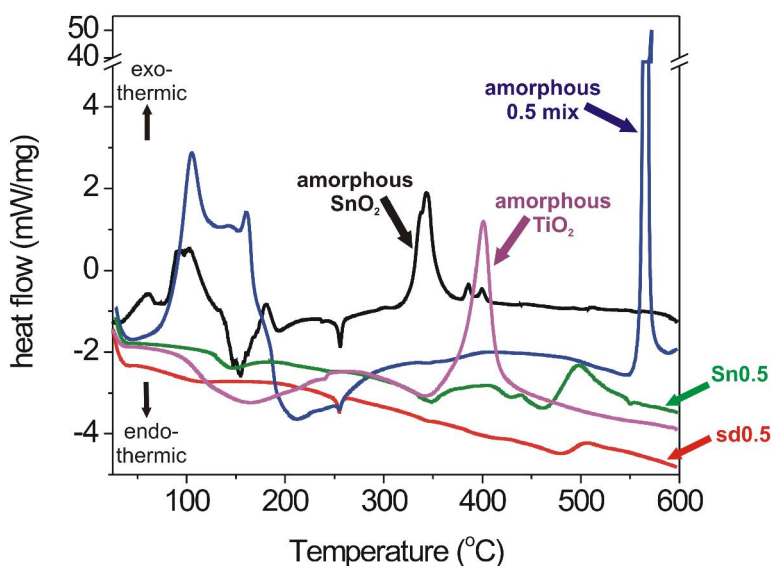
Figure 5.4. Differential scanning calorimetry (DSC) traces of nanoparticle samples Sn0.5 and sd0.5 as prepared in this study, and three amorphous control samples. Crystallization exotherms in the amorphous samples at 343°C (SnO_2), 402°C (TiO_2), and 572°C (0.5 mix) are not observed in the nanoparticle samples, indicating the absence of amorphous precursors.

Seeded-Growth Method

The morphologies of the particles were analyzed using TEM imaging (Figure 5.5). Particle sizes as determined by TEM imaging are included in Figure 5.3 (see Appendix B for complete particle-size-distribution histograms). The SnO_2 seeds initially are ellipsoids

(Figure 5.5a), which is consistent with the reports of Ba et al.[56] The pure anatase TiO_2 particles synthesized in the absence of Sn-precursors (Figure 5.5g) appear relatively monodisperse with $d_{avg,sd/Sn0} = 6.0 \pm 1.1$ nm. Lattice fringes corresponding to the anatase (101) planes (d-spacing = 3.51 Å) are visible with an average measured length of 3.6 ± 0.1 Å. Addition of 5 mol % SnO_2 seeds drastically alters the morphology of the anatase particles (Figure 5.5b), which increase in size to $d_{avg,sd0.05} = 7.7 \pm 1.2$ nm. TEM images show rectangular shapes that are 2D projections of the cuboidal 3D shape of the particles. Analysis of the anatase lattice fringes (average length = 3.6 ± 0.1 Å) reveals that the anisotropy of these particles is orthogonal to the [101] direction. A small population of particles in this sample were identified as SnO_2, based on lattice fringe measurements (3.34 ± 0.03 Å) of the SnO_2 rutile (110) planes (d-spacing = 3.35 Å). Further increasing the seed concentration to $\chi_{sd} = 0.25$ yields mixed-phase samples (Figure 5.5c) with smaller average particle size, but still a high level of polydispersity ($d_{avg,sd0.25} = 5.5 \pm 1.3$ nm). At $\chi_{sd} = 0.5$, the nanoparticles are uniformly faceted, with the TEM projections appearing as rounded squares (Figure 5.5d). These particles have a narrower size distribution than all samples with lower χ_{sd} ($d_{avg,sd0.5} = 4.4 \pm 0.7$ nm) and appear highly crystalline in TEM images (Figure 5.5d inset). At this seed concentration, anatase reflections are no longer detectable in the x-ray diffraction pattern (see above). In the $\chi_{sd} = 0.8$ sample, ($d_{avg,sd0.8} = 5.2 \pm 1.9$ nm) most of the particles appear similar to those for $\chi_{sd} = 0.5$ (Figure 5.5e). Another small population of elongated rod units is also observed in this sd0.8 sample, which may be products of growth by an oriented attachment mechanism, as is discussed below. Lattice fringe measurements yield an average spacing of 3.4 ± 0.1 Å, which is consistent with the d-spacing calculated for the sd0.8 sample (3.35 Å) from the rutile (110) reflection in the powder XRD pattern. This result indicates that the rods are elongated orthogonal to the [110] direction. The $\chi_{sd} = 1.0$ sample (Figure 5.5f), in which SnO_2 NP seeds were reacted only with ligands [i.e. no $Ti(O\text{-}i\text{-}Pr)_4$], shows elongated, necklace-like chains markedly different from the as-synthesized seed particles, indicating that the reaction conditions induce restructuring/fusion of the SnO_2 seeds. The fused structures are also crystalline, as is evidenced by the presence of lattice fringes in all the TEM images. All observed lattice fringes indicate preferential particle elongation/fusion occurring orthogonal to the rutile [110] direction.

107
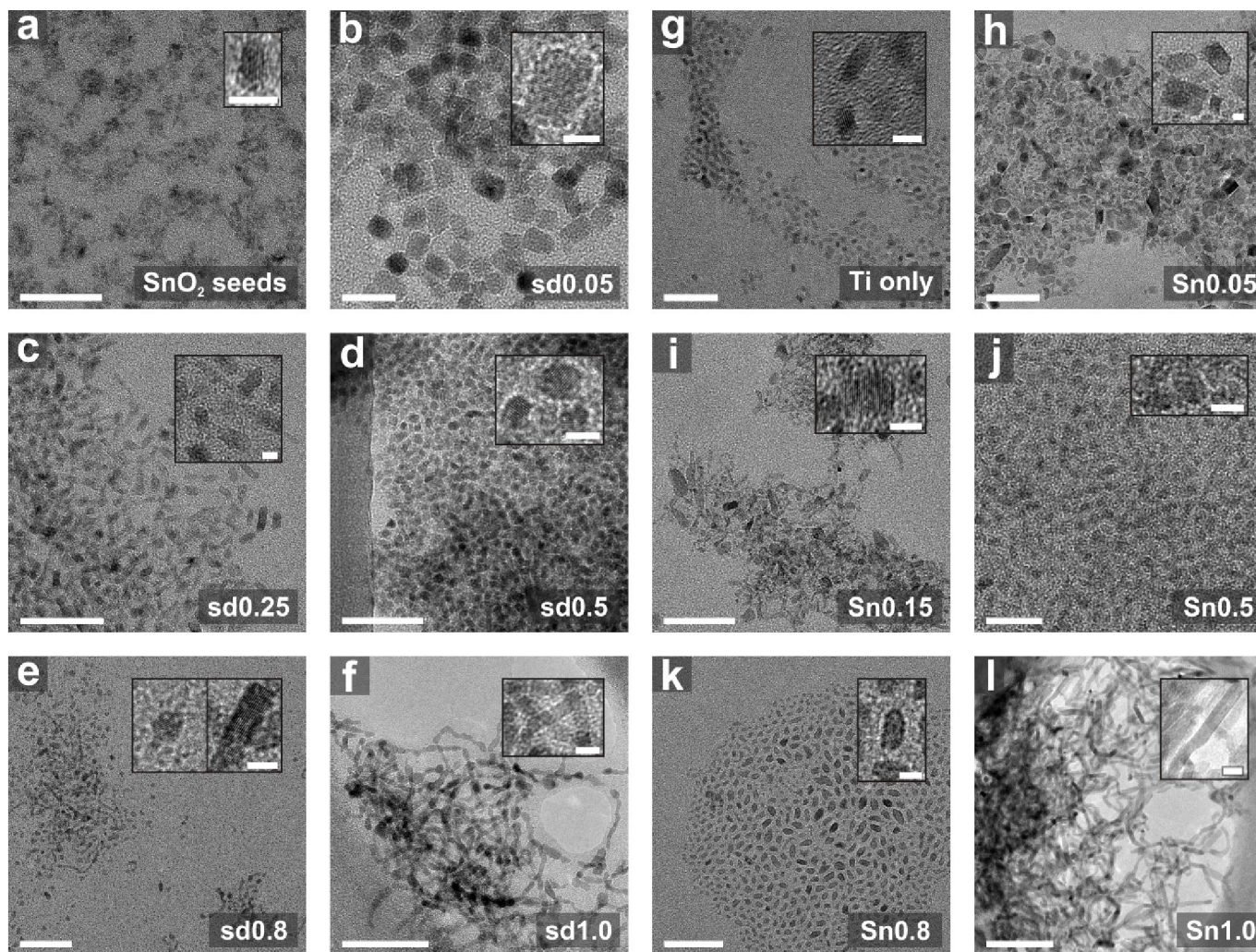
Figure 5.5. Representative TEM images for samples prepared using the seeded-growth method (b–f) and the *in situ* SnCl$_4$ nucleation method (h–l). The as-synthesized SnO$_2$ NP seeds (a) and pure TiO$_2$ NPs (sd/Sn0; g) are included for comparison. Large scale bars indicate 50 nm for all images. Scale bars are 5 nm for the insets, which show continuous lattice fringes across the particles.

Samples synthesized from molecular $SnCl_4$ and $Ti(O\text{-}i\text{-}Pr)_4$ precursors were also imaged. The $\chi_{Sn} = 0.05$ sample (Figure 5.5h) is polydisperse ($d_{avg,Sn0.05} = 8.0 \pm 3.3$ nm) with larger prismatic anatase particles visible amid a mass of smaller particles. The $\chi_{Sn} =$ 0.15 sample (Figure 5.5i) is also polydisperse, but with a smaller average particle size and standard deviation ($d_{avg,Sn0.15} = 4.5 \pm 1.5$ nm). Lattice fringes measured for this sample can be attributed to both the TiO_2 anatase (101) and rutile (110) sets of planes, which is consistent with the appearance of both sets of reflections in the XRD pattern. At $\chi_{Sn} = 0.5$ (Figure 5.5j), particles with less well-defined facets and increased monodispersity with the rutile structure are observed ($d_{avg,Sn0.5} = 3.2 \pm 0.6$ nm). At $\chi_{Sn} =$ 0.8 (Figure 5.5k), some of the particles begin to elongate, increasing polydispersity ($d_{avg,Sn0.8} = 4.5 \pm 1.2$ nm). Imaging of the lattice fringes of the rutile (110) planes indicate particle elongation orthogonal to the [110] direction. In the absence of Ti-containing precursor ($\chi_{Sn} = 1.0$), SnO_2 wires are formed (Figure 5.5l). The average wire diameter was measured to be 3.4 ± 0.6 nm. The average wire length is difficult to determine due to agglomeration on the TEM grid. Lattice fringes measured for the crystalline SnO_2 wires indicate wire growth orthogonal to the [110] direction.

Solid-State ^{119}Sn MAS NMR

Solid-state ^{119}Sn magic angle spinning (MAS) NMR spectra were collected for the as-prepared sd0.5 and Sn0.5 mixed-oxide samples, and for a pure SnO_2 NP sample (Sn1.0). The normalized spectra are shown in Figure 5.6. For each spectrum, the total fitted peak area was normalized to one and the relative peak areas were determined.

The pure SnO_2 sample (Figure 5.6c) shows one ^{119}Sn resonance at -603 ppm, which is consistent with the reference value for pure SnO_2 powder (-604 ppm). The Sn0.5 spectrum (Figure 5.6a) is fit well by two peaks, one at -596 ppm with a normalized area of 0.61, and another at -635 ppm with an area of 0.39. The sd0.5 sample (Figure 5.6b) is also fit well by two peaks at -593 ppm and -640 ppm with normalized areas of 0.89 and 0.11, respectively

	peak (ppm)	norm. area	FWHM (ppm)
Sn0.5	-596	0.61	44
	-635	0.39	41
sd0.5	-593	0.89	28
	-640	0.11	30
SnO$_2$	-603	1.00	21
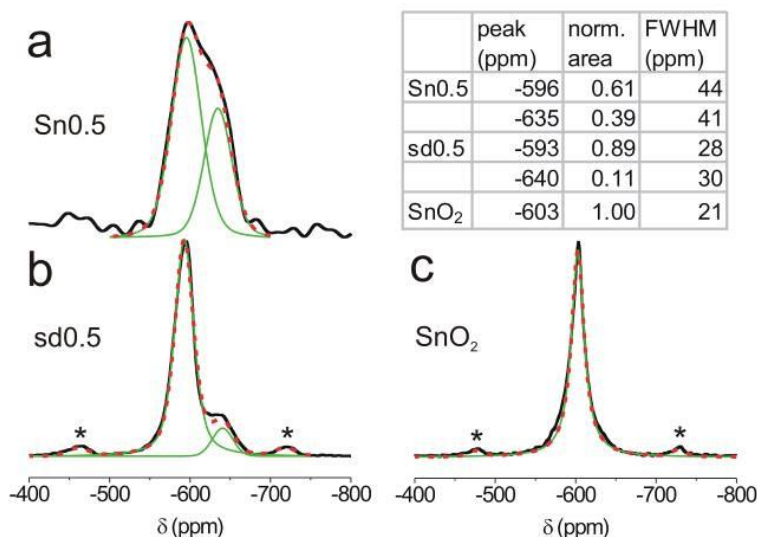
Figure 5.6. Solid-state MAS NMR spectra of Sn0.5, sd0.5, and SnO$_2$ nanoparticle powders. Black lines are the intensity normalized spectra, green lines show the ^{119}Sn resonance fits, and red dashed lines give the sums of the peak fits. Stars indicated the MAS spinning side bands (individual fits not shown, but are included in red sums of peak fits).

Discussion

The experimental results are discussed in the context of three main points. First, the morphologies and crystal structures of the SnO$_2$, TiO$_2$, and SnO$_2$–TiO$_2$ mixed-oxide products are compared to relevant previous work. Second, structural models are proposed and discussed for the SnO$_2$–TiO$_2$ mixed-oxide NP products based on experimental data for each of the synthetic methods. For the seeded-growth method, a case is presented for the formation of NPs with a core/shell architecture, compared with solid-solution NP formation in the SnCl$_4$ *in situ* method. Third, mechanisms of particle nucleation and growth under the two synthetic conditions are discussed in light of the structural models proposed.

Comparison to Previous Work: TiO$_2$, SnO$_2$, and SnO$_2$–TiO$_2$ Mixed-Oxide Products

The solvothermal synthesis procedure employed here is a modified version of that reported by Dinh et al. for anatase phase-pure TiO$_2$ NPs.[32] For the same molar ratios of Ti:OA:OM (1:3:2), Dinh et al. obtain elongated dog-bone shaped particles that appear to be approximately four times larger and are more highly faceted than particles synthesized here. Low magnification images of their particles show a polydisperse sample. As

discussed previously, slight changes in reaction conditions have been shown to markedly affect the morphologies of TiO_2 NPs. The two differences between our synthesis and that of Dinh et al. are the method of water introduction to the reaction mixture (direct vs. azeotropic vapor phase, respectively) and the Ti-containing alkoxide used (isopropoxide vs. *n*-butoxide, respectively), which were both altered in our case for convenience. Ti(O-*i*-Pr)$_4$ is complexed with oleic acid during initial mixing of the precursors, as evidenced by the change from colorless to a yellow solution. The formation of these titanium oxocarboxyalkoxide complexes has been shown to significantly reduce the susceptibility of the titanium precursor to hydrolysis.[78,79] Dinh et al. suggest that the rate of hydrolysis of the Ti-precursor influences particle size, with more available water enabling faster hydrolysis and the growth of larger particles. By adding water (36 μL) directly to the reaction mixture, we form smaller anatase TiO_2 NPs, which is contrary to what the report of Dinh et al. would predict. Our results suggest that faster initial hydrolysis forms smaller particles, likely as a result of an increased driving force for nucleation. The nature of the alkoxide group on the metal center will also affect the rate of hydrolysis, with the bulky isopropoxide expected to hinder access to the metal center by water relative to that of the straight-chain butoxide. Additionally, the nuclearity of the metal oxide clusters formed from titanium alkoxides has been shown to be influenced by the alkoxide group.[83,84] Determining which of these experimental factors dominates the hydrolysis pathway requires further experimentation.

Without the addition of Ti-precursors in the $SnCl_4$ *in situ* method, SnO_2 nanowires are obtained which, to the best of our knowledge, are the first obtained using a solvothermal organic ligand-mediated method. While agglomeration of the nanowires on the TEM grid make it difficult to estimate the wire length, the wire diameters (d_{avg} = 3.4 ± 0.6) approach the lower limits (3.4 nm – 4 nm) of those reported for wires and rods synthesized by other solution-based methods.[51,54] The ease and scalability of this synthetic method (our typical ~4 mL total volume synthesis provides ~0.5 g of material), along with the small resulting wire diameters, may make it of interest for a variety of applications, particularly sensing.[51] Current efforts include incorporating electronic dopants (e.g. F, Sb) to the SnO_2 nanowires to control conductivity.

Additionally, this work appears to be the first report of SnO_2–TiO_2 mixed-oxide nanoparticles prepared by an organic ligand-mediated solvothermal method. The particles are more uniform and have smaller average sizes than those reported for other solution-based methods (Zhao et al. obtain large polydisperse particles with diameters of 8 ± 3 nm for 10% Sn-doping).[69,71] Some of the particles also have unique core-shell geometries, which is discussed below.

Structure of the SnO_2–TiO_2 Mixed-Oxide NP Products

Nanoparticle Structure from XRD Analysis

Analysis of the XRD data can provide information regarding the organization of SnO_2 and TiO_2 in the NP structure. For example, if the oxides form a solid solution, trends in the rutile lattice parameters as a function of the solid-solution composition can be understood on the basis of Végard's law.[85] For a solid solution, Végard's law predicts a linear relationship between lattice parameter and the concentrations of the solid-solution components, and is expressed by:

$$a_{AB} = xa_A + (1-x)a_B \qquad (5.3)$$

Here, a_{AB} is the lattice parameter for the solid solution, a_A and a_B are the lattice parameters of the individual compounds, and x is the mole fraction of component A. Positive deviations from Végard's law (i.e. that the calculated lattice parameter is larger than that predicted by Végard's law) for oxide solid solutions have been documented for a variety of systems,[86-88] including experimental[65,66] and theoretical[62] $Sn_xTi_{1-x}O_2$ solid solutions. Recently, however, Ma and Navrotsky reported a calorimetric study of $Sn_xTi_{1-x}O_2$ solid solutions that obey Végard's law.[67] For the XRD patterns in Figure 1, d-spacings for the rutile (110) and (101) reflections were calculated (see Table 5.1). Assuming the formation of solid-solution particles that obey Végard's law, theoretical d-spacings for these reflections were calculated from the following relationship for the tetragonal rutile lattice:

$$\frac{1}{d^2} = \frac{\left(h^2 + k^2\right)}{a^2} + \frac{l^2}{c^2} \qquad (5.4)$$

where a and c are the lattice constants of the solid-solution phase (given by eq. 5.3 based on the amount of Sn-containing precursor in each sample). Figure 5.7 shows a graphical comparison of the d-spacings based on experimental measurement and those as predicted

for an ideal system obeying Végard's law. Deviations of the experimental data from the ideal Végard's law predictions indicate inhomogeneities in the $Sn_xTi_{1-x}O_2$ solid solutions or the influence of lattice strain, such as would be expected due to a $(SnO_2)_x/(TiO_2)_{1-x}$ core/shell structure. Figure 5.7a shows that rutile samples from the *in situ* $SnCl_4$ nucleation method follow Végard's law, indicating the formation of a rutile $Sn_xTi_{1-x}O_2$ solid solution, consistent with our initial hypothesis. These results suggest that Sn is also being incorporated into the anatase phase. The Sn0.05 and Sn0.09 samples contain approximately 42% and 61% weight rutile, respectively, which means that a significant amount of inorganic material crystallizes in the anatase phase for these samples. If the anatase phase contained no SnO_2, we would expect to see positive deviations from Végard's law for the rutile phase in these samples, as the true value of χ_{Sn} for the rutile phase would be higher than expected (i.e. SnO_2 would be concentrated in the rutile phase). Systematic variation in the *d*-spacing calculated from the anatase (101) reflections is not obvious, however Figure 5.7a does show a slight increase in the anatase (101) *d*-spacing for these samples, which could be the result of substitution of larger Sn^{4+} ions into Ti^{4+} lattice positions. A large shift in anatase XRD peak positions is not necessarily expected for low Sn-incorporation, as the anatase crystal structure is less dense than the rutile structure and thus might accommodate Sn^{4+} ions without significant lattice expansion. This is consistent with other reports of Sn-doped anatase TiO_2, where the anatase reflections were found to shift very little, if at all (i.e. the magnitude of the measured shift is within measurement error), with Sn-doping.[69-72,89]

In contrast to NPs obtained from the *in situ* $SnCl_4$ method, samples obtained from the seeded-growth method (Figure 5.7b) display a clear positive deviation from Végard's law. For other $Sn_xTi_{1-x}O_2$ systems, some examples of positive deviations from Végard's law have been reported.[65,66] However, in these cases the deviation is positive for all samples in the series, with the magnitude of the deviations smallest near the end points (i.e. at $\chi = 0$ and $\chi = 1.0$) and largest near $\chi = 0.5$ (i.e. with a "bowed" shape). For our samples, the magnitude of deviation is larger for small values of χ_{sd} and gradually decreases as χ_{sd} increases.
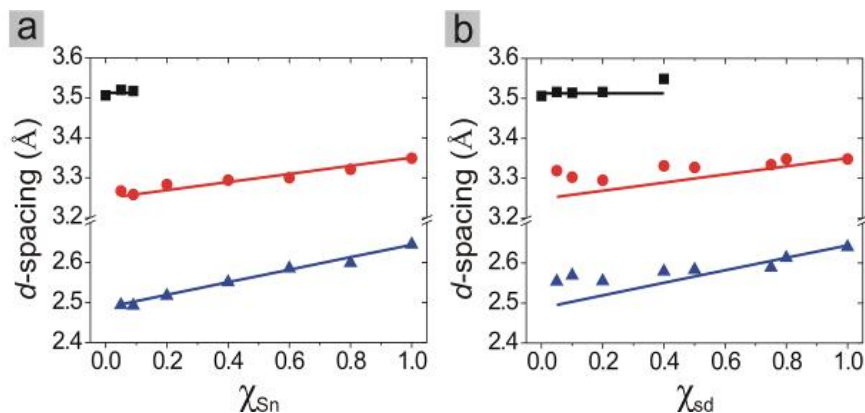
Figure 5.7. Comparison of experimental data to Végard's law for the *in situ* nucleation method (a) and the seeded-growth method (b). Experimental data points (symbols) are plotted on the same axes as ideal Végard's law predictions (lines). Each set of symbols and their corresponding line indicates a different XRD reflection as follows: squares (black) = anatase (101); circles (red) = rutile (110); triangles (blue) = rutile (101). The same data is presented in numerical form in Table 5.1.

We propose that these systematic deviations from Végard's law are due to the formation of particles with a $(SnO_2)_x/(TiO_2)_{1-x}$ core/shell structure. Based on the similarities in lattice constants (SnO_2–TiO_2 fractional lattice mismatch,[90] $f_a = 0.03$; $f_c = 0.07$), SnO_2 seeds in solution should serve as a nucleation site for rutile TiO_2 growth. The strain in the crystal lattice caused by a core/shell architecture where there is lattice mismatch has been shown to shift the position of the Bragg reflections towards that of the pure shell material for CdSe/CdS,[91,92] CdS/ZnS,[93] CdSe/ZnS,[94] and InAs/InP[95] core/shell NPs. Dabbousi et al. show that the magnitude of the shift in the Bragg reflection directly correlates to the shell layer thickness, with thicker shells shifting the reflections closer to that of the pure shell material.[94] Likewise, Ghosh et al. show that for very thin shell layers (i.e. $LaPO_4$:Er/Yb core/shell particles with 1 mol % Yb), the magnitude of the shift is small, and in fact closely resembles that expected for a solid-solution system.[96] For our samples, high seed concentrations show the smallest deviations from Végard's law, which is consistent with the formation of thin rutile TiO_2 shells on the rutile SnO_2 seeds. We expect the shells to be thinner at high seed concentrations, as available seed nuclei are abundant compared to the amount of Ti-precursor. At low seed concentrations, we expect thicker TiO_2 shells to grow. We therefore expect that a decrease in shell thickness with increasing seed concentration will result in a shift in the rutile reflections towards values for pure SnO_2. The data shown in Figure 5b are consistent with this interpretation.

Furthermore, even at the lowest seed concentration where the rutile phase becomes detectable (χ_{sd} = 0.1), the reflection positions do not approach those of pure rutile TiO_2, as is the case in the $SnCl_4$ *in situ* method. This suggests that even at low seed concentrations, the overall contribution of SnO_2-induced strain on the positions of the rutile reflections is significant.

Solid-State ^{119}Sn MAS NMR as a Probe for Core/Shell vs. Solid-Solution Structures

Solid-state NMR provides a probe for local structure. The ^{119}Sn MAS NMR data collected for samples sd0.5, Sn0.5, and Sn1.0 was compared to previous work on $Sn_xTi_{1-x}O_2$ bulk powders to better understand the differences between the NPs obtained by the two methods investigated here. Kulshreshtha et al.[97] studied a series of bulk $Sn_xTi_{1-x}O_2$ ($0.0 \leq x \leq 1.0$) powder samples by ^{119}Sn MAS solid-state NMR and found that with decreasing values of x (i.e. higher Ti content), several additional Sn resonances were observed in the region of δ = -630 to -690 ppm. In pure rutile SnO_2, the Sn^{4+} nuclei are surrounded by ten Sn^{4+} cations as their next-nearest neighbors and one ^{119}Sn resonance is observed in the NMR spectra at δ = -604 ppm. In the mixed-oxide samples, the authors attribute the most intense peaks to those Sn^{4+} nuclei surrounded by ten Sn^{4+} cations as next-nearest neighbors, and the additional lower-intensity peaks at more negative chemical shifts to those Sn^{4+} nuclei with varying numbers of Ti^{4+} as their next-nearest neighbors.

For a constant value of x, we expect to observe significant differences in the ^{119}Sn NMR spectra for particles obtained from the two synthetic methods. For the solid-solution NPs, we expect to observe similar results to those reported for the bulk homogeneous mixtures. For a core/shell NP structure, Sn^{4+} nuclei in the core would still have ten Sn^{4+} next-nearest neighbors, and we expect this peak to have a much larger integrated intensity than that for the Sn^{4+} nuclei close to the core/shell interface or mixed with TiO_2.

For their bulk $Sn_{0.5}Ti_{0.5}O_2$ sample, Kulshreshtha et al. observe two main ^{119}Sn resonances at -591 ppm and -647 ppm, with relative peak areas 0.62 and 0.38, respectively. As expected, these correspond well to the peak positions (-596 ppm and -635 ppm) and relative areas (0.61 and 0.39) obtained from deconvolution of the $Sn_xTi_{1-x}O_2$ Sn0.5 solid-solution NP sample spectrum (Figure 5.6a).

The NMR spectrum obtained for the sd0.5 sample (Figure 5.6b) is different from that for the Sn0.5 sample, and is consistent with a core/shell structure for the sd0.5 particles. The peak positions for the sd0.5 sample (-593 ppm and -640 ppm) are consistent with the $Sn_{0.5}Ti_{0.5}O_2$ sample of Kulshreshtha et al., while the relative areas, now 0.89 and 0.11 respectively, are closer to those determined for the reported bulk $Sn_{0.8}Ti_{0.2}O_2$ sample (relative areas 0.88 and 0.12). We attribute the larger intensity peak to Sn^{4+} in the pure SnO_2 core and the small intensity peak to Sn^{4+} cations at the $(SnO_2)_x/(TiO_2)_{1-x}$ core/shell interface. This interpretation is supported by a simple structural model of an ideal spherical core/shell particle with a diameter of 4.4 nm (equivalent to the average diameter for the sd0.5 samples determined from TEM). For such a particle with an overall composition of $Sn_{0.5}Ti_{0.5}O_2$, we estimate a core diameter of 3.4 nm (which is consistent with the average SnO_2 seed size) and a shell thickness of 0.5 nm (based on the densities and mole fractions of the pure oxides). From this model, we estimate that ~ 25% of Sn^{4+} atoms would be exposed to the core/shell interface (assuming [100] termination), consistent with the experimental observation that the low intensity ^{119}Sn resonance at -640 ppm in the sd0.5 NMR spectrum is ~ 20% the intensity of the higher intensity resonance. Additionally, the absence of a set of pure SnO_2 reflections in the XRD pattern is further evidence for the absence of isolated SnO_2 particles (i.e. without a TiO_2 shell). However, we cannot conclusively rule out the possibility of a small degree of mixing of the two oxides in the NP core/shell, which will be discussed below.

Nucleation and Growth of SnO₂–TiO₂ Mixed-Oxide NPs

NP Growth/Final Structure as It Relates to Sn-Containing Precursor

We propose a simple model for the nanoparticle structure obtained from the two synthetic methods, which is shown in Figure 5.8. In this model, the concentration of the Sn-containing precursor determines the crystal phase of the products, with low initial $\chi_{sd/Sn}$ (i) giving a mixture of anatase and rutile products, and high initial $\chi_{sd/Sn}$ (ii) yielding pure rutile products. Figure 5.8a shows this model for $Sn_xTi_{1-x}O_2$ solid-solution formation for the *in situ* nucleation method. The Sn and Ti nuclei are evenly distributed in the reaction mixture, and, at low χ_{Sn}, Sn nuclei are incorporated into both the rutile and anatase phases. The XRD data in Figure 5.7a are consistent with this model, as the rutile reflections shift in accordance with Végard's law, even for samples rich with anatase.

116
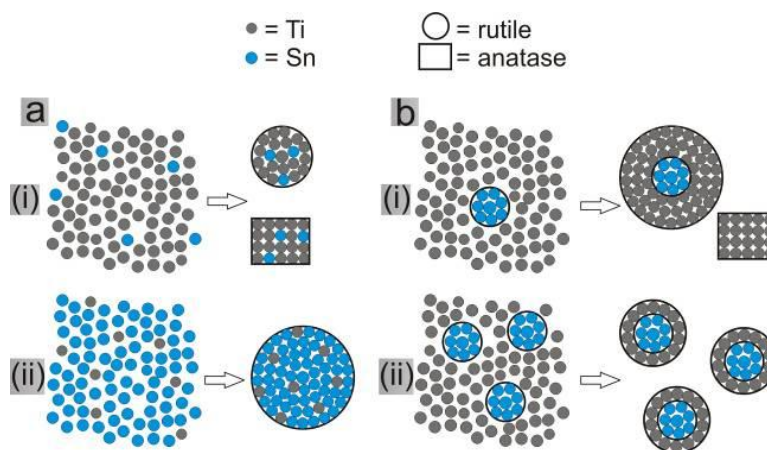
Figure 5.8. Model depicting nanoparticle structure in the SnCl$_4$ *in situ* nucleation method (a) and the seeded-growth method (b), at low (i) and high (ii) Sn-precursor concentrations. Explanation of the figure is contained in the text.

The structural model for the seeded-growth method is shown in Figure 5.8b. At low seed concentrations, some anatase TiO$_2$ nucleates and grows, as there are not enough SnO$_2$ seed nuclei present to accommodate all of the Ti-precursor. Above a threshold seed concentration, the amount of available rutile SnO$_2$ nuclei is sufficient to accommodate all of the Ti-precursor, and anatase nucleation ceases. The stability of the seeds under the reaction conditions is a critical factor in determining whether other nucleation and growth processes also occur. If the seeds are stable during the course of the reaction, we expect the sd1.0 sample, i.e. seeds treated solvothermally without Ti(O-*i*-Pr)$_4$, to resemble the as-synthesized seeds. Comparing the TEM images in Figure 3a for the as-synthesized SnO$_2$ seeds to Figure 5.5f for the sd1.0 sample, it is clear that significant restructuring of the seeds takes place under the reaction conditions. The TEM images for the sd1.0 sample show beaded structures, where the beads are crystalline and approximately the same size as the as-synthesized seeds. This restructuring is discussed below.

Evidence of NP Restructuring by Oriented Attachment – Implications for the Proposed Growth Model

Figure 5.9a shows magnified images of three representative crystals from the sd1.0 sample. The lattice fringes, which originate from the rutile (110) set of planes, run the length of the crystals, even across what appear to be kinks in the growing crystal (indicated by arrows in the Figure). The irregular morphology of the wires formed in the

117

sd1.0 sample suggests particle fusion by an oriented attachment mechanism. Lee et al. expose small, spherical SnO_2 NPs to hydrothermal conditions at 200°C for 24 hours and also discover evidence of oriented attachment.[98] The authors show the formation of elongated and irregularly shaped particles which are similar to our results.

All lattice fringes we measure for these particles indicate anisotropy orthogonal to the [110] direction. Calculations show that the rutile SnO_2 (001) surface is high in energy, following the trend (110) < (010) < (101) < (001),[64] and SnO_2 wires are known to grow preferentially in this direction.[51,53,54] Thus, oriented attachment along the [001] direction is consistent with our experimental findings.

For comparison, Figure 5.9b shows three representative particles found in the Sn1.0 sample. The irregular shape of these particles coupled with the single-crystalline structure also suggests that oriented attachment is the mechanism for wire formation under the reaction conditions. This finding implies that the process of SnO_2 nanoparticle nucleation and growth precedes nanowire formation by oriented attachment. Furthermore, observation of oriented attachment in both synthetic methods implies that this growth mechanism occurs after the nucleation process is completed in the seeded-growth method as well. This implies, along with the visible beaded-structures, that the SnO_2 NP seeds are not completely dissolved under the reaction conditions.

For the seeded-growth method, the model in Figure 5.8b describes the extreme case where the SnO_2 NP seeds are completely stable under the reaction conditions. While all our experimental data for the seeded-growth method support the core/shell hypothesis, we were not able to directly confirm the core/shell structure by TEM.[*] The other extreme is the case where the seeds completely dissolve before any TiO_2 forms (cf. Figure 6a). In this case, we would expect a solid solution to form and to observe XRD and ^{119}Sn NMR results for the seeded-growth samples similar, if not identical, to those of the $SnCl_4$ method. This is not consistent with our data. Alternatively, some dissolved SnO_2 could be incorporated into the TiO_2 shell, giving $SnO_2/Sn_xTi_{1-x}O_2$ core/shell NPs where the core is pure SnO_2 and the shell is a solid solution of the two oxides. The data we have collected

---

[*] In an attempt to confirm the core/shell structure, EDX line scans for single particles were performed on a FEI-Titan 80-300 TEM. However, these ligand-protected particles lacked the necessary stability under the 300 keV beam to collect EDX data sufficient to extract meaningful and reproducible analyses.
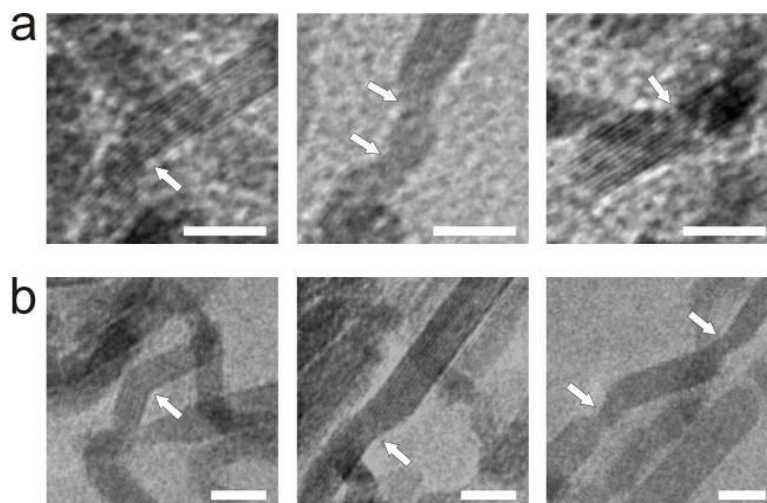
Figure 5.9. (a) TEM images collected for the sd1.0 sample highlighting three irregularly shaped nanocrystals. Lattice fringes corresponding to the (110) planes are visible along the length of the particles, spanning irregularities in particle shape indicated by white arrows. The sizes of the individual segments of the irregular crystals are on the order of the size of the original SnO_2 NP seeds, suggesting preferential oriented attachment orthogonal to the [110] direction. (b) TEM image of the Sn1.0 sample, also suggesting that oriented attachment is occurring under the reaction conditions. All scale bars are 5 nm in length.

could be consistent with this situation, and some mixing of the oxides to give a $SnO_2/Sn_xTi_{1-x}O_2$ core/shell structure cannot be conclusively ruled out.

Nucleation of NPs with the Rutile Structure – Kinetic vs. Thermodynamic Control

While the models presented in Figure 5.8 are consistent with the experimental data with respect to the growth and final structure of the NPs, they do not directly address solid-solution versus core/shell particle nucleation. Two possible pathways for NP nucleation are presented schematically in Figure 5.10. In the first case, we consider what we term "thermodynamic Model A" (Fig. 5.10a), where $Sn_xTi_{1-x}O_2$ forms by crystallization of the solid solution. Based on surface energetics and corroborated by experimental data, the pure TiO_2 anatase phase is more stable (i.e. lower energy) for small nanoparticles than the rutile phase.[99] The magnitude of this energy stabilization is likely small, as many methods yield NPs of both phases. For SnO_2, the rutile phase is thermodynamically preferred in both the bulk and the nanoscale regime. For low Sn concentrations, the solid solutions phase segregate, as the relative energies of the anatase and rutile $Sn_xTi_{1-x}O_2$ are likely similar. However, above a certain χ_{Sn}, formation of the

119

anatase phase becomes increasingly energetically unfavorable, and only the rutile phase is observed. Our data for the *in situ* SnCl$_4$ nucleation method support thermodynamic Model A, indicating that the presence of Sn^{4+} in the reaction from the SnCl$_4$ precursor changes the overall thermodynamics of the NP nucleation/growth process.
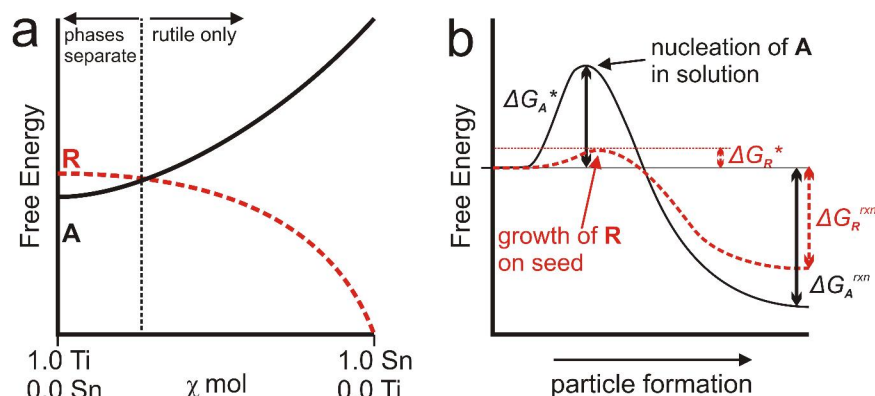

Figure 5.10. Schematic free energy diagrams for NP nucleation in this study as described in the text. R and A denote rutile and anatase, respectively. (a) Thermodynamic Model A for solid-solution NP nucleation. (b) Kinetic Model B for seeded nucleation.

Alternatively, we also consider a "kinetic Model B" (Fig. 5.10b), where particle nucleation (kinetics) controls the final structure. From a classical nucleation and growth perspective, a critical particle size, D^*, must be reached (nucleation) before the particle surface is stable enough to facilitate growth.[100] On a plot of Gibbs free energy, G, vs. particle size, the energy required to complete anatase nucleation is given by the activation barrier ΔG_A^*. If SnCl$_4$ reacts more quickly than Ti(O-*i*-Pr)$_4$, small SnO$_2$ seed clusters could form *in situ*. The presence of pre-formed SnO$_2$ nuclei in solution will lower the activation barrier for particle growth, providing a more kinetically favorable pathway for solid solution formation to occur. Since SnO$_2$ adopts the rutile structure, the solid solution growing from these nuclei will adopt the rutile structure. Over time, some Ti-precursor may inevitably nucleate anatase crystals if inorganic precursors are still available in solution. Anatase nucleation will likely cease above a threshold value of χ_{Sn}, where there are sufficient SnO$_2$ nuclei to accommodate all of the Ti-precursor. Whether or not Model B can be conclusively ruled out as the mechanism for the *in situ* nucleation method will require further investigation.

120

Model B also applies to the seeded-growth system. The presence of pre-formed SnO_2 seeds enables hetero-epitaxial rutile TiO_2 growth by reducing the energy barrier required for particle nucleation, and thus altering the kinetics of particle growth (cf. Fig. 5.10b) to generate rutile NPs with core/shell architectures. The competing anatase nucleation process is more energy intensive than epitaxial rutile shell growth, and if the concentration of seed templates is sufficient, the growth process dominates the nucleation of new particles.

Conclusions

We report the solvothermal synthesis of rutile SnO_2–TiO_2 mixed-oxide nanoparticles by two different methods. By using $SnCl_4$ as the tin-containing precursor, solid-solution $Sn_xTi_{1-x}O_2$ NPs are formed by an *in situ* nucleation method. For $SnCl_4$ concentrations above $\chi_{Sn} = 0.2$, XRD analysis shows that the products contain only the rutile crystal phase. The anatase to rutile phase transformation correlates with the increasing $SnCl_4$ concentration, and we propose a model for particle growth where Sn^{4+} in the lattice lowers the free energy of the rutile solid solution relative to the anatase phase. Furthermore, by adjusting the $SnCl_4$ concentration, we demonstrate tunability of solid-solution NP morphologies and crystal lattice parameters over the entire region studied ($0 \leq \chi_{Sn} \leq 1$). These well-defined NPs with tunable lattice constants could be useful as scaffolds for growth of more complex nanoscale materials, which we are currently investigating. We also report a gram-scale solution-based method for preparation of SnO_2 nanowires with diameters < 5 nm that may be useful for applications such as gas sensing. We are currently investigating the integration of these nanowires into surface-attached assemblies for electrochemical applications, as well as the electronic doping of the nanowires for use as high-surface-area transparent conductive metal oxides.

In a related set of experiments, we used pre-formed SnO_2 NP seeds to generate $(SnO_2)_x/(TiO_2)_{1-x}$ core/shell NPs, whose core/shell structure is supported by XRD, TEM, and solid-state ^{119}Sn NMR experiments. XRD results show a systematic shift of the rutile Bragg reflections to lower 2θ, with positive deviations from Végard's law. By TEM, we observe evidence of oriented attachment of the SnO_2 seeds under the reaction conditions, which demonstrates the stability of the as-prepared seeds during solvothermal treatment.

Solid-state ^{119}Sn NMR analysis show significant differences in the spectra for Sn$_{0.5}$Ti$_{0.5}$O$_2$ samples prepared by the two methods, supporting the formation of nanoparticles with core/shell architectures in the seeded-growth method.

A fundamental aspect of this study is the demonstration that nanoparticle growth and nucleation in the SnO$_2$-TiO$_2$ system can be controlled by changing the method of Sn-precursor introduction. These findings have uses in the design of complex oxide-based functional nanoparticles. We demonstrated that organic-ligand-mediated syntheses are effective for controlling the morphology of SnO$_2$-TiO$_2$ mixed-metal oxide NPs, and the application of this synthetic method in other mixed-metal oxide systems should be possible.

CHAPTER VI

CONCLUSIONS AND OUTLOOK

Portions of this chapter were previously published as Trotochaud, L; Boettcher, S.W. "Precise Oxygen Evolution Catalysts: Status and Opportunities" *Scripta Materialia*, **2014**, *74*, 25-32. L.T. wrote the paper, performed the experimental work, and made the figures. S.W.B. was the principal investigator and provided editorial assistance.

Summary and Conclusions

The work in this dissertation addressed key knowledge gaps in the field of OER catalysis. The work in Chapter II enabled for the first time direct side-by-side quantitative comparisons of the OER activity of a variety of transition metal oxides. The solution-based deposition method we developed can be easily extended to other important heterogeneous electrocatalyst systems where the ultra-thin-film geometry could be useful for side-stepping problems associated with measurements on thick, poorly-defined materials. We were initially surprised to find no synergistic effect on catalyst activity for the mixed-metal $Ni_{1-y}Co_yO_x$ catalysts, although in retrospect, the effect of Fe impurities on the activity of these catalysts is probably quite significant and would be consistent with the activity increase simply with Ni (and thus Fe) content that we observed. A rigorously Fe-free investigation of the OER activity of the $Ni_{1-x}Co_xOOH$ oxyhydroxides would be an interesting area for future work, and work is already underway to explore the electrochemical behavior and catalytic activity of the $Co_{1-x}Fe_x(OH)_2/Co_{1-x}Fe_xOOH$ system.[1]

The work in Chapter II also set the stage for the research described in Chapters III and IV. While Chapter II focused solely on the catalytic and structural properties of the catalysts, Chapter III delved into the significance of parasitic optical absorption by the catalysts. The "opto-catalytic" efficiency term described in this chapter explicates the trade-off between parasitic optical absorption and lowered overpotential as the thickness of the catalyst layer is increased on top of a semiconductor photoanode. The results of this work predict a sub-nm optimal thickness for optically-absorbing catalysts, even when highly active. More recent work in our group shows that the simple description of the

catalyst/semiconductor interface employed in this model composite photoanode may not be directly applicable to some catalysts, particularly catalysts which are fully ion and electrolyte permeable (i.e. "adaptive" semiconductor/catalyst junctions).[2,3] While the opto-catalytic model may need to be refined to account for the differences in these types of adaptive junctions, this work nevertheless provides a framework for first-order evaluation of different catalyst/semiconductor combinations in composite photoanodes.

We calculated in Chapter II an unprecedented OER TOF for $Ni_{0.9}Fe_{0.1}O_x$ and identified structural (and compositional) changes during the OER unique to the Ni-based oxides studied. These results clearly necessitated a more in-depth investigation of the $Ni_{1-x}Fe_xOOH$ catalyst system, which was undertaken in Chapter IV. We determined that Fe impurities incorporate readily into $Ni(OH)_2$ materials, even in the absence of an applied potential. We took advantage of the high affinity of Fe for $Ni(OH)_2$ to develop a simple method for electrolyte purification. This enabled for the first time a systematic investigation of the effects of Fe on the structural, electronic, and catalytic properties of the $Ni_{1-x}Fe_xOOH$ catalysts. We found that even though Fe increased the conductivity of the materials, it was not sufficient to solely explain the dramatic increases in OER activity. Experiments on Au substrates suggest that partial-charge-transfer between Ni and Fe may enhance the catalytic activity of the mixed-metal catalysts, however a detailed description of the electronic structure of these materials is still lacking. Experiments are currently underway to use scanning tunneling microscopy (STM) to study the electronic density of states of $Ni_{1-x}Fe_xOOH$ catalysts. Finally, we showed that the electrochemical behavior of Fe-free $Ni(OH)_2/NiOOH$ is dramatically different from previous reports. Rigorously Fe-free NiOOH is actually quite a poor OER catalyst, suggesting that most reports of highly active NiOOH-based materials most likely contain Fe. Work is currently underway to determine whether Ni-based perovskite and Ni-borate catalysts are affected by Fe impurities. With the development of the electrolyte purification method, a deeper investigation of the fundamental electrochemical behavior of $Ni(OH)_2/NiOOH$ would be an interesting area for future work. Currently, work is also underway to investigate the transition-state speciation of the Ni and Fe centers in these catalysts using electron paramagnetic resonance spectroscopy (EPR).

In Chapter V, synthetic methods were developed for Sn-Ti mixed-metal oxide nanoparticles with tunable lattice constants and morphologies. By controlling the nature of the Sn-containing precursor, we were able to make both $Sn_xTi_{1-x}O_2$ solid-solution and $(SnO_2)_x/(TiO_2)_{1-x}$ core/shell NPs. The ability to synthesize these nanoparticles over the entire compositional range with tunable lattice constants could be useful for the development of designer catalyst supports. In particular, the use of precious-metal rutile oxides such as IrO_2 and RuO_2 could be optimized by depositing thin films of these catalysts on high-surface-area conductive nanoparticle supports.

Outlook

Well-defined nanoparticle and thin film electrocatalyst materials are expanding the approach to the design of OER catalysts. The use of thin film catalysts has led to the direct quantification of a range of intrinsic catalyst activities and the confirmation of $Ni_{1-x}Fe_xOOH$ as one of the best catalysts in basic solution. The dynamic nature of OER oxide/hydroxide/oxyhydroxide electrocatalysts, however, makes them challenging to study. Our view is that, typically, as-synthesized anhydrous oxides are not the active catalyst material. Future efforts to design high-activity OER catalysts should account for the dynamic structures of these catalysts and the nearly unavoidable inclusion of Fe or other trace-metal impurities under practical operating conditions. Sophisticated techniques for the *in situ* characterization of catalyst surfaces are essential for understanding how the OER rates and mechanisms are affected by changes in structure and composition. In particular, determining the role of multiple cations in OER is important.

The future of OER electrocatalysts may be in controlled, three-dimensional, high-surface-area catalyst architectures, as envisioned in Figure 6.1. Previous experimental, theoretical, and computational studies on inorganic heterogeneous electrocatalysts have considered the electrocatalytic reaction occurring on the surface of a dense oxide. For example, Trasatti,[4,5] Nørskov and Rossmeisl,[6,7] and recently Suntivich et al.[8] relate the activity to the strength of the metal–oxygen (M–O) bond at the oxide/solution interface. However, Rossmeisl and Nørskov recognize the need for three dimensional molecular–level control (and theory) of the active site in inorganic catalysts, and conclude that it will

be very difficult to further improve the catalytic activity of planar oxides (studied by their theory) because the binding strength of the M–OH and M–OOH intermediates scale together and the formation of M–OOH is considered to be the rate determining step (as it is the most unstable intermediate).[6] A possible solution, they propose, is to find 3D molecular structures that preferentially stabilize M–OOH over M–OH. In the biological OER complex in photosystem II, the amino acid shell that surrounds the Mn_4CaO_5 cluster active site provides ligands to stabilize intermediates in the water oxidation process and to accept the protons generated by oxygen evolution.[9] The exact structures and stabilization mechanisms of such intermediates are unknown, but it is undoubtedly critical for enhanced activity of the biological catalyst compared to inorganic MnO_2 catalysts.[10]
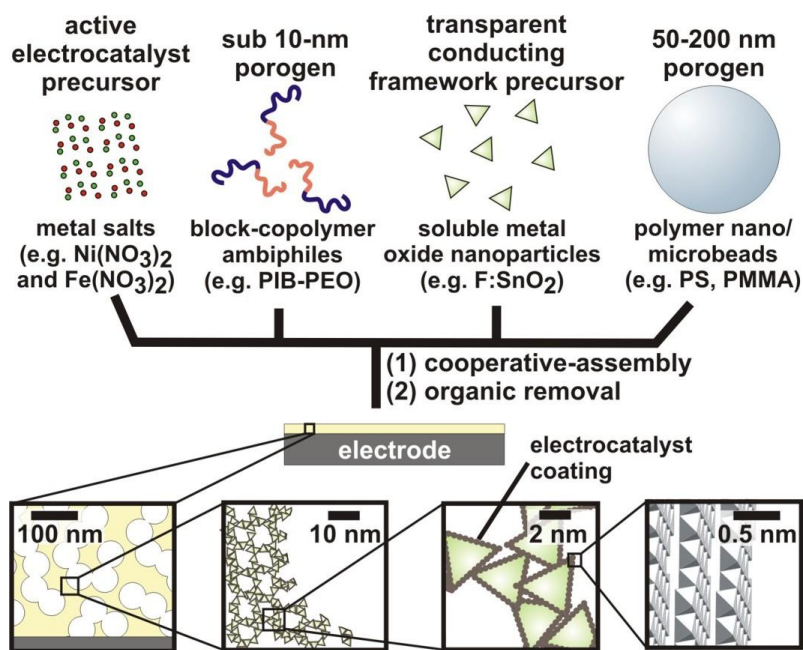
Figure 6.1. Vision of hierarchical 3D catalyst design. The layered molecular structure of the oxyhydroxide catalysts might be optimized and incorporated into hierarchical 3D catalyst structures where porosity is tuned over multiple length scales to optimize intrinsic activity as well as electron and mass transport.

The development of all-inorganic 3D catalysts with precise structures that can be tuned to stabilize different intermediates in multi-electron electrocatalysis reactions would be a major advance. The highly active layered hydrous oxide and oxyhydroxide

catalysts described here provide a starting point to consider the design of higher-order structures for OER catalysis. Work is ongoing to determine the function of the layered structure of these catalysts as it relates to their catalytic activity. Fundamental questions include: Does OER catalysis occur between the catalyst sheets or at under-coordinated edge sites? Does the sheet spacing or inter-sheet chemical environment affect the rate of the OER? Can inter-sheet spacing and chemistry be controlled and tuned to develop designer catalysts?

In combination with tuning structure on the molecular scale, 3D nano- and micro-structuring of OER catalysts could further improve practical water splitting devices by ensuring every metal center is active through electronic connection to the electrode and ionic connection to the solution, and by engineering the porosity to facilitate the escape of evolved gases (see Figure 6.1). These approaches are facilitated by progress in the design and assembly of templated functional porous architectures.[11,12] Combined with a better understanding of OER catalysts and the ability to control their active sites, methods to engineer the nano and microscale architecture of electrocatalysts should enable higher efficiencies for water-splitting devices.

APPENDIX A

MATHEMATICA WORKSHEET FOR EXTRACTION OF

CATALYST ABSORPTION

This appendix contains screenshots of an annotated Mathematica 8.0 workbook used to extract the optical absorption of a catalyst film, a_c, as described in Chapter III. The example shown here is for the NiO$_x$ catalyst. Changing the imported optical data (on Input line 31 as shown below) is the only change necessary to determine a_c values for the other catalysts. The full solution for a_c is shown at the end.
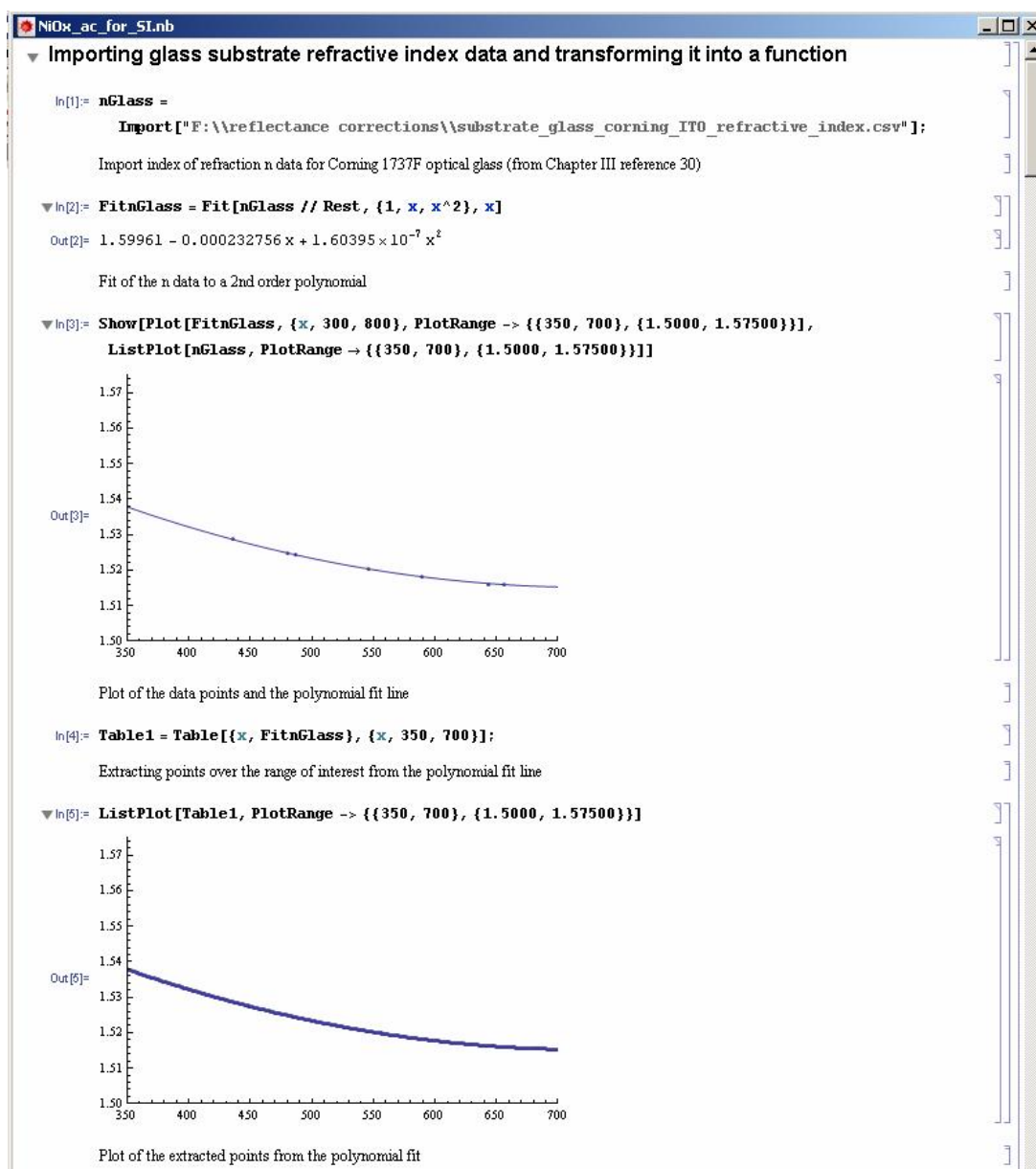
In[6]:= **ng = Interpolation[Table1]**

Out[6]= InterpolatingFunction[{{350., 700.}}, <>]

Transforms the extracted points into an interpolation function for easy mathmatical manipulations

In[7]:= **Show[Plot[ng[lambda], {lambda, 350, 700}, PlotRange -> {{350, 700}, {1.5000, 1.57500}}]]**

Out[7]=
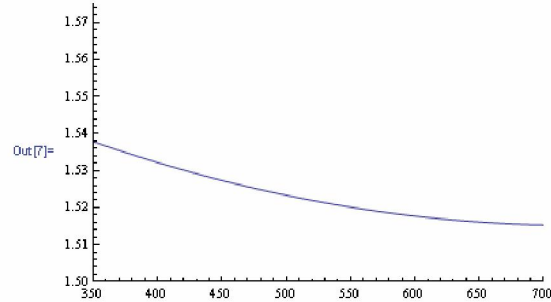
Importing ITO n and k data and transformation into functions

In[8]:= **DatanITO = Import["F:\\reflectance corrections\\ITO_SOPRA_refractive_index_n.csv"];**

In[9]:= **DatakITO = Import["F:\\reflectance corrections\\ITO_SOPRA_refractive_index_k.csv"];**

Import the n and k data for ITO (from Chapter III reference 31)

In[10]:= **nITO = Interpolation[DatanITO // Rest]**
    kITO = Interpolation[DatakITO // Rest]

Out[10]= InterpolatingFunction[{{250., 850.}}, <>]

Out[11]= InterpolatingFunction[{{250., 850.}}, <>]

Transforms ITO n and k data into interpolation functions

In[12]:= **Show[Plot[nITO[lambda], {lambda, 350, 700}]]**
    Show[Plot[kITO[lambda], {lambda, 350, 700}]]

Out[12]=

Out[13]=
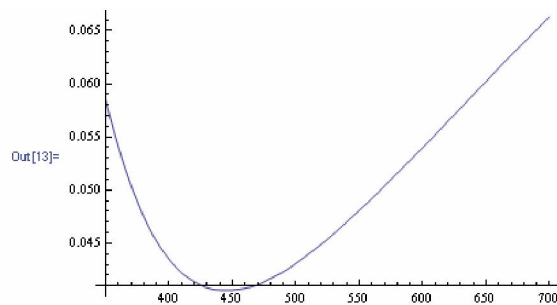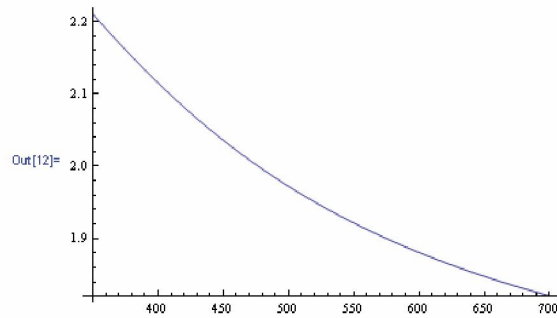
Plots of ITO n and k interpolation functions

Calculation of r2 using Fresnel equation

In[14]:= `Fresnelr2 = ((ng[lambda] - nITO[lambda])^2 + (kITO[lambda])^2) /`
`((ng[lambda] + nITO[lambda])^2 + (kITO[lambda])^2)`

Out[14]= $\big($InterpolatingFunction[{{250., 850.}}, <>][lambda]^2 +
(-InterpolatingFunction[{{250., 850.}}, <>][lambda] +
InterpolatingFunction[{{350., 700.}}, <>][lambda])$^2\big)$ /
$\big($InterpolatingFunction[{{250., 850.}}, <>][lambda]^2 +
(InterpolatingFunction[{{250., 850.}}, <>][lambda] +
InterpolatingFunction[{{350., 700.}}, <>][lambda])$^2\big)$

Insert interpolation functions into Fresnel equation as described in Chapter III equation 3.7

In[15]:= `Plot[Fresnelr2, {lambda, 400, 690}]`

Out[15]=
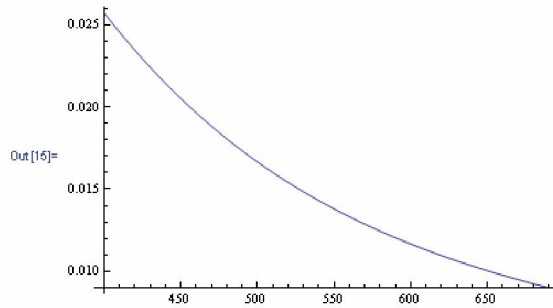
Plot of r2 over the working range of the spectrometer used in these experiments.

Entering of equations for the 5 types of optical measurements (equations 3.2-3.5) and solving for unknown variables

In[16]:= `eq1 = (1 - r2) (1 - a) (1 - r3)`

Out[16]= (1 - a) (1 - r2) (1 - r3)

T(ITO); Equation 3.2, Chapter III

In[17]:= `eq2 = (1 - r2) (1 - a) (1 - r3star) (1 - ac)`

Out[17]= (1 - a) (1 - ac) (1 - r2) (1 - r3star)

T(S); Equation 3.3, Chapter III

In[18]:= `eq3 = r + (1 - r) r`

Out[18]= r + (1 - r) r

R(B); Equation 3.4, Chapter III

In[19]:= `eq4 = r + (1 - r) r2 + (1 - r) (1 - r2) (1 - a) r3 (1 - a) + (1 - r) (1 - r2) (1 - a) (1 - r3) r (1 - a)`

Out[19]= r + (1 - r) r2 + (1 - a)^2 (1 - r) r (1 - r2) (1 - r3) + (1 - a)^2 (1 - r) (1 - r2) r3

R(ITO); Equation 3.5, Chapter III

In[20]:= `eq5 = r + (1 - r) r2 + (1 - r) (1 - r2) (1 - a) r3star (1 - a) +`
`(1 - r) (1 - r2) (1 - a) (1 - r3star) (1 - ac) r (1 - ac) (1 - a)`

Out[20]= r + (1 - r) r2 + (1 - a)^2 (1 - ac)^2 (1 - r) r (1 - r2) (1 - r3star) + (1 - a)^2 (1 - r) (1 - r2) r3star

R(S); Equation 3.6, Chapter III

In[21]:= **SS = Solve[{eq1 == TITO, eq2 == TS, eq3 == RB, eq4 == RITO, eq5 == RS}, {a, r3, r3star, RB, ac}]**

> A very large output was generated. Here is a sample of it:
>
> $$\left\{\left\{a \rightarrow \right.\right.$$
>
> $$\frac{2-2\,r-2\,r2+2\,r\,r2-TITO+2\,r\,TITO-r^2\,TITO-\sqrt{-1+r}\ \sqrt{4\,r+4\,r2-8\,r\,r2-4\,r2^2+4\,r\,r2^2-4\,RITO+4\,r2\,RITO-TITO^2+2\,r\,TITO^2-2\,r^2\,TITO^2+r^3\,TITO^2}}{2\,(1-r-r2+r\,r2)},$$
>
> $$r3 \rightarrow \frac{r+\ll 51\gg+\frac{\sqrt{-1+r}\ r\,r2\,TITO\sqrt{\ll 1\gg}}{2\,(1-r-r2+r\,r2)}}{r+r2-2\,r\,r2-r2^2+r\,r2^2-RITO+r2\,RITO},\ r3star \rightarrow \frac{r2+\ll 204\gg}{\ll 1\gg},\ RB \rightarrow 2\,r-r^2,$$
>
> $$ac \rightarrow \frac{\ll 1\gg}{2\,\left(2\,r2\,TS-2\,r^2\,TS+2\,r\,r2\,TS-4\,r2^2\,TS+2\,r^2\,r2\,TS-2\,r\,RITO\,TS+2\,r2\,RITO\,TS\right)}\right\},\ \{\ll 1\gg\},\ \{\ll 1\gg\},\ \{\ll 1\gg\}\right\}$$
>
> [Show Less] [Show More] [Show Full Output] [Set Size Limit…]

Out[21]=

Solving the system of 5 equations for each of the unknown variables a, r3, r3star, and ac (note that here we also include RB, which can be expressed in terms of r and measured directly; this will dealt with more later)

In[22]:= **Length[SS]**

Out[22]= 4

There are four sets of solutions for these variables

In[23]:= **acs = ac /. SS;**

Defining the 4 solutions for ac as "acs" to be used later

▼ Importing data from experimental measurements and transforming into functions, and solving for r

In[25]:= **DataTITO = Import["F:\\reflectance corrections\\ITO_T_Tito.csv"];**

In[26]:= **fTITO = Interpolation[DataTITO // Rest]**

Out[26]= InterpolatingFunction[{{339.56, 1021.03}}, <>]

T(ITO); Equation 3.2, Chapter III

In[27]:= **DataTS = Import["F:\\reflectance corrections\\NiOx_T_Ts.csv"];**

In[28]:= **fTS = Interpolation[DataTS // Rest]**

Out[28]= InterpolatingFunction[{{339.56, 1021.03}}, <>]

T(S); Equation 3.3, Chapter III

In[29]:= **DataRITO = Import["F:\\reflectance corrections\\ITO_rerun_back_correct.Sample.Raw.csv"];**

In[30]:= **fRITO = Interpolation[DataRITO // Rest]**

Out[30]= InterpolatingFunction[{{400., 950.}}, <>]

R(ITO); Equation 3.5, Chapter III

In[31]:= **DataRS = Import["F:\\reflectance corrections\\NiOx_Rsr.csv"];**

In[32]:= **fRS = Interpolation[DataRS // Rest]**

Out[32]= InterpolatingFunction[{{400., 800.}}, <>]

R(S); Equation 3.6, Chapter III

In[33]:= **DataRB = Import["F:\\reflectance corrections\\2_glass_both_thin.Sample.Raw.csv"];**

In[34]:= **fRB = Interpolation[DataRB // Rest]**

Out[34]= InterpolatingFunction[{{400., 950.}}, <>]

R(B); Equation 3.4, Chapter III

In[35]:= **Solve[RB == eq3, r]**

Out[35]= $\left\{\left\{r \to 1 - \sqrt{1 - RB}\right\}, \left\{r \to 1 + \sqrt{1 - RB}\right\}\right\}$

The value of r can be obtained directly from R(B); there are 2 solutions because of the square root. Which one is right?

In[36]:= **ra = 1 - Sqrt[1 - fRB[lambda]]**

Out[36]= $1 - \sqrt{1 - \text{InterpolatingFunction}[\{\{400., 950.\}\}, <>][\text{lambda}]}$

In[37]:= **rb = 1 + Sqrt[1 - fRB[lambda]]**

Out[37]= $1 + \sqrt{1 - \text{InterpolatingFunction}[\{\{400., 950.\}\}, <>][\text{lambda}]}$

Define the two solutions ra and rb and insert the collected data for R(B)

In[38]:= **Plot[ra, {lambda, 400, 700}]**
Plot[rb, {lambda, 400, 700}]

Out[38]=

Out[39]=
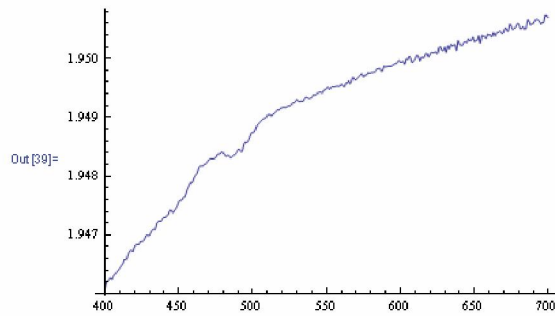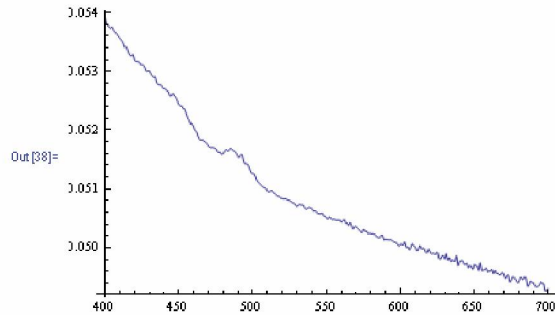
Plots of ra and rb show that only ra gives physically meaningful values for r (between 0 and 1)...

In[40]:= **r = ra**

Out[40]= $1 - \sqrt{1 - \text{InterpolatingFunction}[\{\{400., 950.\}\}, <>][\text{lambda}]}$

...thus we define r as ra

In[41]:= **facs = acs /. {TIT0 → fTIT0[lambda], TS → fTS[lambda], RIT0 → fRIT0[lambda], RS → fRS[lambda], r2 -> Fresnelr2}**

A very large output was generated. Here is a sample of it:

Out[41]=

Show Less | Show More | Show Full Output | Set Size Limit...

Finally, inserting the experimental data into the 4 solutions ("acs") we obtained previously for ac

132

In[42]:= **Plot[facs, {lambda, 400, 690}]**

Out[42]=
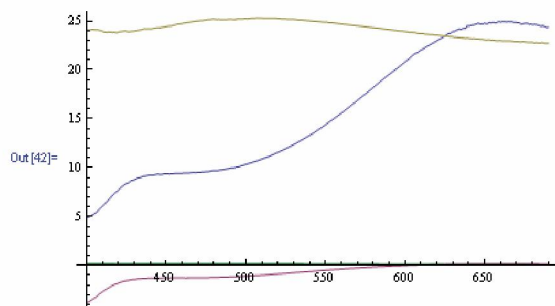
Plot of the four solutions shows that only one (in green) gives meaningful values for ac (between 0 and 1). Taking a closer look at each...

In[43]:= **Plot[facs[[1]], {lambda, 400, 690}]**

Out[43]=
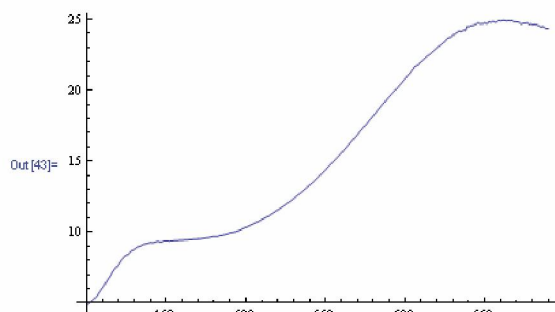
...plot of ac solution 1 (values are greater than 1),...

In[44]:= **Plot[facs[[2]], {lambda, 400, 690}]**

Out[44]=
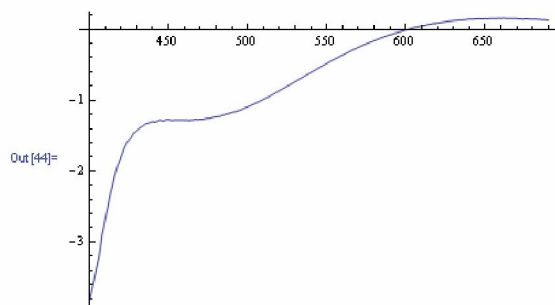
...plot of ac solution 2 (some values are negative),...

In[45]:= **Plot[facs[[3]], {lambda, 400, 690}]**

Out[45]=
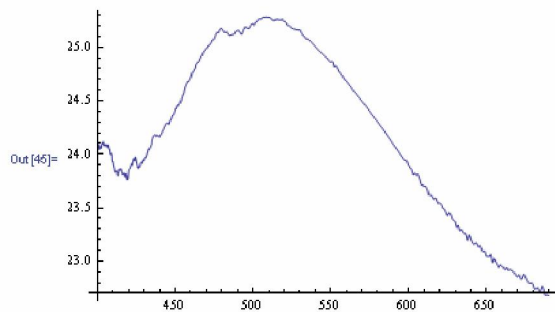
...plot of ac solution 3 (values are greater than 1),...

133

In[46]:= **Plot[facs[[4]], {lambda, 400, 690}]**

Out[46]=
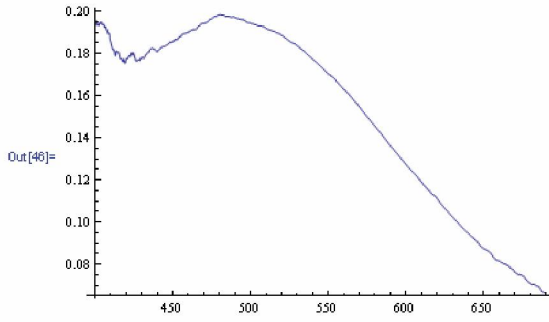
...and plot of solution 4 (values are between 0 and 1).

In[47]:= **acNiOx = facs[[4]];**

Therefore, we take value 4 as ac for this catalyst...

In[48]:= **acTable = Table[{lambda, acNiOx}, {lambda, 400, 690, 0.5}];**

...and export the data to a table for plotting.

▼ Full solution #4 for ac

▼ In[24]:= **acs[[4]]**

Out[24]= $\left(2\,r\,TIT0 - 4\,r^2\,TIT0 + 2\,r^3\,TIT0 + 2\,r2\,TIT0 - 6\,r\,r2\,TIT0 + 6\,r^2\,r2\,TIT0 - 2\,r^3\,r2\,TIT0 - \right.$

$RIT0\,TIT0 + 2\,r\,RIT0\,TIT0 - r^2\,RIT0\,TIT0 - RS\,TIT0 + 2\,r\,RS\,TIT0 - r^2\,RS\,TIT0 + \sqrt{-1+r}\ RIT0$

$\dfrac{\sqrt{4\,r + 4\,r2 - 8\,r\,r2 - 4\,r2^2 + 4\,r\,r2^2 - 4\,RIT0 + 4\,r2\,RIT0 - TIT0^2 + 3\,r\,TIT0^2 - 3\,r^2\,TIT0^2 + r^3\,TIT0^2}}{} -$

$\sqrt{-1+r}\ RS$

$\dfrac{\sqrt{4\,r + 4\,r2 - 8\,r\,r2 - 4\,r2^2 + 4\,r\,r2^2 - 4\,RIT0 + 4\,r2\,RIT0 - TIT0^2 + 3\,r\,TIT0^2 - 3\,r^2\,TIT0^2 + r^3\,TIT0^2}}{} +$

$4\,r^2\,TS - 4\,r^3\,TS + 4\,r\,r2\,TS - 8\,r^2\,r2\,TS + 4\,r^3\,r2\,TS - 4\,r\,RIT0\,TS + 4\,r^2\,RIT0\,TS +$

$\sqrt{\left(\left(-2\,r\,TIT0 + 4\,r^2\,TIT0 - 2\,r^3\,TIT0 - 2\,r2\,TIT0 + 6\,r\,r2\,TIT0 - 6\,r^2\,r2\,TIT0 + 2\,r^3\,r2\,TIT0 + RIT0\,TIT0 - \right.\right.}$

$2\,r\,RIT0\,TIT0 + r^2\,RIT0\,TIT0 + RS\,TIT0 - 2\,r\,RS\,TIT0 + r^2\,RS\,TIT0 - \sqrt{-1+r}\ RIT0$

$\dfrac{\sqrt{4\,r + 4\,r2 - 8\,r\,r2 - 4\,r2^2 + 4\,r\,r2^2 - 4\,RIT0 + 4\,r2\,RIT0 - TIT0^2 + 3\,r\,TIT0^2 - 3\,r^2\,TIT0^2 + r^2\,TIT0^2}}{}$

$+ \sqrt{-1+r}\ RS$

$\dfrac{\sqrt{4\,r + 4\,r2 - 8\,r\,r2 - 4\,r2^2 + 4\,r\,r2^2 - 4\,RIT0 + 4\,r2\,RIT0 - TIT0^2 + 3\,r\,TIT0^2 - 3\,r^2\,TIT0^2 + r^3\,TIT0^2}}{}$

$- 4\,r^2\,TS + 4\,r^3\,TS - 4\,r\,r2\,TS + 8\,r^2\,r2\,TS - 4\,r^3\,r2\,TS + 4\,r\,RIT0\,TS - 4\,r^2\,RIT0\,TS \Big)^2 -$

$4\,\Big(2\,r\,TIT0 - 4\,r^2\,TIT0 + 2\,r^3\,TIT0 + 2\,r2\,TIT0 - 6\,r\,r2\,TIT0 + 6\,r^2\,r2\,TIT0 - 2\,r^3\,r2\,TIT0 -$

$RIT0\,TIT0 + 2\,r\,RIT0\,TIT0 - r^2\,RIT0\,TIT0 - RS\,TIT0 + 2\,r\,RS\,TIT0 - r^2\,RS\,TIT0 + \sqrt{-1+r}\ RIT0$

$\dfrac{\sqrt{4\,r + 4\,r2 - 8\,r\,r2 - 4\,r2^2 + 4\,r\,r2^2 - 4\,RIT0 + 4\,r2\,RIT0 - TIT0^2 + 3\,r\,TIT0^2 - 3\,r^2\,TIT0^2 + r^3\,TIT0^2}}{} -$

$\sqrt{-1+r}\ RS$

$\dfrac{\sqrt{4\,r + 4\,r2 - 8\,r\,r2 - 4\,r2^2 + 4\,r\,r2^2 - 4\,RIT0 + 4\,r2\,RIT0 - TIT0^2 + 3\,r\,TIT0^2 - 3\,r^2\,TIT0^2 + r^3\,TIT0^2}}{} -$

$2\,r\,TS + 4\,r^2\,TS - 2\,r^3\,TS - 2\,r2\,TS + 6\,r\,r2\,TS - 6\,r^2\,r2\,TS + 2\,r^3\,r2\,TS +$

$2\,RIT0\,TS - 4\,r\,RIT0\,TS + 2\,r^2\,RIT0\,TS \Big)$

$\left(2\,r^2\,TS - 2\,r^3\,TS + 2\,r\,r2\,TS - 4\,r^2\,r2\,TS + 2\,r^3\,r2\,TS - 2\,r\,RIT0\,TS + 2\,r^2\,RIT0\,TS \right) \Big) \Big) \Big/$

$\left(2\,\left(2\,r^2\,TS - 2\,r^3\,TS + 2\,r\,r2\,TS - 4\,r^2\,r2\,TS + 2\,r^3\,r2\,TS - 2\,r\,RIT0\,TS + \right.\right.$

$\left.\left. 2\,r^2\,RIT0\,TS \right) \right)$

134

APPENDIX B

TRANSMISSION ELECTRON MICROSCOPY
PARTICLE SIZE DISTRIBUTION HISTOGRAMS

These data were previously published as Supporting Information for the publication Trotochaud, L.; Boettcher, S.W. "Synthesis of Rutile Phase $Sn_xTi_{1-x}O_2$ and $(SnO_2)_x/(TiO_2)_{1-x}$ Core/Shell Nanoparticles with Tunable Lattice Constants and Controlled Morphologies" *Chemistry of Materials*, **2011**, *22*, 4920-4930. L.T. performed the experiments and made the figures. S.W.B. was the principal investigator and provided editorial assistance.

sd0.8

average = 5.23
st. dev. = 1.85
n total = 191

particle size (nm)

Sn0

average =6.04
st. dev. = 1.06
n total = 144

particle size (nm)

Sn0.05

average =7.97
st. dev. = 3.27
n total = 300

particle size (nm)

Sn0.15

average =4.48
st. dev. = 1.48
n total = 170

particle size (nm)

Sn0.5

average =3.21
st. dev. = 0.57
n total = 136

particle size (nm)
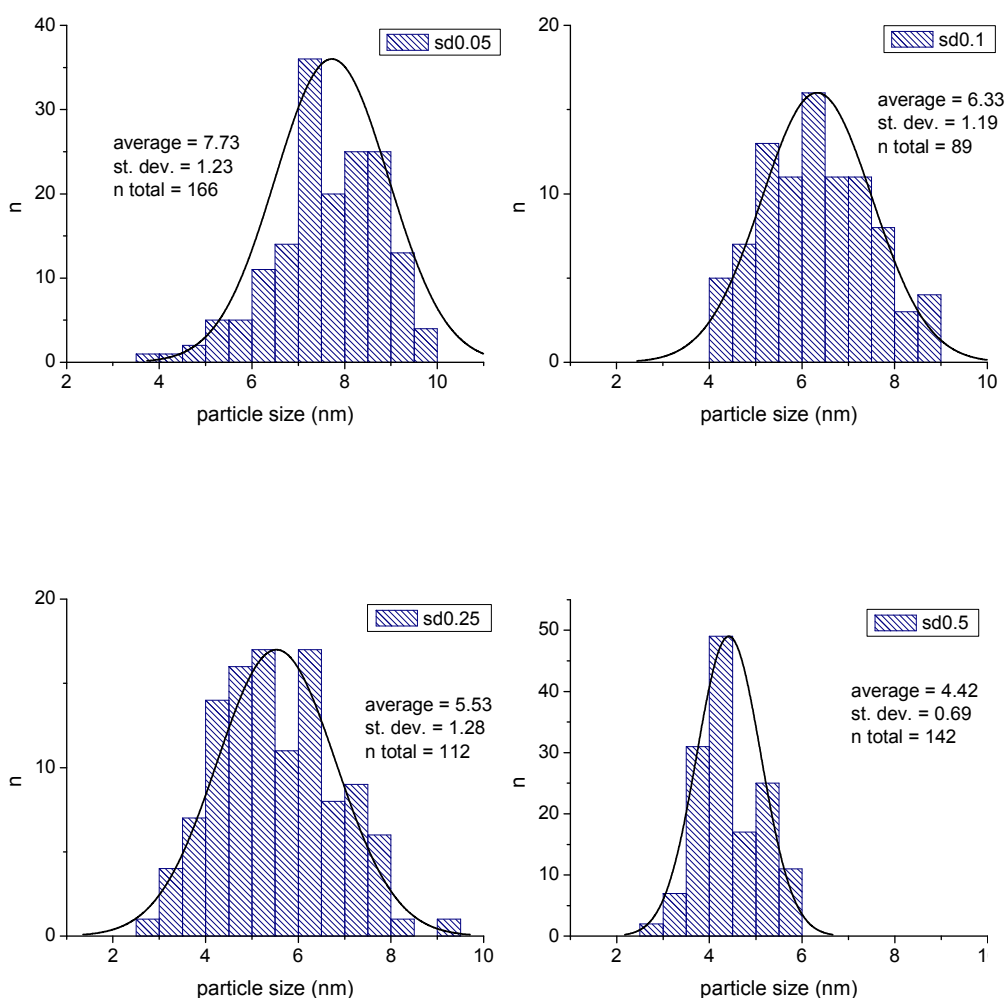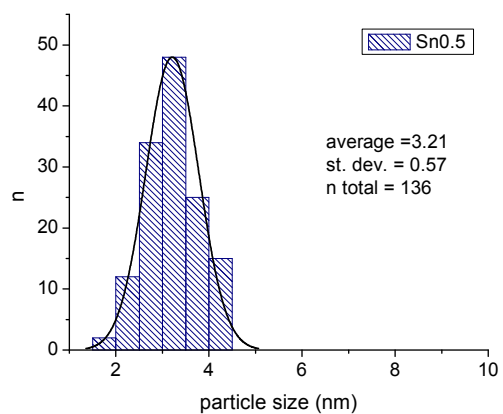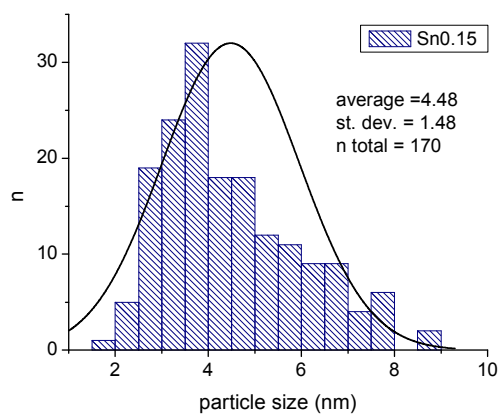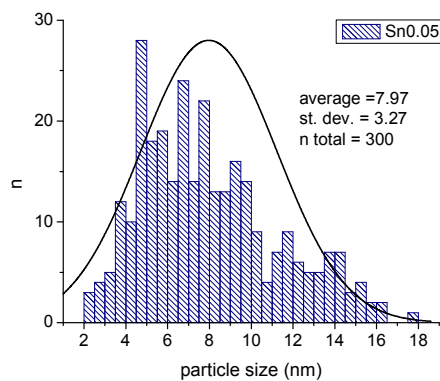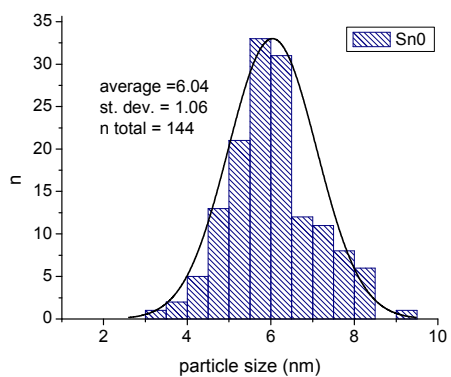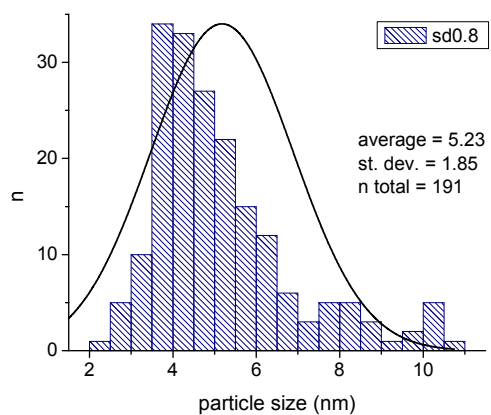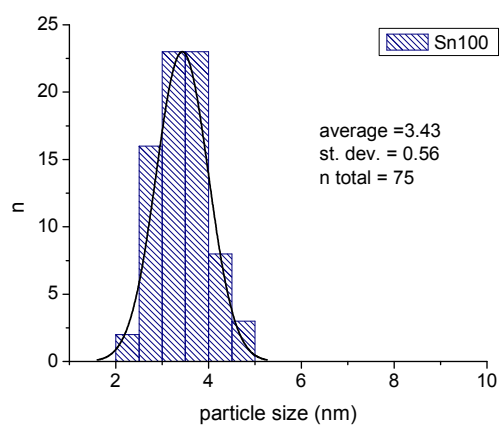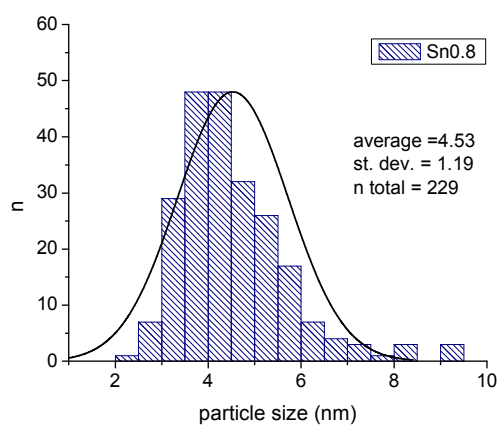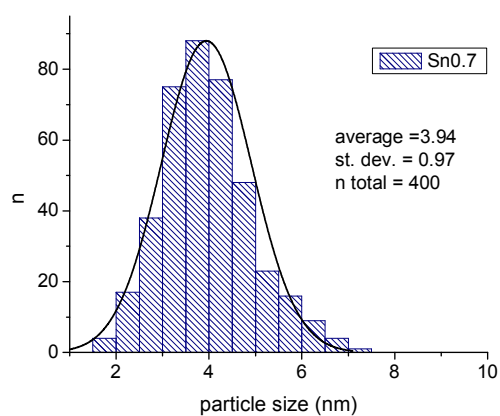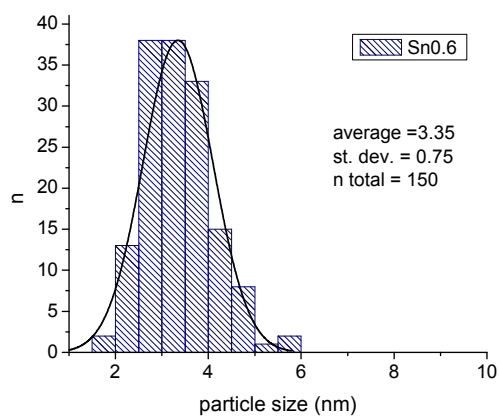
REFERENCES CITED

CHAPTER I

(1) Cook, T. R.; Dogutan, D. K.; Reece, S. Y.; Surendranath, Y.; Teets, T. S.; Nocera, D. G. *Chem. Rev.* **2010**, *110*, 6474.

(2) Lewis, N. S.; Nocera, D. G. *Proc. Natl. Acad. Sci. U.S.A.* **2006**, *103*, 15729.

(3) Walter, M. G.; Warren, E. L.; McKone, J. R.; Boettcher, S. W.; Mi, Q.; Santori, E. A.; Lewis, N. S. *Chem. Rev.* **2010**, *110*, 6446.

(4) Man, I. C.; Su, H.-Y.; Calle-Vallejo, F.; Hansen, H. A.; Martínez, J. I.; Inoglu, N. G.; Kitchin, J.; Jaramillo, T. F.; Nørskov, J. K.; Rossmeisl, J. *ChemCatChem* **2011**, *3*, 1159.

(5) Kinoshita, K. *Electrochemical Oxygen Technology*; Wiley: New York, 1992.

(6) Sivasankar, N.; Weare, W. W.; Frei, H. *J. Am. Chem. Soc.* **2011**, *133*, 12976.

(7) Trasatti, S.; Lodi, G. Oxygen and chlorine evolution at conductive metallic oxide anodes. In *Electrodes of Conductive Metallic Oxides*; Trasatti, S., Ed.; Elsevier: Amsterdam, 1981; Vol. B; p 521.

(8) Trotochaud, L.; Ranney, J. K.; Williams, K. N.; Boettcher, S. W. *J. Am. Chem. Soc.* **2012**, *134*, 17253.

(9) Smith, R. D. L.; Prévot, M. S.; Fagan, R. D.; Zhang, Z.; Sedach, P. A.; Siu, M. K. J.; Trudel, S.; Berlinguette, C. P. *Science* **2013**, *340*, 60.

(10) Smith, R. D. L.; Prévot, M. S.; Fagan, R. D.; Trudel, S.; Berlinguette, C. P. *J. Am. Chem. Soc.* **2013**, *135*, 11580.

(11) Bajdich, M.; García-Mota, M.; Vojvodic, A.; Nørskov, J. K.; Bell, A. T. *J. Am. Chem. Soc.* **2013**, *135*, 13521.

(12) Bard, A. J.; Faulkner, L. R. *Electrochemical Methods: Fundamentals and Applications*; second ed.; John Wiley & Sons: New York, 2001; p 87-136.

(13) Trasatti, S.; Petrii, O. A. *J. Electroanal. Chem.* **1992**, *327*, 353.

(14) Suntivich, J.; Gasteiger, H. A.; Yabuuchi, N.; Shao-Horn, Y. *J. Electrochem. Soc.* **2010**, *157*, B1263.

(15) Guerrini, E.; Consonni, V.; Trasatti, S. *J. Solid State Electrochem.* **2005**, *9*, 320.

(16) Hepel, T.; Pollak, F. H.; O'Grady, W. E. *J. Electrochem. Soc.* **1986**, *133*, 69.

(17) Salvador, P.; Alonso-Vante, N.; Tributsch, H. *J. Electrochem. Soc.* **1998**, *145*, 216.

(18) Crumlin, E. J.; Ahn, S.-J.; Lee, D.; Mutoro, E.; Biegalski, M. D.; Christen, H. M.; Shao-Horn, Y. *J. Electrochem. Soc.* **2012**, *159*, F219.

(19) Komo, M.; Hagiwara, A.; Taminato, S.; Hirayama, M.; Kanno, R. *Electrochemistry (Tokyo, Jpn.)* **2012**, *80*, 834.

(20) Umena, Y.; Kawakami, K.; Shen, J.-R.; Kamiya, N. *Nature* **2011**, *473*, 55.

(21) Krewald, V.; Neese, F.; Pantazis, D. A. *J. Am. Chem. Soc.* **2013**, *135*, 5726.

(22) Kanady, J. S.; Tsui, E. Y.; Day, M. W.; Agapie, T. *Science* **2011**, *333*, 733.

(23) Gao, Y.; Ding, X.; Liu, J.; Wang, L.; Lu, Z.; Li, L.; Sun, L. *J. Am. Chem. Soc.* **2013**, *135*, 4219.

(24) Kärkäs, M. D.; Åkermark, T.; Chen, H.; Sun, J.; Åkermark, B. *Angew. Chem., Int. Ed.* **2013**, *52*, 4189.

(25) Artero, V.; Fontecave, M. *Chem. Soc. Rev.* **2013**, *42*, 2338.

(26) Yin, Q.; Tan, J. M.; Besson, C.; Geletii, Y. V.; Musaev, D. G.; Kuznetsov, A. E.; Luo, Z.; Hardcastle, K. I.; Hill, C. L. *Science* **2010**, *328*, 342.

(27) Song, F.; Ding, Y.; Ma, B.; Wang, C.; Wang, Q.; Du, X.; Fu, S.; Song, J. *Energy Environ. Sci.* **2013**, *6*, 1170.

(28) Stracke, J. J.; Finke, R. G. *J. Am. Chem. Soc.* **2011**, *133*, 14872.

(29) Huang, Z.; Luo, Z.; Geletii, Y. V.; Vickers, J. W.; Yin, Q.; Wu, D.; Hou, Y.; Ding, Y.; Song, J.; Musaev, D. G.; Hill, C. L.; Lian, T. *J. Am. Chem. Soc.* **2011**, *133*, 2068.

(30) Stracke, J. J.; Finke, R. G. *ACS Catal.* **2013**, *3*, 1209.

(31) Vickers, J. W.; Lv, H.; Sumliner, J. M.; Zhu, G.; Luo, Z.; Musaev, D. G.; Geletii, Y. V.; Hill, C. L. *J. Am. Chem. Soc.* **2013**, *135*, 14110.

(32) Hill, C. L.; Vickers, J. W.; Glass, E. N.; Geletii, Y. V.; Sumliner, J. M.; Lv, H.; Lian, T.; Kaledin, A. L.; Musaev, D. G. In *245th ACS National Meeting*; American Chemical Society: New Orleans, LA, 2013, p ENFL-667.

(33) Jun, Y.-W.; Choi, J.-S.; Cheon, J. *Angew. Chem., Int. Ed.* **2006**, *45*, 3414.

(34) Lee, Y.; Suntivich, J.; May, K. J.; Perry, E. E.; Shao-Horn, Y. *J. Phys. Chem. Lett.* **2012**, *3*, 399.

(35) Esswein, A. J.; McMurdo, M. J.; Ross, P. N.; Bell, A. T.; Tilley, T. D. *J. Phys. Chem. C* **2009**, *113*, 15068.

(36) Bockris, J. O.; Otagawa, T. *J. Phys. Chem.* **1983**, *87*, 2960.

(37) Suntivich, J.; May, K. J.; Gasteiger, H. A.; Goodenough, J. B.; Shao-Horn, Y. *Science* **2011**, *334*, 1383.

(38) Vojvodic, A.; Nørskov, J. K. *Science* **2011**, *334*, 1355.

(39) May, K. J.; Carlton, C. E.; Stoerzinger, K. A.; Risch, M.; Suntivich, J.; Lee, Y.-L.; Grimaud, A.; Shao-Horn, Y. *J. Phys. Chem. Lett.* **2012**, *3*, 3264.

(40) Risch, M.; Grimaud, A.; May, K. J.; Stoerzinger, K. A.; Chen, T. J.; Mansour, A. N.; Shao-Horn, Y. *J. Phys. Chem. C* **2013**, *117*, 8628.

(41) Matsumoto, Y.; Sato, E. *Mater. Chem. Phys.* **1986**, *14*, 397.

(42) Trasatti, S.; Petrii, O. A. *Pure Appl. Chem.* **1991**, *63*, 711.

(43) Trotochaud, L.; Mills, T. J.; Boettcher, S. W. *J. Phys. Chem. Lett.* **2013**, *4*, 931.

(44) Surendranath, Y.; Kanan, M. W.; Nocera, D. G. *J. Am. Chem. Soc.* **2010**, *132*, 16501.

(45) Esswein, A. J.; Surendranath, Y.; Reece, S. Y.; Nocera, D. G. *Energy Environ. Sci.* **2011**, *4*, 499.

(46) Farrow, C. L.; Bediako, D. K.; Surendranath, Y.; Nocera, D. G.; Billinge, S. J. L. *J. Am. Chem. Soc.* **2013**, *135*, 6403.

(47) Dincă, M.; Surendranath, Y.; Nocera, D. G. *Proc. Natl. Acad. Sci. U.S.A.* **2010**, *107*, 10337.

(48) Bediako, D. K.; Surendranath, Y.; Nocera, D. G. *J. Am. Chem. Soc.* **2013**, *135*, 3662.

(49) Subbaraman, R.; Tripkovic, D.; Chang, K.-C.; Strmcnik, D.; Paulikas, A. P.; Hirunsit, P.; Chan, M.; Greeley, J.; Stamenkovic, V.; Markovic, N. M. *Nat. Mater.* **2012**, *11*, 550.

(50) Yeo, B. S.; Bell, A. T. *J. Am. Chem. Soc.* **2011**, *133*, 5587.

(51) Corrigan, D. A.; Bendert, R. M. *J. Electrochem. Soc.* **1989**, *136*, 723.

(52) Pourbaix, M. *Atlas of Electrochemical Equilibria in Aqueous Solutions*; Pergamon Press: Oxford, 1966.

(53) Schweitzer, G. K.; Pesterfield, L. L. *The Aqueous Chemistry of The Elements*; Oxford University Press: Oxford, 2010.

(54) Doyle, R. L.; Godwin, I. J.; Brandon, M. P.; Lyons, M. E. G. *Phys. Chem. Chem. Phys.* **2013**.

(55) Cordoba, S. I.; Carbonio, R. E.; Teijelo, M. L.; Macagno, V. A. *Electrochim. Acta* **1986**, *31*, 1321.

(56) Corrigan, D. A. *J. Electrochem. Soc.* **1987**, *134*, 377.

(57) Lu, P. W. T.; Srinivasan, S. *J. Electrochem. Soc.* **1978**, *125*, 1416.

(58) Hall, D. E. *J. Electrochem. Soc.* **1983**, *130*, 317.

(59) Louie, M. W.; Bell, A. T. *J. Am. Chem. Soc.* **2013**, *135*, 12329.

(60) Corrigan, D. A.; Knight, S. L. *J. Electrochem. Soc.* **1989**, *136*, 613.

(61) Subbaraman, R.; Danilovic, N.; Lopes, P. P.; Tripkovic, D.; Strmcnik, D.; Stamenkovic, V. R.; Markovic, N. M. *J. Phys. Chem. C* **2012**, *116*, 22231.

(62) Bediako, D. K.; Lassalle-Kaiser, B.; Surendranath, Y.; Yano, J.; Yachandra, V. K.; Nocera, D. G. *J. Am. Chem. Soc.* **2012**, *134*, 6801.

(63) Lyons, M. E. G.; Brandon, M. P. *Int. J. Electrochem. Sci.* **2008**, *3*, 1386.

CHAPTER II

(1) Walter, M. G.; Warren, E. L.; McKone, J. R.; Boettcher, S. W.; Mi, Q.; Santori, E. A.; Lewis, N. S. *Chem. Rev.* **2010**, *110*, 6446.

(2) Cook, T. R.; Dogutan, D. K.; Reece, S. Y.; Surendranath, Y.; Teets, T. S.; Nocera, D. G. *Chem. Rev.* **2010**, *110*, 6474.

(3) Suntivich, J.; May, K. J.; Gasteiger, H. A.; Goodenough, J. B.; Shao-Horn, Y. *Science* **2011**, *334*, 1383.

(4) Trasatti, S.; Lodi, G. Oxygen and chlorine evolution at conductive metallic oxide anodes. In *Electrodes of Conductive Metallic Oxides*; Trasatti, S., Ed.; Elsevier: Amsterdam, 1981; Vol. B; p 521.

(5) Matsumoto, Y.; Sato, E. *Mater. Chem. Phys.* **1986**, *14*, 397.

(6) Trasatti, S.; Petrii, O. A. *J. Electroanal. Chem.* **1992**, *327*, 353.

(7) Man, I. C.; Su, H.-Y.; Calle-Vallejo, F.; Hansen, H. A.; Martínez, J. I.; Inoglu, N. G.; Kitchin, J.; Jaramillo, T. F.; Nørskov, J. K.; Rossmeisl, J. *ChemCatChem* **2011**, *3*, 1159.

(8) Guerrini, E.; Consonni, V.; Trasatti, S. *J. Solid State Electrochem.* **2005**, *9*, 320.

(9) Hepel, T.; Pollak, F. H.; O'Grady, W. E. *J. Electrochem. Soc.* **1986**, *133*, 69.

(10) Trasatti, S. *J. Electroanal. Chem.* **1980**, *111*, 125.

(11) Rossmeisl, J.; Dimitrievski, K.; Siegbahn, P.; Nørskov, J. K. *J. Phys. Chem. C* **2007**, *111*, 18821.

(12) Rossmeisl, J.; Qu, Z.-W.; Zhu, H.; Kroes, G.-J.; Nørskov, J. K. *J. Electroanal. Chem.* **2007**, *607*, 83.

(13) Subbaraman, R.; Tripkovic, D.; Chang, K.-C.; Strmcnik, D.; Paulikas, A. P.; Hirunsit, P.; Chan, M.; Greeley, J.; Stamenkovic, V.; Markovic, N. M. *Nat. Mater.* **2012**, *11*, 550.

(14) Bediako, D. K.; Lassalle-Kaiser, B.; Surendranath, Y.; Yano, J.; Yachandra, V. K.; Nocera, D. G. *J. Am. Chem. Soc.* **2012**, *134*, 6801.

(15) Bockris, J. O.; Otagawa, T. *J. Phys. Chem.* **1983**, *87*, 2960.

(16) Bockris, J. O.; Otagawa, T. *J. Electrochem. Soc.* **1984**, *131*, 290.

(17) Suntivich, J.; Gasteiger, H. A.; Yabuuchi, N.; Shao-Horn, Y. *J. Electrochem. Soc.* **2010**, *157*, B1263.

(18) Trasatti, S.; Petrii, O. A. *Pure Appl. Chem.* **1991**, *63*, 711.

(19) Schweitzer, G. K.; Pesterfield, L. L. *The Aqueous Chemistry of The Elements*; Oxford University Press: Oxford, 2010.

(20) Sauerbrey, G. *Z. Phys. A: Hadrons Nucl.* **1959**, *155*, 206.

(21) Buttry, D. A.; Ward, M. D. *Chem. Rev.* **1992**, *92*, 1355.

(22) Donovan, J. J.; Lowers, H. A.; Rusk, B. G. *Am. Mineral.* **2011**, *96*, 274.

(23) Phung, T. M.; Jensen, J. M.; Johnson, D. C.; Donovan, J. J.; McBurnett, B. G. *X-Ray Spectrom.* **2008**, *37*, 608.

(24) Wu, G.; Li, N.; Zhou, D.-R.; Mitsuo, K.; Xu, B.-Q. *J. Solid State Chem.* **2004**, *177*, 3682.

(25) de Chialvo, M. R. G.; Chialvo, A. C. *Electrochim. Acta* **1993**, *38*, 2247.

(26) Nikolov, I.; Darkaoui, R.; Zhecheva, E.; Stoyanova, R.; Dimitrov, N.; Vitanov, T. *J. Electroanal. Chem.* **1997**, *429*, 157.

(27) Cui, B.; Lin, H.; Li, J.-B.; Li, X.; Yang, J.; Tao, J. *Adv. Funct. Mater.* **2008**, *18*, 1440.

(28) Tiwari, S. K.; Samuel, S.; Singh, R. N.; Poillerat, G.; Koenig, J. F.; Chartier, P. *Int. J. Hydrogen Energy* **1995**, *20*, 9.

(29) Singh, R.-N.; Hamdani, M.; Koenig, J.-F.; Poillerat, G.; Gautier, J. L.; Chartier, P. *J. Appl. Electrochem.* **1990**, *20*, 442.

(30) Bocca, C.; Barbucci, A.; Delucchi, M.; Cerisola, G. *Int. J. Hydrogen Energy* **1999**, *24*, 21.

(31) Lian, K.; Thorpe, S. J.; Kirk, D. W. *Electrochim. Acta* **1992**, *37*, 169.

(32) Corrigan, D. A.; Knight, S. L. *J. Electrochem. Soc.* **1989**, *136*, 613.

(33) Corrigan, D. A. *J. Electrochem. Soc.* **1987**, *134*, 377.

(34) Corrigan, D. A.; Bendert, R. M. *J. Electrochem. Soc.* **1989**, *136*, 723.

(35) Wehrens-Dijksma, M.; Notten, P. H. L. *Electrochim. Acta* **2006**, *51*, 3609.

(36) McIntyre, N. S.; Cook, M. G. *Anal. Chem.* **1975**, *47*, 2208.

(37) Mitton, D. B.; Walton, J.; Thompson, G. E. *Surf. Interface Anal.* **1993**, *20*, 36.

(38) Biesinger, M. C.; Payne, B. P.; Lau, L. W. M.; Gerson, A.; Smart, R. S. C. *Surf. Interface Anal.* **2009**, *41*, 324.

(39) Chuang, T. J.; Brundle, C. R.; Rice, D. W. *Surf. Sci.* **1976**, *59*, 413.

(40) McIntyre, N. S.; Johnston, D. D.; Coatsworth, L. L.; Davidson, R. D.; Brown, J. R. *Surf. Interface Anal.* **1990**, *15*, 265.

(41) López, G. P.; Castner, D. G.; Ratner, B. D. *Surf. Interface Anal.* **1991**, *17*, 267.

(42) Yang, J.; Liu, H. W.; Martens, W. N.; Frost, R. L. *J. Phys. Chem. C* **2010**, *114*, 111.

(43) Oku, M.; Hirokawa, K. *J. Electron Spectrosc. Relat. Phenom.* **1976**, *8*, 475.

(44) Rasiyah, P.; Tseung, A. C. C.; Hibbert, D. B. *J. Electrochem. Soc.* **1982**, *129*, 1724.

(45) Parmar, N.; Gorby, Y. A.; Beveridge, T. J.; Ferris, F. G. *Geomicrobiol. J.* **2001**, *18*, 375.

(46) Zegeye, A.; Bonneville, S.; Benning, L. G.; Sturm, A.; Fowle, D. A.; Jones, C.; Canfield, D. E.; Ruby, C.; MacLean, L. C.; Nomosatryo, S.; Crowe, S. A.; Poulton, S. W. *Geology* **2012**, *40*, 599.

(47) Konhauser, K. O.; Pecoits, E.; Lalonde, S. V.; Papineau, D.; Nisbet, E. G.; Barley, M. E.; Arndt, N. T.; Zahnle, K.; Kamber, B. S. *Nature* **2009**, *458*, 750.

(48) Merrill, M. D.; Dougherty, R. C. *J. Phys. Chem. C* **2008**, *112*, 3655.

(49) Li, X.; Walsh, F. C.; Pletcher, D. *Phys. Chem. Chem. Phys.* **2011**, *13*, 1162.

(50) Kanan, M. W.; Nocera, D. G. *Science* **2008**, *321*, 1072.

(51) Surendranath, Y.; Kanan, M. W.; Nocera, D. G. *J. Am. Chem. Soc.* **2010**, *132*, 16501.

(52) Yeo, B. S.; Bell, A. T. *J. Am. Chem. Soc.* **2011**, *133*, 5587.

(53) Yeo, B. S.; Bell, A. T. *J. Phys. Chem. C* **2012**, *116*, 8394.

(54) Yin, Q.; Tan, J. M.; Besson, C.; Geletii, Y. V.; Musaev, D. G.; Kuznetsov, A. E.; Luo, Z.; Hardcastle, K. I.; Hill, C. L. *Science* **2010**, *328*, 342.

(55) Jiao, F.; Frei, H. *Angew. Chem., Int. Ed.* **2009**, *48*, 1841.

(56) Lee, Y.; Suntivich, J.; May, K. J.; Perry, E. E.; Shao-Horn, Y. *J. Phys. Chem. Lett.* **2012**, *3*, 399.

(57) Nakagawa, T.; Bjorge, N. S.; Murray, R. W. *J. Am. Chem. Soc.* **2009**, *131*, 15578.

(58) Shao, Z. P.; Haile, S. M. *Nature* **2004**, *431*, 170.

(59) Kuhl, K. P.; Cave, E. R.; Abram, D. N.; Jaramillo, T. F. *Energy Environ. Sci.* **2012**, *5*, 7050.

(60) Li, C. W.; Kanan, M. W. *J. Am. Chem. Soc.* **2012**, *134*, 7231.

CHAPTER III

(1) Walter, M. G.; Warren, E. L.; McKone, J. R.; Boettcher, S. W.; Mi, Q.; Santori, E. A.; Lewis, N. S. *Chem. Rev.* **2010**, *110*, 6446.

(2) Cook, T. R.; Dogutan, D. K.; Reece, S. Y.; Surendranath, Y.; Teets, T. S.; Nocera, D. G. *Chem. Rev.* **2010**, *110*, 6474.

(3) Suntivich, J.; May, K. J.; Gasteiger, H. A.; Goodenough, J. B.; Shao-Horn, Y. *Science* **2011**, *334*, 1383.

(4) Tran, P. D.; Wong, L. H.; Barber, J.; Loo, J. S. C. *Energy Environ. Sci.* **2012**, *5*, 5902.

(5) Sun, J.; Zhong, D. K.; Gamelin, D. R. *Energy Environ. Sci.* **2010**, *3*, 1252.

(6) Klahr, B.; Gimenez, S.; Fabregat-Santiago, F.; Bisquert, J.; Hamann, T. W. *J. Am. Chem. Soc.* **2012**, *134*, 16693.

(7) Seabold, J. A.; Choi, K.-S. *Chem. Mater.* **2011**, *23*, 1105.

(8) Liu, R.; Lin, Y.; Chou, L.-Y.; Sheehan, S. W.; He, W.; Zhang, F.; Hou, H. J. M.; Wang, D. *Angew. Chem., Int. Ed.* **2011**, *50*, 499.

(9) Kay, A.; Cesar, I.; Grätzel, M. *J. Am. Chem. Soc.* **2006**, *128*, 15714.

(10) Tilley, S. D.; Cornuz, M.; Sivula, K.; Grätzel, M. *Angew. Chem., Int. Ed.* **2010**, *49*, 6405.

(11) Abdi, F. F.; van de Krol, R. *J. Phys. Chem. C* **2012**, *116*, 9398.

(12) Gamelin, D. R. *Nat. Chem.* **2012**, *4*, 965.

(13) Zhong, D. K.; Gamelin, D. R. *J. Am. Chem. Soc.* **2010**, *132*, 4202.

(14) Ye, H.; Park, H. S.; Bard, A. J. *J. Phys. Chem. C* **2011**, *115*, 12464.

(15) Zhong, D. K.; Choi, S.; Gamelin, D. R. *J. Am. Chem. Soc.* **2011**, *133*, 18370.

(16) McDonald, K. J.; Choi, K.-S. *Chem. Mater.* **2011**, *23*, 1686.

(17) Barroso, M.; Cowan, A. J.; Pendlebury, S. R.; Grätzel, M.; Klug, D. R.; Durrant, J. R. *J. Am. Chem. Soc.* **2011**, *133*, 14868.

(18) Steinmiller, E. M. P.; Choi, K.-S. *Proc. Natl. Acad. Sci. U.S.A.* **2009**, *106*, 20633.

(19) Surendranath, Y.; Bediako, D. K.; Nocera, D. G. *Proc. Natl. Acad. Sci. U.S.A.* **2012**, *109*, 15617.

(20) Pijpers, J. J. H.; Winkler, M. T.; Surendranath, Y.; Buonassisi, T.; Nocera, D. G. *Proc. Natl. Acad. Sci. U.S.A.* **2011**, *108*, 10056.

(21) Reece, S. Y.; Hamel, J. A.; Sung, K.; Jarvi, T. D.; Esswein, A. J.; Pijpers, J. J. H.; Nocera, D. G. *Science* **2011**, *334*, 645.

(22) Young, E. R.; Costi, R.; Paydavosi, S.; Nocera, D. G.; Bulović, V. *Energy Environ. Sci.* **2011**, *4*, 2058.

(23) Somani, P. R.; Radhakrishnan, S. *Mater. Chem. Phys.* **2002**, *77*, 117.

(24) Baetens, R.; Jelle, B. P.; Gustavsen, A. *Sol. Energy Mater. Sol. Cells* **2010**, *94*, 87.

(25) Haussener, S.; Xiang, C.; Spurgeon, J. M.; Ardo, S.; Lewis, N. S.; Weber, A. Z. *Energy Environ. Sci.* **2012**, *5*, 9922.

(26) Trotochaud, L.; Ranney, J. K.; Williams, K. N.; Boettcher, S. W. *J. Am. Chem. Soc.* **2012**, *134*, 17253.

(27) Bendert, R. M.; Corrigan, D. A. *J. Electrochem. Soc.* **1989**, *136*, 1369.

(28) Conell, R. S.; Corrigan, D. A.; Powell, B. R. *Sol. Energy Mater. Sol. Cells* **1992**, *25*, 301.

(29) Corrigan, D. A.; Knight, S. L. *J. Electrochem. Soc.* **1989**, *136*, 613.

(30) Präzisions Glas & Optik. www.pgo-online.com/intl/katalog/1737.html (accessed Feb 1, 2013), 1737 Low Alkali Glass Specifications.

(31) RefractiveIndex.INFO Refractive Index Database. refractiveindex.info/?group=CRYSTALS&material=ITO (accessed Feb 1, 2013), SOPRA N&K Database: Optical constants of In_2O_3-SnO_2 (ITO, Indium Tin Oxide).

(32) Hall, D. E. *J. Electrochem. Soc.* **1983**, *130*, 317.

(33) Surendranath, Y.; Kanan, M. W.; Nocera, D. G. *J. Am. Chem. Soc.* **2010**, *132*, 16501.

CHAPTER IV

(1) Walter, M. G.; Warren, E. L.; McKone, J. R.; Boettcher, S. W.; Mi, Q.; Santori, E. A.; Lewis, N. S. *Chem. Rev.* **2010**, *110*, 6446.

(2) Cook, T. R.; Dogutan, D. K.; Reece, S. Y.; Surendranath, Y.; Teets, T. S.; Nocera, D. G. *Chem. Rev.* **2010**, *110*, 6474.

(3) Suntivich, J.; May, K. J.; Gasteiger, H. A.; Goodenough, J. B.; Shao-Horn, Y. *Science* **2011**, *334*, 1383.

(4) McCrory, C. C. L.; Jung, S. H.; Peters, J. C.; Jaramillo, T. F. *J. Am. Chem. Soc.* **2013**, *135*, 16977.

(5) Landon, J.; Demeter, E.; Inoglu, N.; Keturakis, C.; Wachs, I. E.; Vasic, R.; Frenkel, A. I.; Kitchin, J. R. *ACS Catal.* **2012**, *2*, 1793.

(6) Kim, T. W.; Choi, K.-S. *Science* **2014**.

(7) Gong, M.; Li, Y.; Wang, H.; Liang, Y.; Wu, J. Z.; Zhou, J.; Wang, J.; Regier, T.; Wei, F.; Dai, H. *J. Am. Chem. Soc.* **2013**, *135*, 8452.

(8) Louie, M. W.; Bell, A. T. *J. Am. Chem. Soc.* **2013**, *135*, 12329.

(9) Smith, R. D. L.; Prévot, M. S.; Fagan, R. D.; Trudel, S.; Berlinguette, C. P. *J. Am. Chem. Soc.* **2013**, *135*, 11580.

(10) Smith, R. D. L.; Prévot, M. S.; Fagan, R. D.; Zhang, Z.; Sedach, P. A.; Siu, M. K. J.; Trudel, S.; Berlinguette, C. P. *Science* **2013**, *340*, 60.

(11) Trotochaud, L.; Ranney, J. K.; Williams, K. N.; Boettcher, S. W. *J. Am. Chem. Soc.* **2012**, *134*, 17253.

(12) Merrill, M. D.; Dougherty, R. C. *J. Phys. Chem. C* **2008**, *112*, 3655.

(13) Kleiman-Shwarsctein, A.; Hu, Y. S.; Stucky, G. D.; McFarland, E. W. *Electrochem. Commun.* **2009**, *11*, 1150.

(14) Corrigan, D. A. Hydrogen Generator Having a Low Oxygen Overpotential Electrode. U.S. Patent 4,882,024, Nov. 21, 1989.

(15) Trotochaud, L.; Mills, T. J.; Boettcher, S. W. *J. Phys. Chem. Lett.* **2013**, *4*, 931.
(16) Corrigan, D. A. *J. Electrochem. Soc.* **1987**, *134*, 377.

(17) Corrigan, D. A.; Bendert, R. M. *J. Electrochem. Soc.* **1989**, *136*, 723.

(18) Haber, J. A.; Cai, Y.; Jung, S.; Xiang, C.; Mitrovic, S.; Jin, J.; Bell, A. T.; Gregoire, J. M. *Energy Environ. Sci.* **2014**, *7*, 682.

(19) Santos, D. M. F.; Amaral, L.; Šljukić, B.; Macciò, D.; Saccone, A.; Sequeira, C. A. C. *J. Electrochem. Soc.* **2014**, *161*, F386.

(20) Xiang, C.; Suram, S. K.; Haber, J. A.; Guevarra, D. W.; Soedarmadji, E.; Jin, J.; Gregoire, J. M. *ACS Comb. Sci.* **2013**.

(21) Gerken, J. B.; Chen, J. Y. C.; Massé, R. C.; Powell, A. B.; Stahl, S. S. *Angew. Chem., Int. Ed.* **2012**, *51*, 6676.

(22) Tessier, C.; Haumesser, P. H.; Bernard, P.; Delmas, C. *J. Electrochem. Soc.* **1999**, *146*, 2059.

(23) Mcewen, R. S. *J. Phys. Chem.* **1971**, *75*, 1782.

(24) Notten, P. H. L. Rechargeable nickel-metalhydride batteries: a successful new concept. In *Interstitial Intermetallic Alloys*; Grandjean, F., Long, G., Buschow, K. H. J., Eds.; Springer Netherlands: 1995; Vol. 281; p 151.

(25) Bernard, M. C.; Bernard, P.; Keddam, M.; Senyarich, S.; Takenouti, H. *Electrochim. Acta* **1996**, *41*, 91.

(26) de Moura, A. P.; Lima, R. C.; Paris, E. C.; Li, M. S.; Varela, J. A.; Longo, E. *J. Solid State Chem.* **2011**, *184*, 2818.

(27) Delmas, C.; Tessier, C. *J. Mater. Chem.* **1997**, *7*, 1439.

(28) Gourrier, L.; Deabate, S.; Michel, T.; Paillet, M.; Hermet, P.; Bantignies, J. L.; Henn, F. *J. Phys. Chem. C* **2011**, *115*, 15067.

(29) Hall, D. S.; Lockwood, D. J.; Poirier, S.; Bock, C.; MacDougall, B. R. *J. Phys. Chem. A* **2012**, *116*, 6771.

(30) Kim, M. S.; Kim, K. B. *J. Electrochem. Soc.* **1998**, *145*, 507.

(31) Balasubramanian, M.; Melendres, C. A.; Mini, S. *J. Phys. Chem. B* **2000**, *104*, 4300.
(32) Axmann, P.; Glemser, O. *J. Alloys Compd.* **1997**, *246*, 232.

(33) Demourgues-Guerlou, L.; Fournès, L.; Delmas, C. *J. Solid State Chem.* **1995**, *114*, 6.

(34) Corrigan, D. A.; Conell, R. S.; Fierro, C. A.; Scherson, D. A. *J. Phys. Chem.* **1987**, *91*, 5009.

(35) Subbaraman, R.; Danilovic, N.; Lopes, P. P.; Tripkovic, D.; Strmcnik, D.; Stamenkovic, V. R.; Markovic, N. M. *J. Phys. Chem. C* **2012**, *116*, 22231.

(36) Kenney, M. J.; Gong, M.; Li, Y. G.; Wu, J. Z.; Feng, J.; Lanza, M.; Dai, H. J. *Science* **2013**, *342*, 836.

(37) Yeo, B. S.; Bell, A. T. *J. Phys. Chem. C* **2012**, *116*, 8394.

(38) Lu, P. W. T.; Srinivasan, S. *J. Electrochem. Soc.* **1978**, *125*, 1416.

(39) Bediako, D. K.; Lassalle-Kaiser, B.; Surendranath, Y.; Yano, J.; Yachandra, V. K.; Nocera, D. G. *J. Am. Chem. Soc.* **2012**, *134*, 6801.

(40) Bediako, D. K.; Surendranath, Y.; Nocera, D. G. *J. Am. Chem. Soc.* **2013**, *135*, 3662.

(41) Yeo, B. S.; Bell, A. T. *J. Am. Chem. Soc.* **2011**, *133*, 5587.

(42) Subbaraman, R.; Tripkovic, D.; Chang, K.-C.; Strmcnik, D.; Paulikas, A. P.; Hirunsit, P.; Chan, M.; Greeley, J.; Stamenkovic, V.; Markovic, N. M. *Nat. Mater.* **2012**, *11*, 550.

(43) Busch, M.; Ahlberg, E.; Panas, I. *Catal. Today* **2013**, *202*, 114.

(44) Busch, M.; Ahlberg, E.; Panas, I. *Phys. Chem. Chem. Phys.* **2011**, *13*, 15062.

(45) Bajdich, M.; García-Mota, M.; Vojvodic, A.; Nørskov, J. K.; Bell, A. T. *J. Am. Chem. Soc.* **2013**, *135*, 13521.

(46) Sauerbrey, G. *Z. Phys. A: Hadrons Nucl.* **1959**, *155*, 206.

(47) Wehrens-Dijksma, M.; Notten, P. H. L. *Electrochim. Acta* **2006**, *51*, 3609.

(48) Corrigan, D. A.; Knight, S. L. *J. Electrochem. Soc.* **1989**, *136*, 613.

(49) Bediako, D. K.; Lassalle-Kaiser, B.; Surendranath, Y.; Yano, J.; Yachandra, V. K.; Nocera, D. G. *J. Am. Chem. Soc.* **2012**, *134*, 6801.

(50) Lyons, M. E. G.; Brandon, M. P. *Int. J. Electrochem. Sci.* **2008**, *3*, 1386.

(51) Kostecki, R.; McLarnon, F. *J. Electrochem. Soc.* **1997**, *144*, 485.

(52) Rajamathi, M.; Kamath, P. V.; Seshadri, R. *J. Mater. Chem.* **2000**, *10*, 503.

(53) Desilvestro, J.; Corrigan, D. A.; Weaver, M. J. *J. Electrochem. Soc.* **1988**, *135*, 885.

(54) Godwin, I. J.; Lyons, M. E. G. *Electrochem. Commun.* **2013**, *32*, 39.

(55) Trotochaud, L.; Boettcher, S. W. *Scr. Mater.* **2014**, *74*, 25.

(56) Nakahira, A.; Kubo, T.; Murase, H. *IEEE. Trans. Magn.* **2007**, *43*, 2442.

(57) Li, Y.; Li, H.; Yang, M.; He, X.; Ni, P.; Kang, L.; Liu, Z.-H. *Appl. Clay Sci.* **2011**, *52*, 51.

(58) Iwasaki, T.; Yoshii, H.; Nakamura, H.; Watano, S. *Appl. Clay Sci.* **2012**, *58*, 120.

(59) Trolard, F.; Bourrié, G. Fougerite a Natural Layered Double Hydroxide in Gley Soil: Habitus, Structure, and Some Properties. In *Clay Minerals in Nature - Their Characterization, Modification and Application*; InTech: 2012; p 171. DOI: 10.5772/50211

(60) Nan, J.; Yang, Y.; Lin, Z. *Electrochim. Acta* **2006**, *51*, 4873.

(61) Doyle, R. L.; Godwin, I. J.; Brandon, M. P.; Lyons, M. E. G. *Phys. Chem. Chem. Phys.* **2013**.

(62) Mcbreen, J.; Ogrady, W. E.; Tourillon, G.; Dartyge, E.; Fontaine, A.; Pandya, K. I. *J. Phys. Chem.* **1989**, *93*, 6308.

(63) Nazri, G.; Corrigan, D. A.; Maheswari, S. P. *Langmuir* **1989**, *5*, 17.

(64) Lo, Y. L.; Hwang, B. J. *Langmuir* **1998**, *14*, 944.

(65) Casas-Cabanas, M.; Rodriguez-Carvajal, J.; Canales-Vazquez, J.; Palacin, M. R. *J. Mater. Chem.* **2006**, *16*, 2925.

(66) Deabate, S.; Henn, F.; Devautour, S.; Giuntini , J. C. *J. Electrochem. Soc.* **2003**, *150*, J23.

(67) Subbaraman, R.; Tripkovic, D.; Strmcnik, D.; Chang, K. C.; Uchimura, M.; Paulikas, A. P.; Stamenkovic, V.; Markovic, N. M. *Science* **2011**, *334*, 1256.

(68) Van der Ven, A.; Morgan, D.; Meng, Y. S.; Ceder, G. *J. Electrochem. Soc.* **2006**, *153*, A210.

(69) Hermet, P.; Gourrier, L.; Bantignies, J. L.; Ravot, D.; Michel, T.; Deabate, S.; Boulet, P.; Henn, F. *Phys. Rev. B* **2011**, *84*.

(70) Man, I. C.; Su, H.-Y.; Calle-Vallejo, F.; Hansen, H. A.; Martínez, J. I.; Inoglu, N. G.; Kitchin, J.; Jaramillo, T. F.; Nørskov, J. K.; Rossmeisl, J. *ChemCatChem* **2011**, *3*, 1159.

(71) Greeley, J.; Nørskov, J. K. *J. Phys. Chem. C* **2009**, *113*, 4932.

(72) Beverskog, B.; Puigdomenech, I. *Corros. Sci.* **1997**, *39*, 969.

(73) Capehart, T. W.; Corrigan, D. A.; Conell, R. S.; Pandya, K. I.; Hoffman, R. W. *Appl. Phys. Lett.* **1991**, *58*, 865.

(74) Risch, M.; Grimaud, A.; May, K. J.; Stoerzinger, K. A.; Chen, T. J.; Mansour, A. N.; Shao-Horn, Y. *J. Phys. Chem. C* **2013**, *117*, 8628.

(75) Natan, M. J.; Belanger, D.; Carpenter, M. K.; Wrighton, M. S. *J. Phys. Chem.* **1987**, *91*, 1834.

(76) Nishizawa, M.; Ise, T.; Koshika, H.; Itoh, T.; Uchida, I. *Chem. Mater.* **2000**, *12*, 1367.

(77) Madou, M. J.; Mckubre, M. C. H. *J. Electrochem. Soc.* **1983**, *130*, 1056.

(78) Kim, S.; Tryk, D. A.; Antonio, M. R.; Carr, R.; Scherson, D. *J. Phys. Chem.* **1994**, *98*, 10269.

(79) Schweitzer, G. K.; Pesterfield, L. L. *The Aqueous Chemistry of The Elements*; Oxford University Press: Oxford, 2010; p 362-367.

(80) *CRC Handbook of Chemistry and Physics*; 76 ed.; Lide, D. R., Ed.; CRC Press: Boca Raton, FL, 1995.

CHAPTER V

(1) Eranna, G.; Joshi, B. C.; Runthala, D. P.; Gupta, R. P. *Crit. Rev. Solid State Mater. Sci.* **2004**, *29*, 111.

(2) Zakrzewska, K. *Thin Solid Films* **2001**, *391*, 229.

(3) Kolmakov, A.; Klenov, D. O.; Lilach, Y.; Stemmer, S.; Moskovits, M. *Nano Lett.* **2005**, *5*, 667.

(4) Kolmakov, A.; Chen, X. H.; Moskovits, M. *J Nanosci. Nanotechnol.* **2008**, *8*, 111.

(5) Li, Y.; Hasin, P.; Wu, Y. *Adv. Mater.* **2010**, *22*, 1926.

(6) Shiju, N. R.; Guliants, V. V. *Appl. Catal. A* **2009**, *356*, 1.

(7) Fernández-García, M.; Martínez-Arias, A.; Hanson, J. C.; Rodriguez, J. A. *Chem. Rev.* **2004**, *104*, 4063.

(8) Jiao, F.; Frei, H. *Energy Environ. Sci.* **2010**, *3*, 1018.

(9) Angelinetta, C.; Trasatti, S.; Atanasoska, L. D.; Minevski, Z. S.; Atanasoski, R. T. *Mater. Chem. Phys.* **1989**, *22*, 231.

(10) Chen, A.; Nigro, S. *J. Phys. Chem. B* **2003**, *107*, 13341.

(11) Chen, X.; Chen, G.; Yue, P. L. *J. Phys. Chem. B* **2001**, *105*, 4623.

(12) Lin, J.; Yu, J. C.; Lo, D.; Lam, S. K. *J. Catal.* **1999**, *183*, 368.

(13) Zhaoliang, Z.; Jun, M.; Xiyao, Y. *Chem. Eng. J.* **2003**, *95*, 15.

(14) Trasatti, S. *Electrochim. Acta* **2000**, *45*, 2377.

(15) Forti, J. C.; Olivi, P.; de Andrade, A. R. *Electrochim. Acta* **2001**, *47*, 913.

(16) Trasatti, S.; Petrii, O. A. *J. Electroanal. Chem.* **1992**, *327*, 353.

(17) Yin, Y.; Alivisatos, A. P. *Nature* **2005**, *437*, 664.

(18) Cushing, B. L.; Kolesnichenko, V. L.; O'Connor, C. J. *Chem. Rev.* **2004**, *104*, 3893.

(19) Gedanken, A. *Ultrason. Sonochem.* **2004**, *11*, 47.

(20) Jana, N. R.; Chen, Y.; Peng, X. *Chem. Mater.* **2004**, *16*, 3931.

(21) Niederberger, M.; Garnweitner, G. *Chem. Eur. J.* **2006**, *12*, 7282.

(22) Pinna, N.; Garnweitner, G.; Antonietti, M.; Niederberger, M. *J. Am. Chem. Soc.* **2005**, *127*, 5608.

(23) Jana, S.; Aksu, Y.; Driess, M. *Dalton Trans.* **2009**, 1516.

(24) Tsaroucha, M.; Aksu, Y.; Irran, E.; Driess, M. *Chem. Mater.* **2011**, *23*, 2428.

(25) Hagfeldt, A.; Grätzel, M. *Acc. Chem. Res.* **2000**, *33*, 269.

(26) Grätzel, M. *Photochem. Photobiol.* **2003**, *4*, 145.

(27) Kay, A.; Grätzel, M. *Sol. Energy Mater. Sol. Cells* **1996**, *44*, 99.

(28) van de Lagemaat, J.; Park, N.-G.; Frank, A. J. *J. Phys. Chem. B* **2000**, *104*, 2044.

(29) Dittrich, T. *Phys. Status Solidi A* **2000**, *182*, 447.

(30) Hore, S.; Vetter, C.; Kern, R.; Smit, H.; Hinsch, A. *Sol. Energy Mater. Sol. Cells* **2006**, *90*, 1176.

(31) Kopidakis, N.; Benkstein, K. D.; van de Lagemaat, J.; Frank, A. J. *J. Phys. Chem. B* **2003**, *107*, 11307.

(32) Dinh, C. T.; Nguyen, T. D.; Kleitz, F.; Do, T. O. *ACS Nano* **2009**, *3*, 3737.

(33) Tang, J.; Redl, F.; Zhu, Y. M.; Siegrist, T.; Brus, L. E.; Steigerwald, M. L. *Nano Lett.* **2005**, *5*, 543.

(34) Niederberger, M.; Bartl, M. H.; Stucky, G. D. *Chem. Mater.* **2002**, *14*, 4364.

(35) Wu, B. H.; Guo, C. Y.; Zheng, N. F.; Xie, Z. X.; Stucky, G. D. *J. Am. Chem. Soc.* **2008**, *130*, 17563.

(36) Seo, J.-w.; Jun, Y.-w.; Ko, S. J.; Cheon, J. *J. Phys. Chem. B* **2005**, *109*, 5389.

(37) Jensen, G. V.; Bremholm, M.; Lock, N.; Deen, G. R.; Jensen, T. R.; Iversen, B. B.; Niederberger, M.; Pedersen, J. S.; Birkedal, H. *Chem. Mater.* **2010**, *22*, 6044.

(38) Hu, Y.-S.; Kienle, L.; Guo, Y.-G.; Maier, J. *Adv. Mater.* **2006**, *18*, 1421.

(39) Qu, Y.; Li, X.; Li, R.; Yan, H.; Ouyang, X.; Wang, X. *Mater. Res. Bull.* **2008**, *43*, 97.

(40) Chen, R.-F.; Zhang, L.; Wei, Y.; Hou, D.-L. *J. Mater. Sci.* **2007**, *42*, 7141.

(41) Huang, X.; Pan, C. *J. Cryst. Growth* **2007**, *306*, 117.

(42) Nussbaumer, R. J.; Smith, P.; Caseri, W. *J. Nanosci. Nanotechnol.* **2007**, *7*, 2422.

(43) Wang, W.; Gu, B.; Liang, L. Y.; Hamilton, W. A.; Wesolowski, D. J. *J. Phys. Chem. B* **2004**, *108*, 14789.

(44) Cheng, H.; Ma, J.; Zhao, Z.; Qi, L. *Chem. Mater.* **1995**, *7*, 663.

(45) Wu, Y.; Liu, H.-M.; Xu, B.-Q. *Appl. Organomet. Chem.* **2007**, *21*, 146.

(46) Testino, A.; Bellobono, I. R.; Buscaglia, V.; Canevali, C.; D'Arienzo, M.; Polizzi, S.; Scotti, R.; Morazzoni, F. *J. Am. Chem. Soc.* **2007**, *129*, 3564.

(47) Li, Y. Z.; Fan, Y.; Chen, Y. *J. Mater. Chem.* **2002**, *12*, 1387.

(48) Dai, Z. R.; Gole, J. L.; Stout, J. D.; Wang, Z. L. *J. Phys. Chem. B* **2002**, *106*, 1274.

(49) Gao, T.; Wang, T. *Chem. Commun.* **2004**, 2558.

(50) Kim, W.-S.; Kim, D.; Choi, K. J.; Park, J.-G.; Hong, S.-H. *Cryst. Growth Des.* **2010**, *10*, 4746.

(51) Chen, Y. J.; Xue, X. Y.; Wang, Y. G.; Wang, T. H. *Appl. Phys. Lett.* **2005**, *87*.

(52) Fan, C.; Song, X.; Yin, Z.; Yu, H.; Sun, S. *J. Mater. Sci.* **2006**, *41*, 5696.

(53) Qin, L.; Xu, J.; Dong, X.; Pan, Q.; Cheng, Z.; Xiang, Q.; Li, F. *Nanotechnology* **2008**, *19*, 185705.

(54) Cheng, B.; Russell, J. M.; Shi, W.; Zhang, L.; Samulski, E. T. *J. Am. Chem. Soc.* **2004**, *126*, 5972.

(55) Jiang, X.; Wang, Y.; Herricks, T.; Xia, Y. *J. Mater. Chem.* **2004**, *14*, 695.

(56) Ba, J.; Polleux, J.; Antonietti, M.; Niederberger, M. *Adv. Mater.* **2005**, *17*, 2509.

(57) de Monredon, S.; Cellot, A.; Ribot, F.; Sanchez, C.; Armelao, L.; Gueneau, L.; Delattre, L. *J. Mater. Chem.* **2002**, *12*, 2396.

(58) Zhang, J.; Gao, L. *J. Solid State Chem.* **2004**, *177*, 1425.

(59) Wu, N.-L.; Wang, S.-Y.; Rusakova, I. A. *Science* **1999**, *285*, 1375.

(60) Huang, H.; Lee, Y. C.; Tan, O. K.; Zhou, W.; Peng, N.; Zhang, Q. *Nanotechnology* **2009**, *20*, 115501.

(61) Long, R.; Dai, Y.; Huang, B. *J. Phys. Chem. C* **2009**, *113*, 650.

(62) Sensato, F. R.; Custodio, R.; Longo, E.; Beltran, A.; Andres, J. *Catal. Today* **2003**, *85*, 145.

(63) Yu, X.; Li, C.; Tang, H.; Ling, Y.; Tang, T.-A.; Wu, Q.; Kong, J. *Comput. Mater. Sci.* **2010**, *49*, 430.

(64) Beltrán, A.; Andrés, J.; Sambrano, J. R.; Longo, E. *J. Phys. Chem. A* **2008**, *112*, 8943.

(65) Cassia-Santos, M. R.; Souza, A. G.; Soledade, L. E. B.; Varela, J. A.; Longo, E. *J. Therm. Anal. Calorim.* **2005**, *79*, 415.

(66) Harunsani, M. H.; Oropeza, F. E.; Palgrave, R. G.; Egdell, R. G. *Chem. Mater.* **2010**, *22*, 1551.

(67) Ma, Y.; Navrotsky, A. *J. Am. Ceram. Soc.* **2010**, *93*, 3432.

(68) Naidu, H. P.; Virkar, A. V. *J. Am. Ceram. Soc.* **1998**, *81*, 2176.

(69) Zhao, Y.; Liu, J.; Shi, L.; Yuan, S.; Fang, J.; Wang, Z.; Zhang, M. *Appl. Catal. B* **2010**, *100*, 68.

(70) Yu, J.; Liu, S.; Zhou, M. *J. Phys. Chem. C* **2008**, *112*, 2050.

(71) Cao, Y.; He, T.; Zhao, L.; Wang, E.; Yang, W.; Cao, Y. *J. Phys. Chem. C* **2009**, *113*, 18121.

(72) Sasikala, R.; Shirole, A.; Sudarsan, V.; Sakuntala, T.; Sudakar, C.; Naik, R.; Bharadwaj, S. R. *Int. J. Hydrogen Energy* **2009**, *34*, 3621.

(73) Asokan, K.; Park, J.Y.; Choi, S.; Chang, C.; Kim, S.S. *Nano Res.* **2010**, *3*, 256.

(74) Qi, B.; Wu, L.; Zhang, Y.; Zeng, Q.; Zhi, J. *J. Colloid Interface Sci.* **2010**, *345*, 181.

(75) Tao, N.; Zhao, J.; Guo, Y.; Jiang, Y.; Ding, X.; Wang, Z. *Mater. Chem. Phys.* **2004**, *84*, 58.

(76) Wojdyr, M. *J. Appl. Crystallogr.* **2010**, *43*, 1126.

(77) Massiot, D.; Fayon, F.; Capron, M.; King, I.; Le Calvé, S.; Alonso, B.; Durand, J.-O.; Bujoli, B.; Gan, Z. H.; Hoatson, G. *Magn. Reson. Chem.* **2002**, *40*, 70.

(78) Cozzoli, P. D.; Kornowski, A.; Weller, H. *J. Am. Chem. Soc.* **2003**, *125*, 14539.

(79) Zhang, Z. H.; Zhong, X. H.; Liu, S. H.; Li, D. F.; Han, M. Y. *Angew. Chem., Int. Ed.* **2005**, *44*, 3466.

(80) Zhou, M.; Yu, J.; Liu, S.; Zhai, P.; Jiang, L. *J. Hazard. Mater.* **2008**, *154*, 1141.

(81) Mittemeijer, E. J.; Scardi, P. *Diffraction Analysis of the Microstructure of Materials*; Springer: Berlin, 2004; p 1-14.

(82) Riwotzki, K.; Meyssamy, H.; Kornowski, A.; Haase, M. *J. Phys. Chem. B* **2000**, *104*, 2824.

(83) Soler-Illia, G. J. d. A. A.; Scolan, E.; Louis, A.; Albouy, P.-A.; Sanchez, C. *New J. Chem.* **2001**, *25*, 156.

(84) Yoldas, B. E. *J. Mater. Sci.* **1986**, *21*, 1087.

(85) Jenkins, R.; Snyder, R. L. *Introduction to X-ray Powder Diffractometry*; Wiley-Interscience: New York, 1996; p 41-43.

(86) Castellanos, M.; West, A. R. *J. Chem. Soc., Faraday Trans. 1* **1980**, *76*, 2159.

(87) Chizmeshya, A. V. G.; Bauer, M. R.; Kouvetakis, J. *Chem. Mater.* **2003**, *15*, 2511.

(88) Ganguly, P.; Shah, N.; Phadke, M.; Ramaswamy, V.; Mulla, I. S. *Phys. Rev. B* **1993**, *47*, 991.

(89) Sayılkan, F.; Asiltürk, M.; Tatar, P.; Kiraz, N.; Arpaç, E.; Sayılkan, H. *J. Hazard. Mater.* **2007**, *148*, 735.

(90) Smith, D. L. *Thin Film Deposition: Principles and Practices*; McGraw-Hill Professional: New York, 1995; p 223.

(91) Peng, X.; Schlamp, M. C.; Kadavanich, A. V.; Alivisatos, A. P. *J. Am. Chem. Soc.* **1997**, *119*, 7019.

(92) Mekis, I.; Talapin, D. V.; Kornowski, A.; Haase, M.; Weller, H. *J. Phys. Chem. B* **2003**, *107*, 7454.

(93) Steckel, J. S.; Zimmer, J. P.; Coe-Sullivan, S.; Stott, N. E.; Bulović, V.; Bawendi, M. G. *Angew. Chem., Int. Ed.* **2004**, *43*, 2154.

(94) Dabbousi, B. O.; Rodriguez-Viejo, J.; Mikulec, F. V.; Heine, J. R.; Mattoussi, H.; Ober, R.; Jensen, K. F.; Bawendi, M. G. *J. Phys. Chem. B* **1997**, *101*, 9463.

(95) Cao, Y.; Banin, U. *J. Am. Chem. Soc.* **2000**, *122*, 9692.

(96) Ghosh, P.; Oliva, J.; De la Rosa, E.; Haldar, K. K.; Solis, D.; Patra, A. *J. Phys. Chem. C* **2008**, *112*, 9650.

(97) Kulshreshtha, S. K.; Sasikala, R.; Sudarsan, V. *J. Mater. Chem.* **2001**, *11*, 930.

(98) Lee, E. J. H.; Ribeiro, C.; Longo, E.; Leite, E. R. *J. Phys. Chem. B* **2005**, *109*, 20842.

(99) Ranade, M. R.; Navrotsky, A.; Zhang, H. Z.; Banfield, J. F.; Elder, S. H.; Zaban, A.; Borse, P. H.; Kulkarni, S. K.; Doran, G. S.; Whitfield, H. J. *Proc. Natl. Acad. Sci. U.S.A.* **2002**, *99*, 6476.

(100) Bryan, J. D.; Gamelin, D. R. *Doped Semiconductor Nanocrystals: Synthesis, Characterization, Physical Properties, and Applications*; John Wiley & Sons, Inc.: New York, 2005; p 47-126.

CHAPTER VI

(1) Burke, M. S.; Trotochaud, L.; Boettcher, S. W., In preparation.

(2) Lin, F. D.; Boettcher, S. W. *Nat. Mater.* **2014**, *13*, 81.

(3) Mills, T. J.; Boettcher, S. W., Accepted, **2014**, *Phys. Rev. Lett.*

(4) Trasatti, S. *J. Electroanal. Chem.* **1980**, *111*, 125.

(5) Trasatti, S.; Lodi, G. Oxygen and chlorine evolution at conductive metallic oxide anodes. In *Electrodes of Conductive Metallic Oxides*; Trasatti, S., Ed.; Elsevier: Amsterdam, 1981; Vol. B; p 521.

(6) Man, I. C.; Su, H.-Y.; Calle-Vallejo, F.; Hansen, H. A.; Martínez, J. I.; Inoglu, N. G.; Kitchin, J.; Jaramillo, T. F.; Nørskov, J. K.; Rossmeisl, J. *ChemCatChem* **2011**, *3*, 1159.

(7) Rossmeisl, J.; Qu, Z.-W.; Zhu, H.; Kroes, G.-J.; Nørskov, J. K. *J. Electroanal. Chem.* **2007**, *607*, 83.

(8) Suntivich, J.; May, K. J.; Gasteiger, H. A.; Goodenough, J. B.; Shao-Horn, Y. *Science* **2011**, *334*, 1383.

(9) Umena, Y.; Kawakami, K.; Shen, J.-R.; Kamiya, N. *Nature* **2011**, *473*, 55.

(10) Debus, R. J. *Coord. Chem. Rev.* **2008**, *252*, 244.

(11) Yang, P.; Rizvi, A. H.; Messer, B.; Chmelka, B. F.; Whitesides, G. M.; Stucky, G. D. *Adv. Mater.* **2001**, *13*, 427.

(12) Caruso, R. A.; Antonietti, M. *Chem. Mater.* **2001**, *13*, 3272.